ABSTRACT

MOUSA, MOATAZBELLAH MAHMOUD. High Throughput Atomic Layer Deposition Processes: High Pressure Operations, New Reactor Designs, and Novel Metal Processing. (Under the direction of Gregory N. Parsons).

Atomic Layer Deposition (ALD) is a vapor phase nano-coating process that deposits very uniform and conformal thin film materials with sub-angstrom level thickness control on various substrates. These unique properties made ALD a platform technology for numerous products and applications. However, most of these applications are limited to the lab scale due to the low process throughput relative to the other deposition techniques, which hinders its industrial adoption. In addition to the low throughput, the process development for certain applications usually faces other obstacles, such as: a required new processing mode (e.g., batch vs continuous) or process conditions (e.g., low temperature), absence of an appropriate reactor design for a specific substrate and sometimes the lack of a suitable chemistry.

This dissertation studies different aspects of ALD process development for prospect applications in the semiconductor, textiles, and battery industries, as well as novel organic-inorganic hybrid materials. The investigation of a high pressure, low temperature ALD process for metal oxides deposition using multiple process chemistry revealed the vital importance of the gas velocity over the substrate to achieve fast depositions at these challenging processing conditions. Also in this work, two unique high throughput ALD reactor designs are reported. The first is a continuous roll-to-roll ALD reactor for ultra-fast coatings on porous, flexible substrates with very high surface area. While the second reactor is an ALD delivery head that allows for *in loco* ALD coatings that can be executed under ambient conditions (even outdoors) on large surfaces while still maintaining very high deposition rates. As a proof of concept, part of a parked automobile window was coated

using the ALD delivery head. Another process development shown herein is the improvement achieved in the selective synthesis of organic-inorganic materials using an ALD based process called sequential vapor infiltration. Finally, the development of a new ALD chemistry for novel metal deposition is discussed and was used to deposit thin films of tin metal for the first time in literature using an ALD process.

The various challenges addressed in this work for the development of different ALD processes help move ALD closer to widespread use and industrial integration.

© Copyright 2015 MoatazBellah Mahmoud Mousa

All Rights Reserved

High Throughput Atomic Layer Deposition Processes: High Pressure Operations, New Reactor Designs, and Novel Metal Processing

by
MoatazBellah Mahmoud Mousa

A dissertation submitted to the Graduate Faculty of
North Carolina State University
in partial fulfillment of the
requirements for the Degree of
Doctor of Philosophy

Chemical Engineering

Raleigh, North Carolina

2015

APPROVED BY:

_____	_____
Dr. Gregory N. Parsons Committee Chair	Dr. Saad A. Khan
_____	_____
Dr. Michael D. Dickey	Dr. Jesse S. Jur

DEDICATION

To my father, Mahmoud, and my mother, Mervat, for your unconditional love and support.

To my brother, Moatasem Bellah, for the fun of learning together.

To my wonderful wife, Hadia, for always giving me the motives to excel.

To my son, Mahmoud, for putting an eternal smile in my heart.

BIOGRAPHY

Moataz Bellah Mousa was born and raised in Cairo, Egypt. After receiving his international general certificate of secondary education (IGCSE), he earned his bachelor's and master's degrees in chemical engineering from Cairo University in 2007 and 2010, respectively. During his M.Sc. studies, he worked as a teaching assistant where he assisted the instruction of multiple courses including transport phenomena and materials engineering. His master's research was focused on developing new reactor designs using computational fluid dynamics (CFD) modeling. In fall 2010, he pursued a Ph.D. in chemical engineering at North Carolina State University under the guidance of Prof. Gregory Parsons. His research focused on thin films deposition and characterization using atomic layer deposition (ALD) processes for applications in polymers modification, surface passivation, and metal coatings for microelectronic devices. He also expanded his experience in reactors design during his Ph.D. years and worked on developing new ALD reactors and chemistry. Along with pursuing his research interest in thin films deposition, Moataz also followed his interest in entrepreneurship and received a graduate certificate in technology commercialization and entrepreneurship from the Poole College of Management in spring 2013. The work done during the commercialization classes was the basis of founding Tethis, inc.; a Raleigh, NC based startup materials company. Moataz will join the R&D team at ASM America in Phoenix, AZ after graduation.

ACKNOWLEDGMENTS

I would like to express my sincere gratitude to several people in the next few lines, without them you would not have been reading these lines. First and foremost, my advisor Prof. Gregory Parsons, who taught me the research attitudes and ethics through being an exemplary eager scientist. He guided me whenever needed and gave me enough space to explore new ideas. Second, my parents, Mahmoud Mousa and Mervat El-Shaarawy, no words can thank you enough but I quoted this proverb for you "One can pay back the loan of gold. But one dies forever in debt to those who are supportive, kind, sacrificing and always caring and sharing".

To my wife, Hadia Elhadidy, your steady support and smile got me to overcome many setbacks. I cannot imagine how I would have achieved any of this without you being by my side. Thanks for being who you are. For my almost one year old son, future scientist, thank you for putting a smile on my face no matter what was going on.

A million thanks to all of the past and present members of Parsons' research group, you made it tough for me to easily enjoy working anywhere else. It was a pleasure to work, chill and travel with all of you. Thank you for the amazing memories that I will cherish forever.

For the Egyptian fellows in Raleigh, thank you for making this city a home away from home. We had a lot of fun together and looking forward to meet all of you again in Egypt. Special acknowledgement is due to Dr. Mohammed Gamal, we have been together through B.S., M.S. and Ph.D. and now it is time to say "until we meet again".

Finally, I would like to thank all of the faculty and staff of the Chemical and Biomolecular Engineering department at NCSU for their great help and support as well as all of the research collaborators from the Textiles Engineering, and Materials Science departments.

TABLE OF CONTENTS

LIST OF FIGURES viii

CHAPTER 1: Introduction and Background 1

1.1 Atomic Layer Deposition (ALD) 2

1.1.1 Process Overview 2

1.1.2 ALD in Manufacturing 4

1.1.3 ALD Reactors 6

1.1.4 Atmospheric Pressure Atomic Layer Deposition (AP-ALD) 8

1.1.5 Sequential Vapor Infiltration (SVI) 10

1.2 Metals and Metal Oxides ALD 11

1.2.1 Metal Oxides Deposition: Water vs Ozone as a Co-reactant 11

1.2.2 Metals Deposition by Thermal ALD: Reducing agents 13

1.3 Overview of the Key Advances in ALD Presented in this Dissertation 16

1.4 References 27

CHAPTER 2: Experimental Tools 35

2.1 Thin Films Deposition Tools 36

2.2 Characterization Tools 37

2.3 References 46

CHAPTER 3: Effect of Temperature and Gas Velocity on Growth per Cycle during Al_2O_3 and ZnO Atomic Layer Deposition at Atmospheric Pressure 47

Abstract 48

3.1 Introduction 49

3.2 Materials and Methods 51

3.3 Results and Discussion 53

3.4 Summary 61

3.5 Acknowledgements 61

3.6 Supplemental Material 66

3.7 References 67

CHAPTER 4: Atmospheric Pressure Atomic Layer Deposition of Al_2O_3 using Trimethyl Aluminum and Ozone 71

Abstract 72

4.1 Introduction 73

4.2 Materials and Methods 76

4.3 Results and Discussion 79

4.4 Summary 88

4.5 Acknowledgments 90

4.6 References 98

CHAPTER 5: Precise Nanoscale Modification and Coating of Macroscale Objects: Open-Environment *in Loco* Atomic Layer Depositon on an Automobile 102

Abstract 103

5.1 Introduction 104

5.2 Materials and Methods 105

5.3 Results and Discussion 108

5.4 Summary 116

5.5 Acknowledgments 117

5.6 Supplemental Material 123

5.7 References 133

CHAPTER 6: Design of a High Throughput Spatial Atomic Layer Deposition Reactor for Functional Nano-coatings on Porous Materials 137

Abstract 138

6.1 Introduction 139

6.2 Materials and Methods 143

6.3 Results and Discussion 147

6.4 Summary 159

6.5 References 169

CHAPTER 7: Atmospheric Pressure Synthesis of Photoluminescent Hybrid Materials by Sequential Organometallic Vapor Infiltration into Polyethylene terephthalate Fibers 173

Abstract 174

7.1 Introduction 175

7.2 Materials and Methods 177

7.3 Results and Discussion 179

7.4 Summary 188

7.5 Acknowledgments 188

7.6 Supplemental Material 197

7.7 References 199

CHAPTER 8: Tin Metal Atomic Layer Deposition using Tin(IV) Chloride and a Silyl Dihydropyrazine Reducing Agent 203

Abstract 204

8.1 Introduction 205

8.2 Materials and Methods 207

8.3 Results and Discussion 210

8.4 Summary 220

8.5 Acknowledgments 221

8.6 References 230

Appendix 234

Appendix A1: Three Reactants Atomic Layer Deposition Process of ZnO using Diethyl Zinc, Water and Ozone 235

LIST OF FIGURES

Figure 1.1. Aluminum oxide cyclic deposition using ALD process starting with hydroxyl terminated surface. (1 and 2) Methyl terminated surface is formed after Tri-methyl Aluminum (TMA) dosing and purging then (3 and 4) turns to hydroxyl terminated surface again, with formation of Al_2O_3 atomic layer, after dosing and purging of water. The occuring half reactions at each dosing step are shown in the figure as well as the net overall reaction. (Adapted with modification from [71]) 23

Figure 1.2. ALD process temperature window. The variation of growth with the substrate temperature where self limiting reactions and surface saturation only occur within the ALD window range (green line).. 24

Figure 1.3. Various designs of ALD reactors for different substrate types. A) Planar substrates involve flow of the gases over the surface either for a-1,2,3) single wafer[31] or a-4) multiple wafers[9]. B) Particles of different sizes coated in b-1) fluidized bed reactor[72-74] and b-2) rotary drum reactor[75,76]. C) ALD reactors for polymer webs and other flexible substrates were illustrated by c-1) Lotus Applied Technologies[77] and c-2) Beneq[78], while D) porous substrates[79] as fibers and textile materials will require a flow through reactor designs. 25

Figure 1.4. Schematics showing the conceptual differences between a) spatial ALD and b) temporal ALD processes, as well as c) an example of a continuous linear spatial ALD reactor. (Adapted from [80]) 26

Figure 2.1. Schematic of a home-built modified ALD flow tube reactor that allows for deposition under wide pressure range. The controlled pneumatic valves positions are not shown. 44

Figure 2.2. A schematic for boundary layer (in red) and velocity profile development for laminar gas flow through a tube reactor. 45

Figure 3.1. Growth per cycle for ALD of Al_2O_3 as a function of deposition temperature for reactor pressures of 2 and 760 Torr. Deposition was performed in a reactor system with specially designed gas delivery to allow operation with adjustable pressure. The figure also identifies the gas pulse timing used for deposition. The growth rate is larger at higher pressure, and under the conditions used, the increase is independent of temperature for T<150 °C. At higher temperatures, the growth rates begin to converge, consistent with the onset of a thermally activated mechanism. 62

Figure 3.2. ALD growth per cycle for ZnO versus temperature. The thickness per cycle at 760 Torr is larger than at 2 Torr for all temperatures between 40 and 200 °C. The gas pulse conditions used for deposition are identified in the figure. 63

Figure 3.3. Growth per cycle of Al_2O_3 at 760 Torr and 130 °C versus water purging time for several values of N_2 purge gas flow rate. Increasing flow rate increases gas velocity and tends to reduce the growth rate for ALD Al_2O_3, at 0.7 m/s flow velocity, the growth rate becomes close to that measured at 2 Torr. 64

Figure 3.4. Schematic diagram showing the diffusion of physisorbed water molecules from the substrate surface and becoming entrained in the bulk purge gas flow. 65

Figure 3.5. AFM images for Al_2O_3 coatings on silicon substrate at (a) low and (b-e) high pressure depositions. The film deposited at (a) 2 Torr was found to be smooth with roughness about ~0.19 nm. For high pressure depositions, the films got smoother with the increase in purge gas flow rate. The scanned areas were 4x4 μm for all of the samples and the scale bar maximum value is 5 nm. 66

Figure 4.1. Growth per cycles showing saturation behavior of atomic layer deposited Al_2O_3 layers using O_3 and TMA at 2 Torr and 205 ^oC with: (a) fixed TMA dose time; (b) fixed O3 dose time. The error bar reflects a typical ±5% uncertainty in the thickness measurement. Quartz crystal microbalance mass uptake using: (c) one TMA dose followed by three ozone doses; and (d) three TMA doses followed by one O_3 dose. Repeated O_3 or TMA doses show no mass uptake, confirming with fully saturated growth. 91

Figure 4.2. Growth per cycle for Al_2O_3 versus O_3 dose time at: (a) 2 Torr; and (b) 760 Torr for different deposition temperatures. The error bar reflects a ±5% uncertainty in the thickness measurement. The growth per cycle shows that a longer exposure time is needed for saturation at high pressure. 92

Figure 4.3. (a) Mass uptake using in-situ QCM vs. processing time for cycles of TMA/O_3 at purge flow rates of 3, 5 and 10 slm at 760 Torr and 70°C. (b) Growth

thickness per cycle at 2 Torr (0.5 slm purge flow rate) and 760 Torr (3 and 10 slm). The error bar represents typical ±5% uncertainty in the thickness measurement. 93

Figure 4.4. Mass uptake using in-situ QCM vs. processing time for cycles of TMA/O_3 at (a) 2 Torr and (b) 760 Torr at 70 ^oC and 205 ^oC. Mass increases during TMA doses for both temperatures but slightly decreases during O_3 at 205 ^oC and showed large increase at 70 ^oC. 94

Figure 4.5. Refractive index at 600 nm calculated using Cauchy model for thick Al_2O_3 films deposited at different temperatures at 2 Torr and 760 Torr. The index decreases when the temperature is below the ALD temperature window. 95

Figure 4.6. ToF-SIMS depth profiles for Al_2O_3 deposited at 205°C and: a) 2 Torr; b) 760 Torr. Similar film composition is attained. 96

Figure 4.7. Lines represent model results for O_3 molar flow rate along the reactor under 2Torr and 760Torr at 100 ^OC, 150 ^OC, and 205 ^OC. The ozone molar flow rate at the inlet was ~6.8x10-5 mol/sec (20 wt. % at 0.5slm), and the gas velocity was 0.10-0.13 m/s (corresponding to ~5.5 slm) at 760 Torr, and 6.2-7.9 m/s (~ 0.75 slm) at 2 Torr. Data points (triangular and crossed square) represent experimental values of film thickness measurements (left axis) for Al_2O_3 deposited at 2 Torr and 760 Torr at 205 ^oC and different positions in the reactor. The gas pulsing sequence was TMA/N_2/O_3/N_2: 2-30-1-30. 97

Figure 5.1. Reactant delivery apparatus, ALD delivery head and gas flow schematic for *in loco* ALD. The system uses sequential dosing of reactants (e.g. TMA and H_2O) separated by inert gas purge (N_2) to deposit Al_2O_3. Dry N_2 flows at up to 15 standard liters per minute (slm) through a central ¼ inch delivery line. Electronic valves allow N_2 at a maximum flow of ~ 1 slm to intermittently flow into reactant bubblers to deliver vapors in the sequence shown. The disk-shaped ALD delivery head with a ~140 μm step milled over half the surface sits flat on the object to be coated. Gas exits through the central 1 mm nozzle and flows radially through the gap between the head and the substrate, thereby creating a semicircular ALD growth zone. 118

Figure 5.2. Results confirming well-defined ALD using the ALD delivery head. Photographs of silicon substrates coated with (a) 150 and (b) 800 TMA/N_2/H_2O/N_2 cycles at 60 °C yielding uniform ALD coatings approximately 15 and 86 nm thick, respectively, in the semicircular ALD region under the delivery head, between the reactant gas entrance point and the head outer edge. Some excess coating appears at the nozzle outlet and outside the coating head, where excess TMA contacts ambient air and water to create a CVD zone. Changing the TMA and water dose times (c) and number of ALD cycles (d) leads to increasing growth saturation and linear thickness with the number of ALD cycles (~1.05 Å/cycle). A point in panel (d) shows that using 500 TMA/N_2 cycles with no water doses leads to less than 1 nm of film deposition, demonstrating negligible diffusion of ambient moisture to the deposition zone. 119

Figure 5.3. (a) Images for films deposited on silicon using different gap spacing and nitrogen gas flow rates. (b) Velocity contours (m/s) from CFD modeling of steady state N_2 flow through the deposition zone at relevant conditions. Using a sufficient gas flow rate, uniform radial flow is obtained for relatively small gap sizes, leading to uniform deposition. For larger gap sizes, gas can flow straight from the nozzle through the gap. The flow gradient creates a Bernoulli force that can pull ambient air and water vapor into the growth zone, leading to visible nonuniformity in the corresponding experimental deposition images. 120

Figure 5.4. (a) *In loco* ALD apparatus adjacent to a Volkswagen automobile. (b) Close-up image of the ALD head affixed to the rear side window glass, delivering 400 cycles of ALD coating to a local region on the window at 50 °C. (c) ALD-coated window removed from the car for ellipsometry analysis. The circled region corresponds to the ALD head mounting location. (d) Close-up image showing the semicircular ALD zone outlined by multicolored CVD growth. (e) Thickness versus number of ALD cycles measured by ellipsometry for ALD coatings on silicon fixed to the car window and on the window itself. The growth per cycle of the *in loco* ALD tool was 0.95-1.05 Å/cycle, corresponding to high growth rate of ~3 nm/min. 121

Figure 5.5. Example applications of *in loco* ALD: (a-d) corrosion protection of copper and (e-h) localized surface modification of fibers and textiles. (a) An untreated copper sheet. (b) Copper coated with a patterned polymer tape layer. (c) The tape is removed after coating under the ALD delivery head (1000 cycles, TMA/N_2/H_2O/N_2: 0.1/2/0.1/2 s, N_2 = 8.5 slm, 65 °C). (d) After oxidation in air (400 °C, 3 h) the ALD-coated region remains unoxidized,

retaining its original copper color. (e) A modified delivery head was used to deposit spot coatings of ~5 mm diameter onto porous fiber substrates. (f) After localized coating (3 cycles, TMA/N_2 = 200/100 s + H_2O 10 s), a hydrophilic polyethylene terephthalate (PET) fabric becomes hydrophobic in the coated region, repelling red-dyed liquid water. (g and h) The same *in loco* ALD treatment on a hydrophobic polypropylene fiber mat creates local hydrophilic regions that collect and hold red-dyed water droplets. 122

Figure 5.6. Schematics of different designs for the ALD delivery head tested in this study with close ups on the nozzle section, image of the nozzle section and images of samples after deposition of different ALD cycles. Silicon substrates were held in position using a low pressure region generated by the high gas speed based on Bernoulli's principle. Orthogonal and oblique flow outlets were tested and images of silicon wafers from the orthogonal flow design are shown on the right. The ALD delivery head is operated in the a traditional temporal recipe scheme with nitrogen flowed continuously through the three leading tubes and alternating TMA and H_2O pulses carried by nitrogen from the respective delivery lines. 124

Figure 5.7. Deposition pattern and radial velocity contours (m/s) using the orthogonal flow ALD delivery head design shown in Figure 5.6. (a) CFD model velocity contours for steady state radial N2 flow through a 250 μm head/substrate gap. (b) Magnification of a coating (c) deposited using the radial flow head. (d) Thickness versus radial position determined by SEM (e). The model and experimental results are aligned to show the four distinct flow zones identified in the model: I, stagnant flow; II, uniform radial flow; III, gas circulation and

turbulence; and IV, uniform radial flow. (f) A sample showing an alternate non–uniform coating pattern produced using the design in Figure 5.6. During coating, this sample was held in place only by the Bernoulli pressure and it vibrated noticeably during the run, likely producing the visible wave–pattern in the deposited film. 125

Figure 5.8. The plot shows a linear relation between the film thickness measured using ellipsometry in Region IV (R=6 mm) shown in figure 5.7 versus number of ALD cycles suggesting growth in this zone follows a characteristic ALD growth mode with a growth per cycle of 0.95-1.05 Å/cycle. It was observed that the deposited film was ~10% thicker when the purge time was decreased from 50 to 20 sec indicating insufficient removal of excess reactants and byproducts at the lower purge time. The plot also shows ~5 nm of Al_2O_3 was deposited after 300 TMA/N_2 dose purges steps with no water doses indicating slight diffusion of ambient moisture into the deposition zone..... 126

Figure 5.9. Turbulence effect on growth at the nozzle outlet of the ALD delivery head. a) Contours of the turbulent kinetic energy (m^2/s^2) over the deposition surface from CFD modeling of steady state N_2 flow. b) and c) Images of the films deposited with 600 ALD cycles on silicon at 140 μm gap and 10 slm purge flow rate with 2 sec and 6 sec purge times respectively. The film thickness at the CVD-point zone decreased with increasing the purge time, consistent with removal of entrained excess reactants at the formed eddies in this zone. 128

Figure 5.10. Extent of CVD beyond the edge of the delivery head for various TMA exposure times per cycle. Longer exposure time produced more unreacted TMA leaving the growth zone, resulting in more CVD beyond the surface covered by the delivery head. 130

Figure 5.11. Drawings showing the positioning of ALD delivery heads on a) low curvature and b) high curvature surfaces. The head design with oblique outlet and ~8 cm^2 flat deposition area cannot contact closely high curvature surface where a design that covers much smaller area is needed like (c) an ALD "pen". The proposed design (c), not to scale, is an orthogonal flow one with inverted vortex shape to avoid formation of stagnant points on the deposition surface. It also should cover low deposition area ($\leq$ 0.5 cm^2) to fit closely on (b) highly curved and irregular surfaces. 132

Figure 6.1. Schematics of the spatial ALD setup. (a) Substrate going through the TMA and H_2O reactant zones separated by N_2 in a tool comprising 3 ALD cycles. (b) Linear reciprocating motion of a substrate under a spatial ALD tool comprising X number of ALD cycles to achieve a total number of cycles equals to X multiplied by the number of reciprocations. (c) Conceptual design of the spatial ALD showerhead where the gas flows through a gas manifold to get distributed to the respective channels and next through the nozzle arrays beneath these channels. 161

Figure 6.2. The building blocks of the spatial ALD reactor for porous materials. (a) The vented cabinet enclosing the roll-to-roll system and the reactor showerheads. (b) The reactor consists of 3 showerheads of equivalent size and design, however reactants flow only through the central showerhead, while the two side ones provide inert gas (N_2) flow only. (c) The

showerhead setup consisting of (c1) gas manifold tubes and (c2) gas channels leading to the outlet nozzle arrays. (c3) and (c4) are the bottom views of the (c1) gas manifold tubes and (c2) channels, respectively. 162

Figure 6.3. The CFD model and results for N_2 flow through the TMA line. (a) CFD geometry of the TMA manifold tube leading to the 5 TMA channels, each having 75 gas outlets (nozzles). (b) The total outlet flow rate through each channel for different inlet flow rates and channel diameters. The results for 1 slm at 1/4 in and 1/8 in channel diameters were plotted on a different scale (right) to clearly show the variation in uniformity. (c) Outlet gas velocity profile of different TMA channels from two separate CFD runs, one with 1/4 in channels and the second with 1/8 in channels. Both runs were done with 1 slm inlet flow rate to a 1/2 in manifold tube. (d) Compiled data for the COV in outlet velocity of several CFD runs using different manifold tube and channel diameters for various inlet gas flow rates. The COV was determined by dividing the standard deviation in velocity per channel by the average outlet velocity of this channel. The error bars represent the different COV values for the 5 channels for each CFD run. 163

Figure 6.4. Outlet gas velocity profiles for (a) the twelve channels of the main N_2 line and (b) the six channels of the water line at inlet flow rates of 9 and 3 slm respectively. Both modeling runs had manifold tubes featuring 1/4 in inlet and 1/8 in outlets, along with 1/4 in channels comprising 75 nozzles outlets of 0.5 mm diameter each. 164

Figure 6.5. Images of the top and bottom sides of the non-woven PP fabrics after 100 ALD cycles using the single nozzle (1/4 in tube) ALD delivery head presented in chapter 4 at

different gap spaces between the nozzle and the fabric. The coated area turns hydrophilic and the extent of which was determined using red-dyed water. The coated area on the top surface of the fabric grew by increasing the gap spacing, however gas penetration through the fabric decreased significantly. 165

Figure 6.6. (a) 3D geometry of the CFD model to determine flow and species uniformity on the porous surface. The model has different flow inlets for the different nozzle arrays, a porous zone and pressure outlets. The inlet volume fractions of H_2O and TMA were set to 0.05 at their respective nozzles. The flow rate through the N_2 channels was set to 10 slm for all the runs. (b-d) The contours of the volume fraction of N_2 on the porous zone top plane at different gap spacing and outlet gas flow rates as indicated in the figure. The red color indicates N_2 zones, with volume fraction ~1, between the two reactant zones (blue color) verifying that the suggested design specifics and process conditions prevents reactants from mixing. 166

Figure 6.7. Velocity contours through the nozzles, gap spacing and the porous zone. Results shown are for gap spacings of 0.4 and 1 mm, and flow rates of 3 and 5 slm. 1 m/s inlet velocity was used for the 3 slm run. The plane where these velocity contours were determined is shown by the dotted lines in the top right image. The velocity profile became more uniform, constant contour color, by increasing the gap spacing from (a) 0.4 mm to (b) 1 mm within the same channel at total flow rate of 3 slm and by increasing the flow rate from (a) 3 slm to (c) 5 slm at gap spacing of 0.4 mm. Eddies formed between the nozzles at the larger gap size of 1 mm, as shown by the close up image of (b). 167

Figure 6.8. Al_2O_3 coatings using the Spatial ALD process for porous substrates. (a) Images of silicon strips placed on top of the PP web were used to determine the extent of ambient moisture diffusion into the deposition area. The process was run with no water flowing to the deposition zone for 100 ALD cycles, thus any film growth could be attributed to ambient moisture. The flow rates beside the images are for the flow through the main N_2 line. (b) Image of the PP fabric after being immersed in red-dyed water post-deposition of 100 ALD cycles using the spatial ALD process. (c) Comparing the change in water contact angle of the non-woven PP fabric against the number of ALD cycles produced using temporal and spatial ALD processes. The dose sequence ($TMA/N_2/H_2O/N_2$) of the temporal ALD was 0.5/30/0.5/30 sec. The spatial ALD process was run at a substrate speed of ~5 m/min with N_2 flow rates at the central showerhead of 15, 0.4 and 0.15 slm through the main N_2 line, TMA bubbler and H_2O bubbler respectively. 168

Figure 7.1. Mass gain of samples treated with SVI at a) 2.5 Torr and b) 760 Torr as a function of number of TMA cycles at various process temperature. 190

Figure 7.2. Comparison of mass gain for samples treated by SVI process with 60 cycles of TMA at 2.5 and 760 Torr for process temperature between 60 °C and 150 °C. 191

Figure 7.3. FTIR spectra of samples treated with SVI a) 30 cycles, b) 60 cycles at 2.5 Torr and c) 30 cycles, b) 60 cycles at 760 Torr for process temperature between 60 °C and 150 °C. 192

Figure 7.4. Consumption of C=O peak in FTIR spectra as function of temperature after 30 and 60 cycle SVI treatment at a) 2.5 Torr and b) 760 Torr. 193

Figure 7.5. Calculated diffusivity values of TMA molecules in N_2 as a function of pressure at 60, 90, 120 and 150 °C..... 194

Figure 7.6. Optical images of samples masked during 30 cycle TMA exposure SVI experiments at 60 °C at 2.5 Torr ((a) and (c)) and 760 Torr ((b) and (d)) under normal light ((a) and (b)) and UV illumination ((c) and (d)). 195

Figure 7.7. Schematic of hybrid materials formation through the fabric cross-section in the case of a) ideal masking, b) low resolution masking at low pressures, and c) good resolution masking at high pressures. 196

Figure 7.8. Effect of vapor infiltration temperature of TMA in PET and the post-deposition heating on the formed hybrid material. (a) Ex situ FTIR spectra of the PET samples infiltrated at 90 and 150 ºC, as well as the sample infiltrated at 90 ºC followed by a 24 hrs heating at 150 ºC in inert atmosphere. Images of the samples after infiltration at (b) 150 ºC and 90 ºC are shown depicting a clear visual difference in color. Also images for the samples treated at similar infiltration conditions but were heated for 24 hrs at 150 ºC after infiltration are shown in (d) and (e). 198

Figure 8.1. (a) A schematic of the precursor delivery setup that allowed measuring the co-reactant (DHP) vapor pressure at different temperatures via a known volume (hold cell). (b)

Measured vapor pressure vs temperature. During deposition, the DHP vessel was kept at ~68 °C. 222

Figure 8.2. Thermal ALD process characteristics for tin deposition using $SnCl_4$ and DHP. (a) Mass uptake per cycle for 3x multi-doses (3x $SnCl_4$/ 3x DHP) at different reactor temperatures between 130 and 210 ^oC. (b) Mass uptake per cycle against the total number of dosed $SnCl_4$ moles at 170 ^oC and 210 ^oC. The number of dosed DHP moles for each $SnCl_4$ exposure is shown besides the data points on the plot. (c) Thin film growth against processing time using three sequential doses of $SnCl_4$ followed by three sequential doses of DHP at 190 ^oC. The results in the figures confirm the self-saturation nature of the $SnCl_4$/DHP ALD process within the shown temperature window. 223

Figure 8.3. Analysis of the deposited tin metal thin film on silicon substrate using 1500 ALD cycles at a deposition temperature of 190 ^oC using a) ToF-SIMS and b) XPS depth profiles. The deposited metal was capped by titanium nitride (TiN) and titanium oxide (TiO_2) layers to prevent its oxidation on air exposure for the shown ex-situ analysis. 224

Figure 8.4. High resolution XPS spectra for (a) Sn 3d, (b) N 1s, (c) C 1s and (d) Cl 2p for the capped tin thin film, with TiO_2 and TiN, deposited at 190 ^oC after 125 min of argon ions sputtering. (e) Comparison of the chlorine content in the tin films deposited at 130 and 190 ^oC using high resolution XPS spectra for the Cl 2p of both films. Magnified Spectra (10X) are also shown for the N 1s, C1s, Cl 2p scans. 225

Figure 8.5. Cross-sectional SEM images at (a) low and (b) high magnifications for the capped tin thin film with TiO_2 and TiN. The results confirmed the deposition of a conductive layer of elemental Sn metal with a good thickness uniformity. The high magnification inset image in (b) was used to determine the Sn film thickness. 226

Figure 8.6. Working hypothesis of different reaction paths for the interaction of the DHP with a chlorine terminated surface. (1) Both tri-methyl silyl groups on the DHP strip off chlorine from the surface and leaves behind pyrazine molecule that desorbs later depending on the substrate temperature. (2) One chlorine atom reacts with each DHP molecule to form tri-methylsilyl chloride (TMS-Cl) and leaves a methyl terminated surface which gets chlorinated again during the $SnCl_4$ dose. 227

Figure 8.7. In Situ QMS data for the $SnCl_4$/DHP ALD process. Analog scans for m/z range 20-240 during (a) $SnCl_4$ and (b) DHP doses through their respective hold cells; the major peaks are labelled. (c) Traces for selected m/z representing various reactant and product species during multiple sequential doses of the reactants. 228

Figure 8.8. In situ FTIR spectra for tin coatings on anodic aluminum oxide (AAO) deposited at 130 ^oC and 190 ^oC. The spectra were taken after different number of ALD cycles and were referenced to the spectrum of the bare AAO substrate. The exposure and purge sequences for the depositions are also shown on the plots. 229

Figure A1.1. Thickness of deposited (a) ZnO and (b) Al_2O_3 films on native oxide silicon using a three reactants process (precursor/H_2O/O_3) against ozone dose time. Spectroscopic

ellipsometry was used to determine the film thickness. Adding ozone dose to the typical DEZ/H_2O and TMA/H_2O processes has led to a significant change in ZnO growth but a minor one for the Al_2O_3 deposition. 236

Figure A1.2. Mass uptake against ALD processing time for the two reactants (DEZ/H_2O) and 3 reactants (DEZ/H_2O/O_3) processes for ZnO deposition. As the dose time of ozone increases, the average mass uptake decreases. Figure (b) is a close up of (a) and shows that the decrease in mass uptake for longer ozone dose times is due to a lower uptake during the DEZ dose. 237

Figure A1.3. QMS analog scans during the doses of (a) DEZ, (b) H_2O and (c) O_3. Some peaks of interest are ascribed to relevant species. The production of CO_2, alcohols and acetaldehyde suggests that ozone leads to a combustion like reaction on the surface even after a long water dose. 238

Figure A1.4. In-situ FTIR differential spectra for the two reactants (a) (DEZ/H_2O) and (b) three reactants (DEZ/H_2O/O_3) ALD of ZnO. Each spectra was referenced to the one collected from the previous dose and all the runs were done on AAO substrate at 110 ^oC. The spectra were collected after 5 ALD cycles of the same reactants sequence, either DEZ/H_2O or DEZ/H_2O/O_3. 239

Figure A1.5. High resolution XPS scans of O 1s for ZnO ALD on native oxide silicon using (a) DEZ/H_2O, (b) DEZ/O_3, and (c) DEZ/H_2O/O_3 processes. A clear difference in the oxygen bonding states occurs for the different processes. In general the use of ozone in the ALD

process lead to a significant increase in the bonding state occurring at ~530.5 eV binding energy..... 240

CHAPTER 1

Introduction and Background

1.1 Atomic Layer Deposition (ALD)

1.1.1 Process Overview

ALD is a vapor phase nano-coating process for oxide, nitride, sulfide and elemental materials deposition as well as growth of organic and hybrid organic-inorganic thin films. The process proceeds in a cyclic manner and depends on the occurrence of sequential self-limiting reactions on the surface of interest to deposit one atomic layer per deposition cycle. Consequently, the desired coating thickness is determined by the total number of the deposition cycles. In a typical ALD process, the reactants pass over the substrate at distinct steps separated by a purging step to ensure the complete removal of one reactant before the introduction of the next one. This segregation ensures the occurrence of a series of self-limiting heterogeneous reactions on the substrate surface only, and that is how the thickness can be precisely controlled. On the other side, excess reactant exposure does not lead to extra growth due to the self-limiting nature of the occurring surface reactions, which allows for the deposition of very uniform and conformal thin films even on very high aspect ratio structures (e.g. ≥1:1000).[1] Moreover, many of the ALD reactions are highly exothermic thus can occur at low temperatures, as low as room temperature[2] in some cases.

A single ALD deposition cycle comprises the flow of the first reactant over the substrate followed by the flow of an inert gas to purge the first reactant and the formed reaction products then the exposure of the substrate to the second reactant, usually oxidant for metal oxides deposition, followed by a second inert gas flow to purge the second reactant and the other formed products. Now, the substrate surface is ready for a second cycle and so on, till the required thickness is achieved. Figure 1.1 shows a single ALD cycle for aluminum

oxide deposition using tri-methyl aluminum (TMA) and water as the process reactants, as well as the surface reactions occurring during each reactant exposure.

Another common example of an ALD chemistry for metal oxides deposition is zinc oxide growth using diethyl zinc (DEZ) and water, and the involved surface reactions are [3]

Overall Reaction: $Zn(C_2H_5)_2 + H_2O \rightarrow ZnO + 2C_2H_6$

DEZ exposure: $ZnOH^* + Zn(C_2H_5)_2 \rightarrow ZnOZn(C_2H_5)^* + C_2H_6$

Water exposure: $Zn\ (C_2H_5)^* + H_2O \rightarrow ZnOH^* + C_2H_6$

Where * denotes the species bonded to surface and all the other molecules are in gas phase.

Contrary to the commonly shown cartoons for the process, each ALD cycle does not lead to a full monolayer growth even with extended reactants exposure to the substrate, either due to steric hindrance between the chemisorbed layers and/or limited number of reactive sites. Another factor affecting the thickness of the deposited layer per cycle is the processing temperature. The process sensitivity to the substrate temperature depends on the surface chemistry, but in general there is a certain temperature range (ALD window), where the growth per cycle (film thickness per ALD cycle) is constant. Figure 1.2 summarizes the overall effect of the substrate temperature on the growth per cycle during ALD. For temperatures below the ALD window, precursor may condense and/or physisorb on the surface leading to a multi-layer growth per an ALD cycle. On the other side, low substrate temperature can lead to a lower growth than that within the ALD window due to slow kinetics of the surface reaction. At high temperatures, low growth can occur if the ligands

desorption rate is higher than their reaction rate. High growth per cycle, relative to the ALD window, can occur at high temperatures if the precursor started to decompose in the gas phase before chemisorbing on the surface which leads to multi-layer deposition of the undesired species.

1.1.2 ALD in Manufacturing

Atomic layer deposition (ALD) process has been used industrially since the early '80s. The process was initially used in the production of thin film electroluminescent (TFEL) displays in 1983[4, 5], primarily because of the process ability to produce very uniform thin coatings of zinc sulfide based films. About twenty years later, the semiconductor industry started to adopt the ALD process in depositing high-*k* dielectric materials for applications as gate oxides for metal-oxide semiconductor field effect transistors (MOSFET) [6], capacitor dielectrics in dynamic random access memories (DRAM) [7] and in forming gap dielectrics for magnetic heads[8]. The main drive for such development was the ability of ALD to deposit ultra-thin uniform coatings over large wafer sizes with very high conformality on high aspect ratio structures, besides its unique ability to precisely control deposition thickness up to atomic level. Although currently these are the key industrial applications of ALD, it is anticipated to be used in multiple other processing steps in the manufacturing of the next generation logic and memory devices. The promising applications of the ALD process in the semiconductor industry is covered further in the introduction section of Chapter 8 of this dissertation.

The twenty years gap between the use of ALD in the TFEL and the semiconductor industries was mainly due to the slowness of the process relative to the other deposition

techniques. However, eventually ALD proved to be the best choice whenever conformal thin films are required for complex 3D structures. Moreover, the very low deposition rate was mitigated by batch processing of large number of wafers, where up to 100 wafers of the 12" size can be coated per run. [9]

In early 2011, Levitech revealed there continuous fast aluminum oxide ALD system for silicon solar cells passivation. The system allows for deposition rates up to ~1500 nm/hr and is based on the spatial ALD processing which is discussed later in this chapter. Shortly after that, Solay Tech announced a similar system with nearly similar deposition rate but with much lower footprint due to the wafer oscillation back and forth through the deposition region. Although these systems showed fast ALD depositions, they are still limited to planar non- flexible substrates.

Currently, the research and development focus is to extend the benefits of spatial ALD concept to design continuous ultra-high throughput ALD processes operating in a roll-to-roll manner. The significant industrial drive for such process development is the proven ability of ALD coatings to form distinctive diffusion barrier coatings over polymers.[10, 11, 12] Passivation coatings are expected to be the next industrial penetration by ALD besides the predicted expansion of the process use in the semiconductor industry. Another promising industrial applications, not expected to happen soon, is fibrous materials functionalization for various applications as filtration and protective fabrics[13], conductive coatings for wearable sensors[14], and self-cleaning apparels[15]. All of these new applications are relying heavily on

the dry processing at low operating temperatures of the ALD process along with its other merits.

1.1.3 ALD Reactors

Many of the existing ALD reactors designs are inspired by chemical vapor deposition (CVD) counterparts but with more rigorous valve controls to allow for the required sequencing of the reactants. In ALD reactors, ensuring enough reactants exposure to react with "all" of the available surface species is more important than ensuring reactants homogeneity in the gas phase as is the case in the CVD process. Good ALD reactor will be one that allows efficient reactants utilization, the percent of dosed precursor that reacts with the substrate surface, and fast removal of the excess reactants away from the substrate to prevent any mixing between the reactants. ALD reactor designs are tailored for different substrates to optimize these parameters of dosing and purging according to the substrate needs and properties. Figure 1.3 summarizes various thermal ALD reactor designs available in the literature for different substrates. However, the gas delivery requirements are not the only factors that determine the reactor design criteria but also the sought throughput and deposited film properties such as uniformity, purity, continuity, morphology, functionality (e.g. conductivity) and processing requirements. For instance, in the semiconductor industry, the single wafer reactors (Figure 1.3a- 1-3) are used instead of the batch reactors whenever ALD process is followed or preceded by another process (e.g. PVD) where air-break needs to be avoided.

All the shown designs in Figure 1.3 operate under temporal ALD mode except for those in Figure 1.3c, where they adapt a spatial ALD mode. Relative to the conventional

temporal ALD, where deposition occurs at different time intervals, for spatial ALD the dosing and purging steps are done at different positions[10-12] as illustrated in Figure 1.4 and b. The deposition rate, in case of the spatial ALD, is mainly controlled by how fast the half reactions will take place and the time required for moving the substrate between the different reaction zones to ensure excess reactants desorption from the substrate.

Spatial ALD allows for process throughputs tens to hundreds times higher than temporal ALD.[16] The concept of separating reactants in space was introduced long time ago by Suntola in the early patents of the ALD process.[17] However, Levy et al.[12] were the first to report an ALD saturation behavior for zinc oxide (ZnO) growth using the spatial ALD concept. The spatial design[13], shown schematically in Figure 1.4c, has different precursor inlets separated by inert gas (named as gas bearing in Figure 1.4c) and exhaust channels, to prevent reactants mixing and removing reaction products. ALD can then be achieved by moving the coating head or the substrate back and forth. Later on, another spatial ALD reactor design was proposed by Poodt et al.[14] They achieved a growth rate of 1.2 nm/s of aluminum oxide (Al_2O_3) deposition at atmospheric pressure in their "proof of concept" reactor, which comprises a rotating table to expose the substrate to the different zones. A point of interest in these spatial ALD designs is that the distance between the gas inlets and substrate, in both cases, is in the order of micrometers (30-50μm). This very close proximity was attributed to the formation of good diffusion barriers between precursor zones to prevent cross reactions and also to seal the whole reaction zone from the surrounding thus achieving open air process. In this dissertation, it is shown that this proximity is also crucial to achieve efficient purging at high pressure and low temperature operations. More details of the spatial

ALD process, reactor designs and its prospective applications are discussed in the introduction section of chapter 6.

1.1.4 Atmospheric Pressure Atomic Layer Deposition (AP-ALD)

ALD process operations at medium to low vacuum in ultra-clean environment are essential for the semiconductor industry which rely on highly demanding process control in a batch processing manner. For other industries, such level of purity is not required, nonetheless process throughput and continuous mode of operation are critical. The ability to carry ALD processing at atmospheric pressure under ambient conditions will facilitate continuous mode operations and thus the process integration for in-line manufacturing in new industries beyond the semiconductor one. Moreover, working at ambient pressure will eliminate the time needed for reactor evacuation as well as pressure control and maintenance. For example, a roll-to-roll ALD process could be particularly useful to coat polymer webs for packaging or to modify fibrous materials surfaces for filtration or protective fabrics. More examples of the industries that can benefit of a high throughput continuous ALD process operating under ambient conditions are mentioned in the introduction sections of chapters 5, 6 and 7 of this dissertation.

ALD processing was done over wide pressure range, more commonly either under high vacuum[18, 19] or medium vacuum[20], where the latter is more commonly used. High vacuum reactors ($<10^{-6}$ bar) operate under molecular flow with Knudsen number greater than one. In this case, the gas mean free path is high and molecules collision is neglected, which leads to good ALD purging step but poor precursor utilization as the number of precursor collisions with the substrate is low and thus result in low reaction probability. [18, 21] One other drawback

of operating at very low pressures is the requirement of a turbo pump, which adds to the difficulty of the process scaling. On the other hand, most of ALD reactors nowadays are operating in medium vacuum (0.01-5 Torr) conditions under laminar viscous flow[20] with Knudsen numbers lower than 0.01. Viscous flow reactors have better precursors' utilization efficiency, besides being cheaper and easier to scale up. It was shown that the optimum pressure for the viscous flow ALD reactors is around ~1 Torr[22] which represents a tradeoff between the gas advection and the diffusion of reactants and products through the inert gas. During the dosing step, pressure needs to be high enough so that the inert gas can carry enough amount of the precursor for surface saturation and also allows enough hitting (low gas mean free path) with the substrate surface for efficient precursor utilization. As for the purging step, low pressure is favored, since gases diffusivities are inversely proportional with pressure. Low diffusivity, under high pressure, can get the excess precursor or reaction products to stay on the surface even under long purge intervals leading to non-uniform ALD layers. The operating pressure in viscous flow reactor is thus determined based on these two competing effects of dosing and purging requirements.

The gas flow through an ALD reactor at atmospheric pressure will also be under viscous regime, except that higher amounts of precursor can be delivered relative to medium vacuum conditions and that the gas mean free path will be much lower (more surface collisions). These factors will lead to higher reactants exposures and thus short dose times will be needed to saturate the available reactive sites on the substrate. On the other hand, gas flow velocity can be lower relative to the flow at medium vacuum due to the increase in the gas density with the pressure rise. Furthermore, the species diffusion will tend to be much

slower because of its inverse relation with the reactor pressure. These two factors will impose strict purge requirements on the ALD process operating under atmospheric pressure unless counteracted by other factors to speed up the species diffusion at high pressure. A large increase in purge time at atmospheric pressure operations should be avoided because it will lead to a large drop in the overall process throughput. Chapters 3 and 4 of this dissertation discuss ways for maintaining low purge time requirements for operations at atmospheric pressure and show that ALD can be carried out efficiently at high pressure with careful control of gas flow and reactor design.

1.1.5 Sequential Vapor Infiltration (SVI)

The vapor infiltration concept is based on allowing reactive spices in the gas phase to infuse and react in a solid substrate that has abundance of active sites, either on its surface or bulk, as is the case with many polymers. Vapor infiltration can be thought of as a sub-category of ALD but with much longer exposures and purges to cover the very high surface area of the targeted substrates. This is a diffusion controlled process where reactants molecular size and concentration in the gas phase play major role, as well as, the process temperature and total pressure. Various ways have been employed to achieve the extended exposures and purges of the vapor infiltration concept and was even named differently such as sequential infiltration synthesis (SIS) [23], multiple pulsed vapor-phase infiltration (MPI) [24] and sequential vapor infiltration (SVI) [25]. While all these techniques generally aim for forming organic-inorganic hybrid materials, the differences in their processing lead to dissimilar extent of the substrate modification. Many applications were demonstrated using these techniques such as improving mechanical resistance of biological and synthetic

polymers[26, 27], nano-patterning for advanced lithography processes[28, 29] and surface energy modification[30].

The sequential vapor infiltration technique used in this dissertation proceeds through dosing of a metal organic precursor (e.g. TMA, DEZ) but instead of directly purging out the reactant, it is held in the reactor chamber for extended time to allow for its diffusion through the substrate. To ensure high reactant concentration in the gas phase and to remove formed byproducts, the reactor chamber gets purged out and new fresh dose and hold of the same reactant occurs. This sequential dosing, holding and purging of the same reactant occurs for as many times as need to ensure the whole substrate modification and then followed by an extended purge step up to tens of minutes. Following the extended purge, the same dose, hold and purge steps can be repeated for a co-reactant or in some cases the infiltration of the organometallic precursor only is sufficient.

More details of the vapor infiltration processes and their processing techniques can be found in the introduction section of chapter 7.

1.2 Metals and Metal Oxides ALD

1.2.1 Metal Oxides Deposition: Water vs Ozone as a Co-reactant

Metal oxides ALD is the most widely studied and applied class of materials relative to nitrides, sulfides, carbides or elemental ALD. By far the three most commonly deposited oxides by ALD are Al_2O_3, ZnO and TiO_2 due to the high reactivity of their precursors which allows fast depositions of high quality thin films at low temperatures. There is also a large field of study for developing metal oxides for microelectronics applications, mostly for high *k*-dielectric materials, such as HfO_2, ZrO_2, rare earth oxides, $SrTiO_3$, $BaTiO_3$.[31] In this

dissertation, Al_2O_3 was deposited using TMA/ H_2O and TMA/O_3 chemistries, while DEZ/H_2O was used to deposit ZnO and titanium dioxide (TiO_2) was deposited using titanium chloride ($TiCl_4$) and titanium tetra-isopropoxide (TTIP).

The common oxygen sources used to deposit metal oxides by thermal ALD processes are water and ozone, whereas oxygen, hydrogen peroxide and metal alkoxides were used in few cases. While water based ALD chemistry proceeds mostly in ligand exchange mechanism as shown earlier for the TMA/H_2O ALD process[32], ozone chemistry are more like combustion reactions with ligand fragmentation occurring. Although the details of the ozone based reactions are not widely explored in the literature, the overall reaction with TMA can be written as[31],

$$2Al(CH_3)_3(g) + nO_3(g) \rightarrow 2Al_2O_3(s) + CO_x(g) + H_2O(g) + \text{possible other products}$$

A review of the TMA/O_3 ALD reaction mechanism studies in the literature is available in the introduction section of chapter 4 of this dissertation.

Ozone has much higher reactivity than water and is commonly used with stable precursors that typically do not react with water like β-diketonates precursors (e.g. $Zr(thd)_4$).[33, 34] Recently, ozone is being investigated to replace water for standard ALD chemistry that proceeds well with water, even the established TMA/H_2O process, since it desorbs faster than water and can be purged out relatively easily, especially from high aspect ratio structures. Ozone also decomposes quickly to non-reactive oxygen which minimizes any CVD characteristics compared to the "sticky" water. Moreover, it was shown that metal oxide thin films deposited by ozone instead of water have better electrical properties for the

high-*k* dielectric applications in the semiconductor industry.[35, 36] On the other side, there are cases where water is favored over ozone as the example of HfO_2 deposition as a gate oxide since ozone high reactivity leads to unacceptable oxidation of the silicon substrate. Also, for lead oxide deposition, there are situations where water is preferred to prevent the formation of volatile and toxic higher oxidized species.[37] In addition, at high temperatures (i.e. $\geq$ 300 ^{o}C), ozone tends to decompose quickly to non-reactive oxygen which will require extended exposure times and suitable reactor design for fast gas delivery. It has also been shown in several studies that metal oxides deposited using ozone had high level of contamination, mainly carbonate, probably due to the formed carbon oxides products.[38, 39] Out of all of these, the major limitation of using ozone in metal oxides ALD is its tendency to recombine on certain surfaces which leads to poor thickness uniformity and conformality.[40-42]

Another interesting ALD chemistry for metal oxides deposition is through using two organometallic precursors. The hydroxyl groups in the metal alkoxides are the source of oxygen in this case.[43, 44] Al_2O_3 and TiO_2 were deposited successfully using aluminum chloride/aluminum alkoxide[43] and titanium chloride/titanium tetra-isopropoxide[45, 46] respectively. The use of two organometallic precursors helps in attaining oxide free interfaces.[43] In this dissertation, the $TiCl_4$/TTIP chemistry was used to form capping layers on deposited elemental tin films to prevent the metal oxidation on air exposure for further ex-situ analysis as shown in chapter 8.

1.2.2 Metals Deposition by Thermal ALD: Reducing agents

Deposition of metals using ALD processes in a layer by layer manner is more challenging relative to the metal oxides deposition. Metal ALD processes are limited to mostly noble, high

work-function materials where uniform nucleation and ultra-thin layer growth can be problematic. Large part of the lack of developed processes for metals deposition is the absence of a universal reaction mechanism and the lack of fundamental understanding of precursor adsorption on metal surfaces with no reaction sites for the cyclic ALD process to occur. Moreover for thermal ALD processes, the absence of a general co-reactant (counterpart to water in metal oxides ALD) with high reduction ability lead to the use of plasma based processes to generate high energy radicals. Hydrogen radicals were able to deposit many metals using plasma enhanced ALD processes like nickel[47], cobalt[48], iridium[49], palladium[50], and even high electropositive metals like aluminum[51], titanium[52] and tantalum[52]. However, plasma based processes are not straight forward and have their complications like damage to delicate substrates, mass transport limitations which leads to a poor thickness conformality in high aspect ratio structures due to the radicals recombination, and the formation of corrosive gases (e.g. HCl, HF) in case of using the hydrogen radicals with halogen based precursors.

For metals deposition using thermal ALD, it has been hard to find an effective reducing agent. Tungsten and Molybdenum deposition processes are the most successful ones that follow the exchange-type reactions of an ALD process, where silanes[53, 54] were used to reduce the metal halides precursors. The tungsten deposition process from tungsten hexa-fluoride (WF_6) and di-silane (Si_2H_6) has wide temperature window (140-300 ^oC) and was reported to deposit pure thin films with very minimal amounts of fluorine, silicon or hydrogen contaminants.[54-56] Molybdenum was also deposited using Molybdenum hexafluoride (MoF_6) and di-silane (Si_2H_6) but showed higher silicon contamination than

tungsten films and had a narrower temperature window (90-120 ^{o}C).[57] Vapors of zinc metal were also used to reduce molybdenum pentachloride ($MoCl_5$) to the metallic state[58], as well as copper(I) chloride (CuCl) to copper[59]. Away from the difficulty of dosing vapors of a metal, the deposited films had high level of zinc contamination and the processes only occurred at very high temperatures.[60] The other successful thermal ALD processes for growing metals are the one employing oxygen to deposit noble metals such as ruthenium[61], platinum[62], palladium[63], and iridium[64]. Nevertheless, this is more of a combustion like chemistry than a reduction one where the oxygen pulse oxidizes the metal surface which then reacts with the ligands of the noble metals precursors. The process is well studied and understood but is not universal and only limited to few noble metals.[65] Finally, due to the lack of a generic mechanism for ALD of metals, a three step process was used in some cases where the metal oxide was deposited first and then reduced through annealing in hydrogen atmosphere.[66] A more comprehensive review of the studied ALD processes for metals deposition can be found in [67].

Pure hydrogen gas was sought to be the generic reducing agent for metals deposition by thermal ALD processes, but only worked in very limited cases owing to its low reactivity. At temperatures $\geq$250 ^{o}C, hydrogen was able to reduce amidinate precursors to deposit some transition metals (Co, Cu, Fe, Ni) in a typical ALD process manner.[68] Recently, new silyl pyrazine based precursors and other derivatives were presented as strong reducing agents that are capable of depositing metals even those with very high negative standard electrochemical potentials in thermal ALD processes.[69] It was shown that titanium can be deposited using 2-methyl- 1,4-bis(trimethylsilyl)-2,5-cyclohexadiene and $TiCl_4$ with a wide ALD temperature

window (120-240 ^{o}C) at a growth rate of ~0.06 nm/cyc and with minimal level of contaminants.[70] Deposition mechanisms are not clear yet and no in-situ characterizations were done so far, also it was not shown if these reducing agents will work for other metal halide precursors to be the pursued universal ALD reducing agent.

1.3 Overview of the Key Advances in ALD Presented in this Dissertation

ALD can be considered a platform technology where many applications and products can be based upon. The technological key strength, beyond its ability to deposit ultra-thin very uniform and conformal coatings, is more about the new functionality and properties that these thin films add to the substrate by adding layers of molecules on top of its surface. Even though the process has shown promising potential to modify, improve, or create new products on the lab scale, industrial production is lacking. The process throughput is often thought of as the hindering factor for the scaling up, however the process development complexity goes beyond just achieving a fast process. In some cases, the industrial adoption requires the process operation in a new untypical environment, which is the case for the continuous roll-to-roll ALD processes where operations need to be done at atmospheric pressure and/or an open air environment. For other applications, it is the lack of a suitable tool design for specific substrate shape that forms the critical process development milestone. For the case of using the ALD process for barrier coating applications on polymers, it is the poor mechanical properties of the deposited films that is considered the major obstacle. Other challenges can be the absence of ALD chemistry for certain thin film materials or the ability to deposit thin films selectively on a given substrate. All of these are examples where the key aspect of ALD process development is not pivoted on the process throughput solely.

This dissertation focuses on overcoming the process development gap of ALD technology for different applications while maintaining or improving the process throughput. This was achieved through understanding the effects of the different process parameters and tailoring them to improve the process outcome, proposing and testing prototypes of new ALD tool designs, and developing new chemistry for novel materials and understanding the underlying surface reaction mechanisms.

In chapters 3 and 4, the effects of the deposition pressure on the ALD process parameters and the deposited Al_2O_3 and ZnO thin films properties were investigated. The findings in these chapters help in the development of ALD processes operating under atmospheric pressure and open to air conditions at low temperatures.

In chapter 3, the processes of Al_2O_3 and ZnO ALD using TMA/H_2O and DEZ/H_2O reactants respectively were investigated. The films deposited at 760 Torr were compared to those grown at 2 Torr under the same growth conditions over wide temperature range (50-200 ^oC). It was found that while the growth per cycle (GPC) was higher (~ 2X) at 760 Torr process, the thin film thickness uniformity was very poor. The drawbacks of operating at high pressure were alleviated through increasing the gas velocity during the purge steps, especially after the water dose, which lead to equivalent process throughput to that of the low pressure ALD process. Longer purge times are typically required for high pressure operations due to the lower gas species diffusivities relative to the low pressure operations. However, increasing the velocity of the purge gas during high pressure operations leads to a decrease in the boundary layer thickness over the substrate which reduces the time required for the

species diffusion before being purged out by the bulk gas flow, thus decreasing the required purge time. The reported understanding of the favorable effect of the gas velocity during the purge step at high pressure and low temperature operations helps in achieving higher process throughputs without compromising the quality of the deposited thin films. This work was published as M.M. Mousa, et. al., J. Vac. Sci. Technol. A (2012) 30, 01A155.

In chapter 4, the use of ozone (O_3) as the oxygen source instead of H_2O for Al_2O_3 ALD was investigated to determine the effect of the new chemistry on the process parameters and deposited films properties at high pressure. The GPC was higher for depositions at high pressure, relative to 2 Torr, and decreased with increasing the gas velocity during the purge step on a similar trend to that of the water based chemistry. However, the required gas velocity was about 1/3 of that for the water based process to achieve GPC and thickness uniformity comparable to those of the depositions carried at 2 Torr. The difference in gas velocity requirements was attributed to the higher desorption rate of O_3 relative to water. It was also noted that longer ozone doses are required at the higher pressure operations to achieve a self-saturation growth and was ascribed due to the higher ozone dissociation rate at the high reactor pressure (760 Torr). Also, the film thickness uniformity over the used flow tube reactor length was found to be lower than that of the water based process and was attributed to the same reason of ozone self-decomposition nature. Finally, the quartz crystal microbalance analysis and the measured refractive indices of the deposited films at different temperatures showed different mass uptake trends and film compositions for the layers deposited at temperatures below 150 ^oC relative to the higher temperatures deposited films. These differences were related to the different reaction mechanisms that occur at low

deposition temperatures where higher carbon content is expected. The ToF-SIMS data confirmed the higher carbon contamination level, both at low and high pressure operations. This chapter in short shows that although using ozone to deposit Al_2O_3 at atmospheric pressure operations leads to shorter purge time requirement relative to the water based process, care need to be taken for the higher dose time needed and the lower film purity especially for low temperature operations. This work was published as M.M. Mousa, et. al., Langmuir (2014) 30, 3741.

In chapters 5 and 6, new high throughput ALD reactors are introduced to extend the process capabilities for *in loco* coatings on huge substrates and for fast coatings on porous substrates aimed for applications in textiles and batteries industries.

The ALD delivery head tool is presented in chapter 5, which allows for *in loco* coatings on macroscale objects, too large to fit in currently available ALD reactors. The tool was used to coat part of an automobile window parked outdoors and showed that the characteristic features of the ALD process can be applied on objects at their native locations under ambient conditions in an open to air environment. High deposition rates of Al_2O_3 up to 3 nm/min were achieved at deposition temperatures as low as 50 ^oC. *In loco* coatings were applied on copper substrate for corrosion protection of specific area on the substrate and on polymer fabrics for local area modification of the wetting properties. Different head designs are proposed and even more can be envisioned for the different surface structures to help protect, encapsulate, repair or optically modify parts of huge objects at their desired

locations. This work was published as M.M. Mousa, et. al., ACS Appl. Mater. Interfaces (2015) 7, 19523.

In chapter 6, a new spatial ALD reactor design for coating porous substrates is explained. Thin films of different materials deposited on fabrics and mesoporous scaffolds by ALD processes in lab scale were shown to have numerous applications in textiles, batteries and solar cells industries. Yet, there is no continuous ALD process to date that can allow for high deposition rates on such porous materials. The chapter discusses the design challenges for developing a spatial ALD tool for porous materials as well as all the gas flow dynamics models used to determine the design specifics and the process parameters. A prototype of the new design is shown, as well as the results of coating a high surface area polypropylene fabric. The preliminary results showed that it took the continuous spatial roll-to-roll ALD tool about 100 sec to deposit 5 nm of Al_2O_3 on ~ 1 m^2 of the fabric surface area, which is a very high area to coat in such short time. The development of such a high throughput tool will speed up the ALD process adoption by the textiles and batteries industries.

The results in chapter 7 show how the disadvantage of slow species diffusion at atmospheric pressure ALD process can be turned to an advantage for developing new applications using a sequential vapor infiltration process. TMA was selectively infiltrated using physical masks in polyethylene terephthalate (PET) fabrics which formed patterns of hybrid organic-inorganic photoluminescent materials on the fabrics. The slow species diffusion at the high process pressure (760 Torr) led to a better patterning resolution relative to the low pressure operations. The extent of the polymer modification, as determined by

gravimetric measurements, was found to be higher at low process pressure and temperatures. As the temperature increased, the pressure effect on the polymer modification became insignificant. These results were explained using simple models showing the difference in species diffusion rates within the reactor, through the polymer matrix and within the fibers at different process pressures. Also, the FT-IR spectra of the samples at different deposition conditions agreed well with the model predictions. Understanding the effect of process parameters on the formed hybrid material, especially with the improved patterning ability, will help in the scaling up of the process for unique applications in flexible electronics and protective identification. This work was published as H.I. Akyildiz, M.M. Mousa, et. al., J. Appl. Phys. (2015) 117, 045301, where the first two authors had equal level of contribution.

Finally, chapter 8 shows another level of the ALD process development where a new chemistry is being investigated for depositing a novel material, tin metal (Sn) thin films. This is the first time in literature to deposit tin metal using an ALD process where tin(IV) chloride and 1,4-Bis(trimethylsilyl)-1,4-dihydropyrazine (in short DHP) were used as a precursor and a reducing agent co-reactant respectively. The quartz crystal microbalance (QCM) analysis showed an ALD process window between ~ 170- 210 ^{o}C. The mass uptake values showed a self-saturation behavior for both reactants with an average uptake per cycle of ~225 ng/cm^2/cyc within the ALD window. The self-saturation was also confirmed using mass spectrometry measurements to track the change in signature peaks of the reactants during multiple sequential doses of $SnCl_4$ and DHP. SEM imaging showed that deposited metal films were uniform over the coated silicon substrate. The formation of Sn-Sn metal bonds was confirmed using X-ray photoelectron spectroscopy analysis and the deposited films were

found to have chlorine, carbon and nitrogen impurities. However, the concentration of impurities were found to drop significantly at high deposition temperatures. Finally, the surface reaction mechanism was investigated using in situ quadrupole mass spectrometer and FTIR analysis.

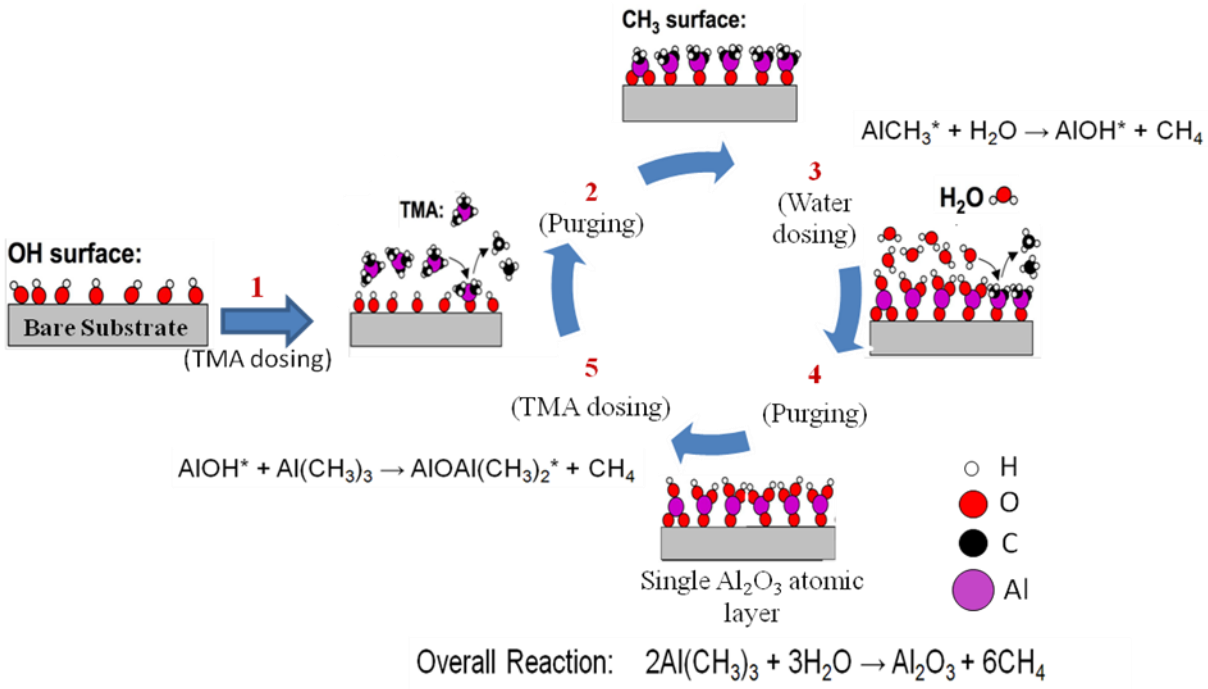


Figure 1.1. Aluminum oxide cyclic deposition using ALD process starting with hydroxyl terminated surface. (1 and 2) Methyl terminated surface is formed after Tri-methyl Aluminum (TMA) dosing and purging then (3 and 4) turns to hydroxyl terminated surface again, with formation of Al_2O_3 atomic layer, after dosing and purging of water. The occurring half reactions at each dosing step are shown in the figure as well as the net overall reaction. (Adapted with modification from [71])

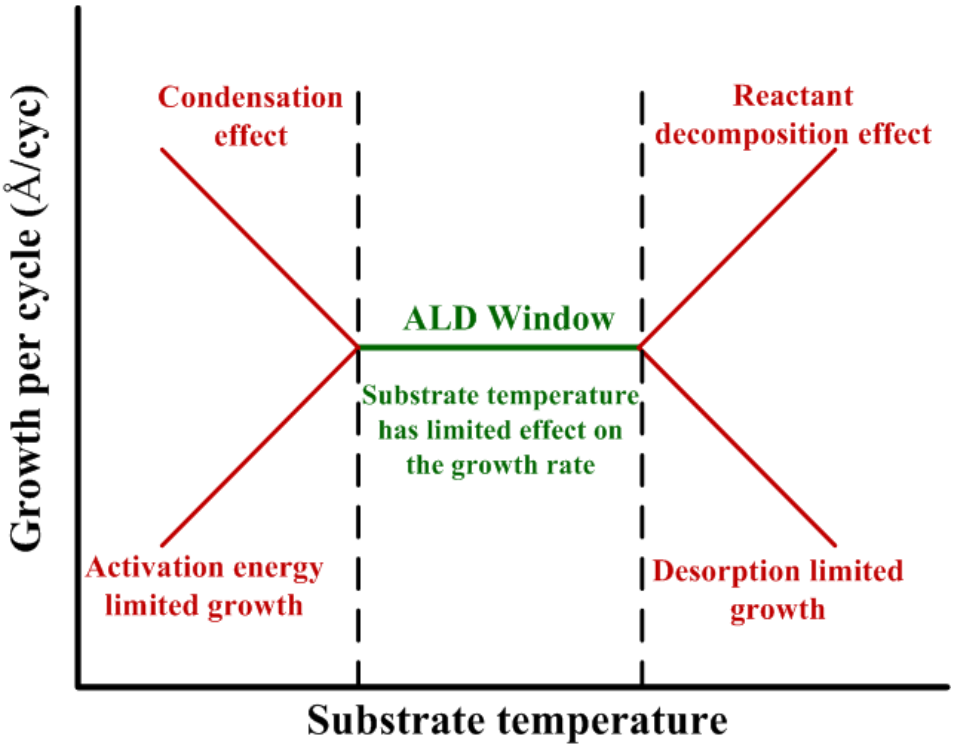


Figure 1.2. ALD process temperature window. The variation of growth with the substrate temperature where self-limiting reactions and surface saturation only occur within the ALD window range (green line).

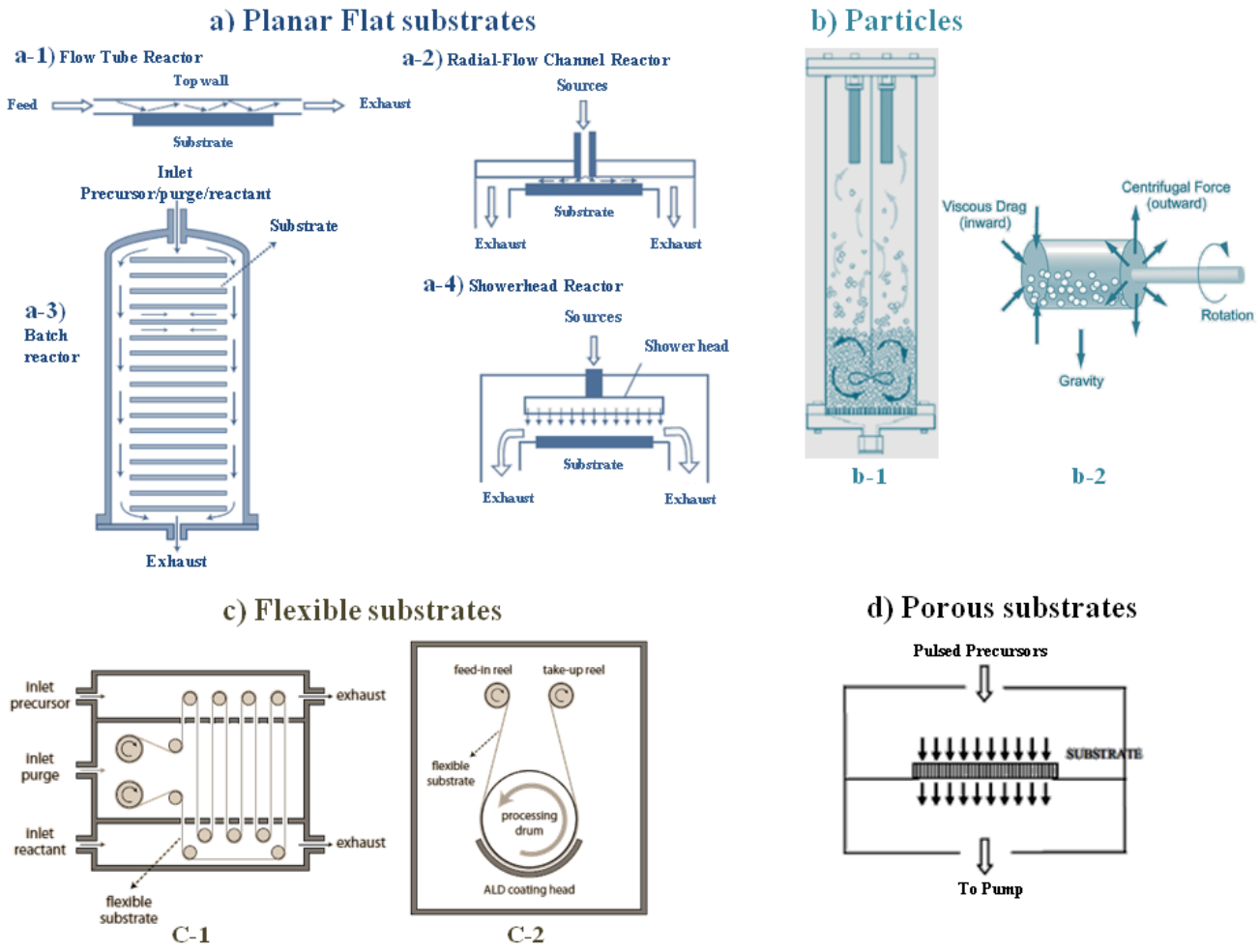


Figure 1.3. Various designs of ALD reactors for different substrate types. A) Planar substrates involve flow of the gases over the surface either for a-1,2,3) single wafer[31] or a-4) multiple wafers[9]. B) Particles of different sizes coated in b-1) fluidized bed reactor[72-74] and b-2) rotary drum reactor[75,76]. C) ALD reactors for polymer webs and other flexible substrates were illustrated by c-1) Lotus Applied Technology[77] and c-2) Beneq[78], while D) porous substrates[79] as fibers and textile materials will require a flow through reactor designs.

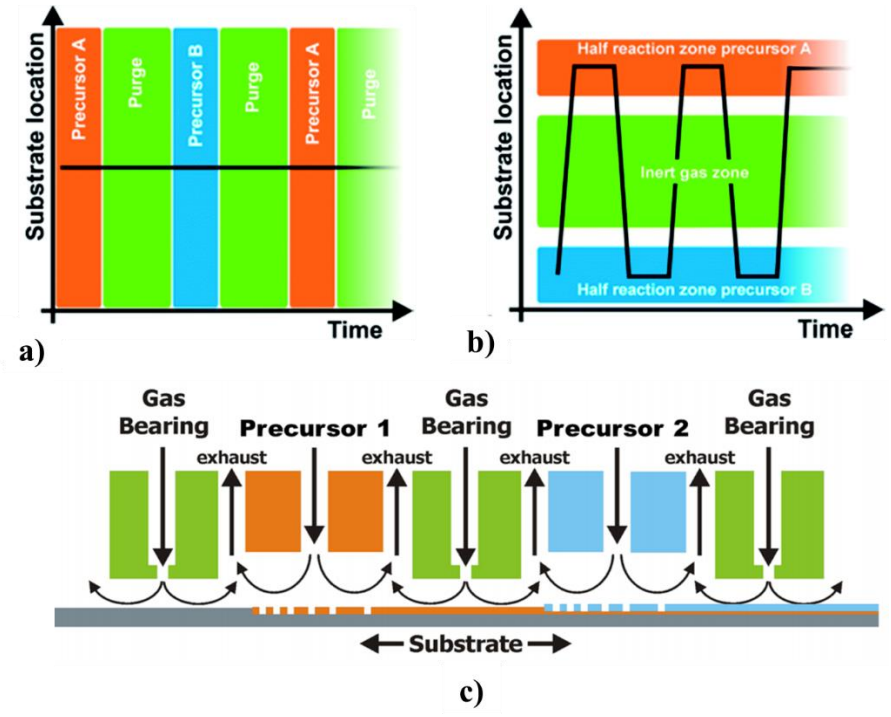


Figure 1.4. Schematics showing the conceptual differences between a) spatial ALD and b) temporal ALD processes, as well as c) an example of a continuous linear spatial ALD reactor. (Adapted from [80])

1.4 References

(1) Gordon, R. g.; Hausmann, D.; Kim, E.; Shepard, J. A Kinetic Model for Step Coverage by Atomic Layer Deposition in Narrow Holes or Trenches. *Chem. Vap. Depos.* **2003**, *9* (2), 73–78.

(2) Groner, M. D.; Fabreguette, F. H.; Elam, J. W.; George, S. M. Low-Temperature Al2O3 Atomic Layer Deposition. *Chem. Mater.* **2004**, *16* (4), 639–645.

(3) Elam, J. W.; Sechrist, Z. A.; George, S. M. ZnO/Al2O3 Nanolaminates Fabricated by Atomic Layer Deposition: Growth and Surface Roughness Measurements. *Thin Solid Films* **2002**, *414* (1), 43–55.

(4) Suntola, T. Atomic Layer Epitaxy. *Mater. Sci. Rep.* **1989**, *4* (5), 261–312.

(5) Suntola, T.; Hyvarinen, J. Atomic Layer Epitaxy. *Annu. Rev. Mater. Sci.* **1985**, *15* (1), 177–195.

(6) Bohr, M. T.; Chau, R. S.; Ghani, T.; Mistry, K. The High-K Solution. *IEEE Spectr.* **2007**, *44* (10), 29–35.

(7) Kim, K. N. Technology for Sub-50nm DRAM and NAND Flash Manufacturing. *Symp VLSI Techn* **2000**, *10*.

(8) Ritala, M.; Niinistö, J. Industrial Applications of Atomic Layer Deposition. *ECS Trans.* **2009**, *25* (8), 641–652.

(9) Granneman, E.; Fischer, P.; Pierreux, D.; Terhorst, H.; Zagwijn, P. Batch ALD: Characteristics, Comparison with Single Wafer ALD, and Examples. *Surf. Coat. Technol.* **2007**, *201* (22–23), 8899–8907.

(10) Charton, C.; Schiller, N.; Fahland, M.; Hollaender, A.; Wedel, A.; Noller, K. Development of High Barrier Films on Flexible Polymer Substrates. *Thin Solid Films* **2006**, *502* (1-2), 99–103.

(11) Hoppe, H.; Sariciftci, N. S. Organic Solar Cells: An Overview. *J. Mater. Res.* **2004**, *19* (7), 1924–1945.

(12) Mayer, A. C.; Scully, S. R.; Hardin, B. E.; Rowell, M. W.; McGehee, M. D. Polymer-Based Solar Cells. *Mater. Today Oxf. U. K.* **2007**, *10* (11), 28–33.

(13) Mahltig, B.; Haufe, H.; Boettcher, H. Functionalisation of Textiles by Inorganic Sol-Gel Coatings. *J. Mater. Chem.* **2005**, *15* (41), 4385–4398.
(14) Jur, J. S.; Sweet, W. J.; Oldham, C. J.; Parsons, G. N. Atomic Layer Deposition of Conductive Coatings on Cotton, Paper, and Synthetic Fibers: Conductivity Analysis and Functional Chemical Sensing Using "All-Fiber" Capacitors. *Adv. Funct. Mater.* **2011**, *21* (11), 1993–2002.
(15) Hyde, G. K.; Park, K. J.; Stewart, S. M.; Hinestroza, J. P.; Parsons, G. N. Atomic Layer Deposition of Conformal Inorganic Nanoscale Coatings on Three-Dimensional Natural Fiber Systems: Effect of Surface Topology on Film Growth Characteristics. *Langmuir* **2007**, *23* (19), 9844–9849.
(16) Poodt, P.; Lankhorst, A.; Roozeboom, F.; Spee, K.; Maas, D.; Vermeer, A. High-Speed Spatial Atomic-Layer Deposition of Aluminum Oxide Layers for Solar Cell Passivation. *Adv. Mater.* **2010**, *22* (32), 3564–3567.
(17) Suntola, T. S.; Pakkala, A. J.; Lindfors, S. G. Apparatus for Performing Growth of Compound Thin Films. US4389973 A, June 28, 1983.
(18) Ott, A. W.; Klaus, J. W.; Johnson, J. M.; George, S. M. Al3O3 Thin Film Growth on Si(100) Using Binary Reaction Sequence Chemistry. *Thin Solid Films* **1997**, *292* (1–2), 135–144.
(19) Sneh, O.; Wise, M. L.; Ott, A. W.; Okada, L. A.; George, S. M. Atomic Layer Growth of SiO2 on Si(100) Using SiCl4 and H2O in a Binary Reaction Sequence. *Surf. Sci.* **1995**, *334* (1–3), 135–152.
(20) Elam, J. W.; Groner, M. D.; George, S. M. Viscous Flow Reactor with Quartz Crystal Microbalance for Thin Film Growth by Atomic Layer Deposition. *Rev. Sci. Instrum.* **2002**, *73* (8), 2981–2987.
(21) Nishizawa, J.; Abe, H.; Kurabayashi, T. Molecular Layer Epitaxy. *J. Electrochem. Soc.* **1985**, *132* (5), 1197–1200.
(22) George, S. M. Atomic Layer Deposition: An Overview. *Chem. Rev. Wash. DC U. S.* **2010**, *110* (1), 111–131.

(23) Peng, Q.; Tseng, Y.-C.; Darling, S. B.; Elam, J. W. A Route to Nanoscopic Materials via Sequential Infiltration Synthesis on Block Copolymer Templates. *ACS Nano* **2011**, *5* (6), 4600–4606.
(24) Lee, S.-M.; Pippel, E.; Gösele, U.; Dresbach, C.; Qin, Y.; Chandran, C. V.; Bräuniger, T.; Hause, G.; Knez, M. Greatly Increased Toughness of Infiltrated Spider Silk. *Science* **2009**, *324* (5926), 488–492.
(25) Gong, B.; Peng, Q.; Jur, J. S.; Devine, C. K.; Lee, K.; Parsons, G. N. Sequential Vapor Infiltration of Metal Oxides into Sacrificial Polyester Fibers: Shape Replication and Controlled Porosity of Microporous/Mesoporous Oxide Monoliths. *Chem. Mater.* **2011**, *23* (15), 3476–3485.
(26) Lee, S.-M.; Pippel, E.; Moutanabbir, O.; Gunkel, I.; Thurn-Albrecht, T.; Knez, M. Improved Mechanical Stability of Dried Collagen Membrane after Metal Infiltration. *ACS Appl. Mater. Interfaces* **2010**, *2* (8), 2436–2441.
(27) Gregorczyk, K. E.; Pickup, D. F.; Sanz, M. G.; Irakulis, I. A.; Rogero, C.; Knez, M. Tuning the Tensile Strength of Cellulose through Vapor-Phase Metalation. *Chem. Mater.* **2015**, *27* (1), 181–188.
(28) Tseng, Y.-C.; Peng, Q.; Ocola, L. E.; Czaplewski, D. A.; Elam, J. W.; Darling, S. B. Enhanced Polymeric Lithography Resists via Sequential Infiltration Synthesis. *J. Mater. Chem.* **2011**, *21* (32), 11722–11725.
(29) Kamcev, J.; Germack, D. S.; Nykypanchuk, D.; Grubbs, R. B.; Nam, C.-Y.; Black, C. T. Chemically Enhancing Block Copolymers for Block-Selective Synthesis of Self-Assembled Metal Oxide Nanostructures. *ACS Nano* **2013**, *7* (1), 339–346.
(30) Gong, B.; Spagnola, J. C.; Parsons, G. N. Hydrophilic Mechanical Buffer Layers and Stable Hydrophilic Finishes on Polydimethylsiloxane Using Combined Sequential Vapor Infiltration and Atomic/molecular Layer Deposition. *J. Vac. Sci. Technol. A* **2012**, *30* (1), 01A156.
(31) Ritala, M.; Niinistö, J. Chapter 4. Atomic Layer Deposition. In *Chemical Vapour Deposition*; Jones, A. C., Hitchman, M. L., Eds.; Royal Society of Chemistry: Cambridge; pp 158–206.

(32) Rahtu, A.; Alaranta, T.; Ritala, M. In Situ Quartz Crystal Microbalance and Quadrupole Mass Spectrometry Studies of Atomic Layer Deposition of Aluminum Oxide from Trimethylaluminum and Water. *Langmuir* **2001**, *17* (21), 6506–6509.
(33) Putkonen, M.; Niinistö, L. Zirconia Thin Films by Atomic Layer Epitaxy. A Comparative Study on the Use of Novel Precursors with Ozone. *J. Mater. Chem.* **2001**, *11* (12), 3141–3147.
(34) Nieminen, M.; Putkonen, M.; Niinistö, L. Formation and Stability of Lanthanum Oxide Thin Films Deposited from β-Diketonate Precursor. *Appl. Surf. Sci.* **2001**, *174* (2), 155–166.
(35) Kim, S. K.; Hwang, C. S. Atomic-Layer-Deposited Al2O3 Thin Films with Thin SiO2 Layers Grown by in Situ O3 Oxidation. *J. Appl. Phys.* **2004**, *96* (4), 2323–2329.
(36) Kim, J. B.; Kwon, D. R.; Chakrabarti, K.; Lee, C.; Oh, K. Y.; Lee, J. H. Improvement in Al[sub 2]O[sub 3] Dielectric Behavior by Using Ozone as an Oxidant for the Atomic Layer Deposition Technique. *J. Appl. Phys.* **2002**, *92* (11), 6739.
(37) Hoffmann-Eifert, S.; Watanabe, T. FeRAM. In *Atomic Layer Deposition for Semiconductors*; Hwang, C. S., Ed.; Springer US, 2014; pp 149–171.
(38) Kosola, A.; Putkonen, M.; Johansson, L.-S.; Niinistö, L. Effect of Annealing in Processing of Strontium Titanate Thin Films by ALD. *Appl. Surf. Sci.* **2003**, *211* (1–4), 102–112.
(39) Goldstein, D. N.; McCormick, J. A.; George, S. M. Al2O3 Atomic Layer Deposition with Trimethylaluminum and Ozone Studied by in Situ Transmission FTIR Spectroscopy and Quadrupole Mass Spectrometry. *J. Phys. Chem. C* **2008**, *112* (49), 19530–19539.
(40) Nilsen, O.; Fjellvåg, H.; Kjekshus, A. Growth of Manganese Oxide Thin Films by Atomic Layer Deposition. *Thin Solid Films* **2003**, *444* (1–2), 44–51.
(41) Klepper, K. B.; Nilsen, O.; Fjellvåg, H. Growth of Thin Films of Co3O4 by Atomic Layer Deposition. *Thin Solid Films* **2007**, *515* (20–21), 7772–7781.
(42) Martinson, A. B. F.; DeVries, M. J.; Libera, J. A.; Christensen, S. T.; Hupp, J. T.; Pellin, M. J.; Elam, J. W. Atomic Layer Deposition of Fe2O3 Using Ferrocene and Ozone. *J. Phys. Chem. C* **2011**, *115* (10), 4333–4339.

(43) Ritala, M.; Kukli, K.; Rahtu, A.; Räisänen, P. I.; Leskelä, M.; Sajavaara, T.; Keinonen, J. Atomic Layer Deposition of Oxide Thin Films with Metal Alkoxides as Oxygen Sources. *Science* **2000**, *288* (5464), 319–321.
(44) Mui, C.; Musgrave, C. B. Atomic Layer Deposition of HfO2 Using Alkoxides as Precursors. *J. Phys. Chem. B* **2004**, *108* (39), 15150–15164.
(45) Chaukulkar, R. P.; Agarwal, S. Atomic Layer Deposition of Titanium Dioxide Using Titanium Tetrachloride and Titanium Tetraisopropoxide as Precursors. *J. Vac. Sci. Technol. A* **2013**, *31* (3), 031509.
(46) Anderson, V. R.; Cavanagh, A. S.; Abdulagatov, A. I.; Gibbs, Z. M.; George, S. M. Waterless TiO2 Atomic Layer Deposition Using Titanium Tetrachloride and Titanium Tetraisopropoxide. *J. Vac. Sci. Technol. A* **2014**, *32* (1), 01A114.
(47) Lee, H.-B.-R.; Bang, S.-H.; Kim, W.-H.; Gu, G. H.; Lee, Y. K.; Chung, T.-M.; Kim, C. G.; Park, C. G.; Kim, H. Plasma-Enhanced Atomic Layer Deposition of Ni. *Jpn. J. Appl. Phys.* **2010**, *49* (5S2), 05FA11.
(48) Yoon, J.; Lee, H.-B.-R.; Kim, D.; Cheon, T.; Kim, S.-H.; Kim, H. Atomic Layer Deposition of Co Using N2/H2 Plasma as a Reactant. *J. Electrochem. Soc.* **2011**, *158* (11), H1179–H1182.
(49) Song, S. I.; Lee, J. H.; Choi, B. H.; Lee, H. K.; Shin, D. C.; Lee, J. W. Hydrogen-Plasma-Assisted Hybrid Atomic Layer Deposition of Ir Thin Film as Novel Cu Diffusion Barrier. *Surf. Coat. Technol.* **2012**, *211*, 14–17.
(50) Eyck, G. A. Ten; Senkevich, J. J.; Tang, F.; Liu, D.; Pimanpang, S.; Karaback, T.; Wang, G.-C.; Lu, T.-M.; Jezewski, C.; Lanford, W. A. Plasma-Assisted Atomic Layer Deposition of Palladium. *Chem. Vap. Depos.* **2005**, *11* (1), 60–66.
(51) Lee, Y. J.; Kang, S.-W. Atomic Layer Deposition of Aluminum Thin Films Using an Alternating Supply of Trimethylaluminum and a Hydrogen Plasma. *Electrochem. Solid-State Lett.* **2002**, *5* (10), C91–C93.
(52) Rossnagel, S. M.; Sherman, A.; Turner, F. Plasma-Enhanced Atomic Layer Deposition of Ta and Ti for Interconnect Diffusion Barriers. *J. Vac. Sci. Technol. B* **2000**, *18* (4), 2016–2020.

(53) Yamamoto, Y.; Matsuura, T.; Murota, J. Surface Reaction of Alternately Supplied WF6 and SiH4 Gases. *Surf. Sci.* **1998**, *408* (1–3), 190–194.
(54) Klaus, J. W.; Ferro, S. J.; George, S. M. Atomic Layer Deposition of Tungsten Using Sequential Surface Chemistry with a Sacrificial Stripping Reaction. *Thin Solid Films* **2000**, *360* (1–2), 145–153.
(55) Grubbs, R. K.; Steinmetz, N. J.; George, S. M. Gas Phase Reaction Products during Tungsten Atomic Layer Deposition Using WF6 and Si2H6. *J. Vac. Sci. Technol. B* **2004**, *22* (4), 1811–1821.
(56) Fabreguette, F. H.; Sechrist, Z. A.; Elam, J. W.; George, S. M. Quartz Crystal Microbalance Study of Tungsten Atomic Layer Deposition Using WF6 and Si2H6. *Thin Solid Films* **2005**, *488* (1–2), 103–110.
(57) Seghete, D.; Rayner, G. B.; Cavanagh, A. S.; Anderson, V. R.; George, S. M. Molybdenum Atomic Layer Deposition Using MoF6 and Si2H6 as the Reactants. *Chem. Mater.* **2011**, *23* (7), 1668–1678.
(58) Juppo, M.; Vehkamäki, M.; Ritala, M.; Leskelä, M. Deposition of Molybdenum Thin Films by an Alternate Supply of MoCl5 and Zn. *J. Vac. Sci. Technol. A* **1998**, *16* (5), 2845–2850.
(59) Juppo, M.; Ritala, M.; Leskelä, M. Deposition of Copper Films by an Alternate Supply of CuCl and Zn. *J. Vac. Sci. Technol. A* **1997**, *15* (4), 2330–2333.
(60) Leskelä, M.; Ritala, M. Atomic Layer Deposition (ALD): From Precursors to Thin Film Structures. *Thin Solid Films* **2002**, *409* (1), 138–146.
(61) Aaltonen, T.; Alén, P.; Ritala, M.; Leskelä, M. Ruthenium Thin Films Grown by Atomic Layer Deposition. *Chem. Vap. Depos.* **2003**, *9* (1), 45–49.
(62) Aaltonen, T.; Ritala, M.; Sajavaara, T.; Keinonen, J.; Leskelä, M. Atomic Layer Deposition of Platinum Thin Films. *Chem. Mater.* **2003**, *15* (9), 1924–1928.
(63) Aaltonen, T.; Ritala, M.; Tung, Y.-L.; Chi, Y.; Arstila, K.; Meinander, K.; Leskelä, M. Atomic Layer Deposition of Noble Metals: Exploration of the Low Limit of the Deposition Temperature. *J. Mater. Res.* **2004**, *19* (11), 3353–3358.

(64) Aaltonen, T.; Ritala, M.; Sammelselg, V.; Leskelä, M. Atomic Layer Deposition of Iridium Thin Films. *J. Electrochem. Soc.* **2004**, *151* (8), G489–G492.
(65) Hämäläinen, J.; Ritala, M.; Leskelä, M. Atomic Layer Deposition of Noble Metals and Their Oxides. *Chem. Mater.* **2014**, *26* (1), 786–801.
(66) Utriainen, M.; Kröger-Laukkanen, M.; Johansson, L.-S.; Niinistö, L. Studies of Metallic Thin Film Growth in an Atomic Layer Epitaxy Reactor Using M(acac)2 (M=Ni, Cu, Pt) Precursors. *Appl. Surf. Sci.* **2000**, *157* (3), 151–158.
(67) Bernal Ramos, K.; Saly, M. J.; Chabal, Y. J. Precursor Design and Reaction Mechanisms for the Atomic Layer Deposition of Metal Films. *Coord. Chem. Rev.* **2013**, *257* (23–24), 3271–3281.
(68) Lim, B. S.; Rahtu, A.; Gordon, R. G. Atomic Layer Deposition of Transition Metals. *Nat. Mater.* **2003**, *2* (11), 749–754.
(69) Knisley, T. J.; Kalutarage, L. C.; Winter, C. H. Precursors and Chemistry for the Atomic Layer Deposition of Metallic First Row Transition Metal Films. *Coord. Chem. Rev.* **2013**, *257* (23–24), 3222–3231.
(70) Klesko, J. P.; Thrush, C. M.; Winter, C. H. Thermal Atomic Layer Deposition of Titanium Films Using Titanium Tetrachloride and 2-Methyl-1,4-Bis(trimethylsilyl)-2,5-Cyclohexadiene or 1,4-Bis(trimethylsilyl)-1,4-Dihydropyrazine. *Chem. Mater.* **2015**, *27* (14), 4918–4921.
(71) Peng, Q.; Sun, X.-Y.; Spagnola, J. C.; Hyde, G. K.; Spontak, R. J.; Parsons, G. N. Atomic Layer Deposition on Electrospun Polymer Fibers as a Direct Route to Al2O3 Microtubes with Precise Wall Thickness Control. *Nano Lett.* **2007**, *7* (3), 719–722.
(72) Hakim, L. F.; Portman, J. L.; Casper, M. D.; Weimer, A. W. Fluidization Behavior and Conformal Coating of Nanoparticles in Fluidized Beds by ALD.
(73) Wank, J. R.; George, S. M.; Weimer, A. W. Nanocoating Individual Cohesive Boron Nitride Particles in a Fluidized Bed by ALD. *Powder Technol. 142* (1), 59–69.
(74) L. F. Hakim, J. B. Nanocoating Individual Silica Nanoparticles by Atomic Layer Deposition in a Fluidized Bed Reactor. *Chem. Vap. Depos.* **2005**, *11* (10), 420–425.

(75) McCormick, J. A.; Cloutier, B. L.; Weimer, A. W.; George, S. M. Rotary Reactor for Atomic Layer Deposition on Large Quantities of Nanoparticles. *J. Vac. Sci. Technol. Vac. Surf. Films* **2007**, *25* (1), 67.
(76) Cavanagh, A. S.; Wilson, C. A.; Weimer, A. W.; George, S. M. Atomic Layer Deposition on Gram Quantities of Multi-Walled Carbon Nanotubes. *Nanotechnology* **2009**, *20* (25), 255602.
(77) Dickey, E.; Barrow, W. A. High Rate Roll to Roll Atomic Layer Deposition, and Its Application to Moisture Barriers on Polymer Films. *J. Vac. Sci. Technol. Vac. Surf. Films* **2012**, *30* (2), 021502.
(78) Kessels, W. M. M.; Hoex, B.; van de Sanden, M. C. M. Atomic Layer Deposition: Prospects for Solar Cell Manufacturing. In *33rd IEEE Photovoltaic Specialists Conference, 2008. PVSC '08*; 2008; pp 1–5.
(79) Ritala, M.; Kemell, M.; Lautala, M.; Niskanen, A.; Leskelä, M.; Lindfors, S. Rapid Coating of Through-Porous Substrates by Atomic Layer Deposition. *Chem. Vap. Depos.* **2006**, *12* (11), 655–658.
(80) Poodt, P.; Cameron, D. C.; Dickey, E.; George, S. M.; Kuznetsov, V.; Parsons, G. N.; Roozeboom, F.; Sundaram, G.; Vermeer, A. Spatial Atomic Layer Deposition: A Route towards Further Industrialization of Atomic Layer Deposition. *J. Vac. Sci. Technol. Vac. Surf. Films* **2012**, *30* (1), 010802.

CHAPTER 2

Experimental Tools

This chapter reviews the main tools used in this dissertation for thin films deposition and analysis.

2.1 Thin Films Deposition Tools

The work done in chapters 3, 4, 7 and 8 of this study was carried out in a hot wall viscous flow tube reactor with a unique gas delivery and pumping systems that allow process operations at pressures ranging between ~1 and 760 Torr, as shown in Figure 2.1.[1] The reactor has two outlets, one to a vacuum mechanical pump and a second connected directly to the laboratory exhaust vent for atmospheric pressure operations. On the other side, the gas delivery system on the reactor allows for controlling the amount of the dosed precursor at the different process conditions where the precursor is charged to an evacuated hold cell, followed by cell pressurization (using N_2) to the desired dosing pressure. The details of reactants dosing and valves control is discussed in the methods section of chapter 3.

All of the depositions using this reactor were done at the middle of the flow tube reactor to avoid inlet and outlet gas flow turbulence effects to achieve consistent results. The velocity profile of the inlet gas flow keeps developing after it enters the reactor, from nearly plug flow to a parabolic one as shown in Figure 2.2. Due to the gas viscosity, boundary layer starts forming around the tube walls and keeps increasing along the tube length until the full parabolic profile is established. Advection gas flow occurs in the longitudinal direction as driven by the existing pressure gradient, while in the radial direction species transport by diffusion as driven by their concentration gradient. The ratio of the species transport by diffusion to that by advection can be determined through Peclet number, which is equal to the

product of the reactor diameter and velocity divided by the diffusion coefficient of a gas species.

The other reactor designs used in this dissertation of *in loco* ALD delivery head reactor and the spatial ALD reactor are described in details in chapters 5 and 6 respectively.

2.2 Characterization Tools

2.2.1 Spectroscopic Ellipsometry

Spectroscopic Ellipsometry technique measures the change in the light polarization state after a standard beam, employing broad range of wave lengths, is reflected from the sample surface. The change in polarization is quantified through measuring the phase difference between the incident and reflected beams and the ratio of their amplitudes.

In this dissertation, a constant-angle alpha-SE spectroscopic ellipsometry (J.A. Woollam Co., Inc.) was used to determine the thickness of different metal oxides thin films and their refractive indices. The light beam was incident on the samples at 70 degrees with a wavelength range between 400-900 nm. By using a suitable model, either cauchy or B-spline, film thicknesses were determined. Both models calculations are based on the assumption that there is a distinct single-layer film with sharp interfaces with the substrate and air. This assumption is highly valid for smooth surfaces. None the less, some of the deposited films in the study were fairly rough. For these films, the root mean square (RMS) roughness values were determined using AFM and then accounted for in the used ellipsometry model.

2.2.2 Quartz Crystal Microbalance

The quartz crystal microbalance (QCM) technique relies on the piezoelectric resonance effect of the quartz material in measuring very small mass changes on the quartz crystal

surface. Any mass change on the crystal will vary the frequency of the quartz crystal resonator. The amount of mass change occurring, either due to a thin layer growth or reaction products removal, is linearly related to the caused change in the frequency. By measuring the frequency shift, the mass uptake or loss on the quartz crystal surface can be calculated.

In this study, QCM was mounted on the viscous flow tube reactor from the samples loading side. Unpolished quartz crystals with gold coating (SC-101, 6 MHz) were purchased from Inficon and used as received. Maxtek BSH-150 bakeable sensor head, where the crystal was mounted, has been modified to supply a nitrogen flow of 150 sccm for depositions under vacuum and 300sccm for the atmospheric pressure ones, to the back surface of the sensor crystal to prevent depositions there.[2] The signals for the frequency change were recorded by a film thickness monitor (Maxtek TM-400), using a home designed LABVIEW program to record the data every 0.01 sec.

In some cases, the QCM results showed non-physical mass uptake or loss due to temperature or pressure fluctuations. Temperature fluctuations showed apparent mass changes and were minimized by monitoring the reactor temperature using a PID controller to damp down any small temperature perturbations. Also, the QCM cell was allowed to stabilize for few hours before any depositions for every new temperature set point. The pressure effects were more difficult to be damped permanently, especially for the atmospheric pressure depositions. However, control runs were carried where TMA source valve was closed and only inert gas was used in dosing and the frequency changes were

monitored and showed that there is no net effect of pressure spikes on the mass uptake values.

2.2.3 Atomic Force Microscope

Atomic Force Microscopy (AFM) operates by passing a probe tip, mounted on a cantilever, over the surface to be tested in very close proximity. Also, there is a laser beam incident on the tip and the reflected beam is detected by a split photo-diode. Any deflection in the probe tip due to the surface morphology will lead to an equivalent change in the laser beam reflection. These variations in reflection are then translated to the surface morphology images and quantitatively to the Root Mean Square (RMS) roughness values.

ALD films are typically very uniform, so RMS values can be a good measure of the quality of the deposited ALD layers. High non uniformities can indicate island growth due to insufficient reactants dosing, poor nucleation or a CVD component effect. Dimension 3000 atomic force microscope (Digital Instruments) with a silicon tip, Veeco Nanoprobe tips (5-10 nm radius of curvature), was used to analyze the surface morphology of multiple deposited films in this dissertation. All scans were done in tapping mode with a frequency of 0.5 Hz.

2.2.4 Time of Flight Secondary Ion Mass Spectrometry (ToF-SIMS)

ToF-SIMS is a very sensitive (can detect ions concentration up to parts per billion) surface characterization technique that allows for determining the chemical species on or under a surface with a sub-micron spatial resolution. On the down side, it is a destructive technique that sputters through the sample.

Depth Profiling using ToF-SIMS was used in different parts of this dissertation. It allowed for comparing the elemental depth uniformity for the films deposited at different conditions. ToF-SIMS depth profiling was also used to confirm the deposition of elemental tin, in chapter 8, for the samples covered with a capping layer, to avoid surface oxidation in air, as well as in determining the contaminant species in the film and their profiles.

A continuous ion beam is used to sputter through the film while another primary ion beam is pulsed to the analysis area to desorb and ionize species from the analysis surface. The produced secondary ions are accelerated, using a high voltage potential, to a mass spectrometer and their mass are determined through measuring the time taken from leaving the substrate until reaching the detector using a simple kinetic energy equation ($ke = \frac{1}{2} mv^2$). For the analysis done in this work, TOF-SIMS V, ION TOF, Inc. Chestnut Ridge, NY tool was used. The instrument has a Bi_{nm}^{+} ($n = 1 - 5$, $m = 1, 2$) liquid metal ion gun as the primary ions source and Cs^{+} ions source for sputtering.

2.2.5 X-ray Photoelectron Spectroscopy

X-ray photoelectron spectroscopy (XPS) is a non-destructive surface analysis technique that allows for determining the existing chemical species at the thin film surface and the bonding between them as well as providing quantitative chemical composition analysis. Monochromatic x-rays from Al or Mg sources are generated by their bombardment with high speed electrons. Then, the generated x-rays are irradiated on the sample surface which results in the emission of electrons at different kinetic energies. The binding energy (BE) of these emitted electrons can be calculated from their measured kinetic energies (KE) as follows[3]:

$$BE = h\nu - KE - \varphi$$

Where $h\nu$ is the x-ray energy (1486.7 eV for kα Al and 1253.5 eV for kα Mg) and φ is the spectrometer work function. Although XPS is known to be a surface analysis tool, the generated electrons are typically produced from the elements in the top 10 nm of the sample.

The counts per second are then determined for each KE and a plot of the calculated BE versus intensity is produced from which all the require analysis can be done. Due to electrons charging effects on the sample surface, the final plot might be shifted by few eV, thus the numbers are usually calibrated to a standard value before carrying out the analysis. For the results in this work, the XPS data was calibrated by referencing adventitious carbon (C 1s peak) to 284.8 eV. Specs XPS system with PHOIBOS 150 analyzer was used in this work and the data reduction and fitting was done using CasaXPS software. The spectral peaks identification was done using data in [3] and [4].

2.2.6 Fourier Transform Infrared Spectroscopy

Fourier Transform Infrared Spectroscopy (FT-IR) is a very useful tool to probe chemical bonding on the sample surface. Ex-situ FTIR was used in this work to determine the changes in the chemical bonding of the polyethylene terephthalate polymer after TMA infiltration. While, in-situ analysis was carried out to determine the surface chemistry occurring during the tin metal deposition.

The basic principle of the FT-IR technique depends on the absorption of parts of the incident infrared beam on a sample where all of the infrared frequencies are measured simultaneously using an interferometer. For the in-situ FTIR measurements, Thermo

Scientific Nicolet 6700 spectrometer was used. The setup of the ALD reactor and the FTIR spectrometer which allowed for in-situ measurements is explained in details in [5]. After each ALD dose step, the reactor was purged out and then allowed to pump down to ~60 mTorr before taking an IR spectrum. During the spectrum recording, the IR beam passed through a single crystal CsI IR window then through the vertically mounted sample in the ALD reactor and then gets reflected off a gold parabolic mirror and focused to MCT-A (mercury cadmium telluride, type A) IR detector after passing through a second CsI IR window.

2.2.7 Quadrupole Mass Spectrometer (QMS)

Mass spectrometry is a powerful technique in identifying and quantifying species in a gas flow through measuring mass-to-charge ratio (m/z) of the ionized species. The various ionized species are separated through deflecting them using electric and magnetic fields then a detector (faraday cup or electron multiplier) records the current induced by the ions of certain m/z when they hit the conducting detector. In this dissertation, the identity of the reaction products for the tin deposition chemistry were determined using MKS Vision 2000c QMS. Also, the self-saturation behavior of both reactants in the tin chemistry were determined by monitoring the change in the reactants amount at the reactor outlet for multiple sequential doses.

The MKS QMS instrument uses a thoriated iridium filament for gas ionization and a triple-filtered quadrupole with a mass range of 1-300 amu (atomic mass unit). Depending on the monitored species partial pressure either a faraday cup was used or an electron multiplier with a gain of 100. The QMS was connected to the outlet of the reactor, where all the exhaust

gas flew by the spectrometer sampling orifice. Care was taken to heat all the lines prior to the QMS to avoid any side reactions that may be occurring at low temperatures. The fragmentation patterns available on NIST Chemistry webbook[6] were used to help in the interpretation of the collected QMS data.

2.2.8 Scanning Electron Microscopy (SEM)

As the name implies, a beam of electrons is used to scan a surface. Electrons are focused on the surface and then back scattered electrons are collected by the detector to image the scanned surface structure. Secondary electrons can also be generated and helps in determining the surface topography. Moreover, the electron bombardment on the surface can lead to x-rays generation which are characteristic of the specific elements of the surface.

The SEM was used in this dissertation multiple times to image surface morphology or determine film thickness via cross-sectional imaging. FEI Verios 460L SEM was used to scan the samples which allows for imaging insulating materials without the need of applying conductive coatings through stage biasing.

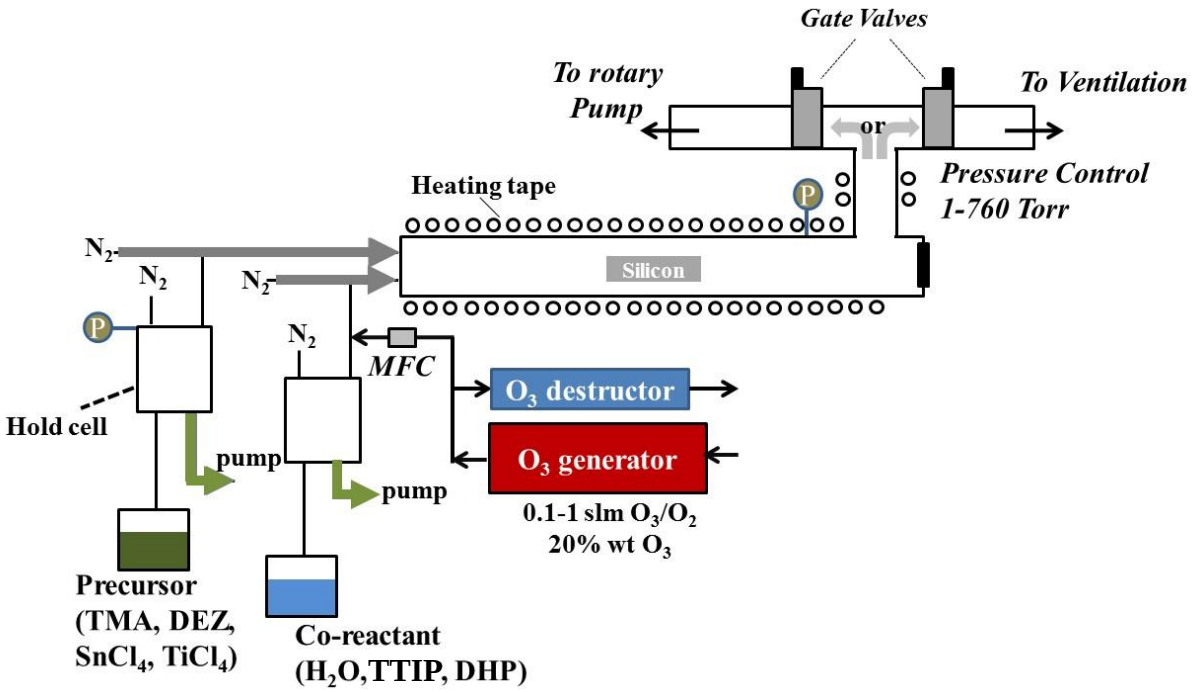


Figure 2.1. Schematic of a home-built modified ALD flow tube reactor that allows for deposition under wide pressure range. The controlled pneumatic valves positions are not shown.

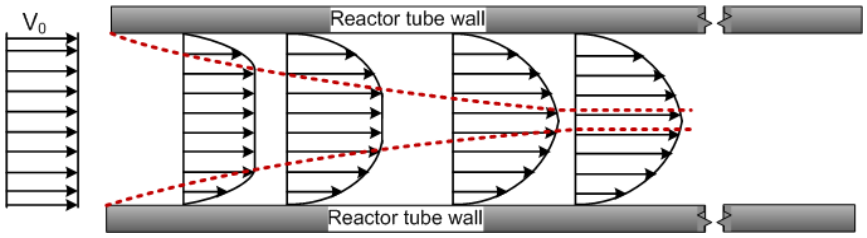


Figure 2.2. A schematic for boundary layer (in red) and velocity profile development for laminar gas flow through a tube reactor.

2.3 References

(1) Jur, J. S.; Parsons, G. N. Atomic Layer Deposition of Al2O3 and ZnO at Atmospheric Pressure in a Flow Tube Reactor. *ACS Appl Mater Interfaces* **2011**, *3* (2), 299–308.

(2) Elam, J. W.; Groner, M. D.; George, S. M. Viscous Flow Reactor with Quartz Crystal Microbalance for Thin Film Growth by Atomic Layer Deposition. *Rev. Sci. Instrum.* **2002**, *73* (8), 2981–2987.

(3) Briggs, D. Handbook of X-Ray Photoelectron Spectroscopy C. D. Wanger, W. M. Riggs, L. E. Davis, J. F. Moulder and G. E.Muilenberg Perkin-Elmer Corp., Physical Electronics Division, Eden Prairie, Minnesota, USA, 1979. 190 Pp. $195. *Surf. Interface Anal.* **1981**, *3* (4).

(4) Nist X-Ray Photoelectron Spectroscopy Database, Version 4.1. National Institute of Standards and Technology 2012.

(5) Gong, B.; Peng, Q.; Parsons, G. N. Conformal Organic−Inorganic Hybrid Network Polymer Thin Films by Molecular Layer Deposition Using Trimethylaluminum and Glycidol. *J. Phys. Chem. B* **2011**, *115* (19), 5930–5938.

(6) Linstrom, P. J.; Mallard, W. G. S.E. Stein Mass Spectra, NIST Chemistry WebBook, NIST Standard Reference Database Number 69. National Institute of Standards and Technology.

CHAPTER 3

Effect of Temperature and Gas Velocity on Growth per Cycle during Al_2O_3 and ZnO Atomic Layer Deposition at Atmospheric Pressure

This chapter is based on a manuscript published as:

Moataz Bellah M. Mousa, Christopher J. Oldham, and Gregory N. Parsons, *Journal of Vacuum Science & Technology A* **2012** 30, 01A155.

Abstract

The growth per cycle as a function of temperature during ALD of Al_2O_3 and ZnO at atmospheric pressure follows very closely the trend measured at typical (~2 Torr) process pressure. However, the overall growth rate is found to be nearly 2× larger at higher pressure and the magnitude of the growth increase can be adjusted by controlling the gas velocity near the growth surface. The growth increase at high pressure is approximately independent of process temperature at T<200°C for Al_2O_3 and ZnO, but the effect begins to become less pronounced at T>150°C, especially for Al_2O_3. The relatively high growth per cycle measured at 760 Torr and T<150°C suggests that excess physisorbed water remains on the aluminum oxide or zinc oxide surface after the water purge step. Increasing the gas velocity in the growth zone reduces the growth rate, consistent with more efficient removal of excess water. To better understand the observed trends, we present analytical expressions for the boundary layer thickness and species diffusivity and describe how these parameters are affected by reactor pressure and bulk gas velocity in the low temperature regime. To optimize ALD films and products, new ALD schemes at ambient pressure will need to understand the interaction between reactor pressure, gas velocity near the growth surface, fluid boundary layer thickness, and product desorption and diffusivity to achieve controlled growth.

3.1 Introduction

Atomic layer deposition (ALD) is useful for nanoscale coatings with high conformality and precise thickness control. The ALD method is compatible with a wide range of oxide, nitride, and elemental materials,[1–3] and related methods are extending to organic and hybrid organic-inorganic thin films.[1,4,5] Low temperature ALD processes, for example, can be used to modify and/or coat synthetic polymers[6–9] or biologically-derived materials.[9] Most commercial ALD processes are developed for batch or single-wafer semiconductor device processing, and operate under optimized conditions at pressures in the 0.1~1.0 Torr range. While batch processing is attractive for many applications, expanding ALD to a continuous process could facilitate significant new application fields like organic electronics and solar cells printing.[10–12] Moreover, working at ambient pressure could facilitate ALD integration for in-line manufacturing and eliminate the time needed for reactor evacuation and pressure control. A roll-to-roll ALD process[13] could be particularly useful to coat polymer webs for packaging[14–16] or for surface modification of fibrous materials for filtration or protective fabrics.[17–19]

There are many reports of tools and processes to perform atomic layer deposition at atmospheric pressure.[10,20–29] One approach is "spatial ALD" where the precursor, reactant and inert gases pass through separate delivery zones, and the substrate is moved through the flow to achieve growth.[11] In one report, Levy et al.[10] showed that the spatial ALD could produce stable low temperature ZnO thin film transistors.

Before continuous ALD can be fully realized in manufacturing, there are several key challenges that researchers must address. For example, for many continuous systems studied

to date the effect of process conditions, including web speed, gas flow rates, pressure and temperature, on film deposition rate and quality are just beginning to be understood. In some spatial ALD tools, the distance between the gas delivery/pumping head and the substrate is controlled near 30-200 μm, and the spacing is important to optimize the pulse timing and achieve well controlled growth.[10, 12] However, analytical models of the gas flow and species transport in these reactors are not widely known. To explore the effect of gas flow and operating pressure on ALD, our group recently constructed a unique reactor system capable of depositing Al_2O_3 and ZnO at a range of pressures between ~2 and 760 Torr.[19] Results showed that at a fixed deposition temperature, the Al_2O_3 and ZnO ALD thickness per cycle increased as pressure was raised from ~2 Torr to 760 Torr, but the overall growth rate could be reduced at high pressure by increasing the purge gas velocity. The increased growth rate at high pressure was attributed to adsorption of water[30]. The effect of temperature on film growth rate was not studied.

A critical aspect of ALD is the temperature range or "window" in which the self-limited adsorption reactions can readily proceed without undesired reactant decomposition, desorption or condensation. In this article, the thickness per cycle of ALD Al_2O_3 and ZnO is studied over a range of temperatures for processing at 2 Torr and 760 Torr, and for several values of purge gas velocity. The higher pressure process proceeds using a much higher gas flow rate than the low pressure process, but even so, higher pressure lead to a higher growth rate that is nearly independent of temperature. We describe these observations in terms of a simple gas flow model, where product species diffusion from the growth surface is impeded

at higher pressure, making more difficult to remove adsorbed species that lead to excess film growth.

3.2 Materials and Methods

ALD of Al_2O_3 and ZnO was carried out in a hot wall viscous flow tube reactor with a unique gas delivery and pumping system that allows operation at pressures between ~1 Torr and 760 Torr. The gas delivery and pumping design was described in detail previously.[19] A continuous flow of inert nitrogen (99.999%, National Welders Supply Co.) was maintained as carrier and purge gas. Before entering the reactor, the N_2 passed through an Aeronex gatekeeper filter (rated to <100 parts per trillion of H_2O and O_2) for further purification. For low pressure runs the operating pressure was fixed to ~2 ± 0.1 Torr and the N_2 flow was set at 0.5 slm (standard liters per minute). For runs at atmospheric pressure, the reactor outlet was vented directly to the lab exhaust, and flow was adjusted between ~5.0 and 34 slm. The ALD of Al_2O_3 and ZnO was previously analyzed as a function of pressure and flow rate between 2 and 760 Torr, and 0.5 and 5 slm, respectively, at a fixed temperature of 100°C.[19] For this study, the effect of deposition temperature is studied under low and high pressure deposition conditions. At each temperature set point, the reactor temperature was calibrated using a thermocouple placed inside the reactor under inert gas flow conditions.

The reaction chamber used for most of the runs was a horizontal stainless steel tube ~60 cm long with a ~3.6 cm inner diameter. For some runs a smaller tube with ~1.4 cm inner diameter was used in place of the 3.6 cm tube. The smaller tube was connected to the reactor using a conical reducer at its inlet. All results presented refer to results from the 3.6 cm tube unless otherwise stated. For growth rate analysis, flat silicon substrates were loaded to the

reactor and placed on a horizontal flat sample stage so the sample sat near the center point of the tube diameter. Also, the sample stage was thin so that gas flow was not significantly impeded, and gas could easily flow over and under the holder.

The gas delivery system on the reactor allows for the introduction of the precursors at pressures higher than their vapor pressures. The concept is simply based on introducing the precursor to an evacuated hold cell, followed by cell pressurization (using N_2) to the desired reactor pressure. For example, for water dosing, the cycle starts by pumping the hold cell to <1mTorr, then charging the hold cell with water for "X" seconds, followed by pressurizing the hold cell with N_2 for "Y" seconds. Finally the hold cell is opened to the reactor for "Z" seconds, followed by purging for "W" seconds. The cycle timing is set so that the "X" and "Y" parts of the cycle proceeds during the purge step for the other co-reactant. For brevity, the cycle sequence will be reported as "A/P/Z/P", where "A" and "Z" are the dosing times for the different precursors and "P" is the purging time.

For Al_2O_3 ALD, trimethylaluminum (TMA, 98%) was purchased from STREM Chemicals and was used as received. Likewise, for ZnO ALD, diethylzinc (DEZ, 98%) was also purchased from STREM. Deionized water (DI-H_2O) was used as the oxygen source. It was supplied from a DI water system (Millipore, Billerica, MA, USA) and maintained in glass vial. All the precursors were kept at room temperature, and their flow time was controlled using electronic solenoid valves.

The films deposited on native-oxidized silicon were characterized by spectroscopic ellipsometry (J.A. Woollam Co., Inc.) using a three-layer (film/native oxide/silicon) Cauchy

model. For QCM analysis, unpolished quartz crystals with gold coating (SC-101, 6 MHz) were purchased from Inficon and used as received. The head, where the crystal was mounted, has been modified to supply a nitrogen flow of 10 sccm to the back surface of the sensor crystal to prevent film deposition on that side.

3.3 Results and Discussion

Atomic layer deposition was performed using TMA/N_2/H_2O/N_2 cycles of 2/45/2/45 seconds, respectively at 2 Torr and 0.5 slm N_2, and at 760 Torr and 5.0 slm N_2 for substrate temperatures between ~40 °C and 260°C. Likewise, ALD of ZnO was performed using DEZ/N_2/H_2O/N_2 cycles with the same dose/purge time sequence. The resulting film growth per cycle is presented in Figures 3.1 and 3.2. Typical runs at low pressure consisted of 100 ALD cycles, whereas at higher pressure, 50 ALD cycles was used. At both high and low pressure, the rate was confirmed to be independent of cycle number. Moreover, control runs performed in this reactor using a quartz crystal microbalance[19] showed that under deposition conditions, multiple TMA cycles (without water) produced no unwanted growth, confirming that any source of extraneous water had been eliminated.

The results in Figures 3.1 and 3.2 show that at low pressure, the ALD temperature "window" follows the trend expected for Al_2O_3 and ZnO.[6,31–33] For Al_2O_3, growth is limited by thermal activation at lower temperatures, whereas at higher temperatures it is determined by the number of active Al-OH and Al-CH_3 surface sites.[6] At 760 Torr, the growth per cycle is larger than at low pressure. For ZnO ALD the rate is >50% larger at 760 Torr, and the difference is nearly independent of temperature across the range studied between 40 and 210 °C. For Al_2O_3, the rate is also >50% higher and independent of temperature between 40 and

~150°C, but at T>150°C the difference decreases and at the highest temperature studied (260°C), the growth rates are different by only ~10%. The temperature profile results in Figures 3.1 and 3.2 indicate that the higher growth rate at high pressure results primarily from gas transport mechanisms that are not strongly temperature dependent, whereas at higher temperatures, thermally activated processes also become important allowing the growth rates nearly convergence at T>250°C for Al_2O_3 ALD. A reasonable explanation is that the excess growth results from additional physisorbed water at high pressure, and the water desorbs more readily at T> 150°C, decreasing the growth rate difference. This is consistent with previous studies that show that large water doses produce additional growth per cycle during alumina ALD.[30]

To more carefully study species transport effects in the low temperature regime, we measured film growth per cycle under different water purge times and purge gas velocities at 130°C, and results are presented in Figure 3.3. At 760 Torr, the growth per cycle was largest for short purge times and low gas velocity. Increasing purge time produced some decrease in growth per cycle, but a larger change was observed by increasing the gas velocity. At 760 Torr and 0.4 m/s (20 slm) N_2 gas flow rate, the growth per cycle was ~1.2 Å/cycle, which is only slightly larger than measured at 2 Torr and 4.0 m/s (0.5 slm). To further study gas velocity effects, the 3.6 cm diameter reactor tube was replaced with a 1.4 cm diameter tube, and growth rate was measured for flow rates between 5 and 34 slm at 130°C. Even though the smaller tube is expected to produce a higher gas velocity for the same flow rate, the growth rate was nearly the same in the smaller tube as measured in the larger tube for the same flow rate. This unexpected trend may be due to changes in sample size or position in

the flow tube that affect the flow in the growth zone but do not precisely scale with the tube size. Another possible reason is that at those high flow rates, the bulk velocity is determined by the inlet tube diameter (1/4") and that the length inside the reactor to the sample is not enough for the flow to develop. However, the trend using a fixed tube diameter is clear: as the gas flow velocity at high pressure approaches the velocity at low pressure, the growth per cycle for TMA/H_2O converges at ~ 1Å/cycle as expected under typical low pressure conditions.

The results in Figures 3.1-3.3 confirm that the effect of pressure on growth rate is strongly influenced by gas transport effects at low temperature, and thermally driven mechanisms become more important at T>150°C. This insight will be important to develop new high throughput ALD methods, including spatial ALD, where different designs produce different gas velocities in the growth zone. Although the film quality was not specifically studied here, films deposited at different rates are likely to have different density or hydroxyl concentrations which could influence encapsulation or electronic performance.

Results above show that gas flow rate near the growth surface will affect overall growth per cycle for atmospheric pressure ALD of Al_2O_3 and ZnO. One of the key steps in ALD is the removal of products and excess reactant out of the reactor before the introduction of the next reactant. As shown schematically in Figure 3.4, vapor flow over a fixed planar surface produces a well-defined boundary layer containing relatively slow-moving fluid.[34] Because of this boundary layer, the removal of species from the surface during the gas purge can be understood to proceed through two parallel processes also shown in Figure 3.4: i) the

diffusion of product or excess adsorbed reactant through the boundary layer into the bulk flow; and ii) the sweeping of the bulk flowing species out of the reactor volume.

The time that it takes for species to be removed from the reactor by the bulk purge flow is determined by the reactor gas residence time. The residence time scales as (reactor volume × pressure) / (molar flow rate). Increasing the pressure at constant temperature and molar flow rate will increase the gas residence time and thus decrease the gas velocity. For instance, an ideal gas at 130°C and 2 Torr flowing at 0.5 slm through a cylindrical tube with an inner diameter of 3.6 cm will have an average velocity of ~4 m/s. For the same flow rate and temperature at 760 Torr, the velocity drops to ~0.01 m/s. Increasing the flow rate to 5.0 slm at 760 Torr increases the velocity to ~0.1 m/s. At this flow, the residence time is ~ 8 s, which is a practical time period for a purge cycle.

As for the diffusion of the undesired species through the boundary layer, the efficiency will depend on the species physisorption kinetics, thickness of the boundary layer (BL) and species diffusivity. At low temperature, water can readily physisorb and stick on the growing surface, and it must be transported off the surface and out of the reactor during the purge step. At T>150°C less water sticks during the water exposure cycle, so less water transport is required. Considering these points, we can develop an analytical picture of the mechanisms that lead to the higher growth rates at higher reactor pressure during low temperature ALD. In the low temperature regime, we consider the removal of water by desorption and diffusion through the boundary layer to be important in determining the

resulting growth rate. For a laminar boundary layer over a flat surface (i.e. the Blasius solution to the Navier-Stokes Equations)[34] the boundary layer thickness is given by:

$$BL = 5\left(\frac{\mu Z}{\rho U_{\infty}}\right)^{1/2} \quad (1)$$

where μ is the gas dynamic viscosity, Z is the lateral distance along the surface and U_∞ is the free stream velocity (i.e. bulk gas velocity). Note that while the boundary layer depends on fluid density, the thickness scales as $(\rho U_\infty)^{-½}$ which is independent of pressure at constant mass flow. In other words, mass flux (ρU_∞) is independent of the pressure, since density is direct proportional to pressure while bulk velocity is inversely proportional. The gas viscosity can also be considered pressure independent at this temperature and pressure range of interest. The boundary layer remains unchanged if pressure is increased under a fixed mass flow rate.

The dependence of species diffusivity on pressure can be derived from the principles of mass transfer using Fick's first law. For diffusion of excess water through a nitrogen boundary layer:

$$N_{H_2O} = -D_{H_2O-N_2}\frac{dc_{H_2O}}{dl} \quad (2)$$

where N_{H2O} is the molar flux of water through the boundary layer, D_{H2O-N2} is the diffusion coefficient of gaseous water in nitrogen and dc_{H_2O}/dl is concentration gradient of water along the boundary layer width. The boundary conditions for integration then lead to:

$$\int_0^{BL} N_{H_2O} \cdot dl = -D_{H_2O-N_2} \int_{c_{H_2O)_{surface}}}^{c_{H_2O)_{bulk}}} dc_{H_2O} \quad (3)$$

Assuming steady flow and constant surface water concentration, integration yields:

$$N_{H_2O} \cdot (BL) = D_{H_2O-N_2} \left(c_{H_2O}\Big|_{surface} - c_{H_2O}\Big|_{bulk} \right) \quad (4)$$

The molar flux also can be expressed in terms of diffusion velocity as follows, assuming the gas behaves ideally,

$$N_{H_2O} = \frac{P_{H_2O} v_d}{RT} \quad (5)$$

where P_{H_2O} is the partial pressure of water, v_d is the diffusion velocity of water through the boundary layer, and RT is the gas constant × temperature. Thus eq. (4) can be written as,

$$\frac{P_{H_2O} v_d}{RT} \cdot BL = D_{H_2O-N_2} \left(c_{H_2O}\Big|_{surface} - c_{H_2O}\Big|_{bulk} \right) \quad (6)$$

If water is removed quickly from the bulk flow, then $c_{H_2O}\Big|_{bulk} \approx 0$. Then, since $c_{H_2O}\Big|_{surface}$ can be written as P_{H_2O} / RT equation (6) can be rearranged to show that the species diffusion velocity is proportional to the diffusion coefficient and inversely related to boundary layer thickness:

$$v_d = \frac{D_{H_2O-N_2}}{BL} \quad (7)$$

Giddings et al.[35] showed that species diffusion coefficient is inversely proportional to pressure, thus diffusion velocity is also inversely proportional to pressure.

As mentioned above, the time needed for species to leave the growth surface and exit the reactor is the sum of the time needed to traverse the boundary layer, and the time needed to be flushed from the reactor. The time to be flushed from the reactor is characterized using residence time, and the time to traverse the boundary layer is the boundary layer thickness/velocity, or from eq. (7)

$$t_D = \frac{BL^2}{D_{H_2O-N_2}} \quad (8)$$

Since BL is independent of P at fixed flow rate, and $D_{H_2O-N_2}$ scales as ~1/P, the value for t_D increases with increasing pressure for fixed flow. However, from equation (1) increasing flow rate (i.e. increasing U_∞) at a fixed pressure will *decrease* BL and therefore decrease t_D, so that increasing flow at fixed pressure will yield more complete water desorption during relatively short purge cycle times.

The results presented above for pressure and flow rate dependence of the ALD growth per cycle are consistent with the trends predicted from this analysis, where transport of physisorbed water across the boundary layer is impeded at low temperature, high pressure and low gas velocity. Specifically, Figures 3.1 and 3.2 show that at T<150°C, ALD growth per cycle increases when pressure is increased by a factor of ~350, even when the gas flow rate (and gas velocity) increases by a factor of 10. Based on equation (8), a factor of >350 increase in flow rate (or purge time) would be needed to achieve the same extent of water

removal at 760 Torr as obtained at 2 Torr and 0.5 slm. A flow rate of ~200 slm is beyond our practical ability in the 3.6 cm diameter flow tube in our lab. However, as shown in Figure 3.4, increasing the flow rate from 5 slm to 34 slm does lead to a decrease in thickness per cycle. Increasing the purge time under fixed flow would also give more time for species to diffuse through the boundary layer. The results in Figure 3.3 also show some decrease in growth rate with increasing purge time, but the change is somewhat smaller than for a change in flow velocity. This indicates that additional mechanisms or process details, including species desorption rates, not included in our rough model can also play an important role in determining the detailed growth rates in the low temperature species desorption-dependent ALD regime.

The results shown here also raise interesting questions about the impact of higher growth per cycle on the performance of ALD materials and process. A higher growth per cycle will mean higher effective deposition rates, which can be beneficial. The factor of 2 increase in growth rate observed over a range of temperatures at high pressure suggests a well-defined water bilayer is present after the water pulse. As mentioned above, films deposited at different rates are likely to have different density or hydroxyl concentrations which could influence application performance. We find, for example, that films deposited at high pressure often have a larger root-mean-squared surface roughness than similar films deposited at lower pressure (review supplemental material). If lower growth per cycle is required for films deposited at higher pressure, increasing the gas flow will likely not be the most cost effective means to achieve high gas velocity. Many reactor designs can be

envisioned where constricted flow area will increase gas velocity under using reasonably moderate overall gas flow rates.

3.4 Summary

The growth per cycle during low temperature (<150°C) ALD of Al_2O_3 and ZnO is strongly dependent on reaction pressure under conditions using modest gas flow velocities near the growth surface. To achieve well defined ALD, vapor phase reaction products and/or physisorbed precursor or water co-reactant must be removed from the growth surface during the purge time, and at high pressure, the species diffusion rate through the surface fluid boundary layer is relatively slow. The relatively high growth/cycle measured at 760 Torr and T<~150°C suggests that excess physisorbed water remains on the alumina or zinc oxide surface after the water purge step. Increasing the gas velocity in the growth zone can reduce the excess water, so that the growth rate at high pressure approaches that at low pressure. This trend is explained in terms of representative analytical expressions for the boundary layer thickness and species diffusivity, by examining how these parameters are affected by reactor pressure in the low temperature regime. This work shows that new ALD reactor schemes that utilize ambient pressure will need to better understand the interplay between reactor pressure, gas velocity near the growth surface, fluid boundary layer thickness, and product desorption and diffusivity to optimize film deposition and achieve good quality ALD film products.

3.5 Acknowledgements

The authors acknowledge support from NSF (CMMI #1000382).

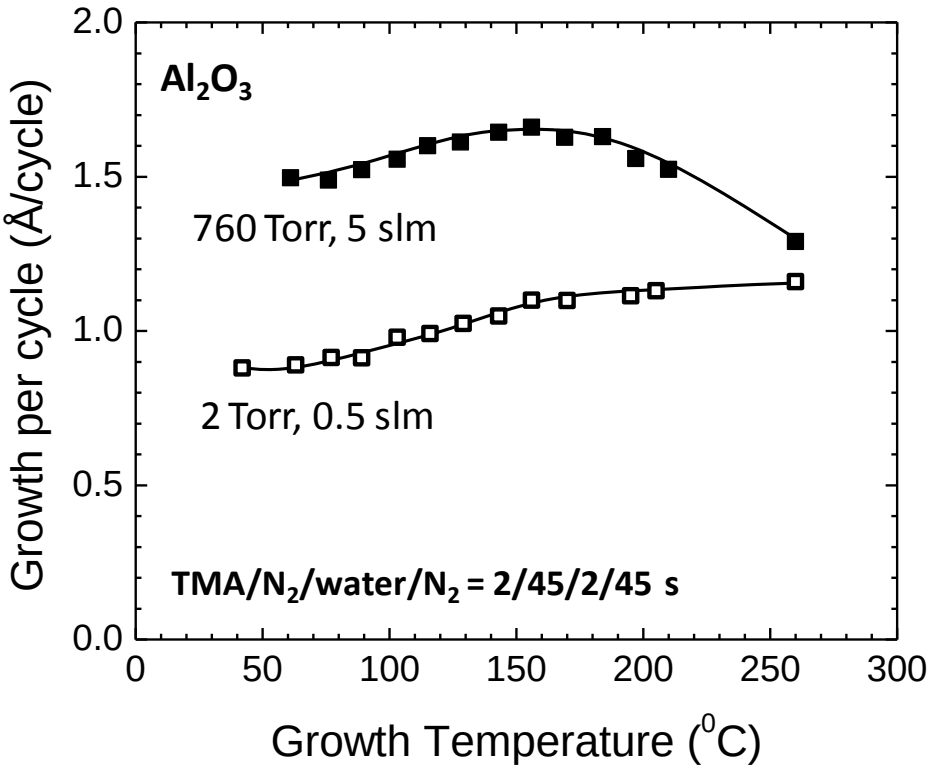


Figure 3.1. Growth per cycle for ALD of Al_2O_3 as a function of deposition temperature for reactor pressures of 2 and 760 Torr. Deposition was performed in a reactor system with specially designed gas delivery to allow operation with adjustable pressure. The figure also identifies the gas pulse timing used for deposition. The growth rate is larger at higher pressure, and under the conditions used, the increase is independent of temperature for T<150 °C. At higher temperatures, the growth rates begin to converge, consistent with the onset of a thermally activated mechanism.

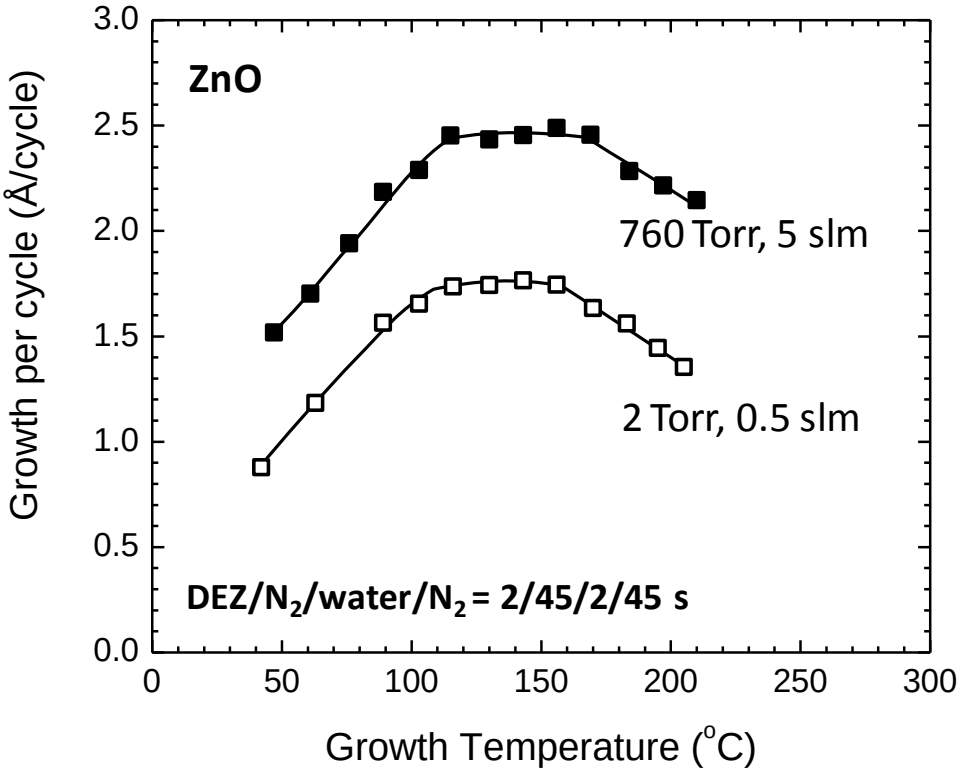


Figure 3.2. ALD growth per cycle for ZnO versus temperature. The thickness per cycle at 760 Torr is larger than at 2 Torr for all temperatures between 40 and 200 °C. The gas pulse conditions used for deposition are identified in the figure.

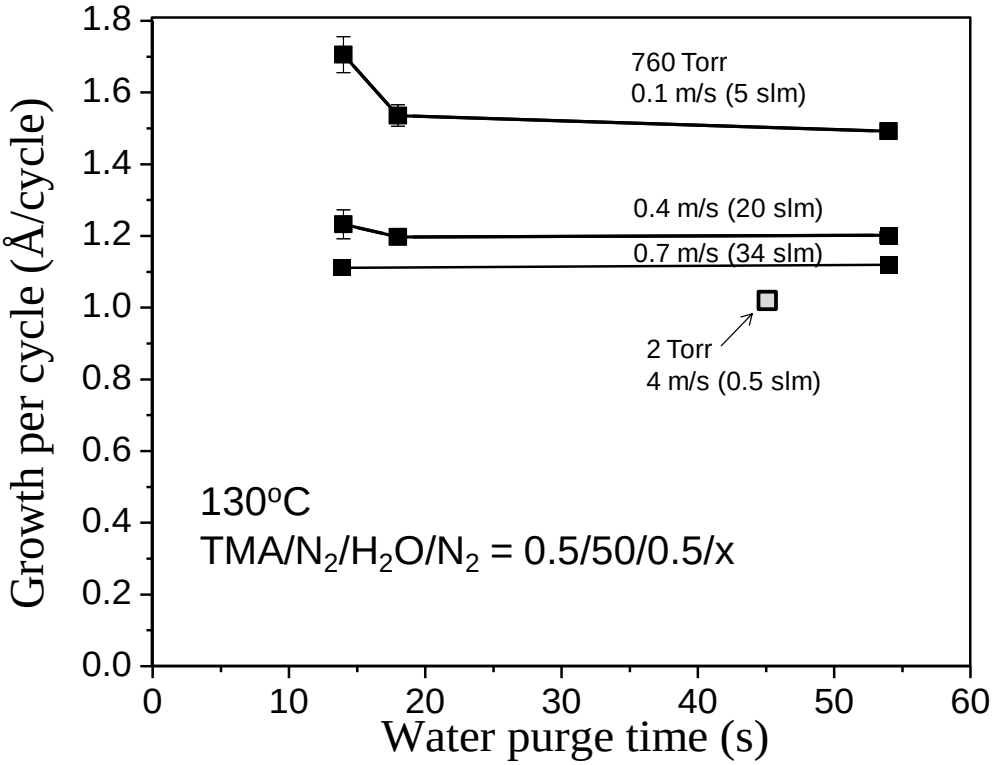


Figure 3.3. Growth per cycle of Al_2O_3 at 760 Torr and 130 °C versus water purging time for several values of N_2 purge gas flow rate. Increasing flow rate increases gas velocity and tends to reduce the growth rate for ALD Al_2O_3, at 0.7 m/s flow velocity, the growth rate becomes close to that measured at 2 Torr.

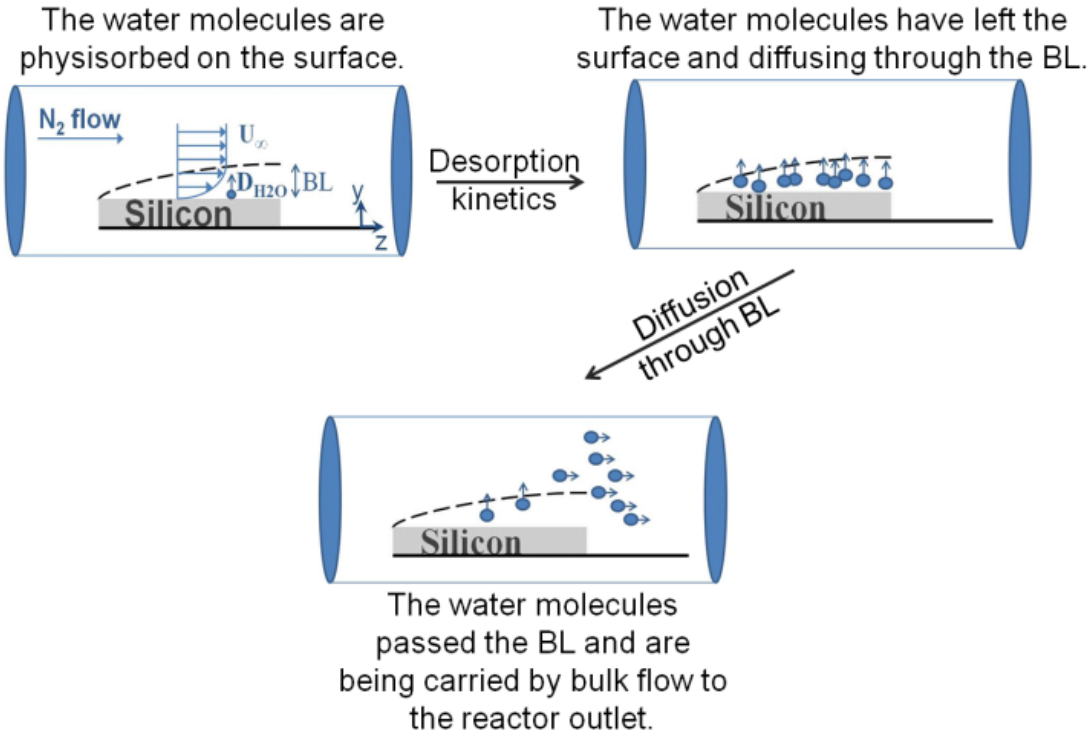


Figure 3.4. Schematic diagram showing the diffusion of physisorbed water molecules from the substrate surface and becoming entrained in the bulk purge gas flow.

3.6 Supplemental Material

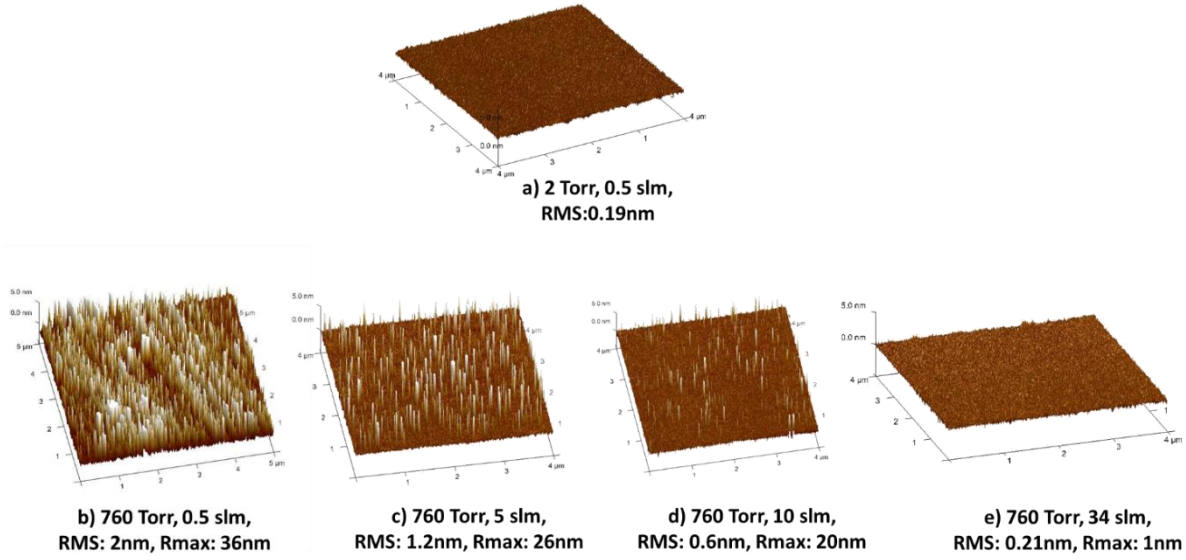


Figure 3.5. AFM images for Al_2O_3 coatings on silicon substrate at (a) low and (b-e) high pressure depositions. The film deposited at (a) 2 Torr was found to be smooth with roughness about ~0.19 nm. For high pressure depositions, the films got smoother with the increase in purge gas flow rate. The scanned areas were 4x4 μm for all of the samples and the scale bar maximum value is 5 nm.

3.7 References

(1) George, S. M. Atomic Layer Deposition: An Overview. *Chem. Rev. Wash. DC U. S.* **2010**, *110* (1), 111–131.

(2) Kim, H. Atomic Layer Deposition of Metal and Nitride Thin Films: Current Research Efforts and Applications for Semiconductor Device Processing. *J. Vac. Sci. Technol. B Microelectron. Nanometer Struct.--Process. Meas. Phenom.* **2003**, *21* (6), 2231–2261.

(3) Leskela, M.; Ritala, M. Atomic Layer Deposition Chemistry: Recent Developments and Future Challenges. *Angew. Chem. Int. Ed.* **2003**, *42* (45), 5548–5554.

(4) Peng, Q.; Gong, B.; VanGundy, R. M.; Parsons, G. N. "Zincone" Zinc Oxide-Organic Hybrid Polymer Thin Films Formed by Molecular Layer Deposition. *Chem. Mater.* **2009**, *21* (5), 820–830.

(5) Parsons, G. N.; George, S. M.; Knez, M. Progress and Future Directions for Atomic Layer Deposition and ALD-Based Chemistry. *MRS Bull.* **2011**, *36* (11), 865–871.

(6) Groner, M. D.; Fabreguette, F. H.; Elam, J. W.; George, S. M. Low-Temperature Al2O3 Atomic Layer Deposition. *Chem. Mater.* **2004**, *16* (4), 639–645.

(7) Hyde, G. K.; Scarel, G.; Spagnola, J. C.; Peng, Q.; Lee, K.; Gong, B.; Roberts, K. G.; Roth, K. M.; Hanson, C. A.; Devine, C. K.; et al. Atomic Layer Deposition and Abrupt Wetting Transitions on Nonwoven Polypropylene and Woven Cotton Fabrics. *Langmuir* **2010**, *26* (4), 2550–2558.

(8) Jur, J. S.; Spagnola, J. C.; Lee, K.; Gong, B.; Peng, Q.; Parsons, G. N. Temperature-Dependent Subsurface Growth during Atomic Layer Deposition on Polypropylene and Cellulose Fibers. *Langmuir* **2010**, *26* (11), 8239–8244.

(9) Knez, M.; Nielsch, K.; Niinistö, L. Synthesis and Surface Engineering of Complex Nanostructures by Atomic Layer Deposition. *Adv. Mater.* **2007**, *19* (21), 3425–3438.

(10) Levy, D. H.; Freeman, D.; Nelson, S. F.; Cowdery-Corvan, P. J.; Irving, L. M. Stable ZnO Thin Film Transistors by Fast Open Air Atomic Layer Deposition. *Appl. Phys. Lett.* **2008**, *92* (19), 192101–192101 – 3.

(11) Poodt, P.; Cameron, D. C.; Dickey, E.; George, S. M.; Kuznetsov, V.; Parsons, G. N.; Roozeboom, F.; Sundaram, G.; Vermeer, A. Spatial Atomic Layer Deposition: A Route

towards Further Industrialization of Atomic Layer Deposition. *J. Vac. Sci. Technol. Vac. Surf. Films* **2012**, *30* (1), 010802.
(12) Poodt, P.; Lankhorst, A.; Roozeboom, F.; Spee, K.; Maas, D.; Vermeer, A. High-Speed Spatial Atomic-Layer Deposition of Aluminum Oxide Layers for Solar Cell Passivation. *Adv. Mater. Deerfield Beach Fla* **2010**, *22* (32), 3564–3567.
(13) Maydannik, P. S.; Kääriäinen, T. O.; Cameron, D. C. An Atomic Layer Deposition Process for Moving Flexible Substrates. *Chem. Eng. J.* **2011**, *171* (1), 345–349.
(14) Charton, C.; Schiller, N.; Fahland, M.; Hollaender, A.; Wedel, A.; Noller, K. Development of High Barrier Films on Flexible Polymer Substrates. *Thin Solid Films* **2006**, *502* (1-2), 99–103.
(15) Hoppe, H.; Sariciftci, N. S. Organic Solar Cells: An Overview. *J. Mater. Res.* **2004**, *19* (7), 1924–1945.
(16) Mayer, A. C.; Scully, S. R.; Hardin, B. E.; Rowell, M. W.; McGehee, M. D. Polymer-Based Solar Cells. *Mater. Today Oxf. U. K.* **2007**, *10* (11), 28–33.
(17) Mahltig, B.; Haufe, H.; Boettcher, H. Functionalisation of Textiles by Inorganic Sol-Gel Coatings. *J. Mater. Chem.* **2005**, *15* (41), 4385–4398.
(18) Russell, S. J.; Textile Institute (Manchester, E. *Handbook of Nonwovens*; CRC Press ; Woodhead Pub. Ltd.: Boca Raton, Fla.; Cambridge, 2007.
(19) Jur, J. S.; Parsons, G. N. Atomic Layer Deposition of Al2O3 and ZnO at Atmospheric Pressure in a Flow Tube Reactor. *ACS Appl Mater Interfaces* **2011**, *3* (2), 299–308.
(20) Suntola, T. S.; Pakkala, A. J.; Lindfors, S. G. Apparatus for the Growth of Compound Thin Films. US4389973A, June 28, 1983.
(21) Dapkus, P. D.; Maa, B. Y.; Chen, Q.; Jeong, W. G.; DenBaars, S. P. Atmospheric Pressure Atomic Layer Epitaxy: Mechanisms and Applications. *J. Cryst. Growth* **1991**, *107* (1-4), 73–82.
(22) Dunlop, L.; Kursumovic, A.; MacManus-Driscoll, J. L. Reproducible Growth of P-Type ZnO:N Using a Modified Atomic Layer Deposition Process Combined with Dark Annealing. *Appl. Phys. Lett.* **2008**, *93* (17), 172111–172111 – 3.

(23) Hunter, A.; Kitai, A. H. A Novel Atmospheric Pressure Technique for the Deposition of Zinc Sulfide by Atomic Layer Epitaxy Using Dimethylzinc. *J. Cryst. Growth* **1988**, *91* (1-2), 111–118.
(24) Kaiya, K.; Yoshii, N.; Omichi, K.; Takahashi, N.; Nakamura, T.; Okamoto, S.; Yamamoto, H. Atmospheric Pressure Atomic Layer Epitaxy of ZnO Using a Chloride Source. *Chem. Mater.* **2001**, *13* (6), 1952–1956.
(25) Kaiya, K.; Yoshii, N.; Takahashi, N.; Nakamura, T. Atmospheric Pressure Atomic Layer Epitaxy of ZnO on a Sapphire (0001) Substrate by Alternate Reaction of ZnCl2 and O2. *J. Mater. Sci. Lett.* **2000**, *19* (23), 2089–2090.
(26) Nonobe, S.; Takahashi, N.; Nakamura, T. Preparation of HfO2 Nano-Films by Atomic Layer Deposition Using HfCl4 and O2 under Atmospheric Pressure. *Solid State Sci.* **2004**, *6* (11), 1217–1219.
(27) Takahashi, N.; Nonobe, S.; Nakamura, T. Growth of HfO2 Films Using an Alternate Reaction of HfCl4 and O2 under Atmospheric Pressure. *J. Solid State Chem.* **2004**, *177* (11), 3944–3948.
(28) Takahashi, N.; Yoshii, N.; Nonobe, S.; Nakamura, T.; Yoshioka, M. Self-Limiting Growth of ZrO2 Films on a Si(100) Substrate Using ZrCl4 and O2 under Atmospheric Pressure. *J. Electron. Mater.* **2003**, *32* (10), 1107–1110.
(29) Yoshii, N.; Takahashi, N.; Nakamura, T.; Yoshioka, M. Preparation of ZrO2 Nano-Films by an Alternate Reaction Using ZrCl4 and O2 under Atmospheric Pressure. *Electrochem. Solid-State Lett.* **2002**, *5* (9), C85–C86.
(30) Matero, R.; Rahtu, A.; Ritala, M.; Leskelä, M.; Sajavaara, T. Effect of Water Dose on the Atomic Layer Deposition Rate of Oxide Thin Films. *Thin Solid Films* **2000**, *368* (1), 1–7.
(31) Matero, R.; Rahtu, A.; Ritala, M. In Situ Reaction Mechanism Studies on the Atomic Layer Deposition of Al2O3 from (CH3)2AlCl and Water. *Langmuir* **2005**, *21* (8), 3498–3502.
(32) Ott, A. W.; Klaus, J. W.; Johnson, J. M.; George, S. M. Al3O3 Thin Film Growth on Si(100) Using Binary Reaction Sequence Chemistry. *Thin Solid Films* **1997**, *292* (1–2), 135–144.

(33) Yousfi, E. .; Weinberger, B.; Donsanti, F.; Cowache, P.; Lincot, D. Atomic Layer Deposition of Zinc Oxide and Indium Sulfide Layers for Cu(In,Ga)Se2 Thin-Film Solar Cells. *Thin Solid Films* **2001**, *387* (1–2), 29–32.
(34) Schlichting, H.; Gersten, K. *Boundary-Layer Theory*; Springer, 2004.
(35) Fuller, E. N.; Schettler, P. D.; Giddings, J. C. New Method for Prediction of Binary Gas-Phase Diffusion Coefficients. *Ind. Eng. Chem.* **1966**, *58* (5), 18–27.

CHAPTER 4

Atmospheric Pressure Atomic Layer Deposition of Al_2O_3 using Trimethyl Aluminum and Ozone

This chapter is based on a manuscript published as:
Moataz Bellah M. Mousa, Christopher J. Oldham, and Gregory N. Parsons, *Langmuir* **2014** *30* (13), 3741-3748.

Abstract

High throughput spatial atomic layer deposition (ALD) often uses higher reactor pressure than typical batch processes, but the specific effects of pressure on species transport and reaction rates are not fully understood. For aluminum oxide (Al_2O_3) ALD, water or ozone can be used as oxygen sources, but how reaction pressure influences deposition using ozone has not previously been reported. This work describes the effect of deposition pressure, between ~2 and 760 Torr, on ALD Al_2O_3 using TMA and ozone. Similar to reports for pressure dependence during TMA/water ALD, surface reaction saturation studies show self-limiting growth at low and high pressure across a reasonable temperature range. Higher pressure tends to increase the growth per cycle, especially at lower gas velocities and temperatures. However, growth saturation at high pressure requires longer O_3 dose times per cycle. Results are consistent with a model of ozone decomposition kinetics versus pressure and temperature. Quartz crystal microbalance (QCM) results confirm the trends in growth rate and indicate that the surface reaction mechanisms for Al_2O_3 growth using ozone are similar under low and high total pressure, including expected trends in reaction mechanism at different temperatures.

4.1 Introduction

High-speed continuous atomic layer deposition (ALD) processes under ambient conditions are offering new advanced capabilities to many different industries for their surface depositions ranging from nanoscale to microscale.[1] ALD is being used to create gas diffusion barriers on flexible polymers[2,3], for example, for advanced organic light emitting displays and solar energy conversion cells.[4,5,6] ALD coatings on fibrous materials are also of interest for applications including filtration and protective fabrics.[7] A key hurdle for process commercialization is transitioning ALD from a low deposition rate batch process to a continuous process with higher throughput while maintaining the same material properties and functionality, especially under low temperature and high pressure conditions.

ALD is a sequential self-limiting vapor phase nano-coating process compatible with many oxide, nitride, and elemental materials. The process can produce very uniform and conformal coatings even on high aspect ratio and 3D structures. In a typical ALD batch process, the reactants pass over the substrate in distinct steps separated by a purging gas flow. The purge step eliminates gas-phase mixing of the co-reactants, thereby promoting ultra- uniform coatings. However, the gas cycling extends the time needed for deposition, especially when long purge times are necessary.

Water is a common oxygen source for ALD of metal oxides. The reaction between water and trimethylaluminum (TMA) to form aluminum oxide (Al_2O_3) is the most widely studied and best understood ALD process.[8,9,10] Although water is readily available, it has a high sticking coefficient to oxides and tends to form hydrogen bonds with surfaces. Water desorption and removal out of the reactor during the purge step becomes challenging under

low temperature and high pressure conditions. Groner et al.[11] showed that under low pressure ALD conditions, Al_2O_3 grown with TMA and water at ~1Torr and ~60 ^oC required a water purge time of 30 seconds compared to 5 seconds to achieve the same growth rate at 177 ^oC. Decreasing the temperature to 33 ^oC required even longer purge times (~180s). They also observed higher hydrogen concentrations for films deposited at lower temperatures. Also, Jur et al.[12] showed that atmospheric pressure ALD of Al_2O_3 and ZnO using TMA/water and diethylzinc/water, respectively, produced film growth rates up to 2× larger than that observed in the same flow tube reactor operating under low pressure conditions (~2 Torr). Further work showed that higher growth rates extended over a relatively wide temperature range, from ~50 ^oC to 200 ^oC, though the growth rate could be decreased using higher gas flow rates.[13] The results suggested that excess physisorbed water present at high pressure and low gas flow produced the excess growth per cycle (GPC). Studies by Al-Abadleh et al.[14] showed that low relative humidity (<10%) is needed to maintain a hydroxide monolayer on α-alumina and avoid molecular water adsorption. Poodt et al.[4] studied ALD at atmospheric pressure at T<100 ^oC to optimize the relative humidity during the water dose step, but found that short gas purge times led to non-uniform film growth.

Researchers have studied the Al_2O_3 ALD process using ozone instead of water, but these studies are limited to only reactions at relatively low pressure. Physisorbed ozone is less strongly bound to oxide surfaces than water, allowing faster completion of the gas purging cycle, especially at low temperature or after high reactant exposure.[15,16] In addition to improved processing times, the oxide dielectric contains fewer hydroxyl groups when ozone is used, leading to improved leakage and charge trapping performance.[17,18,19]

Compared to the TMA/water ALD process, the TMA/ozone sequence generally leads to lower growth rates[16,20] (i.e. ~0.8 Å/cycle versus ~1.1 Å/cycle) and the process is more sensitive to substrate temperature.[21,22,23] While ~0.8 Å/cycle is typical for ALD Al_2O_3 using TMA/ozone, growth rates between 0.6 Å/cycle to 1 Å/cycle are also reported between 150 ^oC and 450 ^oC.[15,24] The different surface reaction mechanisms for ozone versus water can account for the observed growth rates.[21,23] Ozone acts as active oxidant for ligand removal producing C_2H_4, CO, CO_2, and other products, whereas TMA/water follows an acid-base reaction mechanism forming volatile methane. For the ozone process, Goldstein et al.[21] found that oxygen atoms will insert into Al-C and C-H bonds converting the methyl species to surface $AlOCH_3$ (methoxy), Al(OCHO) (formate), Al(OCOOH) (carbonate), and AlOH (hydroxyl) groups. Further reactions and rates depend on the deposition temperature. Rose et al.[25] also studied the reaction and detected CH_4, CO_2 and water during the ozone dose, indicating some surface combustion.

In this work, we explore ozone as an oxygen source for ALD Al_2O_3 at atmospheric pressure (AP-ALD) for temperatures ranging between 70 °C and 250 °C, and compare the growth rate to that observed in the same reactor system under low pressure conditions (~ 2 Torr). The resulting Al_2O_3 films on silicon were characterized by spectroscopic ellipsometry, and growth was monitored using *in-situ* QCM analysis. We find markedly different trends in growth saturation and growth rates at high pressure compared to low pressure. Analytic models show that the results can be understood in terms of pressure-dependent gas phase ozone dissociation and gas species transport during the ozone purge cycle.

4.2 Materials and Methods

All the depositions in this study were carried out in a horizontal hot wall viscous flow tube reactor with a unique gas delivery and pumping systems that allow operations at pressures between ~1 Torr and 760 Torr.[12] The stainless steel reactor is ~60 cm long with a ~3.6 cm inner diameter. The reactor is constructed with two outlet ports, one allowing flow directly to a mechanical vacuum pump and a second connected directly to the laboratory exhaust vent for atmospheric pressure runs. A detailed description of the ALD reactor design and operation is described in a previously published report.[12]

Trimethylaluminum (TMA, 98%, Strem Chemicals) was used as received and was maintained at room temperature during the process. Ozone, ~20 wt.% in oxygen, was generated by flowing high purity oxygen (grade 5) through an MKS Astex-AX8856 ozone generator at 25 pounds per square inch (psi). The oxygen flow rate ranged between 0.2 and 0.6 standard liters per minute (slm). When the ozone/oxygen mixture was not flowing through the reactor, it was redirected to an ozone destruction unit before being exhausted from the lab. Nitrogen gas (99.999%, National Welders) was dehydrated through an Entegris gatekeeper filter (rated to <100 parts per trillion of H_2O and O_2) and used as both a precursor carrier and reactor purge gas. For the low pressure runs, 0.5 slm of N_2 was maintained during the purge step, leading to an operating pressure ~2 ± 0.1 Torr. For the high pressure experiments, the N_2 flow was set at values between ~3 and 10 slm. Increasing the flow tended to decrease the growth rate, as discussed below. The gas-flow design of the reactor allowed for the ozone/N_2 mixture composition to be adjusted independent of the N_2 flow rate,

in order to control the inlet ozone partial pressure during the dose step at various values of the total flow rate.

TMA and ozone were introduced through two separate feed lines, and flow switching was controlled using electronic solenoid valves. N_2 flowed continuously through both lines during the purge steps. The gas delivery system on the reactor allows for the introduction of the precursors at pressures higher than their vapor pressures by using an evacuated hold cell. After TMA delivery into the cell, the cell is pressurized using N_2 to a value slightly larger than the desired reactor pressure. Ozone was introduced directly to the reactor from the ozone generator without any further pressurization for all the experiments.

For growth rate analysis, flat silicon (100) substrate pieces (~1.3cm × 1.3 cm) , with native oxide present, were loaded to the reactor and placed on a horizontal flat sample stage so the sample sat near the center of the tube diameter. The sample stage was thin so that gas flow through the tubular reactor was not significantly impeded, i.e. gas could easily flow over and under the holder. Under some high pressure conditions, the growth rate changed with sample position along the length of the tube (as discussed below), so unless otherwise noted, each sample was maintained at a fixed location, approximately 35 cm from the reactor inlet. A PID temperature controller was used to adjust the deposition temperature. At each set point the reactor temperature was calibrated *in-situ* using a thermocouple placed inside the reactor under inert gas flow.

A constant-angle (70 degrees) alpha-SE spectroscopic ellipsometer (J.A. Woollam Co., Inc.) was used to determine the thickness and the optical constants of the deposited films

on Si/SiO_2 using a three-layer Cauchy model. Also, *in-situ* QCM was used to monitor the mass uptake during the ALD process steps. The QCM was mounted in the viscous flow tube reactor through the inlet port. Unpolished quartz crystals with gold coating (SC-101, 6 MHz) were purchased from Inficon and used as received. The crystal was mounted on a Maxtek BSH-150 Bakeable Sensor Head, modified to supply a N_2 flow to the back surface of the sensor crystal to prevent unwanted film deposition.[26] A flow rate of 25 sccm (standard cubic centimeters per minute) was used for low pressure runs and 50 sccm for higher pressure experiments. Frequency change signals were recorded by a film thickness monitor (Maxtek TM-400) using a home designed LabVIEW program to record the data. The QCM was stabilized for twelve hours at each deposition temperature condition before runs commenced. The PID controller maintained constant temperature, which enabled a stable quartz crystal frequency signal. The gas pulse sequence led to changes in pressure that were noticeable in the quartz crystal frequency signal, especially during growth at atmospheric pressure. Control runs using pulsed inert gas showed that the pressure changes produced rapid frequency spikes that quickly decayed to stable and reproducible frequency values. The QCM data, including the data spikes due to pressure change, is plotted as collected.

After deposition, representative samples were analyzed by Time-of-Flight Secondary Ion Mass Spectroscopy (TOF-SIMS V, ION TOF, Inc. Chestnut Ridge, NY) equipped with a Bi_{nm}^+ (n = 1 - 5, m = 1, 2) liquid metal ion gun. A 180×180 μm^2 area was sputtered using a 1 keV Cs^+ ion beam, and depth profiles were acquired from a 50×50 μm^2 spot within this area using a 25 kV Bi^{3+} primary ion beam. The negative secondary ion mass spectra were calibrated using C^-, O^- and Al^-.

4.3 Results and Discussion

4.3.1 Growth Saturation at Low Pressure

Deposition using various TMA and ozone (O_3) doses was carried at 2 Torr and 205 °C, and results are shown in Figures 4.1a and 4.1b. Figure 4.1a shows the measured growth thickness per ALD cycle (growth per cycle, or GPC) as a function of O_3 dose time (0.25 slm at 20 wt.% in O_2) with other process parameters fixed (2 sec TMA dose, and 30 sec N_2 purge). Growth readily saturates at ~0.8 Å/cycle for an O_3 dose time of 1 second. Likewise, Figure 4.1b shows the saturation at the same growth per cycle for various TMA dose times using a fixed, 1 second O_3 dose time and 30 seconds purge steps. Saturation is attained for TMA dose times < 0.5 seconds per cycle.

Figures 4.1c and 4.1d show representative QCM plots collected at 205°C and 2 Torr that confirm self-limiting growth for TMA/O_3 Al_2O_3. Figure 4.1c shows the QCM response as each TMA dose is followed by three sequential O_3/N_2 dose steps. The TMA dose produces a net mass uptake, and the first O_3 step produces a small mass loss. The next O_3 steps produce no change, as expected for a saturated surface reaction. As a control, Figure 4.1c also includes a trace collected during repeated TMA/O_2 exposures (i.e. the ozone generator was not engaged). Growth is not observed, indicating residual water has been sufficiently removed from the reactor and that there is minimal reaction between TMA and silicon exposed to oxygen. Figure 4.1d shows the QCM mass uptake during the TMA/O_3 sequence at 205 °C, where the TMA dose is repeated three times before each N_2/O_3 step. In this case, the first TMA dose produced a net mass gain, and the O_3 lead to mass loss, similar to Figure

4.1c. The second and third TMA dose produced no change. The net mass loss during O_3 dosing will be discussed further below.

4.3.2 Effect of Reactor Pressure and Temperature on Growth Saturation

Film growth saturation versus O_3 exposures was also measured at different deposition pressures and temperatures, and results are shown in Figures 4.2a (depositions at 2 Torr) and 2b (760 Torr, 10 slm N_2 purge flow rate). At 2 Torr, the saturated growth rate is the same at 205 °C and 150 °C, and increases slightly to ~1 Å/cycle at 100 °C. At each temperature, growth saturates with ~0.5 seconds of O_3 exposure.

Under atmospheric pressure conditions, the saturation curves look markedly different. The growth requires longer O_3 exposures (> 2 seconds) to reach saturation, and the saturated growth rate is notably larger, ~1.1 and 1.5 Å/cycle for 205 °C and 100 °C, respectively. QCM results at 205 °C using multiple O_3 doses per cycle also confirmed full saturation at 1.1 Å/cycle at 760 Torr.

Under high pressure conditions, when the growth conditions were not fully saturated (O_3 dose time of 1 second per cycle), growth rate was non-uniform along the length of the flow-tube reactor. Moving the sample position ~10 cm toward the reactor inlet produced a ~25% increase in film growth rate. At 2 Torr, this change in position did not affect the growth rate. For other experiments discussed here, the sample position was fixed at 35 cm from the reactor inlet. Growth rate vs position data is shown and discussed below in relation to the ozone dissociation kinetics.

4.3.3 Effect of Gas Flow Velocity and Temperature on Growth Rate

In previous studies, increasing the gas flow velocity was found to decrease the growth per cycle during Atmospheric Pressure ALD.[13] We therefore studied the effect of purge gas flow rate (i.e. overall gas velocity) on growth rate at 760 Torr, and QCM results are shown in Figure 4.3(a) for growth at 70 °C. Increasing the purge gas flow rate 3 to 10 slm (0.06 m/s to 0.2 m/s) produced a ~30% decrease in rate of mass uptake. This decrease in growth per cycle with increasing gas velocity is most noticeable at lower temperature at 760 Torr. At 2 Torr, we saw no change in growth rate for increased gas flow. The rate decrease is attributed to improved species desorption rates through the gas flow boundary layer under higher gas velocity.[13] Comparing these result to those previously published for TMA/H_2O, the gas velocity in the TMA/O_3 process has a more pronounced effect on growth rate than in TMA/H_2O, suggesting that the desorption rate for surface reaction products are more influenced by the flowing gas relative to water vapor.[15]

Our gas delivery design allowed us to independently adjust the gas flow rate during the purge and reactant delivery steps. In contrast to the purge-gas velocity effects, we find that when the overall gas velocity is increased during the O_3 exposure step, saturated growth is achieved for shorter O_3 exposure times. The larger gas velocity during the dose step leads to more O_3 in the growth region (less time for O_3 decomposition), thereby promoting surface species reaction and growth rate.

The growth per cycle vs temperature at 2 Torr and for two gas velocities at 760 Torr is plotted in Figure 4.3b. Under all conditions studied, the growth rate is independent of

temperature up to 250 °C (the highest temperature tested),[22] and is up to 60% larger under high pressure conditions. Growth increases as temperature decreases from ~150 °C to 70 °C.

4.3.4 Effect of Temperature on Surface Reaction Processes

Using QCM, we further explored the temperature dependence of TMA/O_3 at 2 Torr (Figure 4.4a) and 760 Torr (4b) at 70 and 205 °C. At 760 Torr, the data shows transients ascribed to the QCM response to pressure change, and they are more pronounced at higher temperature.[12,26] The QCM shows that the net mass change during one ALD cycle (Δm) is larger at the lower temperature for both 2 and 760 Torr, consistent with the growth rate in Figure 4.2.

Considering the data in Figure 4.4a collected at 2 Torr, the TMA exposure produces a positive mass gain at 70 and 205°C, with a larger gain at 205 °C. During O_3 exposure, the mass gain is positive at 70 °C but it is negative (mass loss) at 205 °C. These results can be understood in terms of the surface reaction mechanisms during TMA/O_3 ALD.[21,27,28] In the TMA/O_3 process, the O_3 exposure step leads to methoxy, formate, carbonate and hydroxyl groups on the surface, with the amount of each depending on temperature and extent of O_3 exposure.[21,29,27,30] At low temperature, the O_3 exposure allows O insertion into Al-C bonds leaving methoxy and formate surface species (net mass gain), whereas at higher temperatures the O_3 can oxidize the surface carbon producing volatile products and leaving hydroxyl and carbonate surface groups (mass loss).[21,29] The mass response during the O_3 exposure in Figure 4.4a is consistent with this trend. Moreover, because the methoxy and formate are less reactive with TMA than are the hydroxyl and carbonates, we expect the mass increase during the TMA dose to be larger at higher temperature, also consistent with Figure 4.4a.

Also because the TMA is not as reactive with the hydrocarbon residues, more carbon will be retained in the film at low temperature.[29]

The QCM data at 760 Torr (Figure 4.4b) shows the same trends in mass uptake as observed at 2 Torr, indicating that the change in surface reaction mechanism with deposition temperature also proceed during TMA/O_3 under saturated growth at atmospheric pressure.

Under saturated TMA and O_3 exposures, the growth rate in Figure 4.3(b) depends on temperature and pressure. At low temperature, for both 2 and 760 Torr, extra mass uptake results from O insertion and the rate of thermal desorption decreases, increasing the growth rate. At all temperatures, the growth rate is larger at high pressure because the gas flow conditions (slower species transport through the boundary layer) prevent desorption of growth species that adsorb on the surface.[12] At high pressure, increasing velocity enhances species desorption, allowing growth rates to approach that at 2 Torr. This process is most pronounced at lower temperatures where thermal desorption rates are smaller. We note that under different conditions, opposite trends could appear. For example, if the O_3 exposure is not sufficiently saturating, then increasing the gas flow rate can push more O_3 into the reaction zone, thereby promoting surface saturation which could increase the growth rate.

4.3.5 Film Composition

Refractive index obtained from ellipsometry vs deposition temperature at 2 Torr and 760 Torr is given in Figure 4.5. Refractive index decreases for deposition temperature <150°C, and the films deposited at higher pressure show a somewhat decreased index.

We also measured film composition using ToF-SIMS (Figure 4.6), and we find similar composition profiles for deposition at 205°C at 2 and 760 Torr. Reducing deposition temperature to 70°C increases the C and OH detected by SIMS, but the composition is not markedly dependent on deposition pressure. Comparing the data in Figure 4.6, the higher pressure may show some excess carbon at higher pressure, consistent with the index data in Figure 4.5. The carbon likely results from reduced product species desorption rates at high pressure

4.3.6 Ozone Dissociation Kinetics

Under saturated growth conditions, ALD using TMA/O_3 at 760 Torr follows the same trends and produces films similar to 2 Torr. However, Figure 4.2(b) shows that a longer O_3 dose is needed to reach saturation at 760 Torr. This difference can be attributed to gas transport and O_3 depletion effects at high pressure. O_3 decomposition into O_2 and reactive oxygen radicals is dependent on temperature, pressure and O_3 concentration.[31] To understand the pressure and flow dependence of O_3 depletion, we developed a kinetic model for the O_3 dissociation rate in a flow tube reactor. We then solved the model for net O_3 content versus position in the reactor under various values for reactor pressure, temperature and overall gas velocity. Insight from this model produces an improved understanding of pressure dependence in low temperature ALD reactions.

Benson and Axworthy[31] described an elementary reaction sequence for O_3 decomposition, where decomposition proceeds predominantly through interaction with other gas molecules in the system, i.e. gas collision frequency exceeds wall collision frequency, as

expected under viscous flow conditions used here. In the model, the species M corresponds to another gas molecule which could be O_3, O_2 or inert N_2:

$$O_3 + M \overset{k1}{\rightarrow} O_2 + O + M \quad (1)$$

$$O_2 + O + M \overset{k2}{\rightarrow} O_3 + M \quad (2)$$

$$O + O_3 \overset{k3}{\rightarrow} 2O_2 \quad (3)$$

$$2O_2 \overset{k4}{\rightarrow} O + O_3 \quad (4)$$

Reactions 1 and 2 above were studied by Benson and Axworthy[31] in an $O_3/O_2/N_2$ mixture, and the O_3 was found to more likely decompose during a collision with another O_3 molecule. Specifically, the concentration of species "M" could be defined as:

$$[M] = [O_3] + \alpha[O_2] + \beta[N_2] \quad (5)$$

to reflect the relative reaction probability. The pre-factors α and β were determined for $O_3/O_2/N_2$ mixture as 0.41 and 0.42 respectively using experimental values tabulated by Johnson[32]. Reaction (4) is not considered because it has an appreciable rate only at temperatures >600 ^oC, well above the temperature range studied here. The sequence above yields the following expression for the O_3 degradation versus distance along the reactor length:

$$-\frac{d[O_3]}{dl} = \left[k_1[O_3][M] - k_2[O_2][O][M] + k_3[O_3][O]\right] * \frac{1}{\mathrm{v}} \quad (6)$$

Also, the rate of change of O radical concentration can be expressed as

$$-\frac{d[O]}{dl} = \left[k_1[O_3][M] - k_2[O_2][O][M] - k_3[O][O_3]\right] * \frac{1}{\mathrm{v}} \qquad (7)$$

Since the O radical is an intermediate unstable species, we can apply the quasi steady state assumption (QSSA) on it (i.e. $d[O]/dl \approx 0$), thus,

$$[O] = \frac{k_1[O_3][M]}{k_2[O_2][M]+k_3[O_3]} \qquad (8)$$

By substituting $[O]$ from eq. (8) into eq. (6), the resulting O_3 degradation rate is:

$$-\frac{d[O_3]}{dl} = \frac{2k_1k_3[O_3]^2[M]}{k_2[O_2][M]+k_3[O_3]} * \frac{1}{\mathrm{v}} \qquad (9)$$

where "v" is the total gas velocity inside the plug flow reactor. If the conversion of O_3 to oxygen yields a negligible volume change, then an oxygen mass balance gives:

$$[O_2] = [O_2]_\mathrm{i} + 1.5([O_3]_\mathrm{i} - [O_3]) \qquad (10)$$

where subscript "i" refers to the concentrations at the inlet of the reactor. The rate constants for the elementary reactions were previously estimated by Johnson[32]:

$$k_1 = 1.65 \times 10^{-9} \exp\left(-\frac{22.72}{RT}\right) \qquad \frac{cm^3}{molecule.s}$$

$$k_2 = 4.63 \times 10^{-35} \exp\left(-\frac{2.10}{RT}\right) \qquad \frac{cm^6}{molecule^2.s}$$

$$k_3 = 2.00 \times 10^{-11} \exp\left(-\frac{4.79}{RT}\right) \qquad \frac{cm^3}{molecule.s}$$

The resulting differential equation was integrated using Matlab ODE solver using the Runge-Kutta 4th order method to obtain the O_3 concentration versus position in the reactor. The inlet O_3 partial pressure was determined from the gas mixture flow rates, which varied from 0.2

Torr to 38 Torr as total pressure increased from 2 Torr to 760 Torr. At 2 Torr, for example, the net flow of 0.25 slm N_2 ,during the dose step, combined with 0.5 slm of 20 wt.% O_3/O_2 mixture produced

$$P_{O_3\,inlet} = \frac{\frac{20}{100}*0.5}{0.25+0.5} * 2 \approx 0.27 \text{ Torr}$$

By multiplying the calculated O_3 concentration by the known total volumetric flow rate, the net steady-state O_3 flow rate at each location along the reactor tube was determined as a function of temperature and total gas pressure.

Results from the model analysis are plotted in Figure 4.7. The results show that the local O_3 flow rate (i.e. O_3 partial pressure) is strongly affected by total gas pressure and reactor temperature. At low pressure, the amount of O_3 is uniform across the tube and nearly independent of temperature. At higher pressure, the O_3 quickly becomes depleted, especially at higher temperature. The temperature dependence of the rate constant is also noticeable in the model results, showing a more uniform ozone concentration along the reactor length at lower temperature.

The O_3 depletion at high pressure is consistent with the slower growth saturation shown in Figure 4.2. Increasing pressure decreases the amount of O_3 available to react in the growth zone, so longer exposure times are needed for saturation. It is important to note that fully saturated O_3 exposure can lead to different growth rates at different pressures. At high pressure, slower species transport through the boundary layer will promote excess species adsorption leading to a higher growth rate. Increasing gas velocity decreases the boundary

layer and thereby enhances species desorption, so growth rates at high pressure decrease and approach the lower pressure values.

Also included in Figure 4.7 are data points showing film thicknesses after 110 ALD cycles at 2 and 760 Torr at two different positions along the length of the reactor. Working under sub-saturation conditions (O_3 = 1 sec/cycle) at 760 Torr and 205 °C, moving the sample holder 10 cm upstream increases the growth rate by 25%, whereas at 2 Torr the growth rate is unchanged. The model captures this by showing that the O_3 concentration decays rapidly with distance. We note that under ALD saturation conditions, the ozone surface reaction is complete, so growth rate is not sensitive to position in the growth zone.

4.4 Summary

Aluminum oxide ALD using TMA/O_3 can proceed at atmospheric pressure (~760 Torr) in a flow tube reactor with results similar to those obtained under typical lower pressure (~2 Torr) conditions. At high pressure, longer O_3 exposure times are needed to attain saturated growth. Self-limiting growth is attained between 200 °C and 250 °C at both 2 Torr and 760 Torr, with higher growth observed at higher pressure. Also similar to that observed previously for the TMA/H_2O process, a higher growth rate at high pressure can be due to slower transport of desorbing product species through the boundary layer. Increasing the purge gas velocity helps reduce the boundary layer, thereby promoting species desorption and reducing the growth rate in the ALD temperature widow, approaching values obtained at low pressure. At 760 Torr, the TMA/O_3 process will be most similar to that at low pressure when conditions produce high ozone exposures and high gas velocity. Independently, increasing the O_3 gas velocity delivers more O_3 to the growth surface and therefore allows

faster growth saturation. Under saturated growth conditions, Al_2O_3 films deposited at 2 Torr and 760 Torr have similar composition, with some extra carbon contamination at higher pressure.

At low temperature in the TMA/O_3 ALD process, the O_3 exposure allows O insertion producing surface methoxy and formate groups, whereas the reaction is more complete at higher temperatures leading to surface hydroxyls. Quartz crystal microbalance analysis shows evidence for this temperature-dependent surface reaction mechanism at 2 Torr, and it persist at 760 Torr under saturated conditions.

A model describing the ozone dissociation kinetics in our flow tube reactor follows and helps clarify the observed trends in saturation and growth rate. High pressure increases the rate of ozone dissociation and therefore reduces the amount of ozone that reaches the growth surface. This leads to longer ozone dose times needed to reach saturation. The ozone depletion also predicts an observed gradient in film growth rate under sub-saturation conditions along the length of the reactor. Overall, the model and results demonstrate that similar ALD growth can be achieved for TMA/O_3 at 760 Torr and 2 Torr, where care must be taken to take into account the faster rate of O_3 dissociation at higher pressures, especially at higher temperature. Ozone can therefore be a viable reactant for high throughput atmospheric pressure ALD under batch or spatial ALD conditions.

4.5 Acknowledgments

The authors acknowledge support from NSF CMMI Grant # 1000382. We also acknowledge the use of the Analytical Instrumentation Facility (AIF) at North Carolina State University, which is supported by the State of North Carolina and the National Science Foundation.

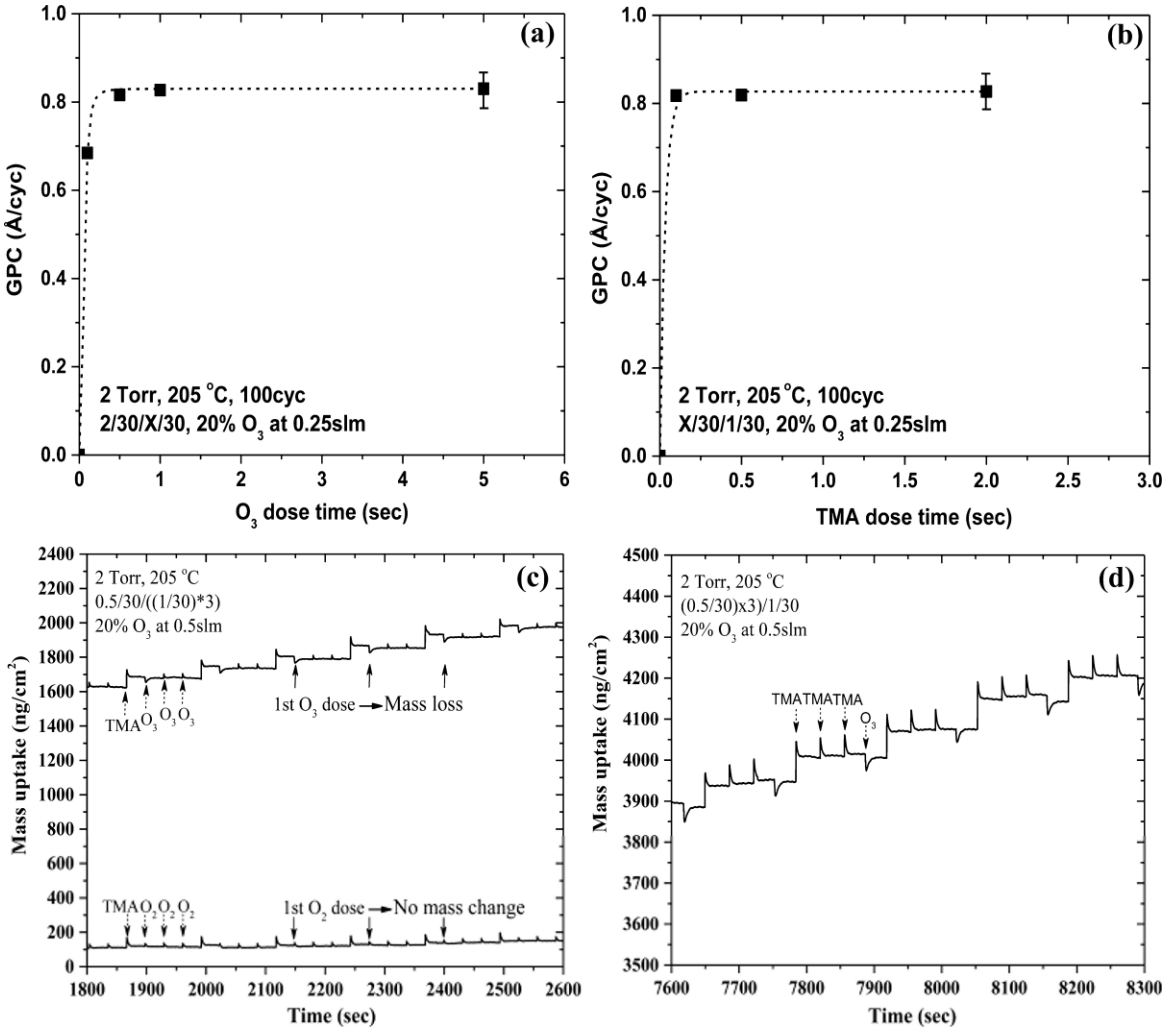


Figure 4.1. Growth per cycles showing saturation behavior of atomic layer deposited Al_2O_3 layers using O_3 and TMA at 2 Torr and 205 ^oC with: (a) fixed TMA dose time; (b) fixed O3 dose time. The error bar reflects a typical ±5% uncertainty in the thickness measurement. Quartz crystal microbalance mass uptake using: (c) one TMA dose followed by three ozone doses; and (d) three TMA doses followed by one O_3 dose. Repeated O_3 or TMA doses show no mass uptake, confirming with fully saturated growth.

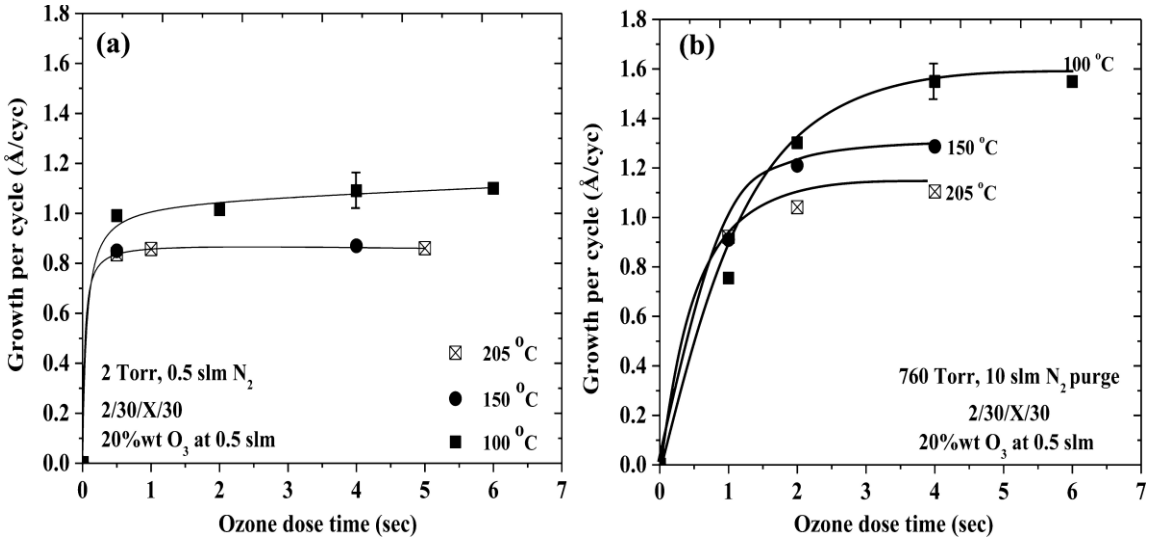


Figure 4.2. Growth per cycle for Al_2O_3 versus O_3 dose time at: (a) 2 Torr; and (b) 760 Torr for different deposition temperatures. The error bar reflects a ±5% uncertainty in the thickness measurement. The growth per cycle shows that a longer exposure time is needed for saturation at high pressure.

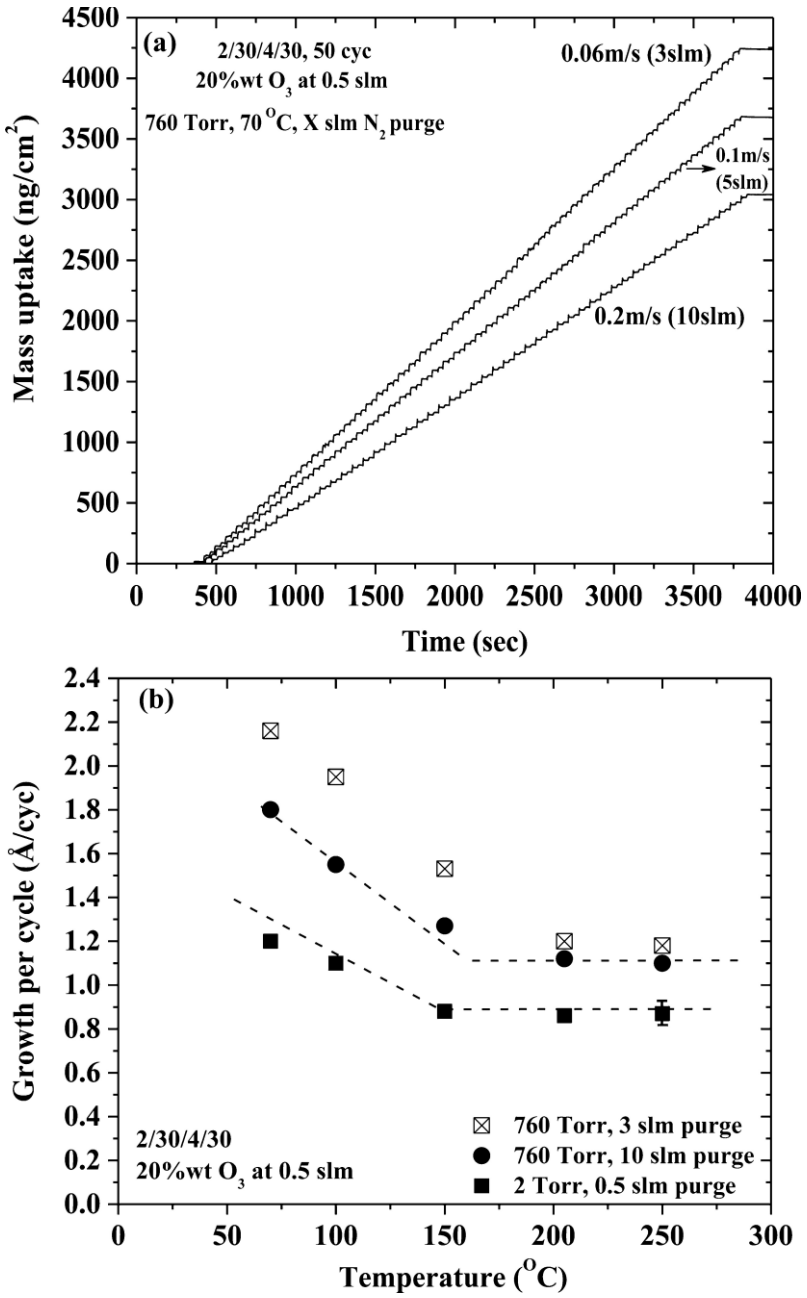


Figure 4.3. (a) Mass uptake using in-situ QCM vs. processing time for cycles of TMA/O_3 at purge flow rates of 3, 5 and 10 slm at 760 Torr and 70°C. (b) Growth thickness per cycle at 2 Torr (0.5 slm purge flow rate) and 760 Torr (3 and 10 slm). The error bar represents typical ±5% uncertainty in the thickness measurement.

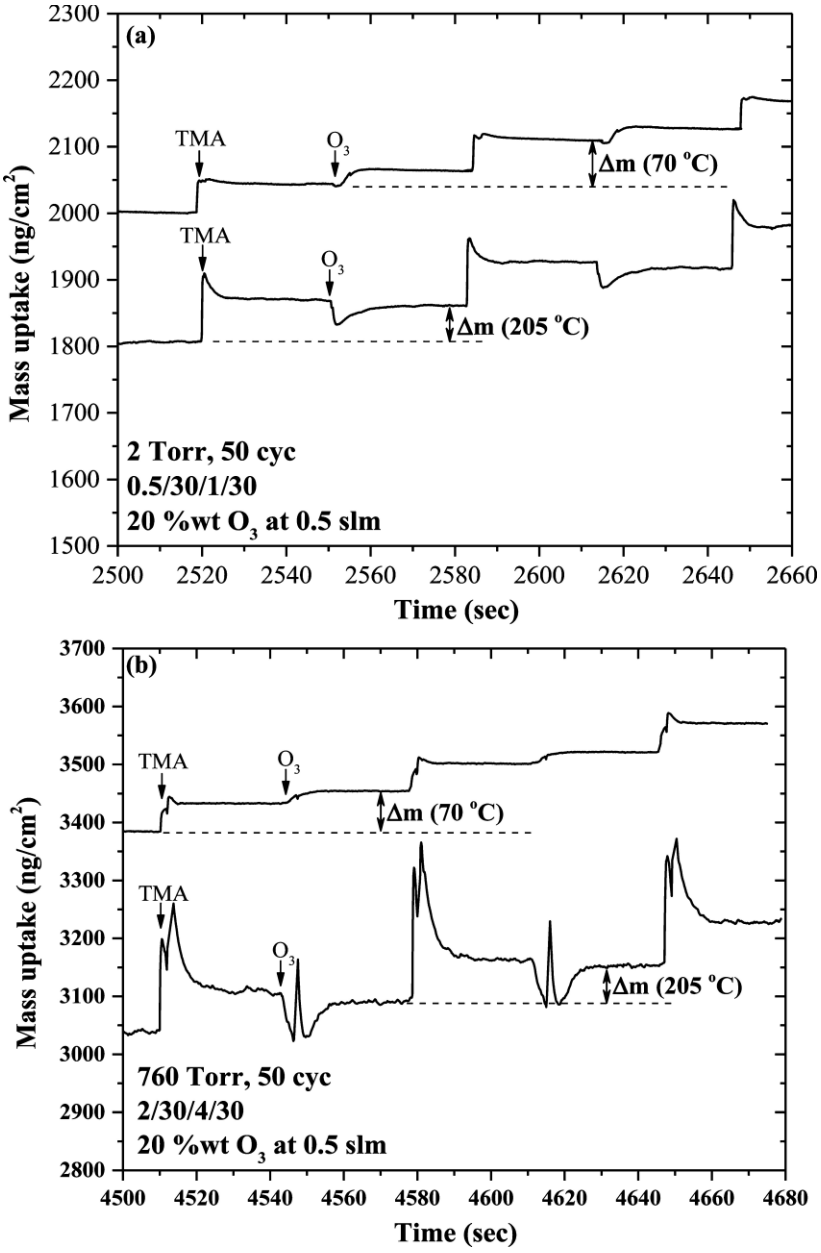


Figure 4.4. Mass uptake using in-situ QCM vs. processing time for cycles of TMA/O_3 at (a) 2 Torr and (b) 760 Torr at 70 ^oC and 205 ^oC. Mass increases during TMA doses for both temperatures but slightly decreases during O_3 at 205 ^oC and showed large increase at 70 ^oC.

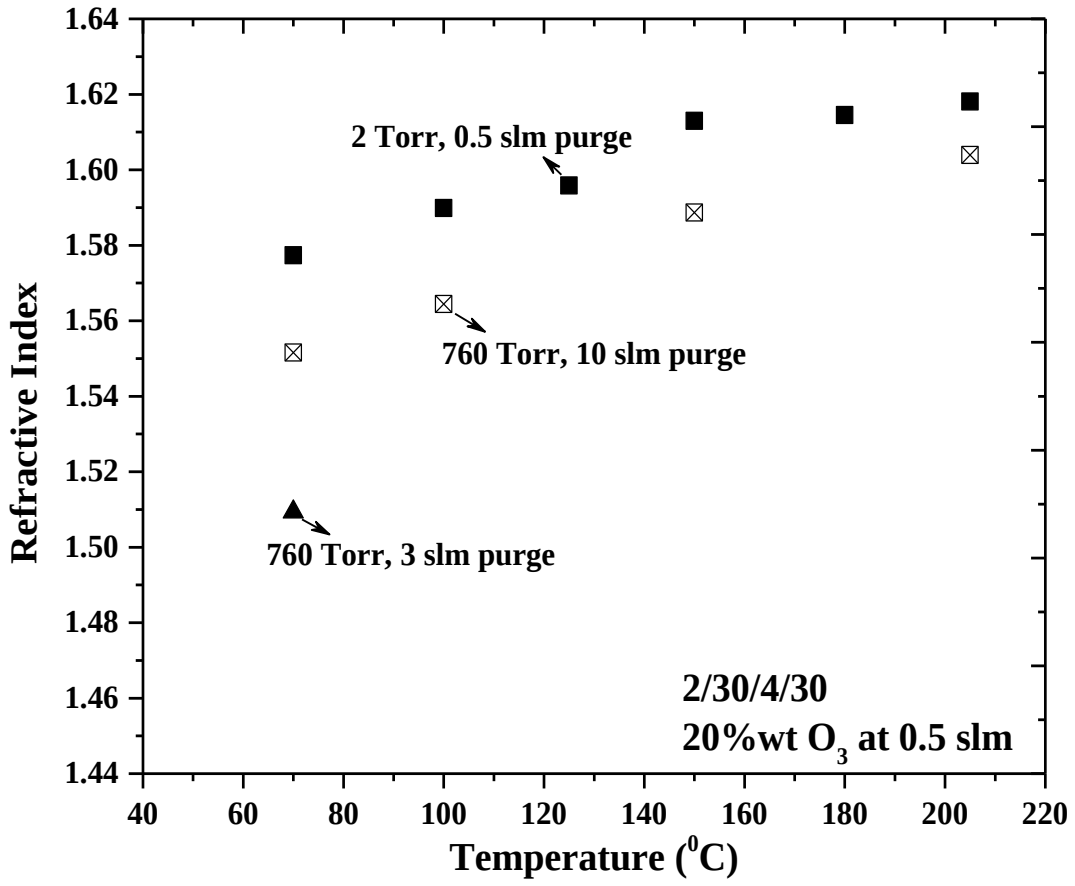


Figure 4.5. Refractive index at 600 nm calculated using Cauchy model for thick Al_2O_3 films deposited at different temperatures at 2 Torr and 760 Torr. The index decreases when the temperature is below the ALD temperature window.

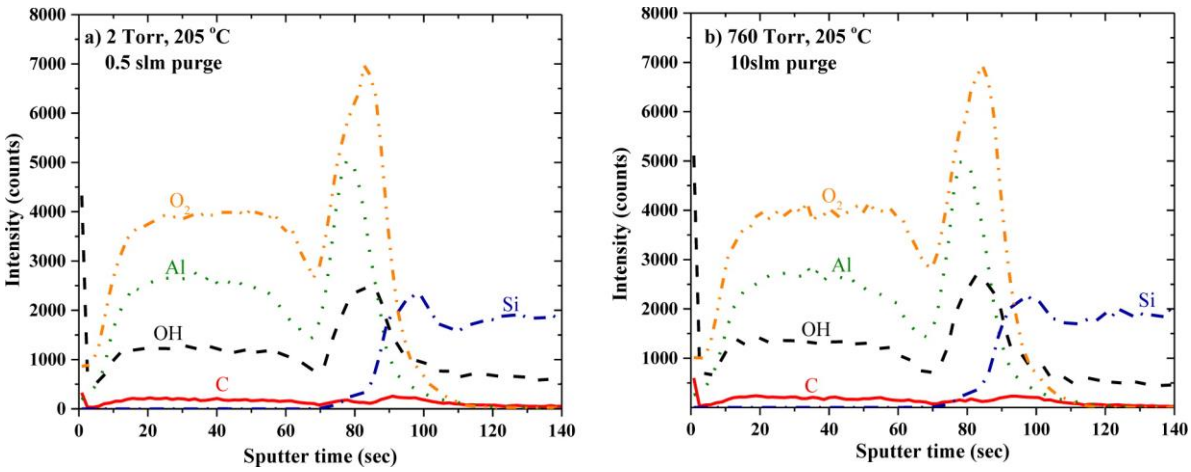


Figure 4.6. ToF-SIMS depth profiles for Al_2O_3 deposited at 205°C and: a) 2 Torr; b) 760 Torr. Similar film composition is attained.

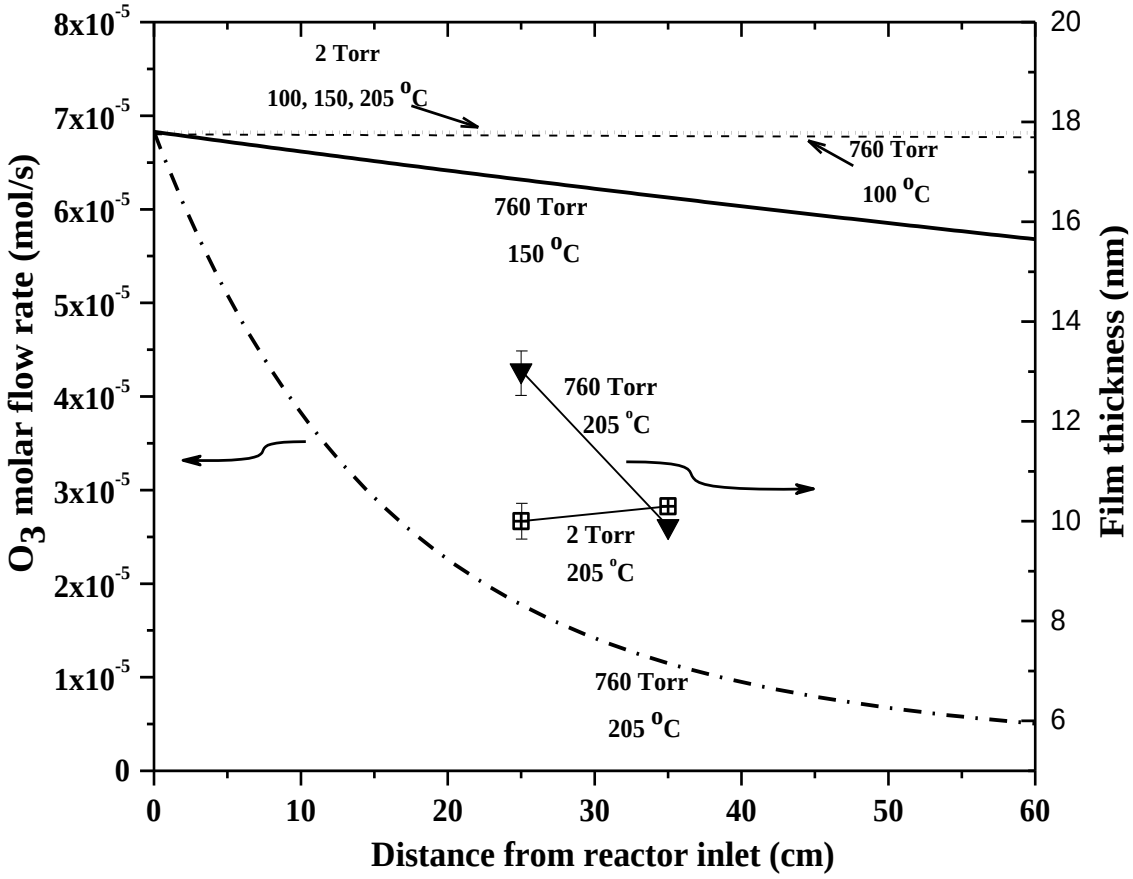


Figure 4.7. Lines represent model results for O_3 molar flow rate along the reactor under 2Torr and 760Torr at 100 ^{O}C, 150 ^{O}C, and 205 ^{O}C. The ozone molar flow rate at the inlet was ~6.8x10-5 mol/sec (20 wt. % at 0.5slm), and the gas velocity was 0.10-0.13 m/s (corresponding to ~5.5 slm) at 760 Torr, and 6.2-7.9 m/s (~ 0.75 slm) at 2 Torr. Data points (triangular and crossed square) represent experimental values of film thickness measurements (left axis) for Al_2O_3 deposited at 2 Torr and 760 Torr at 205 ^{o}C and different positions in the reactor. The gas pulsing sequence was TMA/N_2/O_3/N_2: 2-30-1-30.

4.6 References

1. Poodt P, Cameron DC, Dickey E, George SM, Kuznetsov V, Parsons GN, Roozeboom F, Sundaram G, Vermeer A. Spatial atomic layer deposition: A route towards further industrialization of atomic layer deposition. J Vac Sci Technol A. **2012,** 30, 010802.

2. Kääriäinen TO, Maydannik P, Cameron DC, Lahtinen K, Johansson P, Kuusipalo J, Atomic layer deposition on polymer based flexible packaging materials: Growth characteristics and diffusion barrier properties. Thin Solid Films **2011**, 519, 3146–3154 (2011).

3. Dickey E, Barrow WA. High rate roll to roll atomic layer deposition, and its application to moisture barriers on polymer films. J Vac Sci Technol A. **2012,** 30, 021502.

4. Poodt P, Knaapen R, Illiberi A, Roozeboom F, Asten A van. Low temperature and roll-to-roll spatial atomic layer deposition for flexible electronics. J Vac Sci Technol **2012**, 30(1), 01A142.

5. Poodt P, Lankhorst A, Roozeboom F, Spee K, Maas D, Vermeer A. High-speed spatial atomic-layer deposition of aluminum oxide layers for solar cell passivation. *Adv. Mater.* **2010**, 22, 3564–3567.

6. Levy DH, Nelson SF, Freeman D. Oxide Electronics by Spatial Atomic Layer Deposition. *J. Disp. Technol.* **2009**, 5, 484–494.

7. Mahltig B, Haufe H, Boettcher H. Functionalisation of textiles by inorganic sol-gel coatings. J Mater Chem. **2005**, 15(41), 4385–4398.

8. Sneh O, Wise ML, Ott AW, Okada LA, George SM. Atomic layer growth of SiO2 on Si(100) using $SiCl_4$ and H_2O in a binary reaction sequence. Surf Sci. **1995**, 334(1–3), 135–152.

9. Leskela M, Ritala M. Atomic layer deposition chemistry: recent developments and future challenges. Angew Chem Int Ed. **2003**, 42(45), 5548–5554.

10. Ott AW, Klaus JW, Johnson JM, George SM. Al_2O_3 thin film growth on Si(100) using binary reaction sequence chemistry. Thin Solid Films. **1997**, 292(1–2), 135–144.

11. Groner MD, Fabreguette FH, Elam JW, George SM. Low-Temperature Al_2O_3 Atomic Layer Deposition. Chem Mater. **2004**, 16(4), 639–645.

12. Jur JS, Parsons GN. Atomic Layer Deposition of Al_2O_3 and ZnO at Atmospheric Pressure in a Flow Tube Reactor. ACS Appl Mater Interfaces. **2011**, 3(2), 299–308.
13. Mousa MBM, Oldham CJ, Jur JS, Parsons GN. Effect of temperature and gas velocity on growth per cycle during Al2O3 and ZnO atomic layer deposition at atmospheric pressure. J Vac Sci Technol Vac Surf Films. **2012**, 30(1), 01A155.
14. Al-Abadleh HA, Grassian VH. FT-IR Study of Water Adsorption on Aluminum Oxide Surfaces. Langmuir. **2003**, 19(2), 341–347.
15. Henn-Lecordier L, Anderle M, Robertson E, Rubloff GW. Impact of parasitic reactions on wafer-scale uniformity in water-based and ozone-based atomic layer deposition. J Vac Sci Technol A. **2011**, 29(5), 051509.
16. Campabadal, F., Beldarrain, O., Zabala, M., Acero, M. C. & Rafi, J. M. Comparison between Al_2O_3 thin films grown by ALD using H2O or O3 as oxidant source. in *2011 Spanish Conference on Electron Devices (CDE).* **2011**, 1 –4.
17. Kim JB, Kwon DR, Chakrabarti K, Lee C, Oh KY, Lee JH. Improvement in Al_2O_3 dielectric behavior by using ozone as an oxidant for the atomic layer deposition technique. J Appl Phys. **2002**, 92(11), 6739-6742.
18. Kim SK, Hwang CS. Atomic-layer-deposited Al2O3 thin films with thin SiO_2 layers grown by in situ O_3 oxidation. J Appl Phys. **2004**, 96(4), 2323–2329.
19. Avice M, Grossner U, Monakhov EV, Grillenberger J, Nilsen O, Fjellvåg H, Svensson BG. Electrical Properties of Aluminium Oxide Films Grown by Atomic Layer Deposition on n-Type 4H-SiC. *Materials Science Forum.* **2005**, 705**,** 483–485.
20. Kim J, Chakrabarti K, Lee J, Oh K-Y, Lee C. Effects of ozone as an oxygen source on the properties of the Al_2O_3 thin films prepared by atomic layer deposition. Mater Chem Phys. **2003**, 78(3), 733–738.
21. Goldstein DN, McCormick JA, George SM. Al_2O_3 Atomic Layer Deposition with Trimethylaluminum and Ozone Studied by in Situ Transmission FTIR Spectroscopy and Quadrupole Mass Spectrometry. J Phys Chem C. **2008**, 112(49), 19530–19539.

22. Kim SK, Lee SW, Hwang CS, Min Y-S, Won JY, Jeong J. Low Temperature (< 100 ° C) Deposition of Aluminum Oxide Thin Films by ALD with O_3 as Oxidant. J Electrochem Soc. **2006**, 153(5), F69–F76.
23. Elliott SD, Scarel G, Wiemer C, Fanciulli M, Pavia G. Ozone-Based Atomic Layer Deposition of Alumina from TMA: Growth, Morphology, and Reaction Mechanism. Chem Mater. **2006**, 18(16), 3764–37673.
24. Ha S-C, Choi E, Kim S-H, Sung Roh J. Influence of oxidant source on the property of atomic layer deposited Al2O3 on hydrogen-terminated Si substrate. Thin Solid Films. **2005**, 476(2), 252–257.
25. Rose M, Niinistö J, Endler I, Bartha JW, Kücher P, Ritala M. In Situ Reaction Mechanism Studies on Ozone-Based Atomic Layer Deposition of Al_2O_3 and HfO_2. ACS Appl Mater Interfaces. **2010**, 2(2), 347–350.
26. Elam JW, Groner MD, George SM. Viscous flow reactor with quartz crystal microbalance for thin film growth by atomic layer deposition. Rev Sci Instrum. **2002**, 73(8), 2981–2987.
27. Benson SW, Axworthy AE. Mechanism of the Gas Phase, Thermal Decomposition of Ozone. J Chem Phys. **1957**, 26(6), 1718–1726.
28. Johnston HS. Gas phase reaction kinetics of neutral oxygen species. NSRDS; **1968**.
29. Kwon J, Dai M, Halls MD, Chabal YJ. Suppression of substrate oxidation during ozone based atomic layer deposition of Al_2O_3: Effect of ozone flow rate. Appl Phys Lett. **2010**, 97(16), 162903–162903–3.
30. Rai VR, Vandalon V, Agarwal S. Surface reaction mechanisms during ozone and oxygen plasma assisted atomic layer deposition of aluminum oxide. Langmuir ACS J Surf Colloids. **2010**, 26(17), 13732–13735.
31. Rai VR, Vandalon V, Agarwal S. Influence of Surface Temperature on the Mechanism of Atomic Layer Deposition of Aluminum Oxide Using an Oxygen Plasma and Ozone. Langmuir. **2012**, 28(1), 350–357.

32. Kwon J, Dai M, Halls MD, Chabal YJ. Detection of a Formate Surface Intermediate in the Atomic Layer Deposition of High-κ Dielectrics Using Ozone. Chem Mater. **2008**, 20(10), 3248–3250.

CHAPTER 5

Precise Nanoscale Modification and Coating of Macroscale Objects: Open-Environment *in Loco* Atomic Layer Deposition on an Automobile

This chapter is based on a manuscript published as:
Moataz Bellah M. Mousa, Christopher J. Oldham, and Gregory N. Parsons, *ACS Applied Materials & Interfaces* **2015** *7* (35), 19523-19529.

Abstract

The fundamental chemical reaction conditions that define atomic layer deposition (ALD) can be achieved in an open environment on a macroscale surface too large and complex for typical laboratory reactor-based ALD. We describe the concept of *in loco* ALD using conventional modulated reactant flow through a surface mounted "ALD delivery head" to form a precise nanoscale Al_2O_3 film on the window of a parked automobile. Analysis confirms that the processes eliminated ambient moisture contamination and met other conditions that define ALD growth. Using this tool, we demonstrate open-ambient patterned deposition, metal corrosion protection, and polymer surface modification.

5.1 Introduction

The basic principle of atomic layer deposition (ALD) involves a set of thermodynamically favorable self-limiting surface reactions that enable the formation of uniform and highly conformal nanoscale metal, metal oxide, and organic thin films with near-monolayer precision over large surface areas.[1–5] This self-limiting reaction scheme ensures complete surface coverage with minimal pinhole density. While the primary commercial use for ALD is in advanced electronics, ALD is also used to modify gas diffusion barriers and membranes,[6,7] passivate surfaces from corrosion and wear,[8–10] and add mechanical strength to polymers, fibers, glass and nanostructures.[11–15] Recent advances in ALD and related molecular layer deposition also show promise for the stepwise surface synthesis of polypeptides,[16] integrated nanobatteries,[17] passivation and stabilization of molecular photoelectrochemical solar cells,[18,19] and directed modification of metal organic framework catalysts.[20] In each ALD self-limiting growth cycle, the substrate receives a saturating dose of each reactant (typically a metal-organic and a reductant for metal, or an oxidant for metal oxide) separated in time or physical location[21–25] by inert gas. The earliest patent literature on ALD shows a range of reactor designs compatible with these basic ALD requirements,[1] and many other reactor design schemes have been developed and commercialized. Reactors are known that can operate at ambient pressure in batch,[26] roll-to-roll[22,23] and spatial ALD geometries,[21,22,24,25] where large pliable substrates are fed through an ALD growth zone. Yet all previous batch and spatial ALD reactor designs require the object to be coated to be carried to the reactor and placed or fed into a controlled reactor volume fixed in a laboratory or other fabrication facility. This reliance on prebuilt confined ALD

reactors reflects the needs of most applications to date, but the basic requirements of the ALD process can be met using other system designs that could significantly amplify the field of use for precision nanoscale coatings and surface modification chemistry afforded by ALD.

In this work, we demonstrate a novel ALD delivery head platform that meets the basic principles of ALD without the need for a defined reactor body, and show that a portable delivery head can function outside a controlled fabrication environment to create well-defined uniform nanoscale thin film coatings on macroscale objects that are much too large and complex for any known conventional ALD reactor in use today. We believe that ALD coatings on macroscale objects could be used for example, to avoid or repair damage from mechanical wear or chemical corrosion,[9,10] passivate surface scratches or defects to keep them from expanding and propagating,[12] or add UV resistance or other optical modification. Using the ALD delivery head, we show feasibility for *in loco* ALD by adding a precise nano-coating to the attached window of an automobile parked outdoors adjacent to our laboratory building. Film thickness measurements confirm that the tool and process met the key ALD requirements for surface saturation and linear growth per cycle without undesired side reactions. We show that the tool can create corrosion protection layers by coating copper sheets, and we extend the tool to modify the surfaces of polymer fibers and fabrics, yielding localized and controlled changes in surface wetting.[27]

5.2 Materials and Methods

The disk-shaped delivery head has a semicircular flat base that contacts the substrate, as shown in Figure 5.1. A flat ~140 μm step milled into half of the head creates a gap between the head and the substrate. Reactants flow into the top of the base and out through

an oblique 1 mm outlet nozzle at the center of the step edge. Under controlled flow conditions identified by computational fluid dynamics modeling, gas transport is radially symmetric through the gap region, thereby defining the semicircular atomic layer deposition zone. The gas flow rate through the nozzle is sufficient to eliminate ambient water vapor from the deposition zone.

In the gas flow system, nitrogen gas (99.999%, Machine Welders Supply Company, Dunn NC) was dried and purified using an Entegris gatekeeper filter (<100 parts per trillion H_2O and O_2) then directed using electronically controlled valves to flow directly to the delivery head through the central gas line. The total N_2 flow rate was adjusted to be between 6 and 15 standard liters per minute (slm). To initiate a reactant dose, additional N_2 flow (0.5-1.0 slm) was initiated in the 'by-pass' line adjacent to the bubbler unit containing trimethylaluminum (TMA, 98%, STREM) or the other similar unit containing UV deionized liquid water. The N_2 in the by-pass was then diverted to flow through the bubbler unit, thereby pushing vapor into the gas delivery zone. After the dose, the N_2 flow continued in the by-pass line for a short time to clear any reactant from the delivery line downstream from the source. For the purge step, two valves on the main N_2 line are opened and others are closed, allowing N_2 to flow symmetrically through both delivery lines to reach the delivery head. The pressure and flow conditions eliminate vapor back-streaming in the gas lines, thereby avoiding unwanted reactions in the delivery system.

The gas delivery lines were wrapped with flexible heating strips to electronically control the temperature at ~70 °C. After a few minutes of gas flow, the heated N_2 exiting the

delivery head caused the substrate temperature to reach about 50-60 °C as measured on the substrate using a k-type thermocouple.

The substrates used were silicon (110) with ~1.8 nm native oxide, planar copper sheets, (oxygen-free electronic grade 101, 99.99% , McMaster-Carr), as well as woven PET and non-woven polypropylene fiber sheets. All substrates were used as received. The glass window on the automobile was only wiped with a dry cloth before coating. Some experiments used Kapton polyimide film tape (0.06 mm thick clean room grade, 3M) as a masking material and cut using a laser cutter. The ALD coatings on copper were evaluated for corrosion protection by heating the copper samples in air at 400 °C for 3 hrs.

Film thickness was measured by spectroscopic ellipsometry (J.A. Woollam Co.) and fit to a three-layer Cauchy model (on silicon), or a Cauchy layer on top of B-spline (on copper and glass). For some films, the thickness was confirmed by cross sectional imaging using Field Emission SEM (FEI Verios 460L).

The steady state N_2 gas flow in the growth zone was modeled with Computational Fluid Dynamics (CFD, Ansys FLUENT) using conservation equations for a single phase compressible flow.[28] To include the effect of the oblique incident gas flow the system was modeled as a 3D geometry. By performing multiple calculations using different grid cell dimensions, we confirmed that the solutions obtained were grid-independent. In the model, the gas velocity boundary condition at the inlet was set based on the experimental steady state flow rate. A flow rate of 5 slm led to an inlet gas velocity of 50 m/s, consistent with a gas flow through the 1 mm inlet nozzle. The outlet boundary condition set the pressure to one

atmosphere. All surfaces maintained the no slip condition, and the isothermal temperature was maintained at 55 °C.

5.3 Results and Discussion

The gas flow setup and delivery head schematic are shown in Figure 5.1. The reactants (trimethylaluminum, TMA, and deionized water vapor) flowed separately in a typical ALD scheme (e.g. $TMA/N_2/H_2O/N_2$) to the gas delivery head through ¼ inch stainless steel lines connected to a flexible stainless steel bellows line. The bellows line allows the delivery head to be adjusted and configured to attach to any surface close to the system. The bottom of the 4.5 cm diameter delivery head was milled by 140±10 μm across half of the surface area, as shown in Figure 5.1, so that placing the head against a flat surface created a gap between the head and the surface that defines the ~8 cm^2 deposition zone area. The gap distance could be adjusted using spacers. The substrates for coating were typically silicon wafers with native oxide, heated to temperatures between 50 and 120 °C. The gas flows into the gap through a 1 mm nozzle inclined at 20°, designed to mimic the well-studied confined oblique impinging jet flow condition.[29] Previous experiments and modeling of the gas flow during low temperature atmospheric pressure ALD[26] show that slow species diffusion at high pressure requires longer purge periods to clear products from the growth zone, slowing the overall process throughput. The ALD delivery head shown in Figure 5.1 produces high gas velocities in the growth zone which decreases the surface boundary layer thickness and promotes fast species transport of the substrate's surface. The flow condition also avoids moisture contamination by eliminating ambient moisture diffusion or convective flow into the deposition region.

A typical sequence for the TMA/N_2/H_2O/N_2 dose times were 0.2/1/0.2/1 seconds, respectively, carried by the inert gas flowing at ~10 standard liters per minute (slm), leading to good ALD over ~8 cm^2 with total cycle time at or near 2 seconds, for an overall Al_2O_3 growth rate of >3 nm/min. All experiments in the lab were performed in an enclosed exhaust hood. Using saturating exposures, some excess TMA exited the gap region but it was rapidly consumed within a few millimeters of the head, posing no significant risk.

In addition to the ALD coating head design shown in Figure 5.1, earlier designs using a central gas entrance point and planar 360° radial flow were constructed and tested, as shown in Figure 5.6. For the radial-flow designs, the symmetric flow created a Bernoulli force that could hold small substrates in place over a fixed distance from the planar head. Modeling results showed laminar and turbulent regions within this gap, resulting in regular and repeatable ring patterns corresponding to ALD and chemical vapor deposition (CVD) regimes observable on the silicon substrate, and are shown in Figure 5.7. The delivery head design in Figure 5.1 produced more uniform ALD, so it was preferred for subsequent evaluation.

Figure 5.2 shows the results from the open-ambient ALD delivery head on silicon wafers. The photos in Figure 5.2 a, b show the resulting shape and surface area of the ALD-coated region. The ALD coating is semicircular with excess nonuniform coating at the edge of the delivery head, where unused reactant (TMA) exits the growth zone and reacts with ambient moisture. We find that the extent of this excess growth can be controlled by the gas dose time (as discussed below), but for our studies, we use this excess growth to visibly help

to locate the ALD growth region. Some excess growth is also seen at the gas inlet point, also discussed further below.

The sample in Figure 5.2a received 150 ALD cycles at ~50°C using TMA/N_2/H_2O/N_2 dose times = 0.2/2/0.1/2 seconds. Using ellipsometry at more than 10 locations under the delivery head (within 1 mm from the ambient contact zone and the nozzle outlet), the film thickness was 14.6 ± 0.9 nm (variation is ± one standard deviation). The refractive index was n= 1.53 ± 0.02, consistent with other ALD Al_2O_3 layers formed at low temperature.[30] Growth at 120°C led to ~0.11 nm/cycle and a refractive index of 1.61± 0.02, consistent with a more dense film. A thicker film (t = 86.3 ± 2 nm, n=1.55 ± 0.02) deposited using 800 ALD cycles in Figure 5.2b shows good color uniformity in the growth region. Using 1 s N_2 purge times, we measured the saturation behavior of the TMA and water doses, and the results are shown in Figure 5.2c. After 500 ALD cycles, the film thickness saturates at ~53 ± 4 nm for TMA and water exposure times exceeding ~0.2 seconds. For this reactant delivery head design, a total gas flow rate of ~10 slm leads to an average gas residence time of ~10 μsec in the region above the growth zone. We find that the gas purge time between reactant doses needs to be larger (> 0.5 s) to ensure that the reactants are effectively removed from the manifold leading up to the delivery head. In our system, the manifold design was not optimized to decrease the required cycle time. The growth thickness vs cycle number (Figure 5.2d) under saturation conditions shows a linear trend with a slope of 0.105 ± 0.005 nm/cycle, consistent with traditional ALD Al_2O_3 growth conditions observed in batch and spatial reactor designs. Error bars on the data points in Figure 5.2d are approximately the same size as the data point symbols.

Photographic images of samples produced using 600 ALD cycles with various gap spacing and gas flow rates are shown in Figure 5.3a, demonstrating that nonoptimized conditions led to visible nonuniform film thickness patterns in the growth zone. To understand the observed trends, computational fluid dynamics (CFD) was used to model the gas flow in the growth zone, and model results are shown in Figure 5.3b, where the dark blue regions represent areas where the gas velocity is low and the dark red regions represent areas of high gas velocity. The model shows that thinner gap spacing and higher gas flow rate improve the gas flow uniformity. Using a 50 μm gap with 10 slm N_2 flow, the model shows the gas flow velocity in most of the gap ranging from 45 to 55 m/s, corresponding to viscous flow with a Reynolds number of 105 to 130. The sample photos in Figure 5.3a generally confirm the trend predicted by the model. Using a relatively large gap size, the reactant delivery nozzle pushes the gas in a direction collinear with the gas entrance port (i.e. upward direction in Figure 5.3), decreasing the flow in the radial direction leading to nonuniform growth. The model also shows that under severe conditions, the flow rate variation within the gap can create a pressure gradient that pulls ambient air and water vapor into the growth zone, promoting nonuniform CVD. The experiment using a ~300 μm gap shows white particles in the growth zone, ascribed to homogeneous reaction between TMA and ambient moisture, confirming the model prediction. We also find that, under some conditions, uniformity can also be promoted by increasing the purge time between the reactant exposures. Excess growth is observed at the gas inlet point. Results from CFD modeling show that the high gas velocity, sudden gas expansion, and change in the flow direction increase the turbulent kinetic energy near the inlet, leading to gas entrainment and CVD film

growth. Consistent with flow modeling, the experimental results in Figure 5.9 show that the extent of CVD near the inlet can be minimized by controlling the gas purge time per cycle. Generally, the model and experimental trends show that the ALD delivery head flow design used here performs well under controlled viscous flow, enabling uniform ALD in the growth area.

The overall motive of this work is to demonstrate that controllable nanoscale thin film coatings can be achieved on macroscale objects, without the constraint of a reactor chamber in a well-controlled laboratory environment. Therefore, as a proof-of-concept demonstration, we transported the system shown in Figure 5.1 outside the lab and attached the ALD delivery head to the window of an automobile in a parking area adjacent to our laboratory building. This same system was used to deposit the films shown and analyzed in Figure 5.2. Figure 5.4a shows a photograph of the system on a lab-cart, where the delivery head is attached to the automobile window as shown in Figure 5.4b. In this demonstration, we chose to deposit a film on the window of an older Volkswagen because the window could be readily removed and carried to the lab for ellipsometry analysis.

While a variety of head mounting approaches could be developed, we held the head in place using a neodymium magnet mounting assembly, as shown in Figure 5.4b. A solid bar attached to two magnets was positioned over the substrate-contacting area of the delivery head. Two additional magnets positioned on the inside of window then squeezed the delivery head securely against the glass, reproducibly fixing the head/substrate gap distance. For the

geometry in Figure 5.4b, gas flow is downward, producing a coating in the area under the lower half of the disk.

For the initial experiments, we attached a silicon wafer piece to the automobile window using double-sided tape and then positioned the ALD delivery head on top of the silicon wafer piece. At the start of the tests, the outdoor temperature was approximately 5 °C, warming up to 10 °C during the morning. Before a run was initiated, heated N_2 was set to flow through the mounted delivery head for about 1-2 minutes raising the temperature in the growth zone to 40-50 °C, as measured by a thermocouple fixed on the inside of the window. Although not specifically studied, flowing hotter N_2 could have produced a higher window glass temperature. For the first few test runs, cold spots in the gas delivery lines led to precursor condensation, resulting in no measureable film growth. After adjustment of the line heating, coating was done using 50, 100 and 150 ALD cycles on silicon, and ellipsometry confirmed that the film thickness increased linearly with the ALD cycles. We then attached the delivery head directly to the automobile window and performed 400 ALD cycles. The window was removed from the car (Figure 5.4c) and using ellipsometry in 10 locations across the coated region (circled in Figure 5.4c and shown in Figure 5.4d), the thickness measured on the car window was 396±12 Å. The 12 Å represents the range deviation of measured thickness from the mean of the 10 measured values. Results collected in Figure 5.4e show that the film thickness scales linearly with the number of ALD cycles with a slope of 1.0±0.05 Å /cycle.

As discussed above, excess reactant exiting the growth zone creates a visible multicolored CVD region, and this region is visible in the photo of the glass window in Figure 5.4d, under the semicircular ALD zone. Close examination of Figure 5.4c reveals similar color patterns toward the bottom-middle of the window, adjacent to the locations where the silicon wafers were fixed during those tests. CVD helps us to visually identify the ALD growth zone, but it is desirable to control or eliminate the extent of this CVD growth. Under the conditions used, the 0.1 s TMA dose delivers > $1x10^{17}$ TMA molecules into the growth zone. This is more than 10 time larger than the number of molecules needed to achieve saturated coverage on the ~16 cm^2 surface area of the substrate and the delivery head face (see the supplemental material). Therefore, increasing the TMA dose time enlarges the CVD region (Figure 5.10) and indicates that the extent of CVD can be controlled by the reactor and process design. The CVD growth on the substrate can also be eliminated using a physical mask as discussed below.

Other applications for open air *in loco* ALD can also be imagined. Parts a-d of Figure 5.5 display examples for corrosion protection and visible pattern design on planar surfaces. It shows photographs of a clean copper plate and the copper plate after it was covered by a patterned Kapton polymer tape mask (~60 μm thick) and coated with 1000 ALD cycles at 60 °C using the open air ALD delivery head. The pattern on the tape mask was formed using a laser cutter and then removing the cut area to partially expose the copper substrate (i.e., within the letters “NCS”, Figure 5.5b). Parts c and d of Figures 5.5 respectively show the patterned ALD coating after removal of the mask, and the coated copper sample after oxidation in air at 400 °C for 3 h. The patterned ALD layer protects the coated copper

regions from oxidative corrosion, creating a visible image that faithfully mimics the patterned mask and ALD metal oxide. In these tests, the polymer mask extends under the coating head base and beyond the coating head edge, Therefore, the flow gap spacing between the delivery head and the tape surface remains unchanged, but increases by 60 μm (e.g., from ~120 to 180 μm) in the region being coated. Using a purge time of 1 s after the TMA and water dose steps for 1000 ALD cycles, the non–uniform gap spacing leads to some excess growth at the edges of the mask, likely due to local reactant trapping. Using the same number of ALD cycles, increasing the purge time to 2 s per cycle eliminated the visible non–uniformity.

We further find that the in–loco ALD design can be adapted to coat porous substrates such as nonwoven fiber mats and woven textiles for controlled surface wetting and localized liquid capture. The Photographs in Figure 5.5 e-g show an ALD gas delivery tube directing reactant flow down onto a fiber substrate, and results of polyethylene terephthalate (PET) and polypropylene (PP) fiber samples coated locally with ALD Al_2O_3. On the native hydrophobic PP, a conformal ALD Al_2O_3 coating deposited at low temperature is known to create a relatively smooth hydrophilic surface finish.[27,31] As shown here in Figure 5.5h, the surface is sufficiently hydrophilic to fix and hold a water droplet when suspended. Exposing the hydrophilic PET fibers to water (containing a red dye for visualization), the coated region becomes hydrophobic completely through the substrate thickness, likely due to surface roughening.[27,31] Such fiber patterning could be effective, for example, for low cost microfluidics, localized biomedical absorbents, fiber material labeling, branding or personal identification, rapid micro-volumetric liquid collection and separation, and other future uses.

The *in loco* ALD design requires sufficient gas flow through the gap region between the growth head and the substrate (or between fibers for coating of fabrics) to exclude or minimize ambient gas contamination. While beyond the scope of this work, the results and scaling trends demonstrated here suggest that design modifications could achieve *in loco* ALD on other surfaces, including microscopically rough and/or macroscopically nonplanar objects. For flat rough surfaces, transporting reactants through stagnant flow regions would require longer exposure times per cycle. A smooth curved surface could be coated using a small delivery head, sized to be smaller than the surface radius of curvature (see the supplemental material). Surfaces that are both rough and curved (such as rock sculptures, engineered structures or any abraded surface), would require more sophisticated or tailored head designs.

5.4 Summary

Overall, we show that the fundamental conditions for self-limited monolayer scale control of surface thin film formation reactions that define ALD can be achieved in an open environment on a macroscale surface too large and complex for typical laboratory reactor-based ALD. We developed the concept of a flexible ALD delivery-head and demonstrated it by coating an automobile window with ALD Al_2O_3 outside of a well-controlled laboratory environment. Combining modeling and experiments, we defined process requirements and demonstrated surface-saturating growth and effective elimination of ambient moisture contamination, even in a demanding open-air outdoor environment, giving ALD growth rates of 1.0±0.05 Å/cycle consistent with laboratory ALD. The design allowed fast growth of Al_2O_3 at ~2 seconds per cycle or ~ 3 nm/min. The ALD delivery head tool is compatible with

patterned surface coating and the resulting ALD films function similarly to typical laboratory ALD for corrosion protection and polymer surface modification. The basic ALD delivery head, gas system design, and process conditions shown here could be substantially simplified and tailored to enable *in loco* ALD to protect, encapsulate, repair, optically or physically modify, or otherwise improve objects of any size fixed in most any location.

5.5 Acknowledgments

This work was supported by the National Science Foundation under grants CMMI-1000382 and CBET-1344618.

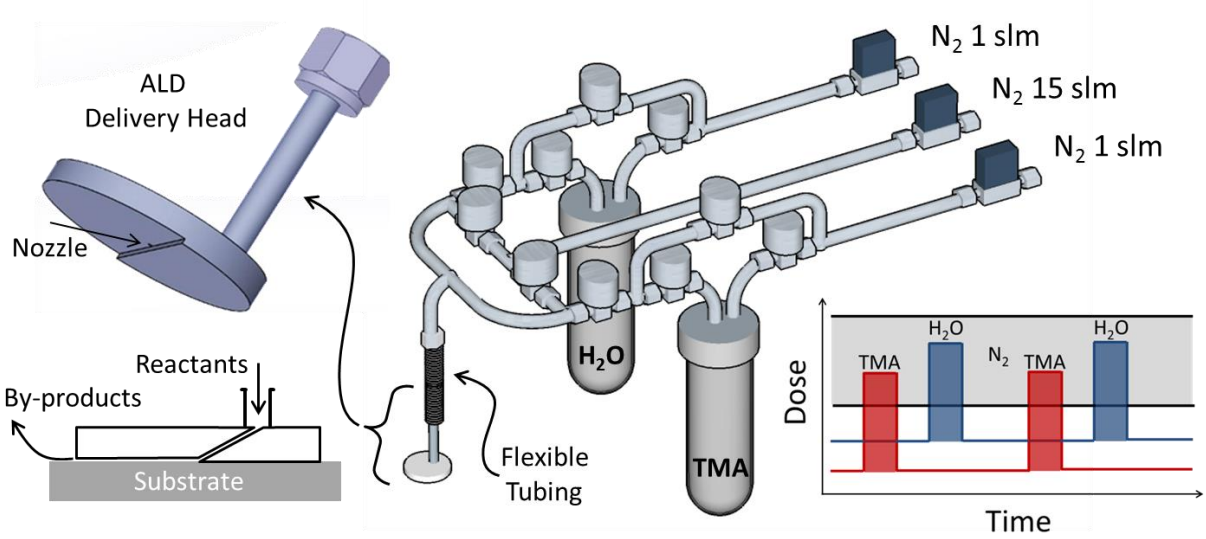


Figure 5.1. Reactant delivery apparatus, ALD delivery head and gas flow schematic for *in loco* ALD. The system uses sequential dosing of reactants (e.g. TMA and H_2O) separated by inert gas purge (N_2) to deposit Al_2O_3. Dry N_2 flows at up to 15 standard liters per minute (slm) through a central ¼ inch delivery line. Electronic valves allow N_2 at a maximum flow of ~ 1 slm to intermittently flow into reactant bubblers to deliver vapors in the sequence shown. The disk-shaped ALD delivery head with a ~140 μm step milled over half the surface sits flat on the object to be coated. Gas exits through the central 1 mm nozzle and flows radially through the gap between the head and the substrate, thereby creating a semicircular ALD growth zone.

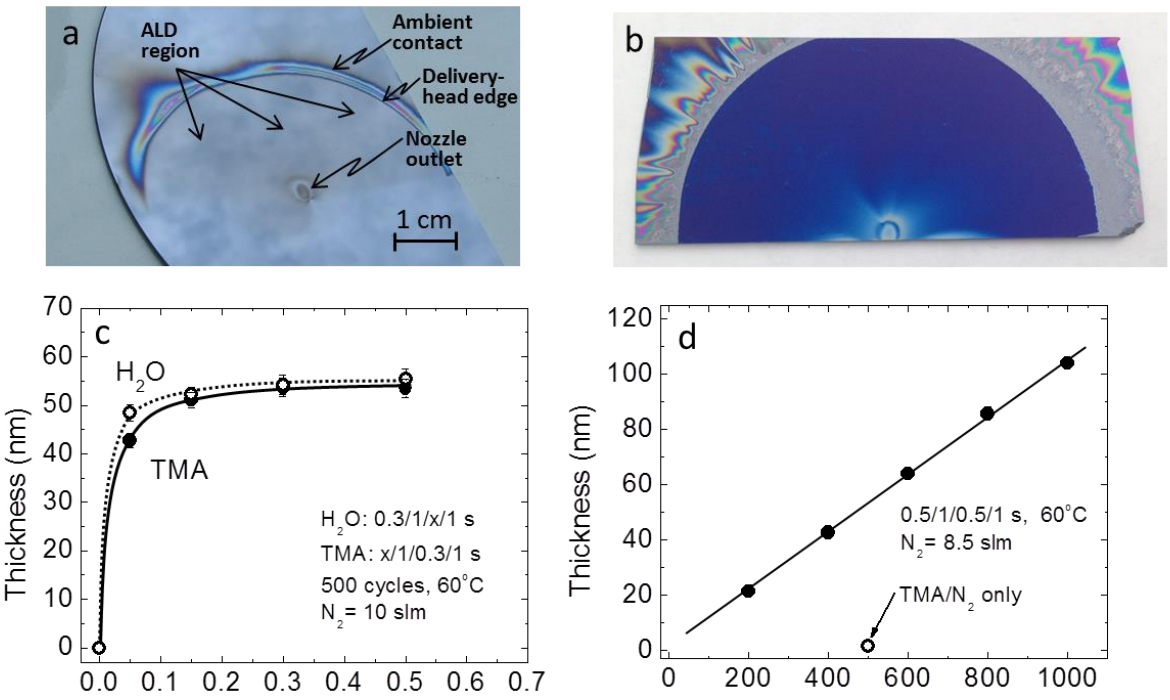


Figure 5.2. Results confirming well-defined ALD using the ALD delivery head. Photographs of silicon substrates coated with (a) 150 and (b) 800 $TMA/N_2/H_2O/N_2$ cycles at 60 °C yielding uniform ALD coatings approximately 15 and 86 nm thick, respectively, in the semicircular ALD region under the delivery head, between the reactant gas entrance point and the head outer edge. Some excess coating appears at the nozzle outlet and outside the coating head, where excess TMA contacts ambient air and water to create a CVD zone. Changing the TMA and water dose times (c) and number of ALD cycles (d) leads to increasing growth saturation and linear thickness with the number of ALD cycles (~1.05 Å/cycle). A point in panel (d) shows that using 500 TMA/N_2 cycles with no water doses leads to less than 1 nm of film deposition, demonstrating negligible diffusion of ambient moisture to the deposition zone.

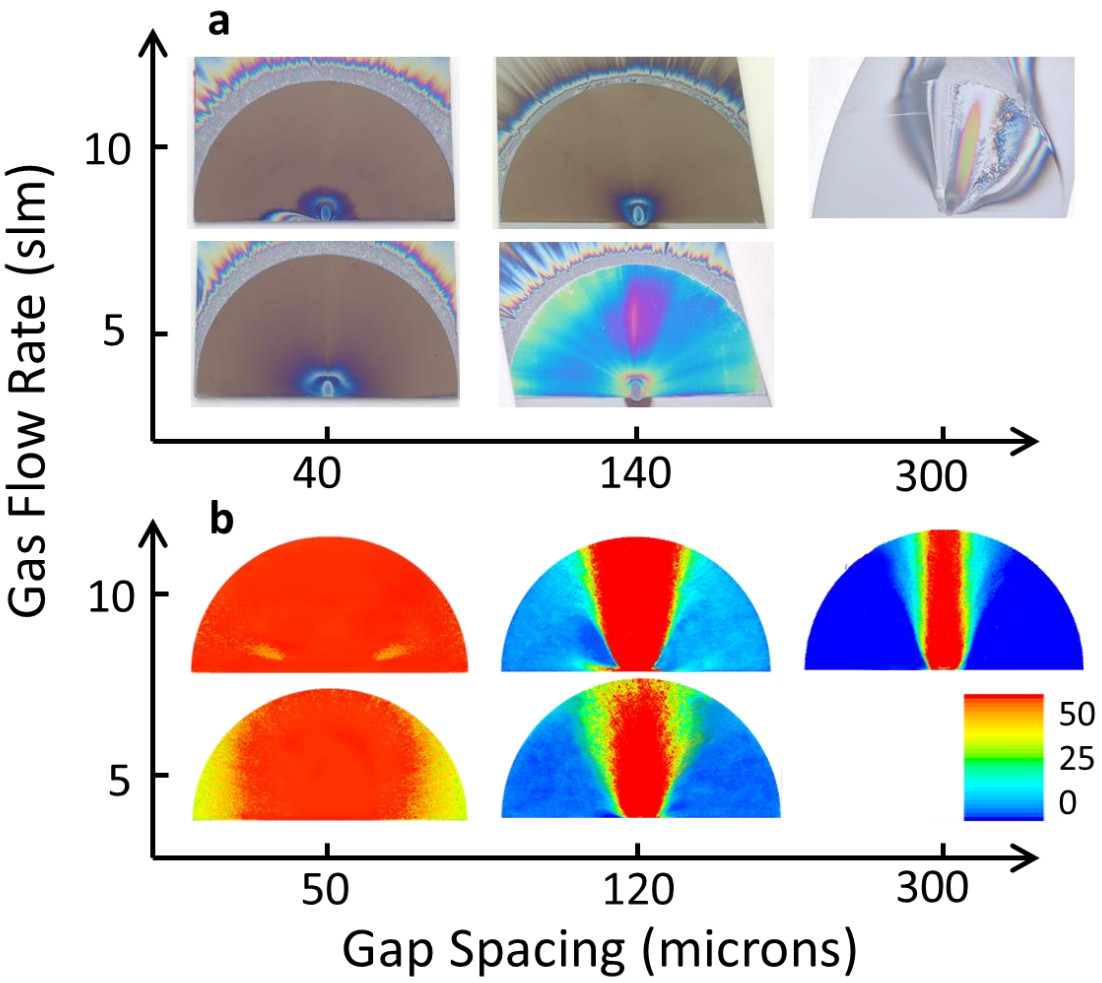


Figure 5.3. (a) Images for films deposited on silicon using different gap spacing and nitrogen gas flow rates. (b) Velocity contours (m/s) from CFD modeling of steady state N_2 flow through the deposition zone at relevant conditions. Using a sufficient gas flow rate, uniform radial flow is obtained for relatively small gap sizes, leading to uniform deposition. For larger gap sizes, gas can flow straight from the nozzle through the gap. The flow gradient creates a Bernoulli force that can pull ambient air and water vapor into the growth zone, leading to visible nonuniformity in the corresponding experimental deposition images.

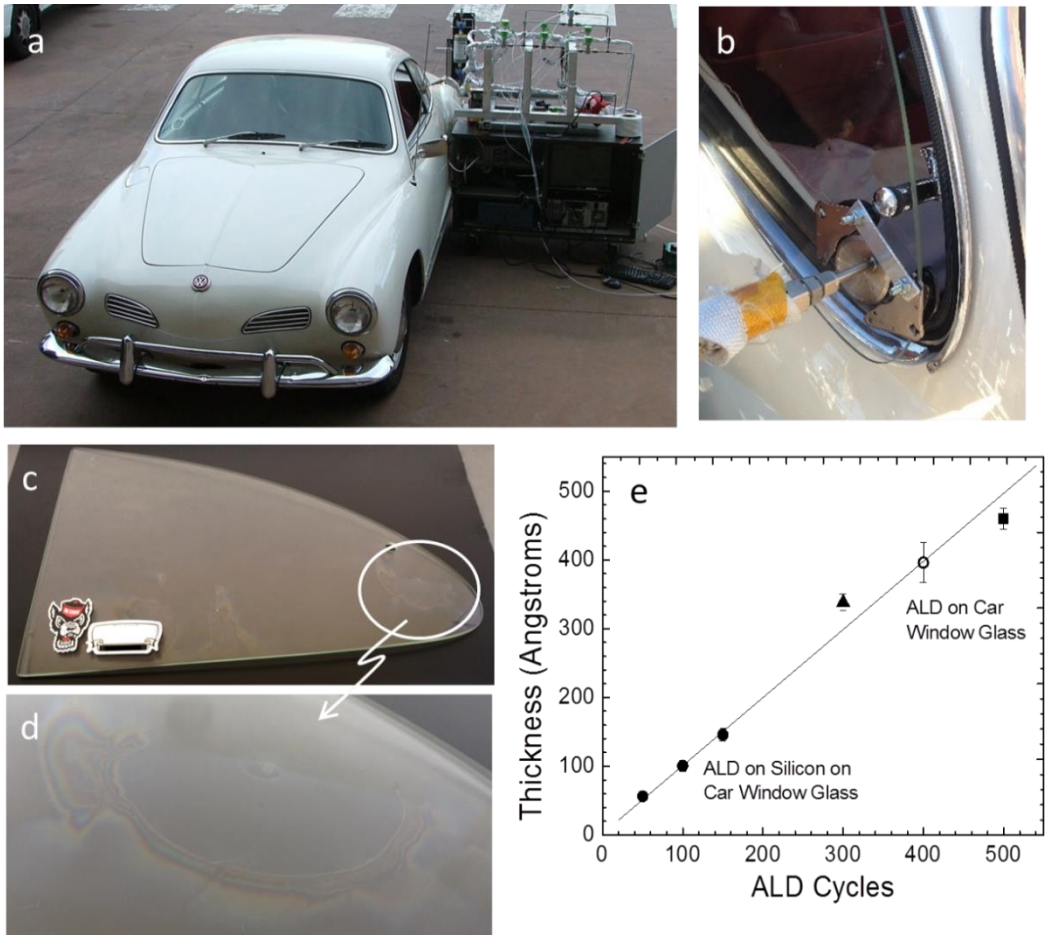


Figure 5.4. (a) *In loco* ALD apparatus adjacent to a Volkswagen automobile. (b) Close-up image of the ALD head affixed to the rear side window glass, delivering 400 cycles of ALD coating to a local region on the window at 50 °C. (c) ALD-coated window removed from the car for ellipsometry analysis. The circled region corresponds to the ALD head mounting location. (d) Close-up image showing the semicircular ALD zone outlined by multicolored CVD growth. (e) Thickness versus number of ALD cycles measured by ellipsometry for ALD coatings on silicon fixed to the car window and on the window itself. The growth per cycle of the *in loco* ALD tool was 0.95-1.05 Å/cycle, corresponding to high growth rate of ~3 nm/min.

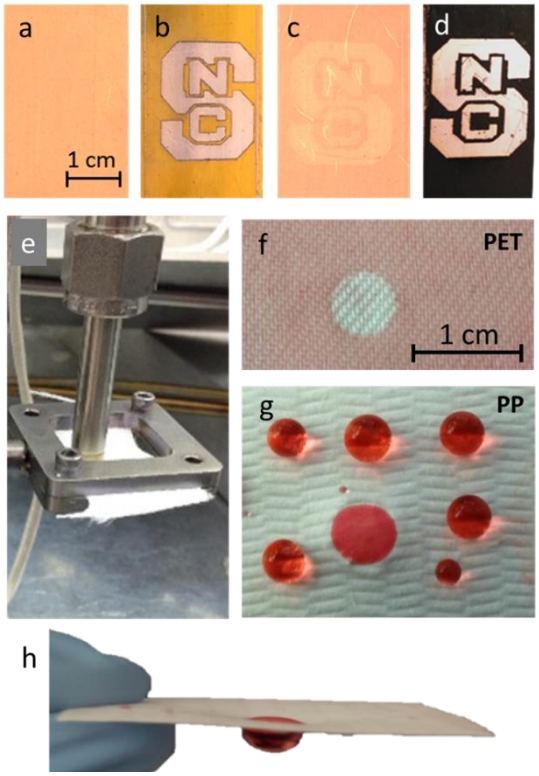


Figure 5.5. Example applications of *in loco* ALD: (a-d) corrosion protection of copper and (e-h) localized surface modification of fibers and textiles. (a) An untreated copper sheet. (b) Copper coated with a patterned polymer tape layer. (c) The tape is removed after coating under the ALD delivery head (1000 cycles, TMA/N_2/H_2O/N_2: 0.1/2/0.1/2 s, N_2 = 8.5 slm, 65 °C). (d) After oxidation in air (400 °C, 3 h) the ALD-coated region remains unoxidized, retaining its original copper color. (e) A modified delivery head was used to deposit spot coatings of ~5 mm diameter onto porous fiber substrates. (f) After localized coating (3 cycles, TMA/N_2 = 200/100 s + H_2O 10 s), a hydrophilic polyethylene terephthalate (PET) fabric becomes hydrophobic in the coated region, repelling red-dyed liquid water. (g and h) The same *in loco* ALD treatment on a hydrophobic polypropylene fiber mat creates local hydrophilic regions that collect and hold red-dyed water droplets.

5.6 Supplemental Material

5.6.1 Alternate Designs for ALD Delivery Head and Resulting Coatings

Beyond the ALD delivery head in Figure 5.1, other designs were fabricated and tested, as shown in Figure 5.6. For the design in Figure 5.6, we found that the radial gas flow from a central delivery point delivered downward onto a planar substrate created a Bernoulli pressure, and using flow rates in the 5-10 slm range, the pressure was sufficient to fix small silicon wafer pieces (1×1 cm^2) in place against the head without vertical support. A small rim on the outer edge of the delivery head kept the substrates from moving laterally. Under these conditions we found repeatable and visually striking ring patterns in the film growth, and ellipsometry and cross-sectional SEM analysis confirmed excess growth in a circular region a few millimeters away from the central gas inlet, as shown in Figure 5.7. Computational Fluid Dynamics modeling results verified that stagnant and turbulent zones are expected in the flow geometry used, leading to trapped reactants and therefore localized CVD growth conditions. Even so, at local positions upstream from the turbulent zone, the film thickness scales linearly with number of ALD cycles (Figure 5.8), consistent with good ALD growth at local areas under the delivery head.

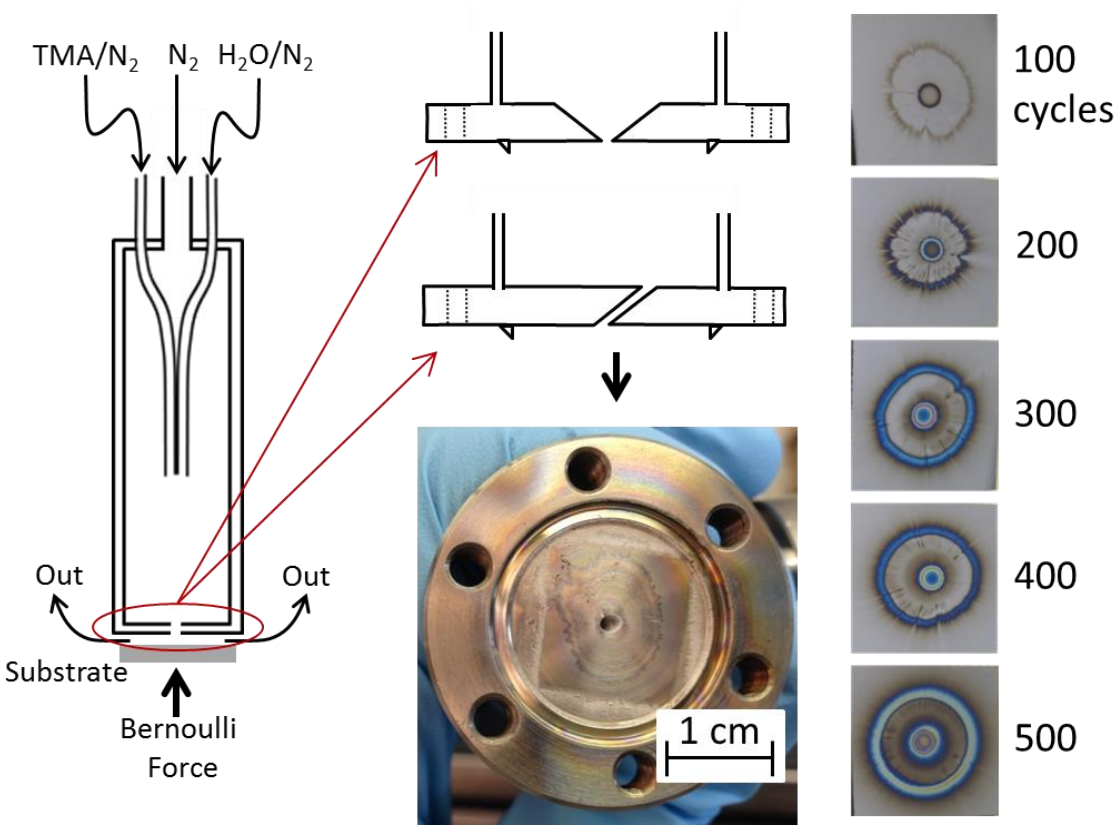


Figure 5.6. Schematics of different designs for the ALD delivery head tested in this study with close ups on the nozzle section, image of the nozzle section and images of samples after deposition of different ALD cycles. Silicon substrates were held in position using a low pressure region generated by the high gas speed based on Bernoulli's principle. Orthogonal and oblique flow outlets were tested and images of silicon wafers from the orthogonal flow design are shown on the right. The ALD delivery head is operated in the a traditional temporal recipe scheme with nitrogen flowed continuously through the three leading tubes and alternating TMA and H2O pulses carried by nitrogen from the respective delivery lines.

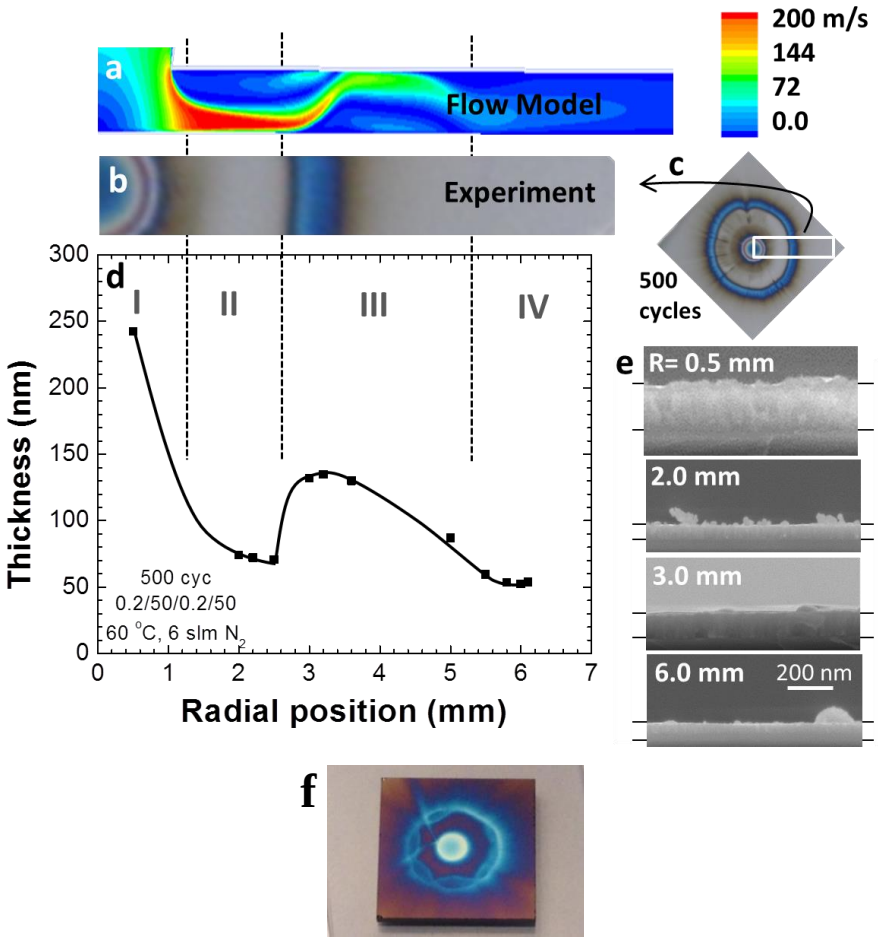


Figure 5.7. Deposition pattern and radial velocity contours (m/s) using the orthogonal flow ALD delivery head design shown in Figure 5.6. (a) CFD model velocity contours for steady state radial N2 flow through a 250 μm head/substrate gap. (b) Magnification of a coating (c) deposited using the radial flow head. (d) Thickness versus radial position determined by SEM (e). The model and experimental results are aligned to show the four distinct flow zones identified in the model: I, stagnant flow; II, uniform radial flow; III, gas circulation and turbulence; and IV, uniform radial flow. (f) A sample showing an alternate non–uniform coating pattern produced using the design in Figure 5.6. During coating, this sample was held in place only by the Bernoulli pressure and it vibrated noticeably during the run, likely producing the visible wave–pattern in the deposited film.

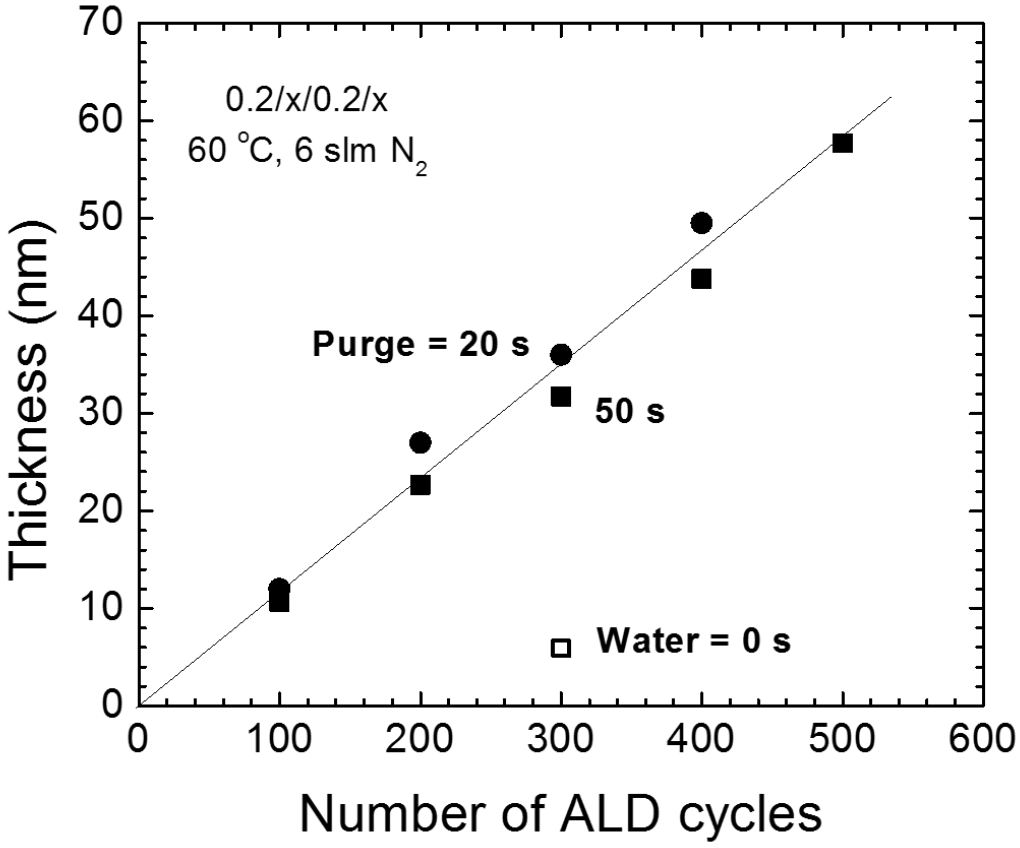


Figure 5.8. The plot shows a linear relation between the film thickness measured using ellipsometry in Region IV (R=6 mm) shown in figure 5.7 versus number of ALD cycles suggesting growth in this zone follows a characteristic ALD growth mode with a growth per cycle of 0.95-1.05 Å/cycle. It was observed that the deposited film was ~10% thicker when the purge time was decreased from 50 to 20 sec indicating insufficient removal of excess reactants and byproducts at the lower purge time. The plot also shows ~5 nm of Al_2O_3 was deposited after 300 TMA/N_2 dose purges steps with no water doses indicating slight diffusion of ambient moisture into the deposition zone.

5.6.2 Film Growth at the Reactant Inlet

The sudden expansion of the gas flow going from the ~1 mm nozzle to the wide deposition surface at the inlet of the deposition volume can lead to vortex formation. Moreover, the change in flow direction from the 20^o inclined nozzle to a 0^o flow over the deposition surface, will lead to the formation of a minor stagnant point followed by eddies. Figure 5.9a shows CFD model results of the calculated turbulent kinetic energy in the growth area (including the gas inlet nozzle zone). The model uses a total gas flow rate of 10 slm and a gap spacing of 100 μm. The change in gas flow direction and rapid gas expansion produce high turbulent kinetic energy at the nozzle outlet in a zone extending ~1.5 mm from the gas inlet point. Turbulent kinetic energy is a good parameter for tracking eddies as it depends on the RMS velocity fluctuations of the flow. These minor eddies trap reactants and promote CVD growth at the inlet zone. The model indicates that increasing the gas purge time between reactant doses will increase the gas clearing from the inlet turbulent zone and therefore decrease the size of the inlet CVD zone.

Consistent with the model, we find experimentally that increasing the purge time decreases the extent of CVD–like growth near the nozzle inlet. Specifically, using a total gas flow rate of 10 slm and TMA/water dose times of 0.1/0.07 s, the extent of CVD at the gas inlet point was observed for various purge times. Photographs of the resulting coatings, given in Figures 5.9 a and b, show that increasing the purge time from 2 to 6 s per cycle decreases the size of the CVD region from ~3 mm to less than 1 mm. Further optimization of the nozzle diameter, nozzle inclination angle, purge gas flow rate, purge time and reactants dose could further help improve uniformity near the nozzle inlet.

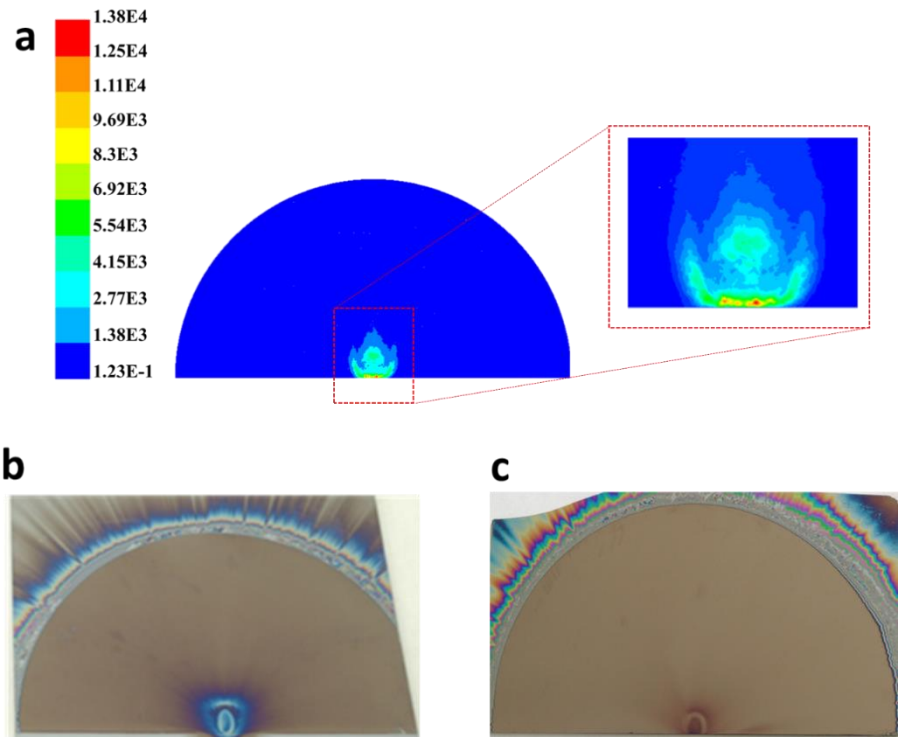


Figure 5.9. Turbulence effect on growth at the nozzle outlet of the ALD delivery head. a) Contours of the turbulent kinetic energy (m^2/s^2) over the deposition surface from CFD modeling of steady state N_2 flow. b) and c) Images of the films deposited with 600 ALD cycles on silicon at 140 μm gap and 10 slm purge flow rate with 2 sec and 6 sec purge times respectively. The film thickness at the CVD-point zone decreased with increasing the purge time, consistent with removal of entrained excess reactants at the formed eddies in this zone.

5.6.3 Excess Film Growth beyond the Coating Head

When excess TMA exits the deposition zone, it reacts with ambient moisture which leads to a CVD coating outside the coating head periphery, where the extent of CVD is expected to depend on the total TMA dose, ambient humidity and total gas flow. Under saturated growth conditions at low temperature, the Al atom surface coverage after the TMA dose is ~$5x10^{14}$ cm^{-2}.[2] Therefore, for the 8 cm^2 coating area of the current design, the total molecule dose needed to saturate the planar substrate and the delivery head face is $8x10^{15}$ molecules. For the conditions used, 0.1 s TMA dose time, ~500 sccm of N_2 flow through the TMA bubbler, and TMA vapor pressure of ~15 Torr, the total TMA dose is >$1x10^{17}$ molecules/dose, which exceeds the required dose by more than 10x. This excess TMA is consistent with the observed CVD zone which extends 0.2-2.0 cm beyond the outer edge of the ALD delivery head. From this analysis, the extent of the CVD zone can be adjusted by either decreasing the TMA dose and/or increasing the growth area of the delivery head. Results in Figure 5.10 show the effect of TMA gas dosing time on CVD growth. Increasing the TMA dose time from 0.05 to 0.4 seconds leads to more visible CVD, consistent with more excess TMA exiting the growth zone. Other designs could also help reduce excess growth and improve uniformity. For example, including low–pressure exhaust around the delivery head could collect any excess reactants before they could interact with the ambient.

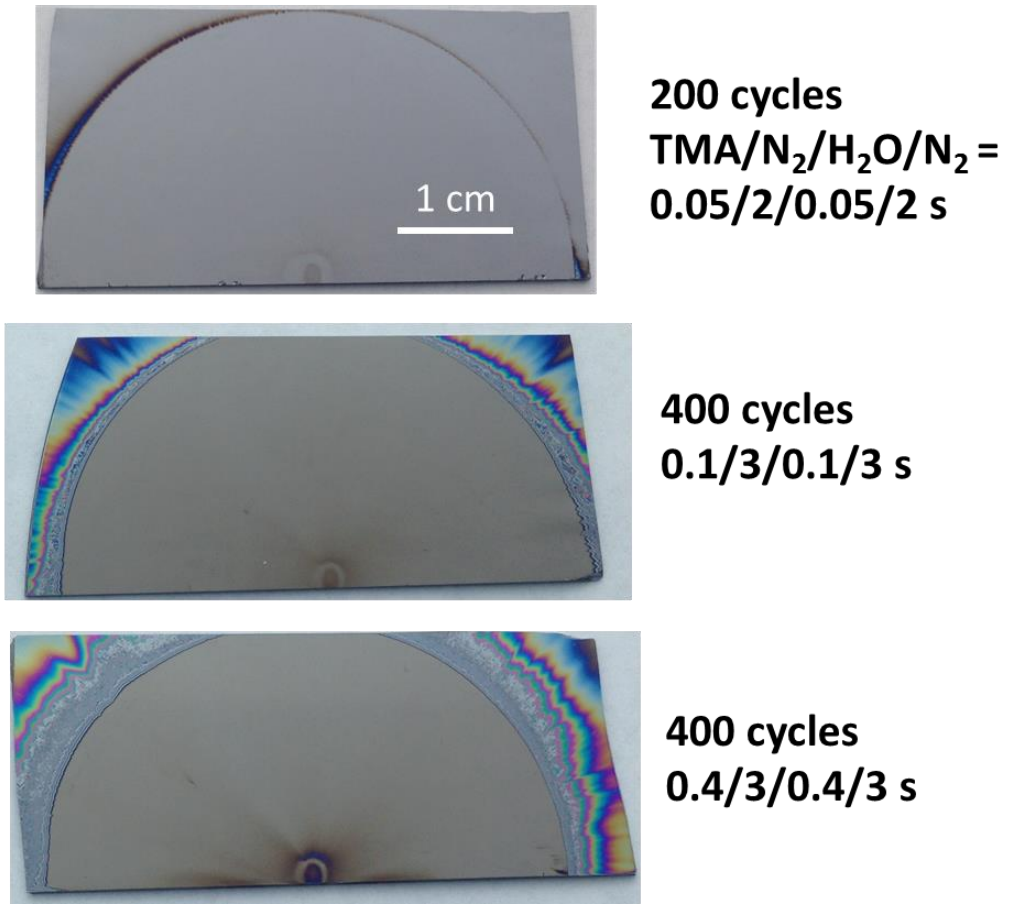


Figure 5.10. Extent of CVD beyond the edge of the delivery head for various TMA exposure times per cycle. Longer exposure time produced more unreacted TMA leaving the growth zone, resulting in more CVD beyond the surface covered by the delivery head.

5.6.4 Coating non-planar surfaces

Design modifications could enable *in loco* ALD coating on microscopically rough and/or macroscopically non–planar surfaces. *In loco* ALD requires the gap between the growth head and the substrate to be sufficiently narrow, and the purge gas flow rate to be sufficient large and uniform to ensure that ambient moisture is excluded from the deposition zone. If moisture is controlled, then uniform metal oxide ALD coatings could be achieved on microscopically rough non–planar surfaces if reactant exposure conditions achieve sufficient species transport to the growth surface area.

Curved surface could also be coated with modified designs. Figure 5.11 shows the relation between delivery head size and surface curvature. The ~8 cm^2 flat delivery head used here could coat a curved surface of low curvature (Figure 5.11a), while a surface with a smaller radius of curvature will require a smaller delivery head (Figure 5.11b). For highly curved surfaces, a point–source deliver head could apply discrete coatings in small areas so as to ensure close proximity with the surface to prevent ambient moisture diffusion to the deposition zone. One point–source design (Figure 5.11c) provides orthogonal flow with no stagnant flow zones or eddies. Design variations could include a diffuser at the nozzle outlet, similar to a shower head reactor type, or an inverted vortex shaped outlet.[32] Diffusers lead to a high pressure drop and will reduce the gas velocity sharply at the deposition surface which will effect growth uniformity. An inverted vortex is more likely to produce uniform coatings using orthogonal flow over a small deposition area.

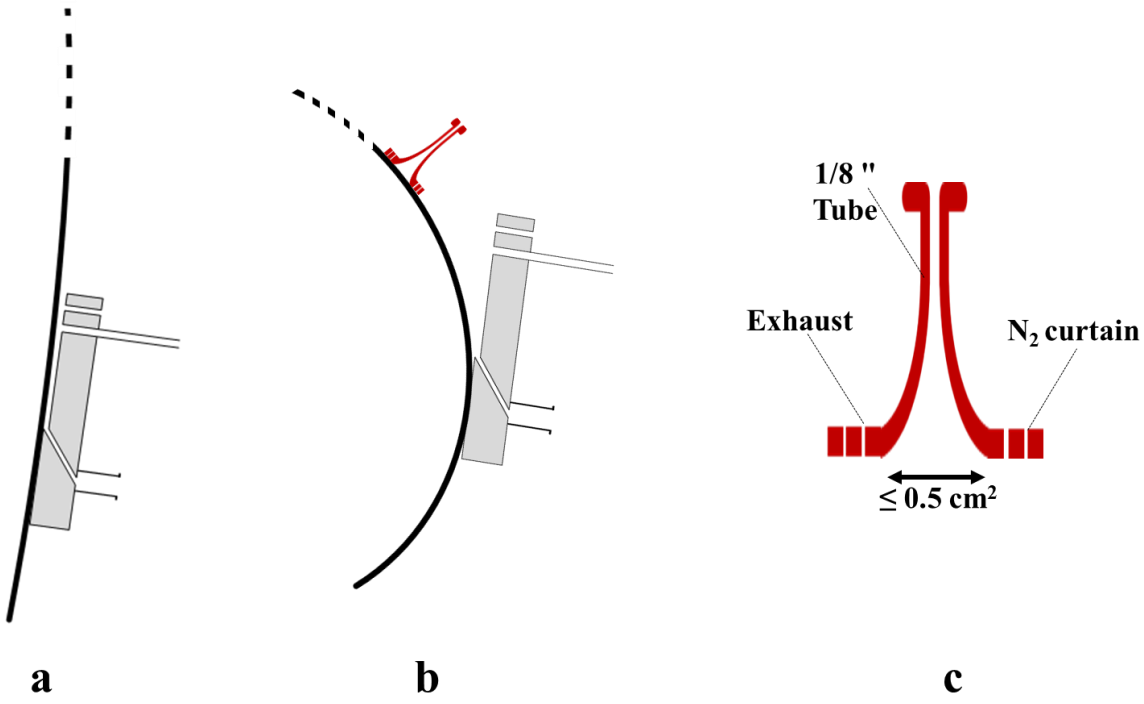


Figure 5.11. Drawings showing the positioning of ALD delivery heads on a) low curvature and b) high curvature surfaces. The head design with oblique outlet and ~8 cm^2 flat deposition area cannot contact closely high curvature surface where a design that covers much smaller area is needed like (c) an ALD "pen". The proposed design (c), not to scale, is an orthogonal flow one with inverted vortex shape to avoid formation of stagnant points on the deposition surface. It also should cover low deposition area (≤ 0.5 cm^2) to fit closely on (b) highly curved and irregular surfaces.

5.7 References

(1) Suntola, T. S.; Pakkala, A. J.; Lindfors, S. G. Apparatus for Performing Growth of Compound Thin Films. US4389973 A, June 28, 1983.

(2) Puurunen, R. L. Surface Chemistry of Atomic Layer Deposition: A Case Study for the Trimethylaluminum/water Process. *J. Appl. Phys.* **2005**, *97* (12), 121301.

(3) Knez, M.; Nielsch, K.; Niinistö, L. Synthesis and Surface Engineering of Complex Nanostructures by Atomic Layer Deposition. *Adv. Mater.* **2007**, *19* (21), 3425–3438.

(4) George, S. M. Atomic Layer Deposition: An Overview. *Chem. Rev.* **2010**, *110* (1), 111–131.

(5) Miikkulainen, V.; Leskelä, M.; Ritala, M.; Puurunen, R. L. Crystallinity of Inorganic Films Grown by Atomic Layer Deposition: Overview and General Trends. *J. Appl. Phys.* **2013**, *113* (2), 021301.

(6) Dameron, A. A.; Davidson, S. D.; Burton, B. B.; Carcia, P. F.; McLean, R. S.; George, S. M. Gas Diffusion Barriers on Polymers Using Multilayers Fabricated by Al2O3 and Rapid SiO2 Atomic Layer Deposition. *J. Phys. Chem. C* **2008**, *112* (12), 4573–4580.

(7) Jiang, Y.-B.; Liu, N.; Gerung, H.; Cecchi, J. L.; Brinker, C. J. Nanometer-Thick Conformal Pore Sealing of Self-Assembled Mesoporous Silica by Plasma-Assisted Atomic Layer Deposition. *J. Am. Chem. Soc.* **2006**, *128* (34), 11018–11019.

(8) Mayer, T. M.; Elam, J. W.; George, S. M.; Kotula, P. G.; Goeke, R. S. Atomic-Layer Deposition of Wear-Resistant Coatings for Microelectromechanical Devices. *Appl. Phys. Lett.* **2003**, *82* (17), 2883–2885.

(9) Nistorica, C.; Liu, J.-F.; Gory, I.; Skidmore, G. D.; Mantiziba, F. M.; Gnade, B. E.; Kim, J. Tribological and Wear Studies of Coatings Fabricated by Atomic Layer Deposition and by Successive Ionic Layer Adsorption and Reaction for Microelectromechanical Devices. *J. Vac. Sci. Technol. A* **2005**, *23* (4), 836–840.

(10) Abdulagatov, A. I.; Yan, Y.; Cooper, J. R.; Zhang, Y.; Gibbs, Z. M.; Cavanagh, A. S.; Yang, R. G.; Lee, Y. C.; George, S. M. Al2O3 and TiO2 Atomic Layer Deposition on Copper for Water Corrosion Resistance. *ACS Appl. Mater. Interfaces* **2011**, *3* (12), 4593–4601.

(11) Lee, S.-M.; Pippel, E.; Gosele, U.; Dresbach, C.; Qin, Y.; Chandran, C. V.; Brauniger, T.; Hause, G.; Knez, M. Greatly Increased Toughness of Infiltrated Spider Silk. *Science* **2009**, *324* (5926), 488–492.
(12) Jylhae, O.; Putkonen, M.; Pakkala, A. J.; Jylha, O. Strengthened Structural Module Used for Display Device Comprises Coating Arranged Conformally on Glass Substrate, Second Substrate and Spacer Element, on Surfaces Facing the outside of Module for Increasing Strength of Module. US 2012307193-A1.
(13) Meza, L. R.; Das, S.; Greer, J. R. Strong, Lightweight, and Recoverable Three-Dimensional Ceramic Nanolattices. *Science* **2014**, *345* (6202), 1322–1326.
(14) Atanasov, S. E.; Oldham, C. J.; Slusarski, K. A.; Taggart-Scarff, J.; Sherman, S. A.; Senecal, K. J.; Filocamo, S. F.; McAllister, Q. P.; Wetzel, E. D.; Parsons, G. N. Improved Cut-Resistance of Kevlar® Using Controlled Interface Reactions during Atomic Layer Deposition of Ultrathin (< 50 A) Inorganic Coatings. *J. Mater. Chem. A* **2014**, *2* (41), 17371–17379.
(15) Gregorczyk, K. E.; Pickup, D. F.; Sanz, M. G.; Irakulis, I. A.; Rogero, C.; Knez, M. Tuning The Tensile Strength Of Cellulose Through Vapor Phase Metallization. *Chem. Mater.* **2014**.
(16) Fu, Y.; Li, B.; Jiang, Y.-B.; Dunphy, D. R.; Tsai, A.; Tam, S.-Y.; Fan, H.; Zhang, H.; Rogers, D.; Rempe, S.; et al. Atomic Layer Deposition of L-Alanine Polypeptide. *J. Am. Chem. Soc.* **2014**, *136* (45), 15821–15824.
(17) Liu, C.; Gillette, E. I.; Chen, X.; Pearse, A. J.; Kozen, A. C.; Schroeder, M. A.; Gregorczyk, K. E.; Lee, S. B.; Rubloff, G. W. An All-in-One Nanopore Battery Array. *Nat. Nanotechnol.* **2014**, *9* (12), 1031–1039.
(18) Hanson, K.; Losego, M. D.; Kalanyan, B.; Ashford, D. L.; Parsons, G. N.; Meyer, T. J. Stabilization of [Ru(bpy)2(4,4′-(PO3H2)bpy)]2+ on Mesoporous TiO2 with Atomic Layer Deposition of Al2O3. *Chem. Mater.* **2013**, *25* (1), 3–5.
(19) Son, H.-J.; Prasittichai, C.; Mondloch, J. E.; Luo, L.; Wu, J.; Kim, D. W.; Farha, O. K.; Hupp, J. T. Dye Stabilization and Enhanced Photoelectrode Wettability in Water-Based Dye-

Sensitized Solar Cells through Post-Assembly Atomic Layer Deposition of TiO2. *J. Am. Chem. Soc.* **2013**, *135* (31), 11529–11532.
(20) Mondloch, J. E.; Bury, W.; Fairen-Jimenez, D.; Kwon, S.; DeMarco, E. J.; Weston, M. H.; Sarjeant, A. A.; Nguyen, S. T.; Stair, P. C.; Snurr, R. Q.; et al. Vapor-Phase Metalation by Atomic Layer Deposition in a Metal–Organic Framework. *J. Am. Chem. Soc.* **2013**, *135* (28), 10294–10297.
(21) Levy, D. H.; Freeman, D.; Nelson, S. F.; Cowdery-Corvan, P. J.; Irving, L. M. Stable ZnO Thin Film Transistors by Fast Open Air Atomic Layer Deposition. *Appl. Phys. Lett.* **2008**, *92* (19), 192101–192101.
(22) Poodt, P.; Cameron, D. C.; Dickey, E.; George, S. M.; Kuznetsov, V.; Parsons, G. N.; Roozeboom, F.; Sundaram, G.; Vermeer, A. Spatial Atomic Layer Deposition: A Route towards Further Industrialization of Atomic Layer Deposition. *J. Vac. Sci. Technol. Vac. Surf. Films* **2012**, *30* (1), 010802.
(23) Dickey, E.; Barrow, W. A. High Rate Roll to Roll Atomic Layer Deposition, and Its Application to Moisture Barriers on Polymer Films. *J. Vac. Sci. Technol. Vac. Surf. Films* **2012**, *30* (2), 021502.
(24) Ellinger, C. R.; Nelson, S. F. Selective Area Spatial Atomic Layer Deposition of ZnO, Al2O3, and Aluminum-Doped ZnO Using Poly (vinyl Pyrrolidone). *Chem. Mater.* **2014**, *26* (4), 1514–1522.
(25) Muñoz-Rojas, D.; MacManus-Driscoll, J. Spatial Atmospheric Atomic Layer Deposition: A New Laboratory and Industrial Tool for Low-Cost Photovoltaics. *Mater. Horiz.* **2014**, *1* (3), 314–320.
(26) Mousa, M. B. M.; Oldham, C. J.; Jur, J. S.; Parsons, G. N. Effect of Temperature and Gas Velocity on Growth per Cycle during Al2O3 and ZnO Atomic Layer Deposition at Atmospheric Pressure. *J. Vac. Sci. Technol. A* **2012**, *30* (1), 01A155.
(27) Hyde, G. K.; Scarel, G.; Spagnola, J. C.; Peng, Q.; Lee, K.; Gong, B.; Roberts, K. G.; Roth, K. M.; Hanson, C. A.; Devine, C. K.; et al. Atomic Layer Deposition and Abrupt Wetting Transitions on Nonwoven Polypropylene and Woven Cotton Fabrics. *Langmuir* **2010**, *26* (4), 2550–2558.

(28) Anysys Fluent 14.0: User's Guide. Canonsburg, Pennsylvania: Ansys Inc 2011.
(29) Garimella, S. V. Heat Transfer and Flow Fields in Confined Jet Impingement. *Annu. Rev. Heat Transf.* **2000**, *11* (11), 413–494.
(30) Groner, M. D.; Fabreguette, F. H.; Elam, J. W.; George, S. M. Low-Temperature Al2O3 Atomic Layer Deposition. *Chem. Mater.* **2004**, *16* (4), 639–645.
(31) Jur, J. S.; Spagnola, J. C.; Lee, K.; Gong, B.; Peng, Q.; Parsons, G. N. Temperature-Dependent Subsurface Growth during Atomic Layer Deposition on Polypropylene and Cellulose Fibers. *Langmuir* **2010**, *26* (11), 8239–8244.
(32) Seong Hwang, C.; Yoo, C. Y. *Atomic Layer Deposition for Semiconductors*; 2014.

CHAPTER 6

Design of a High-Throughput Spatial Atomic Layer Deposition Reactor for Functional Nano-coatings on Porous Materials

This chapter may be revised for a future publication by Moataz Bellah M. Mousa, Alexandra H. Brozena, Christopher J. Oldham and Gregory N. Parsons.

Department of Chemical and Biomolecular Engineering, North Carolina State University, Raleigh, NC, USA

Abstract

Thin films deposited by atomic layer deposition (ALD) on fabrics and mesoporous scaffolds have shown major success in key applications in the textiles and energy industries. However, the significant hurdle for industrial adoption of ALD is its intrinsic low throughput. Recently, the development of spatial ALD has offered process throughputs tens to hundreds times more than conventional temporal ALD process, however all reported designs have been limited to solid surfaces. In this study, a new spatial ALD reactor design is presented, which operates in a continuous roll-to-roll style under ambient conditions for coating porous substrates. The prototype shown is believed to be a key milestone towards incorporating the ALD process into existing production lines at manufacturing facilities, especially within the textiles and batteries industries. The results of rigorous computational fluid dynamics modeling was used to determine process parameters and design specifics, which are presented herein. Moreover, preliminary experimental data is presented and shows that aluminum oxide thin films deposited using the spatial ALD process leads to a similar surface modification on polypropylene fabric as that induced by a batch ALD process operating under vacuum in a temporal ALD mode.

6.1 Introduction

In the semiconductor industry, atomic layer deposition (ALD) is used and operated in a batch manner under vacuum pressures, offering a satisfactory throughput for the highly-demanding process control manufacturing environment. The semiconductor industry originally adopted the ALD process due to its ability to precisely control film thickness and deposit very conformal and uniform layers with a typical one-sigma film thickness uniformity requirement of less than 1%.[1] For other industries, different merits of the ALD process are more appealing. For example, industries depending on temperature sensitive materials, such as synthetic and bio-based polymers, will value the ability of ALD to deposit functional nano-layers at low processing temperatures under dry vapor environments more so than the technique's ability to deposit ultra-uniform layers. In addition, the high level of the process conformality attracts many industries looking to coat complex 3D structures, like catalysts. For industries beyond the semiconductor field, ALD process offers key improvements to their materials processing. Yet, the process scalability of ALD is always the key hurdle for industrial implementation. The throughput obstacle is even more difficult to overcome for porous materials where the ALD process tends to be orders of magnitude slower.[2]

Perhaps the most commonly studied porous substrates in ALD research are textiles and catalysts.[3] In the textiles industry, ALD offers the ability to modify the surface or bulk of each individual fiber, both uniformly and conformally in the dense fabric matrix without negatively affecting the fabric's appearance, feel, or weight.[4] Thin films deposited using

ALD have been shown to influence the fiber properties of many woven and non-woven fabrics for applications like wearable electronics and sensors,[5-7]filtration,[8] water repellent finishes for self-cleaning apparels,[9,10] flame retardant clothing, and stab and ballistic resistant garments.[11]

ALD research has studied the modification of many types of fiber polymers, including cellulose, polypropylene, polyethylene terephthalate, and nylon.[12] On the other hand, mesoporous nanostructured materials are now widely being used for energy related applications, such as dye sensitized solar cells[13] and batteries[14,15]. ALD excels at the deposition of functional thin films in tortuous and narrow pore 3D structures, yet for all these applications, the key challenge is to engineer an ALD process that can coat these porous substrates at a high enough throughput and reasonable cost in order to allow for the method's incorporation into the existing manufacturing lines.

Spatial ALD[16] is a variation on the method which aims to address the scaling issues of conventional ALD on porous substrates. It is usually achieved by moving the substrate under different reactant zones separated in space by inert gas "curtains" as shown in Figure 6.1a. This spatial gas delivery allows for very high throughput, achieving up to a few microns per hour of deposition thickness, which is hundreds of times higher than conventional temporal ALD.[17] In spatial ALD, the reactants flow continuously to their respective zones. When the substrate enters a reaction zone, the corresponding half reaction occurs on the substrate. The ALD cycle is not completed until that same substrate reaches the second reactant zone. The number of times that the substrate is exposed to both reactant zones

determines the number of ALD cycles and hence the film thickness. The exposure to multiple ALD cycles can be done by having multiple reactant zones in series (Figure 6.1a), therefore the total number of ALD cycles is determined by the reactor length. Alternatively, the substrate can be "reciprocated" back and forth under a specific number of zones (Figure 6.1b) and in this case the total number of ALD cycles will be determined by the number of oscillations and the set number of reaction zones of the reactor.[18,19]

The spatial ALD process has been studied under inert atmosphere[20,21] and ambient conditions.[17,22] For operations under ambient conditions, the reactor design must include gas "shields" at the reactor boarders to keep the deposition area clean and prevent any moisture diffusion into the reaction zones. Other key design goals include preventing reactants mixing, supply reactant uniformly over the substrate, and to have enough reactant exposure and inert gas purging. To achieve these goals, the key design parameters for spatial ALD include substrate velocity, spatial separation of reactants, gas flow rates, and the gap size between the substrate and the reactor head, and in some cases, pumping rate between reactant zones. Different reactor designs have been tested based on the spatial ALD concept, either in a roll-to-roll fashion, [21,23,24] linear reciprocation, [18,22,25] spinning,[17,26] or in a rotary drum.[20] Current research and development has focused on deposition on silicon and polymers for solar cells passivation,[17,19] barrier coatings,[21] and flexible electronic[27,28] applications. Current spatial ALD reactor designs were made to apply coatings on non-porous substrates, whether rigid or flexible. To date, no spatial ALD reactor has been designed for coating porous materials.

To extend the spatial ALD concept to porous substrates, both new and existing challenges must be addressed. The key design goals will be similar to those stated for solid substrates, though the primary difference will be to ensure that the flowing gas will penetrate all the way through the substrate at each reactant zone. Previous spatial ALD designs used the solid substrate itself to ensure uniform gas coverage over the whole surface, as gas directed from each reaction zone nozzle tend to hit the substrate and flow over it. However, in the case of porous substrates, gases will tend to flow through the substrate thus the diameter of the nozzles and their distribution within the same gas zone will require more rigorous design of the gas manifold. Moreover, solid substrates tend to help in the formation of inert gas shields by maintaining the micro-sized gap between the substrate and the gas manifold, similar to what was shown in chapter 4 with the delivery head reactor. The gas "shields" challenge is not intuitive in the case of porous substrates, especially from the gas manifold sides (short length). Last but not least, due to the high specific surface area of porous materials as compared to planar ones, higher reactant exposures are needed which impart added difficulty in ensuring that reactants remain separated during deposition, especially as they travel through the tortuous 3D substrate. The key design parameters to address these issues include gas nozzle diameter and spacing within the same gas zone and between different reactant zones, gas flow rates, gap size between the reactor and the substrate, gas manifold tube diameters and substrate speed.

In this study we present a unique continuous high throughput atmospheric pressure flow-through Spatial ALD reactor for depositing uniform and conformal functional thin films on porous substrates, such as textiles and mesoporous scaffolds. This proof of concept

reactor will help us understand how to scale ALD for industrial adoption by the textile and energy sectors. The conceptual design of the main gas manifold is shown in Figure 6.1c. The manifold consists of rows of nozzles (channels) for each reactant (trimethylaluminum (TMA) and water for this study), separated by intervening rows of nozzles (channels) for the inert gas flow (nitrogen). Nitrogen acts as a carrier gas for the reactants as well. The gas going to the channels is supplied through three gas manifolds, which distribute the nitrogen and reactant gas flows as shown in Figure 6.1c. Our prototype consists of five ALD cycles beneath which the substrate reciprocates back and forth to grow thicker films as shown in Figure 6.1b. The design specifications and process parameters were determined using extensive gas flow dynamics modeling. The results of these different models will be shown first before discussing the experimental data derived using the new spatial ALD reactor tool to deposit aluminum oxide (Al_2O_3) films on polypropylene (PP) fabric.

6.2 Materials and Methods

6.2.1 Spatial ALD System

The prototype of the spatial ALD system has a small footprint and was contained inside a movable vented cabinet as shown in Figure 6.2a for any possible safety and health concerns, mostly related to the possibility of aluminum oxide (Al_2O_3) nano-particles formation. The substrate handling system consists of two rollers, an accumulator and a set of tensioners. A roll of the material to be coated was loaded on the driving roller and then the substrate end was fixed to the other roller using aluminum tape. The rollers were operated using a belt driven motor system that allows web speed up to 10 m/min. The web system was

also equipped with light sensors at the two ends of the reactor to allow reciprocation of the web back and forth beneath the gas-depositing reactor head.

The spatial ALD reactor consisted of three showerheads in series as shown in figure 6.2b, following the conceptual design shown in Figure 6.1c. Each showerhead is 15cm wide and 60 cm long with 23 nozzle arrays on the underside as shown in Figure 6.2c4. Each array has 76 nozzles of 0.5 mm in diameter. The 23 nozzle arrays allows each showerhead to include 5 ALD cycles, starting and ending with inert N_2 arrays as shown in Figure 6.2c4. In our setup, out of the three combined showerheads, only the central showerhead will flow the ALD reactants. The two surrounding showerheads to the right and left flow only inert nitrogen to ensure that the area being coated will not be exposed to ambient air as it is reciprocated back and forth beneath the central "5 ALD" showerhead. The flow of gases within the central showerhead is shown in detail in Figure 6.2c. For the TMA line for instance, the TMA carried by nitrogen from the TMA bubbler flows through the manifold inlet shown in Figure 6.2c1, before it is distributed through 5 outlets (Figure 6.2c3 which is the bottom view of the schematic in Figure 6.2c1). These 5 manifold outlets lead to 5 different channels, each corresponding to a nozzle array as shown in Figure 6.2c2 and 6.2c4. The same gas flow design is used for the inert nitrogen and water lines except that the number of manifold outlets and channels varies for each. By reciprocating the substrate back and forth under the showerheads, increments of 10 ALD cycles are applied for each back and forth reciprocation.

Nitrogen gas (99.999%, National Welders) was dried and purified by flowing through an Entegris gatekeeper filter (<100 parts per trillion of H_2O and O_2) before being used as purge gas or reactants carrier gas. The flow rate going to the gas manifold was controlled using mass flow controllers for the TMA, H_2O and N_2 lines. Liquid H_2O and TMA precursors were kept in a flow over bubblers at room temperature. The bubblers setups included bypass lines to allow for flow of N_2 only (without carrying reactants) through the TMA and H_2O lines during process initialization steps.

All reactor gas-flow lines were heated using resistive heating tape. The temperature of the showerheads was monitored using a temperature controller set to 120 ^oC. The substrate temperature was much lower than 120 ^oC due to different sources of heat loss, especially since the fabric was only heated by the flow of the heated gases.

All modeling and experimental work in this study were carried out on a 0.33mm thick non-woven polypropylene fabric with a basis weight of 75 gm/m^2 and surface area of1.4 m^2/g.

6.2.2 Computational Fluid Dynamics (CFD) Models

Two main sections of the spatial ALD system were modeled using CFD: the gas flow in the showerhead; and the flow out of the nozzle arrays and through the porous medium. Ansys FLUENT 14.0 package was used to generate the solution grids, specify the balance equations and apply finite volume solution algorithms for the coupled partial differential equations. All models were solved for steady state flow under isothermal conditions. For all models, it was confirmed that the solution is grid independent when different cases were

solved for different number of grid cells using the grid adapting option in Ansys FLUENT. Due to the involved complex geometry, all cases were solved as 3D models as will be shown in the results and discussion section. Inlet boundary conditions were set to "velocity inlet" and their values were chosen to achieve the required steady state gas flow rate, while atmospheric pressure was set as outlet boundary condition and all other surfaces were set as fixed "wall" with a no slip condition. In the model of the outlet flow from the nozzle arrays, the porous medium was kept stationary and no moving mesh conditions were applied. Also, the porous medium was modeled by adding a momentum source term to the flow equations, defined by the viscous and inertial loss terms which depend mainly on the gas flow velocity. The viscous and inertial resistance coefficients of these loss terms can be determined in variety of different ways. For this study, the viscous resistance coefficient, the reciprocal of substrate permeability, was determined based on the widely accepted Kozeny-Carman equation[29] that agreed well with other experimental data obtained for other fiber mats.[30] The inertial resistance coefficient was determined using Ergun equation.[31]

6.2.3 Process Operation and Characterization

Before the start of each experiment, the PP fabric was kept under the showerheads for 15 min to dry under a constant stream of N2, flowing at a rate of 20 slm through each of the three showerheads. The N_2 flow was maintained at 20 slm for the left and right showerheads during the deposition, while for the central showerhead different flow rates were tested for the TMA, H_2O and N_2 lines. The deposition process was started by redirecting the N_2

through the H_2O and TMA bubblers by shutting off the bypass lines while the PP fabric was reciprocated back and forth under the showerheads at linear speeds of 2-10 m/min.

PP fabric was used for the preliminary experiments because it was found to turn hydrophilic after applying 90+ ALD cycles of TMA/H_2O.[4] In this preliminary study, surface wetting properties were used to determine deposition uniformity. Static water contact angle was used to compare the quality of deposited Al_2O_3 films to those deposited using a batch reactor under vacuum pressure and traditional temporal ALD conditions. The contact tangle was determined using Rame-Hart, Inc. Goniometer, model 200-FI.

6.3 Results and Discussion

6.3.1 Reactants Exposure and Turbulence Preclusion

Any ALD process is defined by the reactant exposure required to saturate all the reaction sites on the substrate and then the purge flow needed to remove all of the reaction products and excess reactants before the next exposure step. Before going through more rigorous modeling of the process parameters, we did simple calculations to determine flow rate requirements to supply enough reactants to saturate the total area of the substrate and as well as to penetrate all the way through the fabric. Assuming that reactant zone extends for 0.25 in (~6 mm) long and 15cm wide, then the total surface area of the fabric per zone will be ~0.12 m^2 based on the 75 g/m^2 basis weight and 1.4 m^2/g specific surface area. For the water zone, the number of Al-CH_3 reaction sites will be 6E17 based on the specific number of methyl sites of 5E14 per cm^2.[32] Hence, the number of water moles required to saturate these reaction sites will be ~1E-6 mol. The maximum flow rate required will depend on the

residence time of the (15X0.6 cm^2) fabric in the H_2O zone. The shortest exposure time will be 0.038 sec for the maximum web speed of 10 m/min leading to a maximum water supply requirement of 2.6E5 mol/sec. Since water is carried by nitrogen, then it makes more sense to calculate the required flow rate of N_2 to go through the water bubbler, which can be calculated from the equation of carried vapor flow rate:[33]

$$F = F_{vap}.R.T_{std}.\frac{P_{bubbler} - p_{vap}}{p_{vap}.P_{bubbler}}$$

Where F is the volumetric flow rate of the carrier gas through the bubbler, F_{vap} is the molar flow rate of carried gas, p_{vap} is the saturated vapor pressure of the liquid precursor at the bubbler temperature, $P_{bubbler}$ is the total pressure in the bubbler, R is the universal gas constant and T_{std} is 273 K.

By doing the math, we can determine that the N_2 flow rate required to supply enough water molecules to react with all of the available reaction sites on the PP fabric is ~1 slm. Following the same procedure for TMA, the required N_2 flow rate is ~1.5 slm, which is slightly higher than water since TMA has a lower vapor pressure at room temperature. These tentative flow rates will be the basis for the gas manifold design using the CFD as will be shown next.

Another key aspect of the spatial ALD process through porous substrates is the purge quality. Due to the tortuous and complex structure of the porous materials, eddies can easily form. We need to make sure that reactants will flow in smooth stream lines through the fabric with minimum eddies to avoid any trapped reactants which could lead to undesired CVD

growth. Porous media leads to viscous and inertial resistance for the gas flow. The former is mainly due to friction with the substrate surface, while the latter is mainly due to "collision" of the gas with the surfaces which can lead to greater eddy formation. The extent of inertial resistance occurrence can be estimated using Reynold's number, although there is not good consensus in the literature as to what characteristic length should be used for such a calculation nor what is the threshold value for the transition between viscous to inertial resistant flow.[34] Fiber diameter is the trivial choice as a characteristic length for Reynold's number calculation since it does not fully represent the conduit where the gas flows through. The reciprocal of the specific surface area of the fiber mat (m^3/m^2), the square root of the porosity and the ratio of inertial resistance coefficient (β) to viscous resistance coefficient (α) according to Forchheimer equation were all suggested as possible characteristic lengths for the flow through porous media.[3536] The first two were found to be in the same range of the intra-fiber pore size while the ratio of the constants of Forchheimer equation agreed better with the inter-fiber pore size values and thus better represent the gas flow space.[3736] Based on that, the modified Reynold's number will be

$$Re_m = \frac{\rho v}{\mu}\frac{\beta}{\alpha}$$

where ρ and μ are the gas density and dynamic viscosity at the flow temperature and pressure, α is the reciprocal of substrate permeability and β is the inertial resistance coefficient as defined by Forchheimer.[34] Although not widely studied for different materials and porosities, inertial resistance was shown to start ~Re_m= 0.11 which corresponded to a flow with 10% inertial resistance and 90% viscous resistance.[34] The outlet velocity from the

showerhead will depend on the number of nozzles per nozzle array and their diameter. For 75 nozzles of 0.5 mm diameter, a 0.2 slm total flow rate (1 slm divided over 5 channels of TMA for instance) will lead to an outlet velocity of ~0.3 m/s. The calculated values of α and β using Kozeny-Carman and Ergun equations respectively, will result in a Re_m of 0.02 which is in the viscous regime range and thus a minimum level of eddies are expected at such flow rate. We found that the upper limit of viscous flow (Re_m) will correspond to a total flow rate of ~ 5 slm.

As mentioned earlier, the results of these simple calculations offers a good guideline for what range of flow rates to use for the more rigorous modeling of the CFD analysis. For the TMA and H_2O gas manifolds a flow in the range of 0.5-5 slm seems reasonable in terms of supplying enough reactants to saturate the PP total surface area and also to avoid eddy formation within the fabric. As for the main N_2 line, which acts as gas curtain to separate the two reaction zones in the spatial ALD setup as well as a "purging step" higher flow rates are needed. As shown earlier in Chapter 1, to achieve uniform Al_2O_3 coatings at atmospheric pressure and low temperature, high gas velocity is necessary. Also, the number of N_2 channels is nearly double that of each reactant. Based on this, a flow rate as high as 10-30 slm will be required for the main N_2 line, in order to produce gas outlet velocities of ~0.9-2.6 m/s for an array consisting of 75 nozzles of 0.5 mm diameter each.

6.3.2 Showerhead Design: Uniform Outlet Flow

The flow through each of the three lines (N_2, TMA and H_2O) was modeled to determine the diameters of the tubes and their inlets and outlets during the conceptual design

for the spatial ALD reactor showerhead component, shown in Figure 6.1c, using the flow rate ranges (which ensure uniform gas outflow) determined by the previous section's simple calculations. The CFD geometry used for the TMA line is shown in Figure 6.3a, where gas enters the manifold tube and is distributed to 5 channels, each of which has 75 nozzles of 0.5 mm diameter. The outflow gas uniformity will depend on the inlet gas flow rate and diameters of the manifold and channel tubes as well as their inlet and outlet diameters. These are 6 parameters to be optimized, thus we set the values for some of them based either on simple CFD geometry modeling, machining constraints or engineering rules of thumb. For instance, the number and diameter of the outlet nozzles were chosen to fit the maximum number of nozzles in the 15 cm long channel as well as to satisfy some machining constraints. Also, the gas manifold was modeled separately to ensure uniform velocity from its 5 outlets. The results show that an inlet diameter of 1/4 in and outlet diameter of 1/8 in lead to uniform outlet velocity for different manifold tube diameters. The uniformity of the gas flow out of the TMA line was determined based on the variation in out flow rates between the five channels and the velocity variation within each channel. Figure 6.3b shows how the flow was evenly distributed among the different channels for inlet flow rates in the range of 0.5 – 3 slm for 1/4 in channels and a 1/2 in diameter manifold. The percentage coefficient of variation (COV), or standard deviation divided by mean value, of the flow rates for the different runs was less than 0.5% for the 1/4 in diameter channels while it was ~2.1% for the flow through 1/8 in channel at 1 slm inlet flow rate. When the channel diameter was reduced to 1/8 in, more flow tended to go to the channels near by the manifold inlet leading to non-uniform flow distribution between the different channels which also affected the

outflow velocity uniformity within the same channel. To determine the outflow uniformity within each channel, we checked the outlet velocity of each of the 75 nozzles for the different channels at different channel and tube diameters as well as inlet flow rates as shown in Figure 6.3c and 6.3d. The velocity profiles through the second and fifth channels for the 1/8 in channels case are shown in Figure 6.3c and are compared to the profile through the 5^{th} channel for 1/4 in diameter channels case, both runs were carried for an inlet flow of 1 slm. The non-uniformity in flow distribution for the 1/8 in channels leads not only to variation of outlet flow between channels, but it also leads to higher non-uniformity within the same channel, especially the nozzles furthest away from the manifold inlet. On the other hand, the flow through the 1/4 in channels is very uniform, even for the farthest channel from the manifold inlet as shown in Figure 6.3c. To compile the outlet velocity data for the different runs, the percentage COV in velocity was were compared for the different channel and manifold diameters as well as inlet flow rates. For instance, the COV in velocity for the 1/4 in channel, 1/2 in manifold, and 1 slm inlet flow run was calculated by dividing the standard deviation of the 75 data points shown in figure 6.3c by their mean values for each of the 5 channels. The error bars shown in Figure 6.3d indicates the variation in COV of the 5 channels for the same run. In general, we found that using 1/8 in channels always leads to high flow non-uniformity relative to the 1/4 in ones. Moreover, the higher the inlet flow rate and manifold diameter, the better the outlet uniformity. However, the slight improvement in outlet uniformity from increasing manifold diameter does not justify building a larger reactor especially because it is more challenging to uniformly heat large reactors.

Similar to the analysis of the TMA line, the same procedure was repeated for H_2O and main N_2 lines. The velocity profiles of all the channels are shown in Figure 6.4a and b for 1/4 in channels, 1/2 in diameter manifold at 3 slm and 9 slm inlet flow rates for H_2O and N_2 lines respectively. The COV for both lines was ~4% which is slightly higher than TMA line for comparable conditions, probably due to the higher number of channels especially for the main N_2 line.

The previous analysis shows that uniform gas outflow can be achieved for TMA and H_2O lines using flow rates in the tested range of 0.25-3 slm and up to 10 slm for the main N_2 line. Although not tested, higher flow rates should lead to more uniform flow based on the trend of the tested flow rates. The use of 1/4 in channels will favor better separation between reactants, relative to smaller channels, but at the same time adds extra difficulty on gas coverage over the substrate. At relatively low flow rates (e.g. 1 slm) the reactants channels with 0.5 mm diameter nozzles will not cover the whole 1/4 in spacing between the channels. The unreached space will probably be occupied by N_2 which will have a higher flow rate. If spreading of the N_2 gas is unable to cover the whole range, then there will be the possibility of ambient moisture to diffuse in from the reactor sides. By applying proper gas curtains on the reactor sides, ambient moisture diffusion can be prevented. On the other hand, the spreading of the gas over the substrate will depend greatly on the gap size between the showerhead and the substrate as will be discussed next.

6.3.3 Gap Spacing and Reactants Spatial Separation

Figure 6.4 shows how the coated areas on the top and bottom sides of a polypropylene (PP) fabric change with varying the gap size between a single nozzle setup and the fabric (discussed earlier in chapter 4). The nozzle has ~ 0.15 in inner diameter and the coating area was determined using a red food-dyed water. Since the areas coated with Al_2O_3 (TMA/H_2O ALD process) change the normally hydrophobic PP to hydrophilic,[4] treated regions absorb the colored water as shown in the Figure 6.5. At low gap spacing, 0.2 mm, the gas tends to flow straight through the fabric without spreading which leads to coating area of diameter equal to the nozzle's inner diameter. The area coated on the top and bottom sides of the fabric were similar sized, which indicates that the gas was able to penetrate all the way through the fabric in a straight path. As the gap size is increased, 0.6 and 1mm, the coated area extends beyond the size of the nozzle's inner diameter due to the spreading of gas over the fabric. However, variation was also noticed between the size of the coated areas on the top and bottom of the fabric. While larger area was coated on the top side of the fabric at 1 mm gap spacing, the size of the coating on the bottom side was lower than that for 0.6 mm gap spacing. As the gap spacing increases, gas tends to spread more on the surface and penetrate less through the fabric since the gas velocity will decrease as it expands away from the nozzle perimeter. The optimum gap spacing is the one that leads to maximum coverage while coating a similar area on both the top and bottom of the fabric. This optimum value is also expected to vary with the outlet velocity from the nozzle, which depends on the gas flow rate and nozzle diameter. For that reason, we modelled the flow through the fabric using the 0.5 mm diameter nozzles at different flow rates and gap spacings.

Due to the intensive computational requirements for 3D CFD models, just one ALD cycle (N_2/TMA/N_2/H_2O/N_2) was modelled featuring 24 nozzles per array with 2 mm spacing between them and 1/4 in between the channels, as shown in Figure 6.6a. The model was solved using 3 phases of N_2, TMA and H_2O which allows the determination of each component volume fraction in addition to the other flow properties. The inlet volume fractions of TMA and H_2O to the nozzles were set to 0.05. Velocity was set as an inlet boundary condition for the nozzles and atmospheric pressure outlet was set at the bottom and sides. The results were determined through the channels in the X-Y plane and at the porous surface in the X-Z plane.

For all the conditions tested, the reactants were spatially separated with distinct zones for TMA and H_2O. Figure 6.6b-d shows the contours of N_2 volume fraction at the porous zone surface, where the dark blue color represents a volume fraction of 0.95 corresponding to the 0.05 inlet volume fraction of both reactants. By decreasing the total flow rate going through the TMA and H_2O lines from 3 to 1 slm, the width of the reactant zones decreased as shown in Figure 6.6 b and c due to the decrease in the amounts of the supplied reactant. Another reason for the decrease of the sizes of the reactant zones is due to the lower spreading of the gas as it comes out of the nozzle at lower flow rates. Increasing the gap size to 1 mm does not change the zone width significantly but leads to higher non-uniformity within the reactant zone (Figure 6.6d). The variation in the reactant volume fraction may be due to the formation of eddies between the nozzles within the same array at higher gap sizes as will be shown next. We also found that the N_2 volume fraction midway between the reactant channels was 0.995 for of the model featuring a 1 mm gap size. Although, the value

is very low and in the range of parts per million contamination, it also suppourts the hypothesis of the formation of eddies and dead spaces as the gap spacing increases.

The volume fraction contours showed uniform coverage of the reactants on the substrate especially at 0.4 mm gap spacing. However, the uniform coverage does not necessairly translate to uniform coating because a sufficiently high velocity is also required to get the gas all the way through the porous material. The velocity contours within the gap spacing at the channels outlet were checked and the results are shown in Figure 6.7. Low velocity uniformity on the substrate was found at gap spacing of 0.4 mm and low gas flow rate, as shown in Figure 6.7a where the blue-green areas indicate low velocity zones (~0.15 m/s) between the high velocity zones (red spread, ~1 m/s). Reactants reach these low velocity regions, which leads to the uniform volume fraction on the upeer side of the substrate shown in Figure 6.6b at similar conditions, however such a low velocity will not be enough to move the reactants through the entire fabric thickness, leading to non-uniform coating on the fabric back side. As the gap spacing increases, the velocity uniformity increases (Figure 6.7b) where the extent of the low velocity zones became smaller as the gas is given more space to spread before hitting the porous surface. On the downside, increasing the gap spacing leads to significant eddies between the nozzles as shown in the close up image of Figure 6.7b. These eddies can lead to trapped reactants which will start diffusing slowly, thus affecting the reactants uniformity over the surface and eventually leading to reactant mixing, causing a CVD effect. The velocity uniformity was also enhanced by increasing the gas flow rate, as shown in Figure 6.7c, even at small gap spacing. As the flow rate increases, the gas will tend to reach everwhere on the surface at higher velocity which can mitigate the effect of having

low velocity areas especially at low gap spacing. It can be concluded that the low gap spacing leads to more uniform reactant coverage over the surface but suffers from the drawback of gas channeling through the porous material without spreading enough which can be overcome by increasing the outlet velocity from the nozzles.

6.3.4 Spatial ALD Coating on Polypropylene Fabric

The foremost condition in qualifying an open to air ALD reactor for metal oxides deposition is to verify that no ambient moisture is diffusing into the deposition region. In the current prototype version of the spatial ALD reactor for porous material presented in this chapter, side gas curtains were not applied and the reactor sides were sealed up by pressing the showerheads against the bottom exhaust box to minimize the moisture diffusion effects. According to that setup, the expectations were that the ambient moisture will not diffuse beyond the first few nozzles of each array on each side of the reactor (5-10 mm). To verify the extent of water diffusion, we attached small strips of silicon (~10 cm X 3 mm) on top of the PP fabric and run ran the web back and forth under the reactor head for time equivalent of 200 ALD cycles with only N_2 and TMA flowing with no water. This experiment ensures that any Al_2O_3 growth that may occur on the silicon can be assumed to be due to diffused ambient moisture reacting with the flowing TMA. Results of the silicon wafers after runs using different N_2 flow rates and 1 slm of TMA through the central showerhead are shown in Figure 6.8a. The extent of ambient diffusion was high at low N_2 flow rates of 5 and 10 slm, leading to Al_2O_3 thickness of 40 and 4 nm respectively as measured by ellipsometry.

However, Al_2O_3 deposition decreases sharply to less than 0.5 nm when the N_2 flow rate is increased to 15 slm.

Next, we run the spatial ALD process on polypropylene fabric for 100 ALD cycles while flowing water and determined coating uniformity through wetting the coated fabric with red-dyed water. As shown in Figure 6.8b, the uncoated part of the fabric sheet remained hydrophobic, while the area exposed to the 100 cycles of Al_2O_3 turned fully hydrophilic. It was also noted that the fabric was more wetting ~20 mm from the edges of both sides of the web, which is probably due to CVD reaction because of the diffused ambient moisture, leaving a large area (~10 cm X 60 cm) with very uniform visual wetting.

The reason PP was chosen for the preliminary spatial ALD experiments because it has been previously studied using temporal ALD, showing a clear change in wetting properties after Al_2O_3 coating.[4] As a simple way of comparing the spatial and temporal ALD processes on porous substrates, the change in water contact angle was studied for PP fabric coated with the same the number of ALD cycles for both processes. While both processes were carried out at a substrate temperature of 60 ^oC, the temporal ALD was done at ~1 Torr in an enclosed chamber, while the spatial ALD process occurred under atmospheric pressure in an open air environment. The spatial ALD process took about 2.5 min for 100 ALD cycles, which was 40 times faster than the temporal ALD process (~100 min). The contact angle of the modified PP fabrics were measured in 5 different spots within the area that showed a uniform wetting visually. Figure 6.8c shows how the water contact angle changes as a function of ALD cycles, demonstrating that both processes produce comparable surface

wetting results. While the transition to a zero degree contact angle for the spatial ALD process occurs after 10 additional cycles compared to the temporal ALD produced sample, this is probably due to sub-saturation growth using the spatial ALD process. These results are very promising especially that the contact angle was found to be similar on the top and bottom sides of the modified PP fabric by the spatial ALD process, which indicates coating through the whole fabric thickness.

In addition to further characterizing the process for the common ALD characteristics like exposure and purge effects, more systematic analysis needs to be carried out to determine the effect of more universal parameters like the substrate porosity and the gas flow below the substrate. For instance, although the process ensures no reactants mix on the substrate surface, CVD reactions may occur after passing through the substrate where the flow is of much lower velocity, especially for low porosity substrates. Preliminary modeling data showed that the design of the gas exhaust manifold and its closeness to the back side of the substrate will play major roles in avoiding reactants mixing in this area. Moreover, the next version of the prototype design will need to include gas curtains to avoid the ambient moisture diffusion totally.

6.4 Summary

Spatial ALD helps overcome the typically low throughput of ALD, allowing for its industrial incorporation in applications such as solar cell passivation and barrier coatings for polymers. Extending the spatial ALD process beyond solid substrates (e.g. silicon wafers and polymers) to porous materials will enable industries such as those involved with textiles and

batteries to include the process in their manufacturing lines. In this work, we presented a prototype of a spatial ALD tool for coating porous materials in a roll-to-roll fashion under ambient conditions. PP fabric of 75 gsm was coated with Al_2O_3 using the spatial ALD process to showcase the tool's ability to coat porous substrates. The wetting properties of the modified PP fabric were compared to those modified using a temporal ALD process operated under a standard vacuum pressure and inert environment. The change in water contact angle with number of ALD cycles agreed favorably between both processes. The work also discussed the key design parameters for the new tool and showed how to determine these parameters using simple gas flow modeling techniques as well as CFD modeling. The prototype of the spatial ALD tool for coating porous materials is an important step in extending the industrial adoption of ALD.

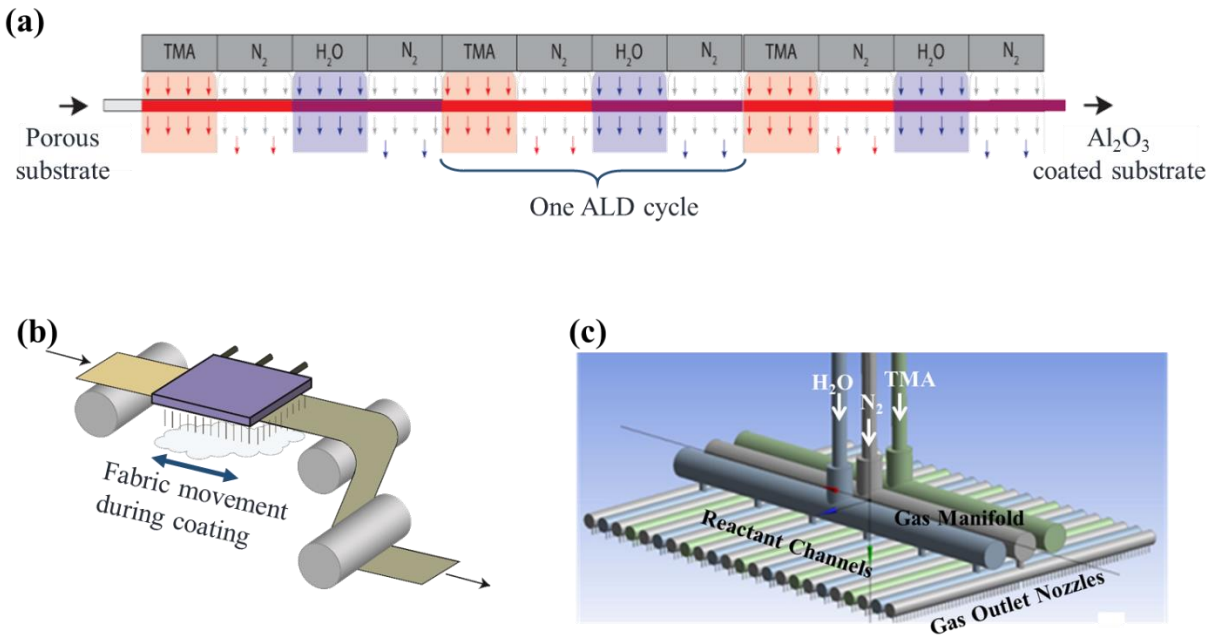


Figure 6.1. Schematics of the spatial ALD setup. (a) Substrate going through the TMA and H_2O reactant zones separated by N_2 in a tool comprising 3 ALD cycles. (b) Linear reciprocating motion of a substrate under a spatial ALD tool comprising X number of ALD cycles to achieve a total number of cycles equals to X multiplied by the number of reciprocations. (c) Conceptual design of the spatial ALD showerhead where the gas flows through a gas manifold to get distributed to the respective channels and next through the nozzle arrays beneath these channels.

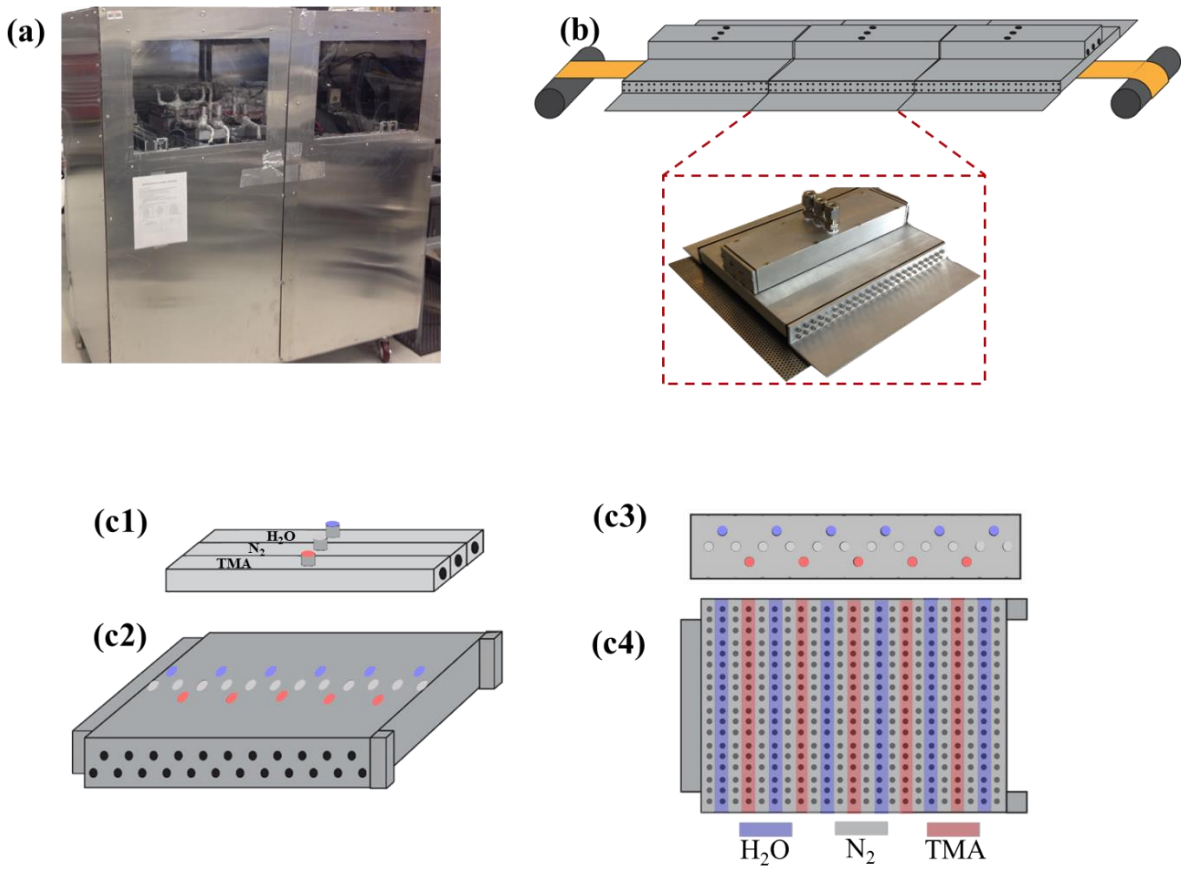


Figure 6.2. The building blocks of the spatial ALD reactor for porous materials. (a) The vented cabinet enclosing the roll-to-roll system and the reactor showerheads. (b) The reactor consists of 3 showerheads of equivalent size and design, however reactants flow only through the central showerhead, while the two side ones provide inert gas (N_2) flow only. (c) The showerhead setup consisting of (c1) gas manifold tubes and (c2) gas channels leading to the outlet nozzle arrays. (c3) and (c4) are the bottom views of the (c1) gas manifold tubes and (c2) channels, respectively.

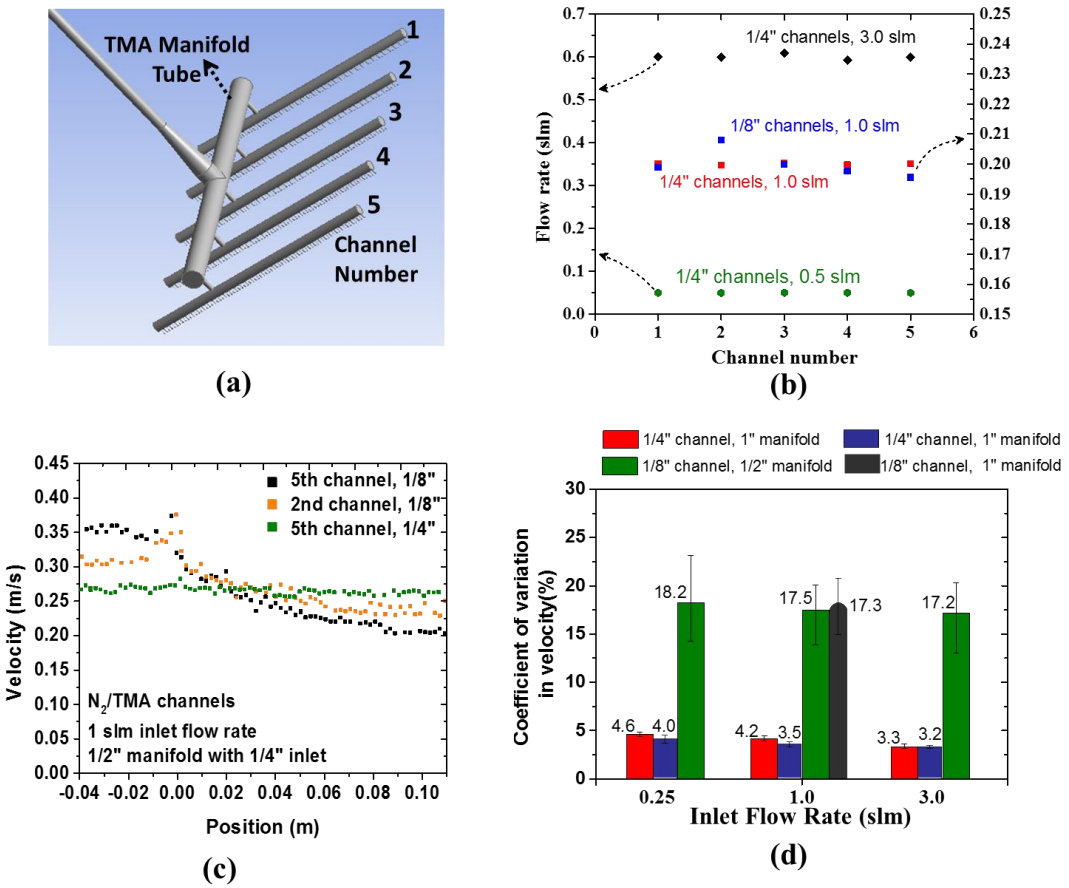


Figure 6.3. The CFD model and results for N_2 flow through the TMA line. (a) CFD geometry of the TMA manifold tube leading to the 5 TMA channels, each having 75 gas outlets (nozzles). (b) The total outlet flow rate through each channel for different inlet flow rates and channel diameters. The results for 1 slm at 1/4 in and 1/8 in channel diameters were plotted on a different scale (right) to clearly show the variation in uniformity. (c) Outlet gas velocity profile of different TMA channels from two separate CFD runs, one with 1/4 in channels and the second with 1/8 in channels. Both runs were done with 1 slm inlet flow rate to a 1/2 in manifold tube. (d) Compiled data for the COV in outlet velocity of several CFD runs using different manifold tube and channel diameters for various inlet gas flow rates. The COV was determined by dividing the standard deviation in velocity per channel by the average outlet velocity of this channel. The error bars represent the different COV values for the 5 channels for each CFD run.

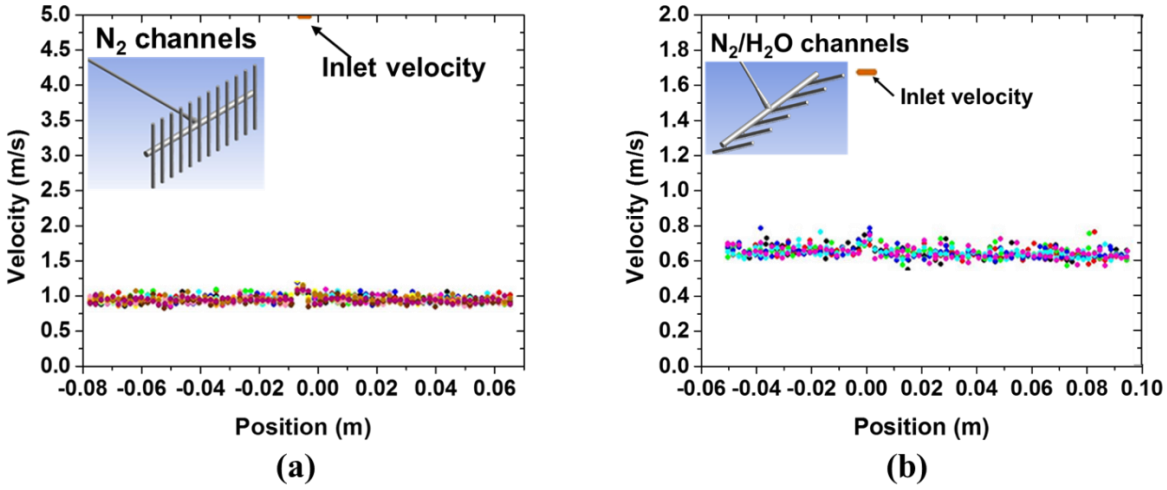


Figure 6.4. Outlet gas velocity profiles for (a) the twelve channels of the main N_2 line and (b) the six channels of the water line at inlet flow rates of 9 and 3 slm respectively. Both modeling runs had manifold tubes featuring 1/4 in inlet and 1/8 in outlets, along with 1/4 in channels comprising 75 nozzles outlets of 0.5 mm diameter each.

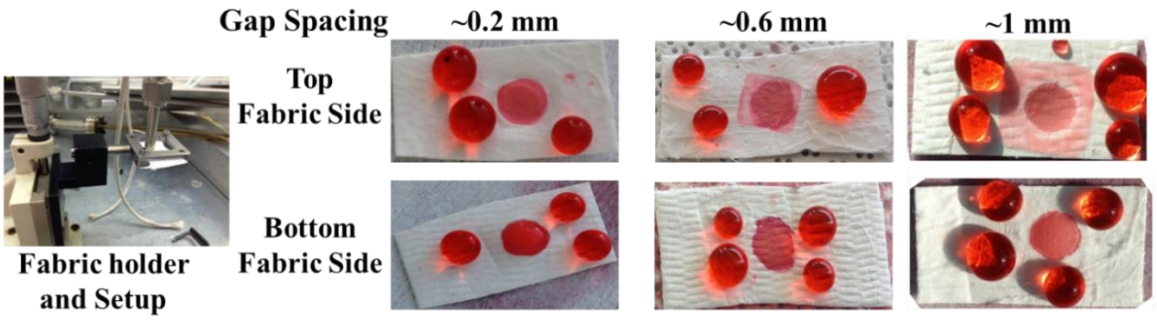


Figure 6.5. Images of the top and bottom sides of the non-woven PP fabrics after 100 ALD cycles using the single nozzle (1/4 in tube) ALD delivery head presented in chapter 4 at different gap spaces between the nozzle and the fabric. The coated area turns hydrophilic and the extent of which was determined using red-dyed water. The coated area on the top surface of the fabric grew by increasing the gap spacing, however gas penetration through the fabric decreased significantly.

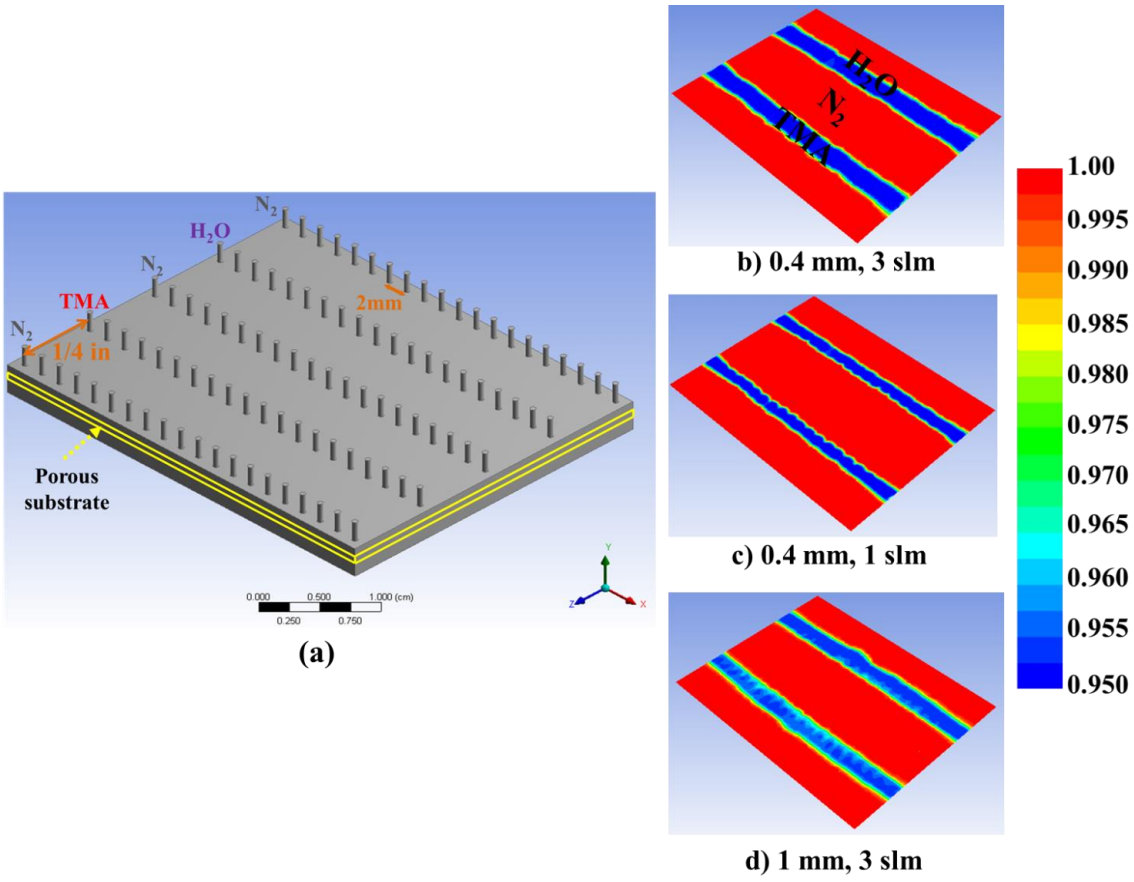


Figure 6.6. (a) 3D geometry of the CFD model to determine flow and species uniformity on the porous surface. The model has different flow inlets for the different nozzle arrays, a porous zone and pressure outlets. The inlet volume fractions of H_2O and TMA were set to 0.05 at their respective nozzles. The flow rate through the N_2 channels was set to 10 slm for all the runs. (b-d) The contours of the volume fraction of N_2 on the porous zone top plane at different gap spacing and outlet gas flow rates as indicated in the figure. The red color indicates N_2 zones, with volume fractions ~1, between the two reactant zones (blue color) verifying that the suggested design specifics and process conditions prevents reactants from mixing.

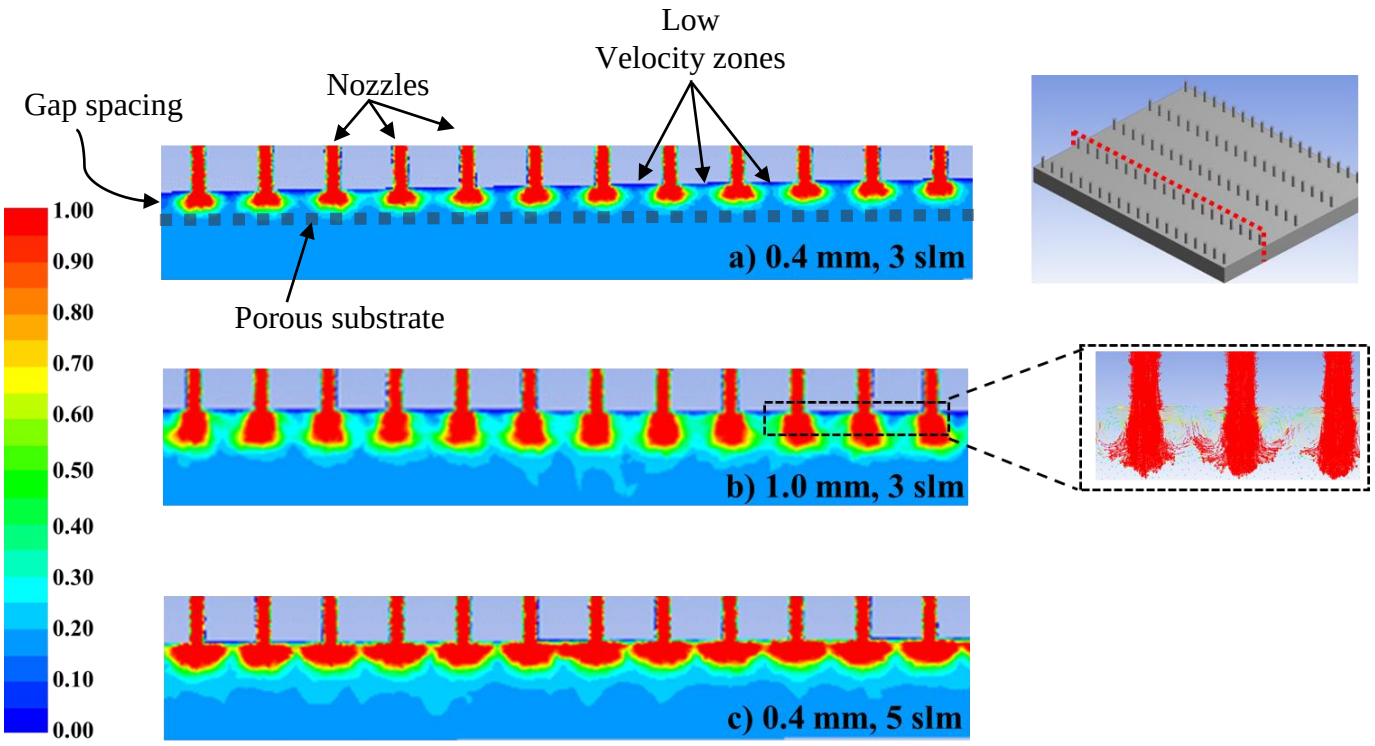


Figure 6.7. Velocity contours through the nozzles, gap spacing and the porous zone. Results shown for gap spacings of 0.4 and 1 mm, and flow rates of 3 and 5 slm. 1 m/s inlet velocity was used for the 3 slm run. The plane where these velocity contours were determined is shown by the dotted lines in the top right image. The velocity profile became more uniform, constant contour color, by increasing the gap spacing from (a) 0.4 mm to (b) 1 mm within the same channel at total flow rate of 3 slm and by increasing the flow rate from (a) 3 slm to (c) 5 slm at gap spacing of 0.4 mm. Eddies formed between the nozzles at the larger gap size of 1 mm, as shown by the close up image of (b).

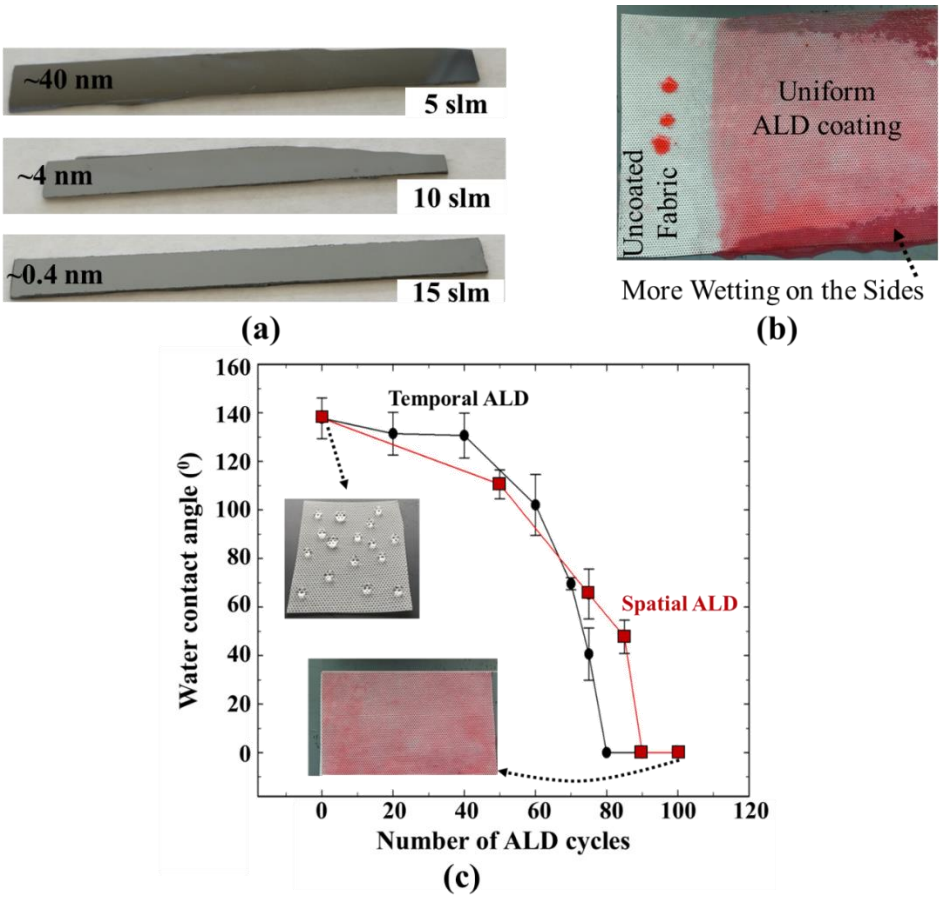


Figure 6.8. Al_2O_3 coatings using the Spatial ALD process for porous substrates. (a) Images of silicon strips placed on top of the PP web were used to determine the extent of ambient moisture diffusion into the deposition area. The process was run with no water flowing to the deposition zone for 100 ALD cycles, thus any film growth could be attributed to ambient moisture. The flow rates beside the images are for the flow through the main N_2 line. (b) Image of the PP fabric after being immersed in red-dyed water post-deposition of 100 ALD cycles using the spatial ALD process. (c) Comparing the change in water contact angle of the non-woven PP fabric against the number of ALD cycles produced using temporal and spatial ALD processes. The dose sequence ($TMA/N_2/H_2O/N_2$) of the temporal ALD was 0.5/30/0.5/30 sec. The spatial ALD process was run at a substrate speed of ~5 m/min with N_2 flow rates at the central showerhead of 15, 0.4 and 0.15 slm through the main N_2 line, TMA bubbler and H_2O bubbler respectively.

6.5 References

(1) *Atomic Layer Deposition for Semiconductors*; Hwang, C. S., Ed.; Springer US: Boston, MA, 2014.

(2) Longrie, D.; Deduytsche, D.; Detavernier, C. Reactor Concepts for Atomic Layer Deposition on Agitated Particles: A Review. *J. Vac. Sci. Technol. A* **2014**, *32* (1), 010802.

(3) George, S. M. Atomic Layer Deposition: An Overview. *Chem. Rev. Wash. DC U. S.* **2010**, *110* (1), 111–131.

(4) Hyde, G. K.; Park, K. J.; Stewart, S. M.; Hinestroza, J. P.; Parsons, G. N. Atomic Layer Deposition of Conformal Inorganic Nanoscale Coatings on Three-Dimensional Natural Fiber Systems: Effect of Surface Topology on Film Growth Characteristics. *Langmuir* **2007**, *23* (19), 9844–9849.

(5) Kalanyan, B.; Oldham, C. J.; Sweet, W. J.; Parsons, G. N. Highly Conductive and Flexible Nylon-6 Nonwoven Fiber Mats Formed Using Tungsten Atomic Layer Deposition. *ACS Appl. Mater. Interfaces* **2013**, *5* (11), 5253–5259.

(6) Jur, J. S.; Sweet, W. J.; Oldham, C. J.; Parsons, G. N. Atomic Layer Deposition of Conductive Coatings on Cotton, Paper, and Synthetic Fibers: Conductivity Analysis and Functional Chemical Sensing Using "All-Fiber" Capacitors. *Adv. Funct. Mater.* **2011**, *21* (11), 1993–2002.

(7) Sweet, W. J.; Jur, J. S.; Parsons, G. N. Bi-Layer Al2O3/ZnO Atomic Layer Deposition for Controllable Conductive Coatings on Polypropylene Nonwoven Fiber Mats. *J. Appl. Phys.* **2013**, *113* (19), 194303.

(8) Zhao, J.; Losego, M. D.; Lemaire, P. C.; Williams, P. S.; Gong, B.; Atanasov, S. E.; Blevins, T. M.; Oldham, C. J.; Walls, H. J.; Shepherd, S. D.; et al. Highly Adsorptive, MOF-Functionalized Nonwoven Fiber Mats for Hazardous Gas Capture Enabled by Atomic Layer Deposition. *Adv. Mater. Interfaces* **2014**, *1* (4), n/a – n/a.

(9) Lee, K.; Jur, J. S.; Kim, D. H.; Parsons, G. N. Mechanisms for Hydrophilic/hydrophobic Wetting Transitions on Cellulose Cotton Fibers Coated Using Al2O3 Atomic Layer Deposition. *J. Vac. Sci. Technol. A* **2012**, *30* (1), 01A163.

(10) Hyde, G. K.; Scarel, G.; Spagnola, J. C.; Peng, Q.; Lee, K.; Gong, B.; Roberts, K. G.; Roth, K. M.; Hanson, C. A.; Devine, C. K.; et al. Atomic Layer Deposition and Abrupt Wetting Transitions on Nonwoven Polypropylene and Woven Cotton Fabrics. *Langmuir* **2010**, *26* (4), 2550–2558.
(11) Atanasov, S. E.; Oldham, C. J.; Slusarski, K. A.; Taggart-Scarff, J.; Sherman, S. A.; Senecal, K. J.; Filocamo, S. F.; McAllister, Q. P.; Wetzel, E. D.; Parsons, G. N. Improved Cut-Resistance of Kevlar® Using Controlled Interface Reactions during Atomic Layer Deposition of Ultrathin (<50 Å) Inorganic Coatings. *J. Mater. Chem. A* **2014**, *2* (41), 17371–17379.
(12) Parsons, G. N.; Atanasov, S. E.; Dandley, E. C.; Devine, C. K.; Gong, B.; Jur, J. S.; Lee, K.; Oldham, C. J.; Peng, Q.; Spagnola, J. C.; et al. Mechanisms and Reactions during Atomic Layer Deposition on Polymers. *Coord. Chem. Rev.* **2013**, *257* (23–24), 3323–3331.
(13) Alibabaei, L.; Farnum, B. H.; Kalanyan, B.; Brennaman, M. K.; Losego, M. D.; Parsons, G. N.; Meyer, T. J. Atomic Layer Deposition of TiO2 on Mesoporous nanoITO: Conductive Core–Shell Photoanodes for Dye-Sensitized Solar Cells. *Nano Lett.* **2014**, *14* (6), 3255–3261.
(14) Manthiram, A.; Chung, S.-H.; Zu, C. Lithium–Sulfur Batteries: Progress and Prospects. *Adv. Mater.* **2015**, *27* (12), 1980–2006.
(15) Luo, J.; Liu, J.; Zeng, Z.; Ng, C. F.; Ma, L.; Zhang, H.; Lin, J.; Shen, Z.; Fan, H. J. Three-Dimensional Graphene Foam Supported Fe3O4 Lithium Battery Anodes with Long Cycle Life and High Rate Capability. *Nano Lett.* **2013**, *13* (12), 6136–6143.
(16) Suntola, T. S.; Pakkala, A. J.; Lindfors, S. G. Apparatus for Performing Growth of Compound Thin Films. US4389973 A, June 28, 1983.
(17) Poodt, P.; Lankhorst, A.; Roozeboom, F.; Spee, K.; Maas, D.; Vermeer, A. High-Speed Spatial Atomic-Layer Deposition of Aluminum Oxide Layers for Solar Cell Passivation. *Adv. Mater.* **2010**, *22* (32), 3564–3567.
(18) Poodt, P.; Cameron, D. C.; Dickey, E.; George, S. M.; Kuznetsov, V.; Parsons, G. N.; Roozeboom, F.; Sundaram, G.; Vermeer, A. Spatial Atomic Layer Deposition: A Route towards Further Industrialization of Atomic Layer Deposition. *J. Vac. Sci. Technol. Vac. Surf. Films* **2012**, *30* (1), 010802.

(19) Muñoz-Rojas, D.; MacManus-Driscoll, J. Spatial Atmospheric Atomic Layer Deposition: A New Laboratory and Industrial Tool for Low-Cost Photovoltaics. *Mater. Horiz.* **2014**, *1* (3), 314–320.
(20) Maydannik, P. S.; Kääriäinen, T. O.; Cameron, D. C. An Atomic Layer Deposition Process for Moving Flexible Substrates. *Chem. Eng. J.* **2011**, *171* (1), 345–349.
(21) Dickey, E.; Barrow, W. A. High Rate Roll to Roll Atomic Layer Deposition, and Its Application to Moisture Barriers on Polymer Films. *J. Vac. Sci. Technol. Vac. Surf. Films* **2012**, *30* (2), 021502.
(22) Levy, D. H.; Freeman, D.; Nelson, S. F.; Cowdery-Corvan, P. J.; Irving, L. M. Stable ZnO Thin Film Transistors by Fast Open Air Atomic Layer Deposition. *Appl. Phys. Lett.* **2008**, *92* (19), 192101–192101 – 3.
(23) Poodt, P.; Knaapen, R.; Illiberi, A.; Roozeboom, F.; van Asten, A. Low Temperature and Roll-to-Roll Spatial Atomic Layer Deposition for Flexible Electronics. *J. Vac. Sci. Technol. Vac. Surf. Films* **2012**, *30* (1), 01A142.
(24) Yersak, A. S.; Lee, Y. C.; Spencer, J. A.; Groner, M. D. Atmospheric Pressure Spatial Atomic Layer Deposition Web Coating with in Situ Monitoring of Film Thickness. *J. Vac. Sci. Technol. A* **2014**, *32* (1), 01A130.
(25) Fitzpatrick, P. R.; Gibbs, Z. M.; George, S. M. Evaluating Operating Conditions for Continuous Atmospheric Atomic Layer Deposition Using a Multiple Slit Gas Source Head. *J. Vac. Sci. Technol. A* **2012**, *30* (1), 01A136.
(26) Suh, S.; Park, S.; Lim, H.; Choi, Y.-J.; Hwang, C. S.; Kim, H. J.; Won, S.-J. Investigation on Spatially Separated Atomic Layer Deposition by Gas Flow Simulation and Depositing Al2O3 Films. *J. Vac. Sci. Technol. A* **2012**, *30* (5), 051504.
(27) Illiberi, A.; Cobb, B.; Sharma, A.; Grehl, T.; Brongersma, H.; Roozeboom, F.; Gelinck, G.; Poodt, P. Spatial Atmospheric Atomic Layer Deposition of InxGayZnzO for Thin Film Transistors. *ACS Appl. Mater. Interfaces* **2015**, *7* (6), 3671–3675.
(28) Ellinger, C. R.; Nelson, S. F. Selective Area Spatial Atomic Layer Deposition of ZnO, Al2O3, and Aluminum-Doped ZnO Using Poly(vinyl Pyrrolidone). *Chem. Mater.* **2014**, *26* (4), 1514–1522.

(29) Carman, P. C. Flow of Gases through Porous Media; Academic Press, 1956.
(30) Labrecque, R. P. An Investigation of the Effects of Fiber Cross Sectional Shape on the Resistance to the Flow of Fluids through Fiber Mats, Institute of Paper Science and Technology: Appleton, Wisconsin, 1967.
(31) Ergun, S.; Orning, A. A. Fluid Flow through Randomly Packed Columns and Fluidized Beds. *Ind. Eng. Chem.* **1949**, *41* (6), 1179–1184.
(32) Puurunen, R. L. Surface Chemistry of Atomic Layer Deposition: A Case Study for the Trimethylaluminum/water Process. *J. Appl. Phys.* **2005**, *97* (12), 121301.
(33) Zilko, J. L. 4 - Metal Organic Chemical Vapor Deposition: Technology and Equipment. In *Handbook of Thin Film Deposition Processes and Techniques (Second Edition)*; Seshan, K., Ed.; William Andrew Publishing: Norwich, NY, 2001; pp 151–203.
(34) Zeng, Z.; Grigg, R. A Criterion for Non-Darcy Flow in Porous Media. *Transp. Porous Media* **2006**, *63* (1), 57–69.
(35) Polat, O.; Crotogino, R. H.; Douglas, W. J. M. Transport Phenomena Analysis of through Drying Paper. *Ind. Eng. Chem. Res.* **1992**, *31* (3), 736–743.
(36) Polat, O. Through Drying of Paper. **1989**.
(37) Douglas, D. W. J. M.; Crotogino, D. R. H. Through Drying of Paper. *Dry. Technol.* **1991**, *9* (1), 297–301.

CHAPTER 7

Atmospheric Pressure Synthesis of Photoluminescent Hybrid Materials by Sequential Organometallic Vapor Infiltration into Polyethylene terephthalate Fibers

This chapter is based on a manuscript published as:

Halil I. Akyildiz[1,2], Moataz Bellah M. Mousa[3] and Jesse S. Jur[1], *Journal of Applied Physics* **2015** 117, 045301.

Moataz and Halil had equal contribution to this work as mentioned in the first page of the publication.

[1]Department of Textile Engineering, Chemistry and Science, [2]Department of Materials Science and Engineering, [3]Department of Chemical and Biomolecular Engineering

North Carolina State University, Raleigh, NC 27695 USA

Abstract

Exposing a polymer to sequential organometallic vapor infiltration (SVI) under low pressure conditions can significantly modify the polymer's chemical, mechanical and optical properties. We demonstrate that SVI of trimethylaluminum (TMA) into polyethylene terephthalate (PET) can also proceed readily at atmospheric pressure, and at 60 °C the extent of reaction determined by mass uptake is independent of pressure between 2.5 Torr and 760 Torr. At 120 °C, however, the mass gain is 50% larger at 2.5 Torr relative to that at 760 Torr, indicating that the precursor diffusion in the chamber and fiber matrix decreases at higher source pressure. Mass gain decreases in general as the SVI process temperature increases both at 2.5 Torr and 760 Torr attributed to the faster reaction kinetics forming a barrier layer which prevents further diffusion of the reactive species. The resulting PET/Al-O_x product shows high photoluminescence compared to untreated fibers. A physical mask on the polymer during infiltration at 760 Torr is replicated in the underlying polymer, producing an image in the polymer that is visible under UV illumination. Because of the reduced precursor diffusivity during exposure at 760 Torr, the image shows improved resolution compared to SVI performed under typical 2.5 Torr conditions.

7.1 Introduction

Organic-inorganic hybrid materials have drawn attention for advanced electronics,[1] biotechnology,[2] optics[3,4] and catalysis[5] applications. Sequential vapor infiltration (SVI) is one of the techniques where hybrid materials are formed within organic materials by exposure to an organometallic precursor vapor. The technique is inspired by observations from atomic layer deposition (ALD) on polymers with moderate reactive functional groups (i.e. C=O) toward the ALD precursors.[6–8] During ALD, an organic-inorganic hybrid material layer is observed at the interface of the inorganic film and polymer substrate.[6–8] Motivated by these hybrid materials formation, techniques using the idea of extended ALD precursor exposures to form hybrid materials such as multiple pulsed vapor-phase infiltration (MPI),[9–11] sequential infiltration synthesis (SIS),[12,13] and SVI[14,15] have been proposed. While the techniques vary by slight differences in processing, all incorporate a common elongated exposure in order to enhance the infiltration. Biomolecules such as spider silk and collagens processed with MPI demonstrated improved strength by this hybridization.[9–11,16] SIS has been studied for the formation of nano-patterning by selective infiltration into self-assembly block copolymers composed of one polymer that can react with the ALD precursor to form hybrid material and the other is inert towards the same precursor. The unreacted polymer is removed by plasma etching process while hybrid material remains and hence nano-sized patterns are created.[12,17–19]

SVI utilizes a series of precursor exposures in a separated manner different from other infiltration methods. An exposure consists of an organometallic vapor dose into a reactor volume, whereafter the vapor is held in the reactor for a period of time and then purged from

the reactor volume with inert gas. This dose-hold-purge can be repeated to increase the overall exposure of the organometallic vapor within the reactor. Afterwards, an oxidation agent (i.e. H_2O) is also cycled in the same sequential order to oxidize the material.[14] The SVI mechanism has been studied as a function of temperature, exposure conditions and surface area on C=O containing polymers such as polyamides and polyesters.[14,20] SVI on PET and polybutylene terephthalate (PBT) fibers have been studied to create mesoporous hybrid materials for catalysis applications.[15] Also, SVI on PET fibers showed the ability to tune optical properties of organic materials by formation of PET-alumina coordination complexes.[20]

Sol-gel is the common technique for organic-inorganic hybrid material formation, in which precursors reacts in an appropriate solvent.[21] Solvent removal during the sol-gel process adds time and expense. One key advantage of SVI is that it utilizes precursors in the vapor phase thus allowing dry processing of the polymers and eliminates liquid solvents post processing. Furthermore, hybrid materials formation can be performed on a polymeric material that is already shaped as film or fiber. Therefore, the integration of the SVI process into polymer production lines, which is known for high throughput production, can produce hybrid materials or modify polymers with high throughput rates. Previous studies have shown that shape of the pristine polymeric material is mostly preserved even after high temperature calcination process or plasma etching.[15,17] This offers SVI additional advantages from a materials processing perspective since polymers may be molded into more complex shapes and structures that can subsequently be modified with the hybrid materials afforded through SVI. To this point, one major limitation of the SVI process is that it has been only conducted under low to medium vacuum conditions with batch processing, which reduces the materials production speed. It is

highly desired to have atmospheric pressure conditions, to apply the process for roll-to-roll manufacturing of hybrid materials. Operating at atmospheric pressure provides the opportunity to eliminate the time needed for reactor evacuation and pressure control, and facilitates integration for in-line manufacturing. This work provides the first investigation of the SVI mechanism as a function of pressure and aims to investigate feasibility of the roll-to-roll SVI under atmospheric pressure conditions. PET is one of the most common polymers used in textiles, packaging, and electrical insulation applications. Due to its high chemical and thermal resistance and low moisture permeability, PET has shown application as a substrate for flexible electronics.[22–24] With respect to optical applications, PET shows a weak photoluminescence by absorption of UV light both in solid state and in solution due to the presence of pi electrons on the polymer backbone.[25–27] Prior work by our team has shown SVI processing of PET fibers to increase the photoluminescence intensity by an order of magnitude.[20] Here along with the mechanistic analysis of SVI process at various pressures we also demonstrate advantages for atmospheric pressure SVI to selectively modify optical properties of the substrate with improved resolution.

7.2 Materials and Methods

PET fabrics were obtained with 2/1 twill woven structure, made of 100% PET round fibers in a 330/70 denier multifilament yarn and were used as received. Fabrics are cut into 2x1" pieces and the 2-3 yarns from each side is pulled out to make sure they are not separated during later handling of the samples, hence the initial mass for the samples remain the same. Fabric samples are weighed prior to SVI processing and they were in the range of 0.25-0.3 g. SVI treatments were conducted in a custom made viscous flow type ALD reactor described

previously that has special system design that allows variable pressure operation up to 760 Torr.[28–30] The ability of precursor delivery at pressures higher than the vapor pressure of the precursor is enabled by pressurization of a hold cell on the gas delivery line. The evacuated hold cell is filled with the precursor or oxygen source (charge time) and then pressurized with N_2 (pressurizing time). Afterwards, the hold cell is opened to the reactor through the main N_2 line (dose time). In order to conduct the SVI hold steps (hold time), a pneumatic gate valve is added to the end of the reactor, either on vacuum side or atmospheric pressure exhaust side depending on the SVI operation pressure. The gate valve is opened during the reactor purging after each hold step (purge time).

Following the sample loading, the reactor chamber was evacuated for 5 minutes by opening the pump side of the exhaust before every run. The chamber was then purged at the operation pressure for 10 minutes. To achieve 2.5 Torr operation pressure, the N_2 flow rate was 0.5 slm and for 760 Torr the flow rate was 5 slm. SVI process is conducted by first cycling trimethylaluminum (min. 98%, Strem Chemicals) in a dose/hold/purge sequence, followed by H_2O (deionized) cycles in the same sequence. An inert purge step for 5 minutes is conducted in between TMA and H_2O cycles. After the process is completed, 2 minutes of purging is conducted and the samples are removed to ambient conditions. For the mass gain calculations, the PET samples were weighed before loading to the reactor and after sitting at ambient conditions for 30 minutes after infiltration. For masking during the SVI processing, premium vinyl adhesive films (from Silhouette) were cut to a desired pattern using a Silhouette Cameo die cutting tool. The adhesive-backed films were stuck on the fabric surface and pressed manually.

In order to analyze the changes in chemical structure of the fibers, Fourier transform infrared (FTIR) spectra of the untreated and treated fabrics are obtained using a Nicolet Nexus 470 FTIR spectrometer with a germanium crystal attenuated total reflectance (ATR) attachment. Samples were placed on a germanium crystal and a force normal to the crystal surface is applied using a 3 mm diameter metal tip. Each FTIR-ATR measurement consisted of 64 scans from 700 to 4000 cm^{-1}.

7.3 Results and Discussion

In order to be consistent between low pressure and high pressure conditions, we first investigated the optimum dosing conditions that allowed for consistency in the amount of TMA delivered to the reactor. Since the hold cell is always charged with TMA up to 18 Torr, the pressurizing and dose times need to be adjusted to ensure that the maximum amount of TMA molecules are delivered to the reactor under both pressure conditions to achieve a saturated reaction between the sample and TMA (as observed by mass gain). For an ideal gas, the known hold cell temperature, volume and pressure allows for calculating the number of TMA moles in the hold cell, n ~2.8×10^{-5} mol. At 2.5 Torr, 0.5 s N_2 charge and 0.5 s dose conditions are sufficient for saturation for SVI at 120 °C. At 760 Torr and 120 °C, a 10 s N_2 charge and a 6 s dose is required for saturation. Furthermore, we investigated effect of purge time at different temperatures, with 6 s and 35 s purging at 2.5 Torr and with 15 s and 45 s purging at 760 Torr. At both pressures, longer purge times resulted in slightly lower mass gain values. In order to minimize the effect of left over TMA in the reactor we fixed the purging time to >35 s. We therefore fixed these exposure conditions at the temperature and pressure values studied.

Figure 7.1 (a) and (b) presents the mass gain observed at 2.5 Torr and 760 Torr, respectively, as a function of number of TMA cycles in a temperature range of 60-150 °C. At 2.5 Torr, highest mass gain values are observed at 90 °C with a linear relationship to the number of TMA cycles. At 60 °C a slightly lower mass gain is observed, also with a linear trend. However as the temperature increases, the mass gain deviates from linearity and higher mass gain is observed at 120 °C than that at 150 °C. In Fig. 1 (b), 760 Torr samples show a pronounced mass gain decrease as the process temperatures increases. At 60 and 90 °C a linear mass gain increase is observed as a function of the number of TMA cycles. As temperature is increased, a saturation behavior begins to be observed. It is interesting to note that the mass gain trend at 60 °C is independent of pressure. As the temperature increases, the differences in mass gain due to pressure arises and becomes more pronounced. This result is important for determining the feasibility of the process for atmospheric pressure as temperature is varied. The scale of the mass gain is very similar for both pressures (between 2-10 wt. %), which is promising for applying the SVI process at higher pressures and low temperatures.

In Figure 7.2, the mass gain of the PET fabrics is compared as a function of temperature after 60 TMA SVI cycles at 2.5 and 760 Torr. The first observation is the marginal difference in mass gain of the samples processed at 2.5 and 760 Torr at 60 and 150 °C. Secondly, mass gain is highest at 90 °C at 2.5 Torr whereas the maximum mass gain occurred at 60 °C at 760 Torr. Moreover, the mass gain of the samples at 2.5 Torr and 760 Torr shows a ~3 wt. % difference between the 90 °C and 120 °C samples. This behavior is a consequence of the process being a combination of precursor diffusion along the reactor, through the fiber matrix (between fibers), and through the polymer bulk as well as chemical reactions taking place between precursor

and polymer functional groups at the surface and in the bulk of the polymer. As for reaction rate, it is only affected by temperature, for constant TMA partial pressure. However, diffusion of the precursor in the gas phase is affected by both temperature and pressure, which will affect the speed of precursor delivery to the surface of the fibers. As discussed in previous studies,[8,14,20] for constant pressure the reaction rate between precursor and the polymer is reduced at low temperatures which permits more diffusion, and is observed as higher mass gain in the sample. This statement remains true for this study as at 60 °C for both pressures results in high mass gain. Similarity of the mass gains at both pressures at 60 °C suggests that, despite the diffusivity of the TMA in N_2 is changing with the pressure; the diffusivity in the bulk polymer is for the most part dependent on temperature. As the temperature increases, it is expected that the reaction rate between the precursor and C=O groups increases, as well as the diffusion rate of the TMA in N_2 and polymer. While an increase in mass gain is observed at 2.5 Torr at 90 °C as compared to that at 60 °C, the mass gain slightly decreases at 760 Torr. Considering that the diffusion of the precursor in polymer matrix is primarily dependent on the temperature, we can attribute this difference to the pressure dependency of the precursor diffusion in N_2. Faster diffusion will keep the surface concentration of TMA higher at 2.5 Torr resulting in higher mass gain. At 760 Torr the diffusion rate does not increase as much, resulting in lower mass gain. Furthermore, faster reaction kinetics at 90 °C can lead to a barrier layer close to the surface and result in less mass gain as noted at the 760 Torr sample. As the temperature increases to 120 °C, mass gain decreases at both pressures which indicates that the reaction rate starts to dominate over the diffusion rate independent of pressure. Finally, as the process temperature reaches 150 °C, the reaction rate dominates the diffusion rate effect.

The formed barrier layer prevents further diffusion resulting in similar mass gain for both pressures. However, the evolution of the mass gain at 150 °C by increasing number of the TMA cycles is very different for different pressures, as can be seen in Fig. 1. At low pressure this barrier layer starts to form at initial cycles whereas at high pressure it forms gradually. This can be attributed to slower kinetics at the surface at high pressures due to the lower partial pressure of the precursor as a result of slower diffusion.

To examine the reactivity of the TMA and PET as a function of pressure and temperature, FTIR analysis was conducted on samples using an attenuated total reflectance (ATR) set up, the spectra of which are provided in Figure 7.3. All spectra show two common features, independent of the SVI temperature and pressure that are related to the TMA-PET reaction, and have been previously determined in literature.[14,15,20,31,32] The first feature is the peak at 1716 cm^{-1} that upon SVI processing is decreased due to the ligand exchange reaction taking place between TMA and C=O groups. The second feature is a broad peak from 3000 to 3600 cm^{-1} wavenumber, which is attributed to the formation of OH groups by oxidation of Al-CH_3 groups during water exposures.

As an indication of the reaction extent in the probing depth of the ATR setup, we calculated the consumption of the C=O peaks in Figure 7.3 following: Carbonyl Consumption (%) = 100 x (Peak $Intensity_{(control)}$ – Peak $Intensity_{(sample)}$)/ Peak $Intensity_{(control)}$. In Figure 7.4 (a) and (b), the C=O consumption of the SVI treated samples are provided as a function of temperature at 2.5 Torr and 760 Torr respectively. After 30 cycles at 2.5 Torr (Fig. 4 (a)), a maximum consumption of C=O peak is observed for the 120 °C sample followed by 90, 150 and 60 °C

respectively. In contrast, the mass gain analysis in Fig. 1(a) is quite different than the ATR analysis. Recall that in the mass gain analysis after 30 TMA cycles, the samples processed at 60, 120 and 150 °C samples show similar mass gain and the 90 °C sample shows higher mass gain. The difference in both trends can be attributed to the surface sensitivity in the ATR method and the limitation of its ultimate probe depth. This surface sensitivity provides important inferences as to the characteristics of the SVI materials modification to the PET at different pressures. First, the discrepancy in the relative magnitude of the mass gain and C=O consumption at 120 °C can be attributed to the reaction occurring close to the surface of the PET fiber. At low temperatures, the higher mass gain means that precursor diffuses more into the material and the consumption of the C=O groups close to the surface, is lower. After 60 cycles at 2.5 Torr, the trends for mass gain and ATR analysis of the C=O consumption changes. As Fig. 4 (a) shows, a marked decrease in the C=O concentration is observed at all temperatures except 60 °C. Even though after 60 cycles of SVI the mass gain increased significantly at 60 °C, the C=O concentration (at the surface) is not considerably higher than 30 cycle SVI. In comparison, at all other temperatures, the C=O peak is nearly all consumed. This can be interpreted that the surface is nearly saturated with AlO_x at higher temperatures.

A similar analysis is performed for the samples processed at 760 Torr, as provided in Figure 7.4 (b) for 30 and 60 SVI cycles. After 30 cycles, the highest C=O consumption occurs at 150 °C then 90, 120 and 60 °C respectively. In comparison, mass gain of 150 °C sample after 30 cycles is slightly lower whereas other temperatures are very similar. As compared to the 2.5 Torr, the C=O consumption values after 30 cycles in Fig. 4 (a), show a wider dispersion then 760 Torr samples. This suggests that the change of diffusion rate of the precursor shows little

dependence on temperature at high pressure and much higher dependence at low pressure. After 60 cycles, the ATR spectra in Fig. 3 (d) suggests that all the samples have similar C=O peak intensities. However, mass gain of the samples increase as the processing temperature decreases. By comparing the trend of C=O consumption to the mass gain trend, it can be observed that the diffusion rate of the TMA in the samples is less temperature dependent at high pressures.

In order to support the above discussion of the operating pressure effect on the TMA diffusion rate along the reactor and consequently its concentration at the polymer surface, diffusion coefficients of TMA in N_2 are calculated using the equation suggested by Fuller et al.[33] as derived from Chapman–Enskog.

$$D_{TMA-N_2} = \frac{10^{-8} T^{1.75} \left(\frac{1}{M_{TMA}} + \frac{1}{M_{N_2}}\right)^{\frac{1}{2}}}{p\left[\left(\Sigma_{TMA} v_i\right)^{\frac{1}{3}} + \left(\Sigma_{N_2} v_i\right)^{\frac{1}{3}}\right]^2}$$

where T is the gas mixture temperature, p is the total pressure, M are the molecular weights of the gas components, and v_i are diffusion parameters considering the molecule structure of the diffusing species.

Calculated diffusion coefficients of TMA in N_2 as a function of temperature at the low and high pressures during the hold step, 14 and 760 Torr respectively, are given in Figure 7.5. At high-pressure, the diffusion coefficients show significant lower values as compared to those at low pressure. Therefore, the overall mass gain at high pressure is expected to be lower than that observed at low pressure. At low pressure, TMA molecules have higher diffusion rates in

N_2 along the reactor and between fibers than at atmospheric pressure. This is especially true at lower temperatures, where at 60 °C the time required to diffuse one centimeter is ~0.04 sec at low pressure and ~2.04 sec at 760 Torr. The diffusion times were calculated based on the equation derived from Fick's first law as calculated by Mousa et al.[29] Due to the faster diffusion along the reactor and between fibers at low pressure, a constant TMA partial pressure is maintained at the polymer surface, especially at high temperature, while a much lower TMA partial pressure is expected at polymer surface at atmospheric pressure. The TMA molecules that will react with the polymer surface will not be quickly substituted by new TMA molecules at atmospheric pressure due to the very slow diffusion rate along the reactor and between fibers. Such low TMA partial pressure at polymer surface will consequently lead to low TMA diffusion through the polymer bulk due to the low TMA concentration gradient between polymer surface and bulk.

It can also be noted from Fig. 5 that the change in diffusion coefficients with temperature at 760 Torr (0.74 cm^2/sec at 150 °C to 0.49 cm^2/sec at 60 °C) is much lower than the change at low pressure (40.4 cm^2/sec to 26.6 cm^2/sec). The difference in TMA diffusion coefficients can be used as a good estimate for the difference in the precursor diffusion through the polymer as discussed earlier. Accordingly, the difference in diffusion coefficients shown if Fig. 5 can explain the temperature dependence of mass gain observed in Fig. 1 and Fig. 2. An increase in temperature from 60 °C to 90 °C at 2.5 Torr shows an increase in mass gain as a result of the higher TMA diffusion in the polymer. However for the same temperature values at 760 Torr, the mass gain is low as a result of a small increase in the diffusion coefficient. As the temperature increased to 120 °C and 150 °C, the decrease in mass gains at both high and low

pressures is a result of change in reaction rate between the polymer and the precursor rather than change in diffusion rates. Higher reaction rates at these temperatures, leads to the formation of a barrier layer close to the fiber surface, which eventually reduces the diffusion of the precursor. Samples treated at 150 °C, show similar mass gain and C=O consumption in the FTIR spectra at both pressures which is attributed to the reaction rate being the primary factor that determines the mass gain values at this temperature.

While it has been shown that the lower diffusion rate of TMA through the ***polymer matrix*** at high pressure affects the mass uptake, the diffusion in the ***fiber matrix*** (between fibers) will also be altered. We investigated the effect of TMA diffusion through the ***fiber matrix*** by noting the percentage decrease in mass uptake after masking ~82% of the sample upper surface. The change in mass uptake due to masking was noted by comparing the values for masked and bare samples,

$$Change\ in\ mass\ uptake_{masking} = \frac{Mass\ uptake_{bare} - Mass\ uptake_{masked}}{Mass\ uptake_{bare}} X100$$

The samples were masked using a film with a vinyl adhesive and subsequently treated with SVI at different pressures. The sample processed at low pressure at 60 ^{o}C with 30 TMA cycles showed ~20% lower mass uptake compared to the unmasked sample. On the other side the masked sample processed under similar conditions but at high pressure (low TMA diffusion) showed ~80% lower mass uptake as compared to the unmasked sample. The lower TMA diffusion through the fiber matrix at higher pressure may have strategic benefits in patterning. To demonstrate the diffusion differences at low and high pressures, the pattern resolution of masked fabric was investigated. As previously demonstrated, SVI of TMA can induce an

increase in the photoluminescence of PET.[20] Optical images of the treated fabrics with and without UV illumination are provided in Figure 7.6. It is observed that all of the treated samples do not show any indication of the patterned SVI process under normal light conditions. When the samples are exposed to UV light in dark room, a photoluminescent pattern appears, as observed in Fig. 6 (a-d). The resolution of the luminescent pattern is a direct indicator of the diffusion behavior of the TMA into the fiber matrix as pressure is altered. The sample treated at 2.5 Torr and 60 °C is not readable because precursor reached the masked sites due to the high diffusion rate at low pressure. By increasing the pressure to 760 Torr, the resolution of the pattern is greatly improved due to the lower diffusion into the masked regions because of the low precursor diffusion rate.

Assuming an infinitely large mask on top of a fabric surface on which there is a finite opening for precursor diffusion into the substrate; the cases of ideal, low, and good resolution are given schematically in Figure 7.7. For best pattern resolution, precursor should diffuse into the fiber matrix through only the exposed part of the mask. Penetration depth through the fiber matrix should also be very limited and hybrid modification happens only in the fibers close to the surface (Fig. 7 (a)). For the demonstrated masked sample at 2.5 Torr, masking is limited to small areas under the label and precursor diffuses beyond the pattern definition and the resolution is very low (Fig. 7(b)). At 760 Torr, diffusion coefficients are much lower and the masking is significantly more effective (Fig. 7 (c)). Limited and very low diffusion through the pattern definition results in better resolution. The ability to have fine photoluminescent patterning using the SVI process at atmospheric pressure has the potential for unique applications in flexible electronics and protective identification applications.

7.4 Summary

This research demonstrates the mechanistic differences for the synthesis of hybrid materials formed via sequential vapor infiltration of TMA at vacuum and atmospheric pressure. Results showed that SVI can be conducted at atmospheric pressure which is very important for utilization of the process for roll-to-roll polymer material (fiber and film) modification applications. Differences in the extent of infiltration into the polymer matrix, as determined through mass gain and FT-IR analysis, are related to the precursor diffusion in N_2 along the reactor and between fibers as well as its diffusion through the polymer and the reaction rate with the functional groups on polymer surface and bulk. The much slower diffusion of TMA in N_2 at atmospheric pressure, leads to lower TMA partial pressure at the polymer surface and thus lower diffusion rate through the polymer bulk as compared to the processing under lower pressure. Also, at higher temperatures, faster reaction kinetics leads to the formation of a barrier hybrid layer that prevents the reactants diffusion into and through the samples resulting in a lower mass gain values in general. Finally, the effect of diffusion through the fiber matrix (between fibers) on the ability to pattern the photoluminescent behavior of the hybrid materials is shown to improve with increasing pressure. Patterns created at higher pressure showed more defined edges, which shows great advantage for the feasibility of the pattern-based roll-to-roll processing of SVI.

7.5 Acknowledgments

Authors would like to thank Prof. Gregory Parsons at Chemical and Biomolecular Engineering department at North Carolina State University for his help in this work. Authors also acknowledge partial funding from National Science Foundation Industry & University

Cooperative Research Program: Center for Dielectrics and Piezoelectrics (CDP) (Grant number: 1361503), National Science Foundation CMMI project number 1000382 and Republic of Turkey Ministry of National Education.

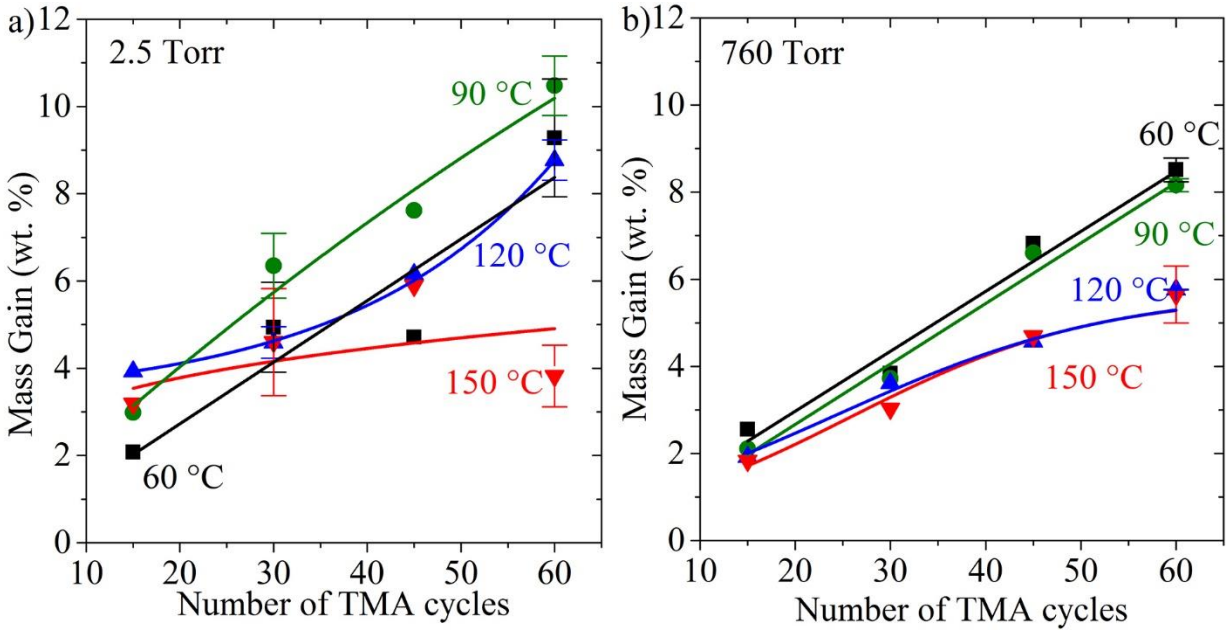


Figure 7.1. Mass gain of samples treated with SVI at a) 2.5 Torr and b) 760 Torr as a function of number of TMA cycles at various process temperature.

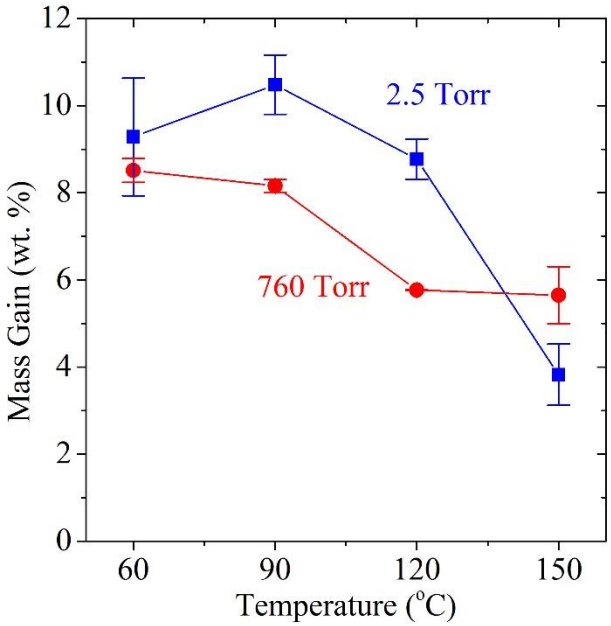


Figure 7.2. Comparison of mass gain for samples treated by SVI process with 60 cycles of TMA at 2.5 and 760 Torr for process temperature between 60 °C and 150 °C.

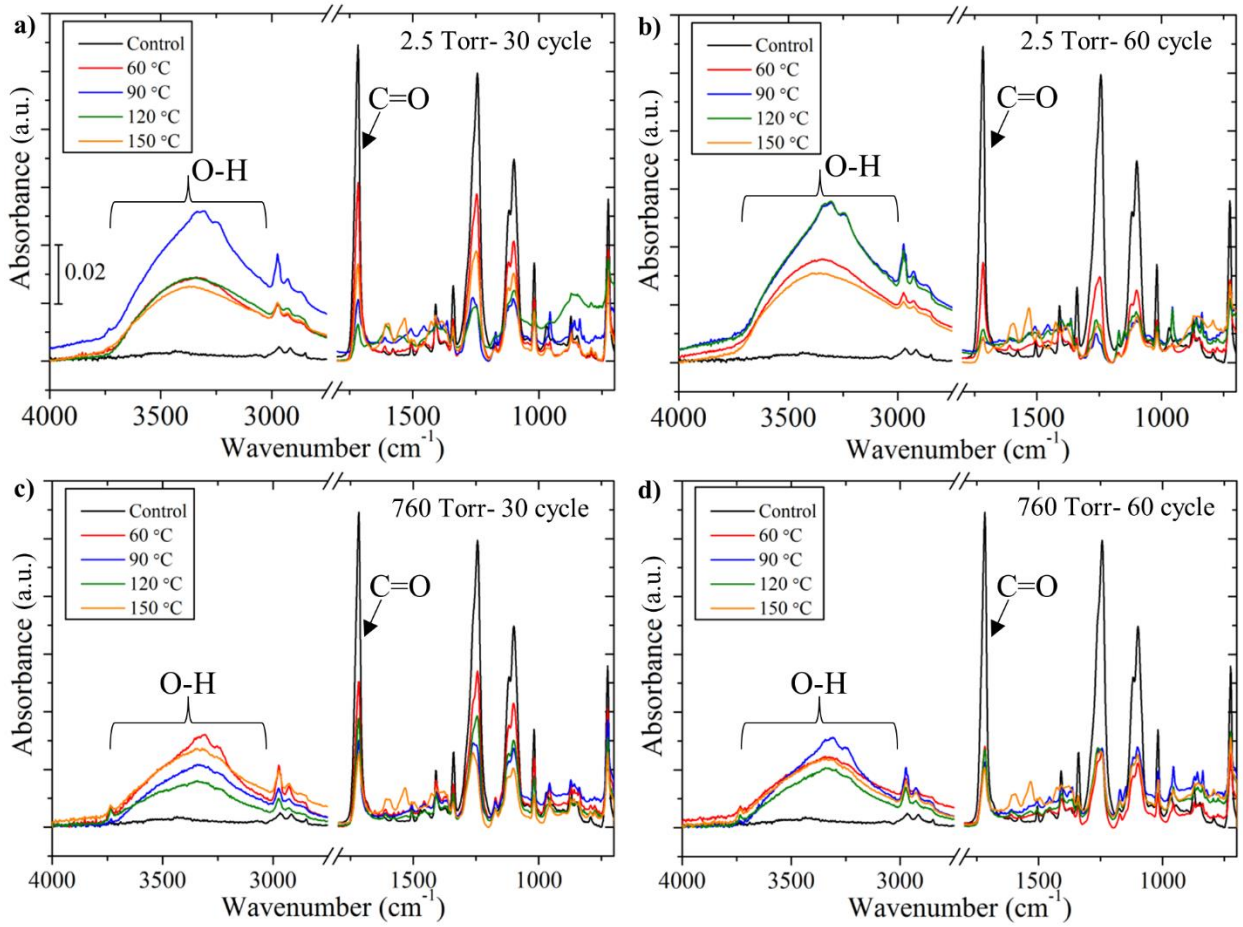


Figure 7.3. FTIR spectra of samples treated with SVI a) 30 cycles, b) 60 cycles at 2.5 Torr and c) 30 cycles, b) 60 cycles at 760 Torr for process temperature between 60 °C and 150 °C.

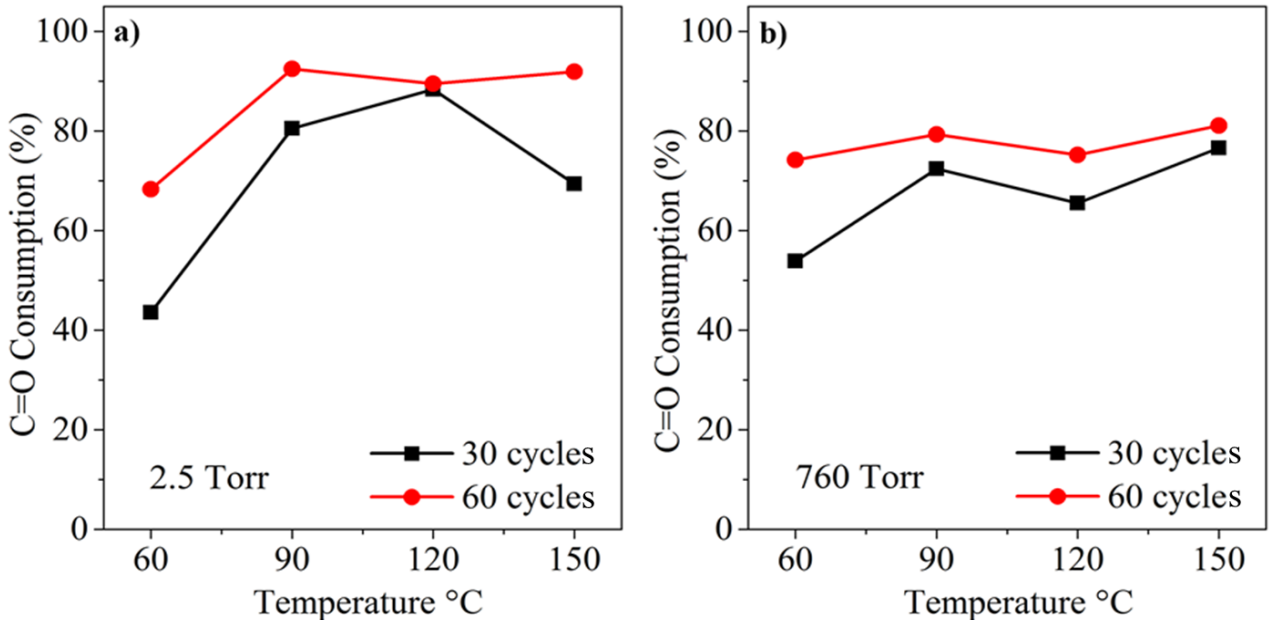


Figure 7.4. Consumption of C=O peak in FTIR spectra as function of temperature after 30 and 60 cycle SVI treatment at a) 2.5 Torr and b) 760 Torr.

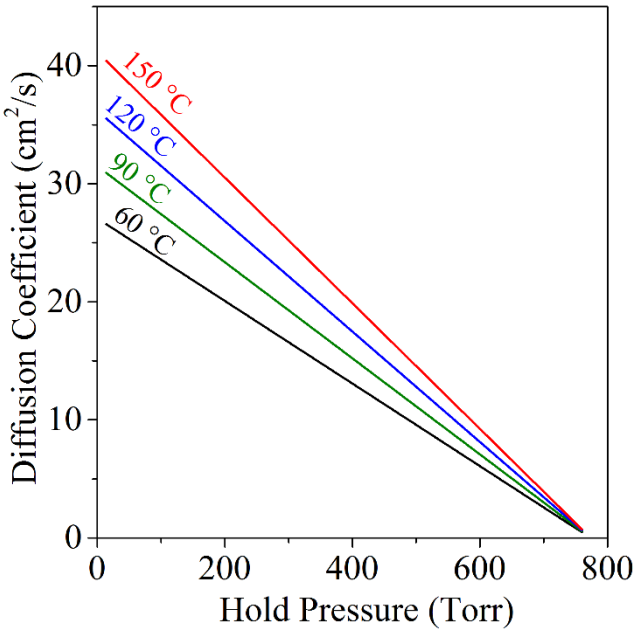


Figure 7.5. Calculated diffusivity values of TMA molecules in N_2 as a function of pressure at 60, 90, 120 and 150 °C.

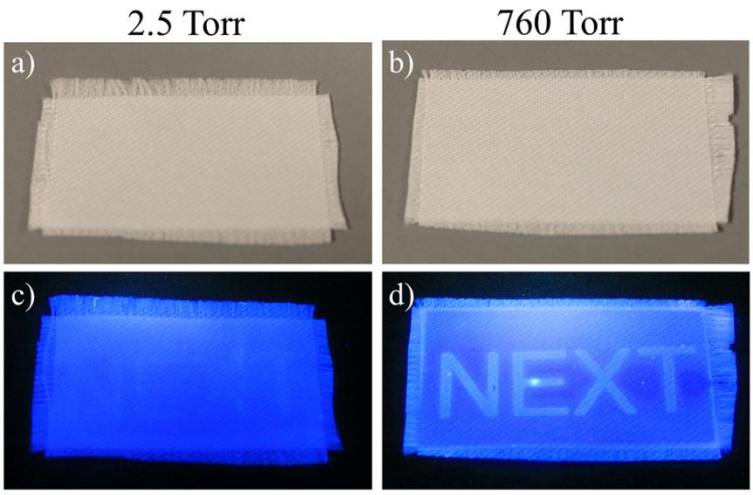


Figure 7.6. Optical images of samples masked during 30 cycle TMA exposure SVI experiments at 60 °C at 2.5 Torr ((a) and (c)) and 760 Torr ((b) and (d)) under normal light ((a) and (b)) and UV illumination ((c) and (d)).

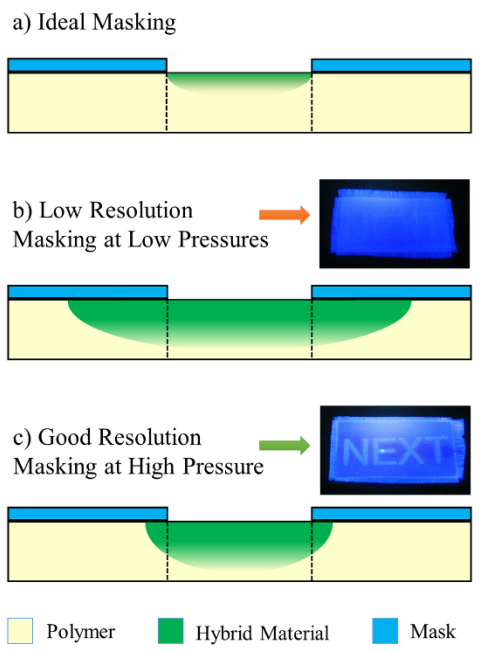


Figure 7.7. Schematic of hybrid materials formation through the fabric cross-section in the case of a) ideal masking, b) low resolution masking at low pressures, and c) good resolution masking at high pressures.

7.6 Supplemental Material

During the experiments, it was noted that PET fabrics treated at high temperatures (120, 150 ^{o}C) tend to have a characteristic yellow color relative to the samples treated at 60, 90 ^{o}C where no visual change in color occur. The visual color difference may indicate different coordination of the aluminum atom to the PET organic groups as indicated by the difference in the FTIR spectra of the fabrics treated at low and high temperature as shown in Figure 7.3. Moreover, it was found that a post-deposition heating at 150 ^{o}C of the fabrics deposited at 60 and 90 ^{o}C under inert atmosphere will lead to a visual color change as shown in Figure 7.8. These results agree with recent reports for the occurring surface reaction mechanisms during vapor infiltration treatment of poly (methyl methacrylate).[31,34] In both studies, it was found that at low temperatures TMA tends to physisorb on the polymer at low temperature forming weak adducts with the present carbonyl groups, which both reacts and desorbs very slowly. On the other side at high temperatures the reaction proceeds readily forming covalent bonds. Equivalent coordination states is probably occurring between TMA and PET at the different temperatures. Post-deposition heating might have increased the reaction rate of the physisorbed TMA molecules thus leading to a final coordination states close by from those achieved through infiltration at high temperature directly with no post-deposition heating. The exact mechanisms for the occurring reactions on PET were not investigated any further. However, understanding the underlying mechanisms will help in tailoring the process to maximize the photoluminescency of the formed hybrid material and can lead to other new interesting applications as well.

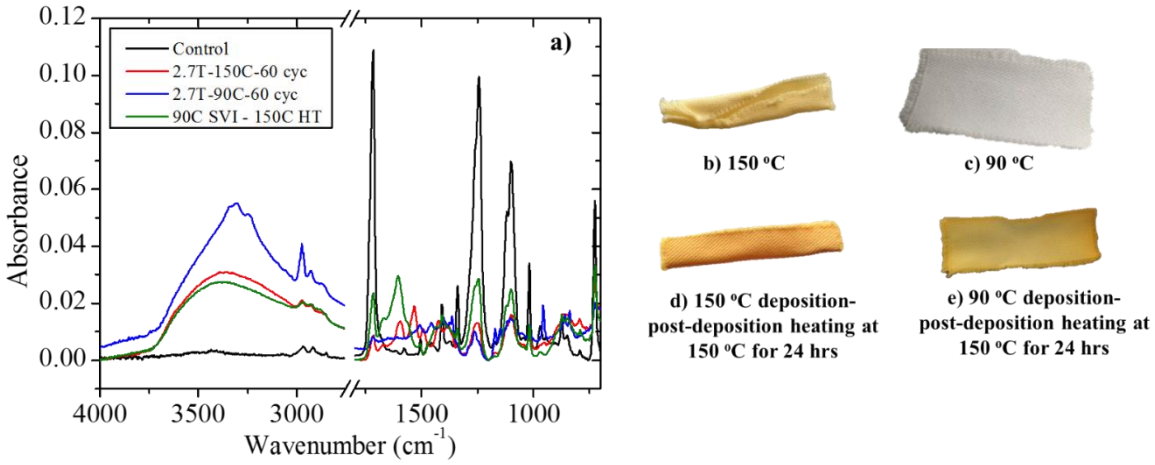


Figure 7.8. Effect of vapor infiltration temperature of TMA in PET and the post-deposition heating on the formed hybrid material. (a) Ex situ FTIR spectra of the PET samples infiltrated at 90 and 150 ºC, as well as the sample infiltrated at 90 ºC followed by a 24 hrs heating at 150 ºC in inert atmosphere. Images of the samples after infiltration at (b) 150 ºC and 90 ºC are shown depicting a clear visual difference in color. Also images for the samples treated at similar infiltration conditions but were heated for 24 hrs at 150 ºC after infiltration are shown in (d) and (e).

7.7 References

(1) You, J.-O.; Auguste, D. T. Conductive, Physiologically Responsive Hydrogels. *Langmuir* **2010**, *26* (7), 4607–4612.

(2) Costa, H. S.; Stancioli, E. F. B.; Pereira, M. M.; Oréfice, R. L.; Mansur, H. S. Synthesis, Neutralization and Blocking Procedures of Organic/inorganic Hybrid Scaffolds for Bone Tissue Engineering Applications. *J. Mater. Sci. Mater. Med.* **2008**, *20* (2), 529–535.

(3) Franville, A.-C.; Zambon, D.; Mahiou, R.; Troin, Y. Luminescence Behavior of Sol−Gel-Derived Hybrid Materials Resulting from Covalent Grafting of a Chromophore Unit to Different Organically Modified Alkoxysilanes. *Chem. Mater.* **2000**, *12* (2), 428–435.

(4) Sanchez, C.; Lebeau, B.; Chaput, F.; Boilot, J.-P. Optical Properties of Functional Hybrid Organic–Inorganic Nanocomposites. *Adv. Mater.* **2003**, *15* (23), 1969–1994.

(5) Wight, A. P.; Davis, M. E. Design and Preparation of Organic−Inorganic Hybrid Catalysts. *Chem. Rev.* **2002**, *102* (10), 3589–3614.

(6) Jur, J. S.; Spagnola, J. C.; Lee, K.; Gong, B.; Peng, Q.; Parsons, G. N. Temperature-Dependent Subsurface Growth during Atomic Layer Deposition on Polypropylene and Cellulose Fibers. *Langmuir* **2010**, *26* (11), 8239–8244.

(7) Spagnola, J. C.; Gong, B.; Arvidson, S. A.; Jur, J. S.; Khan, S. A.; Parsons, G. N. Surface and Sub-Surface Reactions during Low Temperature Aluminium Oxide Atomic Layer Deposition on Fiber-Forming Polymers. *J. Mater. Chem.* **2010**, *20* (20), 4213–4222.

(8) Sun, Y.; Padbury, R. P.; Akyildiz, H. I.; Goertz, M. P.; Palmer, J. A.; Jur, J. S. Influence of Subsurface Hybrid Material Growth on the Mechanical Properties of Atomic Layer Deposited Thin Films on Polymers. *Chem. Vap. Depos.* **2013**, *19* (4-6), 134–141.

(9) Lee, S.-M.; Ischenko, V.; Pippel, E.; Masic, A.; Moutanabbir, O.; Fratzl, P.; Knez, M. An Alternative Route Towards Metal–Polymer Hybrid Materials Prepared by Vapor-Phase Processing. *Adv. Funct. Mater.* **2011**, *21* (16), 3047–3055.

(10) Lee, S.-M.; Pippel, E.; Gösele, U.; Dresbach, C.; Qin, Y.; Chandran, C. V.; Bräuniger, T.; Hause, G.; Knez, M. Greatly Increased Toughness of Infiltrated Spider Silk. *Science* **2009**, *324* (5926), 488–492.

(11) Lee, S.-M.; Pippel, E.; Knez, M. Metal Infiltration into Biomaterials by ALD and CVD: A Comparative Study. *ChemPhysChem* **2011**, *12* (4), 791–798.
(12) Peng, Q.; Tseng, Y.-C.; Darling, S. B.; Elam, J. W. A Route to Nanoscopic Materials via Sequential Infiltration Synthesis on Block Copolymer Templates. *ACS Nano* **2011**, *5* (6), 4600–4606.
(13) Tseng, Y.-C.; Peng, Q.; Ocola, L. E.; Elam, J. W.; Darling, S. B. Enhanced Block Copolymer Lithography Using Sequential Infiltration Synthesis. *J. Phys. Chem. C* **2011**, *115* (36), 17725–17729.
(14) Akyildiz, H. I.; Padbury, R. P.; Parsons, G. N.; Jur, J. S. Temperature and Exposure Dependence of Hybrid Organic–Inorganic Layer Formation by Sequential Vapor Infiltration into Polymer Fibers. *Langmuir* **2012**, *28* (44), 15697–15704.
(15) Gong, B.; Peng, Q.; Jur, J. S.; Devine, C. K.; Lee, K.; Parsons, G. N. Sequential Vapor Infiltration of Metal Oxides into Sacrificial Polyester Fibers: Shape Replication and Controlled Porosity of Microporous/Mesoporous Oxide Monoliths. *Chem. Mater.* **2011**, *23* (15), 3476–3485.
(16) Lee, S.-M.; Pippel, E.; Moutanabbir, O.; Gunkel, I.; Thurn-Albrecht, T.; Knez, M. Improved Mechanical Stability of Dried Collagen Membrane after Metal Infiltration. *ACS Appl. Mater. Interfaces* **2010**, *2* (8), 2436–2441.
(17) Peng, Q.; Tseng, Y.-C.; Darling, S. B.; Elam, J. W. Nanoscopic Patterned Materials with Tunable Dimensions via Atomic Layer Deposition on Block Copolymers. *Adv. Mater.* **2010**, *22* (45), 5129–5133.
(18) Tseng, Y.-C.; Mane, A. U.; Elam, J. W.; Darling, S. B. Enhanced Lithographic Imaging Layer Meets Semiconductor Manufacturing Specification a Decade Early. *Adv. Mater.* **2012**, *24* (19), 2608–2613.
(19) Tseng, Y.-C.; Peng, Q.; Ocola, L. E.; Czaplewski, D. A.; Elam, J. W.; Darling, S. B. Etch Properties of Resists Modified by Sequential Infiltration Synthesis. *J. Vac. Sci. Technol. B* **2011**, *29* (6), 06FG01.

(20) Akyildiz, H. I.; Lo, M.; Dillon, E.; Roberts, A. T.; Everitt, H. O.; Jur, J. S. Formation of Novel Photoluminescent Hybrid Materials by Sequential Vapor Infiltration into Polyethylene Terephthalate Fibers. *J. Mater. Res.* **2014**, *29* (23), 2817–2826.
(21) Judeinstein, P.; Sanchez, C. Hybrid Organic–inorganic Materials: A Land of Multidisciplinarity. *J. Mater. Chem.* **1996**, *6* (4), 511–525.
(22) Gustafsson, G.; Cao, Y.; Treacy, G. M.; Klavetter, F.; Colaneri, N.; Heeger, A. J. Flexible Light-Emitting Diodes Made from Soluble Conducting Polymers. *Nature* **1992**, *357* (6378), 477–479.
(23) Nomura, K.; Ohta, H.; Takagi, A.; Kamiya, T.; Hirano, M.; Hosono, H. Room-Temperature Fabrication of Transparent Flexible Thin-Film Transistors Using Amorphous Oxide Semiconductors. *Nature* **2004**, *432* (7016), 488–492.
(24) Lim, W.; Jang, J. H.; Kim, S.-H.; Norton, D. P.; Craciun, V.; Pearton, S. J.; Ren, F.; Shen, H. High Performance Indium Gallium Zinc Oxide Thin Film Transistors Fabricated on Polyethylene Terephthalate Substrates. *Appl. Phys. Lett.* **2008**, *93* (8).
(25) Corrales, T.; Peinado, C.; Bosch, P.; Catalina, F. Study of Secondary Relaxations of Poly(ethylene Terephthalate) by Photoluminescence Technique. *Polymer* **2004**, *45* (5), 1545–1554.
(26) Takai, Y.; Mizutani, T.; Ieda, M. Photoluminescence Study in Polymers. *Jpn. J. Appl. Phys.* **1978**, *17* (4), 651.
(27) Teyssèdre, G.; Menegotto, J.; Laurent, C. Temperature Dependence of the Photoluminescence in Poly(ethylene Terephthalate) Films. *Polymer* **2001**, *42* (19), 8207–8216.
(28) Jur, J. S.; Parsons, G. N. Atomic Layer Deposition of Al2O3 and ZnO at Atmospheric Pressure in a Flow Tube Reactor. *ACS Appl Mater Interfaces* **2011**, *3* (2), 299–308.
(29) Mousa, M. B. M.; Oldham, C. J.; Jur, J. S.; Parsons, G. N. Effect of Temperature and Gas Velocity on Growth per Cycle during Al2O3 and ZnO Atomic Layer Deposition at Atmospheric Pressure. *J. Vac. Sci. Technol. A* **2012**, *30* (1), 01A155.

(30) Mousa, M. B. M.; Oldham, C. J.; Parsons, G. N. Atmospheric Pressure Atomic Layer Deposition of Al2O3 Using Trimethyl Aluminum and Ozone. *Langmuir* **2014**, *30* (13), 3741–3748.
(31) Dandley, E. C.; Needham, C. D.; Williams, P. S.; Brozena, A. H.; Oldham, C. J.; Parsons, G. N. Temperature-Dependent Reaction between Trimethylaluminum and Poly(methyl Methacrylate) during Sequential Vapor Infiltration: Experimental and Ab Initio Analysis. *J. Mater. Chem. C* **2014**, *2* (44), 9416–9424.
(32) Parsons, G. N.; Atanasov, S. E.; Dandley, E. C.; Devine, C. K.; Gong, B.; Jur, J. S.; Lee, K.; Oldham, C. J.; Peng, Q.; Spagnola, J. C.; et al. Mechanisms and Reactions during Atomic Layer Deposition on Polymers. *Coord. Chem. Rev.* **2013**, *257* (23–24), 3323–3331.
(33) Fuller, E. N.; Schettler, P. D.; Giddings, J. C. New Method for Prediction of Binary Gas-Phase Diffusion Coefficients. Ind. Eng. Chem. 1966, 58 (5), 18–27.
(34) Biswas, M.; Libera, J. A.; Darling, S. B.; Elam J. W. New Insight into the Mechanism of Sequential Infiltration Synthesis from Infrared Spectroscopy. Chem. Mater. 2014, 26 (21), 6135-6141.

CHAPTER 8

Tin Metal Atomic Layer Deposition using Tin(IV) Chloride and a Silyl Dihydropyrazine Reducing Agent

This chapter is a manuscript in preparation by Moataz Bellah M. Mousa, Eric C. Stevens and Gregory N. Parsons.

Department of Chemical and Biomolecular Engineering, North Carolina State University, Raleigh, NC, USA

Abstract

Tin metal thin films were grown by an atomic layer deposition (ALD) process using 1,4-bis(trimethylsilyl)-1,4-dihydropyrazine as a reducing agent for tin(IV) chloride ($SnCl_4$) precursor. The key properties of an ALD process were confirmed, including self-limiting reactions, surface saturation, and process temperature window where a linear mass uptake was observed using quartz crystal microbalance measurements for temperatures between 170-210 ^oC. Cross-sectional SEM images of a ~40 nm metal film deposited at 190 ^oC showed uniform thickness, common for an ALD process. ToF-SIMS and XPS measurements confirmed the deposition of Sn in its metallic state with low carbon, nitrogen, and chlorine contamination. The contaminants concentrations were found to be much higher in the grown films at low deposition temperatures. Furthermore, in situ FTIR and quadrupole mass spectrometry (QMS) techniques were used to investigate the underlying surface chemistry of the process and the data supports the proposed reaction mechanism and initial reports in the literature to a good extent. However, more in depth studies are needed to gain a deeper understanding of the surface reaction mechanisms involved in using these electron-rich organo-silane reducing agents. The results in this work represent the first demonstration of an ALD process for elemental Sn deposition.

8.1 Introduction

As the features in micro and nano-electronics are getting smaller and more complex, advanced thin film deposition techniques are needed for the production of the required new complex nanoscale 3D structure designs.[1] The ideal deposition process will produce highly conformal and uniform thin films at relatively low temperatures for a wide selection of materials; these are the hallmarks for the atomic layer deposition (ALD) process, besides its ability to precisely control the thickness of deposited films up to angstroms level. More specifically, metal thin films are receiving wide attention due to their various applications in many industries (e.g., semiconductor, batteries, sensors and wearable electronics). For example in logic devices, ALD of metals can be used for back end of line (BEOL) interconnects and interconnect barriers as well as a seed layer for copper electrodeposition and tungsten chemical vapor deposition (CVD).[2] It can also be used for dual-gate MOSFETs to deposit high- and low-work function metals or just for high-k based transistors. Moreover, for memory devices, ALD of metals like nickel or cobalt can be used for magnetoresistive random access memory (MRAM), chromium for many new flash memory devices, and platinum as an electrode material in dynamic random access memory (DRAM).[3]

Although the need is rapidly increasing for high quality, conformal and uniform metal thin films, few elemental metals are available by ALD.[4] Many of the trials to develop ALD chemistry for metals were unsuccessful except for noble metals due to their positive reduction potentials and the fundamental understanding of the involved reaction mechanisms through using oxygen and/or ozone as a co-reactant.[5] Even so, nucleation non-uniformity prohibits deposition of ultra-thin noble metal films. Other challenges for understanding metal

ALD are the absence of a suitable mechanism for precursors to adsorb on metal surfaces where no reactive sites exist. Furthermore, the lack of strong reducing co-reactants capable of converting metal precursors to their elemental state leads to the use of plasma based processes to generate high energy radicals. The issue with these plasma processes is the uncertainty regarding conformality due to radical combination in high aspect ratio structures. Thus, the existence of a thermal ALD process with a co-reactant capable of reducing metal precursors with highly negative reduction potentials will expand on the types of metal films that can be deposited for the various applications over different industries.

Tin (Sn) based thin films are used in many different applications such as in intermetallic micro-bumps in the semiconductor industry[6], in CZTS thin film solar cells[7], for metal layers in organic molecular thin films,[8] and as metal electrodes for CO_2 reduction[9]. They have also attracted huge interest for their use as anode materials for lithium ion batteries due to their very high specific electrical capacity (994 mAh/g),[10] which surpasses currently used graphite anodes (372 mAh/g)[11]. However, the use of the Sn-based thin films is accompanied by huge volume changes (up to 250X) during the battery operation for the lithiation and de-lithiation processes. These huge volume changes leads to cracking of the electrodes and thus shorten its cycle life. The problem was approached in different ways, but film thicknesses,[12] microstructure, [13,14] and morphology[15,16] were found to play key roles in overcoming the volume change issue.[17] Electrodeposition[18-20] and physical vapor deposition[13,15,21] were the main techniques used for depositing Sn thin films in the literature. The use of chemical vapor deposition in forming tin thin films is very limited due to the low melting point of Sn (~230 ^{o}C) relative to other metals. For all of the reported CVD

processes[22, 23], Sn is deposited way above its melting point which greatly affects the quality of the deposited films. An ALD process for tin deposition can help solve many of these problems where very thin films can be deposited with good control over their microstructure and morphology with deposition temperatures below the material melting point. Moreover, most battery architectures are turning to more complex 3D structures or highly porous scaffolds,[24] which suggests the need for a Sn ALD process[25].

In this work, we investigate the use of 1,4-bis(trimethylsilyl)-1,4-dihydropyrazine (abbreviated as DHP) as a reducing agent for tin(IV) chloride during ALD of elemental tin. Tin(IV) chloride has a high vapor pressure and relatively low standard reduction potential ($Sn^{4+} + 2e- \rightarrow Sn^{2+}$ (0.15 eV), $Sn^{2+} + 2e- \rightarrow Sn^{0}$ (-0.14 eV))[26] which makes it easier to reduce relative to other metals (e.g. titanium). The key ALD process characteristics of linear growth with number of cycles and self-saturation nature were tested in addition to the deposited films thickness uniformity and purity as well as the underlying surface chemistry.

8.2 Materials and Methods

For the ex-situ analysis done in this work, the deposited tin metal films were capped with thick titanium oxide (TiO_2) and titanium nitride (TiN) layers to prevent oxidation and adventitious carbon contamination upon exposure to air. The depositions were done in situ on the metal layer before pulling it out of the reactor, TiN was deposited directly on top of the tin layer by Tetrakis(dimethylamido) titanium (TDMAT) and ammonia (NH_3) ALD process, followed by TiO_2 using titanium(IV) chloride ($TiCl_4$) and titanium tetra-isopropoxide (TTIP) ALD process. Both capping layers were deposited at 190 ^{o}C.

Time-of-flight secondary ion mass spectroscopy (TOF-SIMS) (ION TOF, Inc. Chestnut Ridge, NY) was used to determine the depth profile of the deposited films. First, a 220 × 220 μm^2 area was sputtered using a 1 keV Cs^+ ion beam, then a depth profile was acquired from a 50 × 50 μm^2 area within the sputtered region using a 25 kV Bi^{3+} primary ion beam. The depth of the formed crater was measured using a Dektak 150 profilometer which allowed plotting the ions intensity against the sputtering depth.

Cross-sectional samples of Sn coated silicon substrates were prepared by focused ion beam (FIB) processing and imaged using FEI Verios 460L scanning electron microscope (SEM). For the FIB processing, the multi-layer coated sample (TiO_2/TiN/Sn) was coated with a gold/palladium layer to avoid charges accumulation during the milling process. A 25 μm × 2 μm × 2 μm bar of platinum was deposited while the sample was inside the FIB chamber to protect an area of interest from destruction during the ion milling process.

Elemental analysis for the deposited tin films was performed to determine their purity using a SPECS X-ray photoelectron spectroscopy (XPS) system with a PHOIBOS 150 analyzer. An Al Kα X-ray source operated at 400 W was used to generate the x-ray beam and Ar ions were used for the sputtering whenever needed. The collected data was calibrated by referencing adventitious carbon (C 1s peak) to 284.8 eV. CasaXPS software was used to fit the spectra and determine the elements concentrations, also NIST XPS database[27] was used for spectral peaks identification.

Quartz crystal micro-gravimetric analysis (QCM), quadrupole mass spectrometry (QMS), and FTIR were the in situ characterization techniques used in this work to study the

ALD process. QCM analysis tested the self-limiting nature of the reactants and determined the average mass uptake per cycle at different temperatures. For the surface saturation tests, each reactant was dosed multiple times in sequence, separated by inert gas purge steps, before introducing the other reactant in the same manner. This dosing sequence will be referred to as a multi-dose hereafter. MKS Vision 2000c QMS equipped with a triple-filtered quadrupole with a mass range of 1-300 amu was used to perform the in situ mass spectrometry characterization. The instrument was connected to the outlet of the reactor so that all of the exhaust gas passed through the sampling chamber before going to the rotary vacuum pump. NIST mass spectrometry database was used to help interpret the collected data through defining the m/z values of some of the reactants and the products. Finally, the details of the in situ FTIR system used in this work and the ALD reactor connected to it are described in details in [28].

The ALD experiments were carried out in a custom-built, hot-wall ALD reactor with an operating pressure of ~1.3 Torr, described in details in [29]. Precursors were charged into a known volume (which will be referred to as a hold cell), and then subsequently dosed to the reactor using nitrogen carrier gas, thus allowing the dose of the same reactant amount for each ALD cycle. This setup allowed for measuring the vapor pressure of DHP at different source temperatures, as shown in Figure 8.1, which helped in determining the co-reactant exposure and ensured consistent and constant dosing. During all of the deposition experiments, the DHP source was heated to ~68 ^{o}C to maintain a vapor pressure ~1.4 Torr.

8.3 Results and Discussion

8.3.1 ALD Temperature Window and Growth Saturation

The results from the QCM analysis for the mass change during reactant exposure and purge are shown in Figure 8.2. The measured mass uptakes per ALD cycle at different temperatures after 3 multi-doses of each reactant are shown in Figure 8.2a and indicates an ALD temperature window between 170-210 ^{o}C. The highest temperature investigated was 210 ^{o}C since Sn metal melts at ~232 ^{o}C. Below 170 ^{o}C, the growth was higher than that observed within the ALD window, most likely due to prohibitively long purge times needed for lingering reaction byproducts and excess reactants. Furthermore, low temperature depositions showed long nucleation delay (e.g., ~300 cycles at 130 ^{o}C) which decreased significantly with rising the growth temperature (e.g., ~20 cycles at 210 ^{o}C). The shown mass uptake per cycle values are the average of 200 cycles after the nucleation phase at each deposition temperature. To test the self-saturation nature of the $SnCl_4$/DHP process within the ALD window, the mass change with extended exposures of both reactants was monitored, where exposures were varied by changing the number of the multiple doses for each reactant. Figure 8.2b shows the average mass uptake per cycle at different total number of moles dosed at 170 ^{o}C and 210 ^{o}C for both reactants. The growth was found to saturate at ~200-250 ng/cm^2/cyc for exposure levels of ~8E-5 moles of $SnCl_4$ and 1E-5 moles of DHP. Four complete ALD cycles of the three multi-doses run at 190 ^{o}C are shown in Figure 8.2c, where no apparent mass change is noted after the second $SnCl_4$ dose and the first DHP one. The growth saturation trend was the same at 210 ^{o}C, while it took two DHP doses at 170 ^{o}C before seeing no apparent mass change. This very low mass changes at extended exposures

of both reactants confirm the self-saturation nature of the $SnCl_4$/DHP ALD process within the determined temperature window. For the growth below 170 ^oC, it was difficult to saturate the surface; a mass change was observed even after 5 multi-doses of each reactant. It can be hypothesized that the continuous mass increase during $SnCl_4$ doses can be due to physisorption of $SnCl_4$ at low temperatures, with minimal removal during purge steps. These multi-layers of physisorbed $SnCl_4$ may also prevent incoming DHP from reacting with all of the available chlorine functional groups, despite multiple consecutive DHP exposures, leading to a continuous mass change during the DHP doses as well.

8.3.2 ToF-SIMS, XPS and SEM Analysis

ToF-SIMS and XPS were used to analyze the capped Sn film deposited at 190 ^oC after 1500 $SnCl_4$/DHP ALD cycles to confirm the deposition of elemental Sn. Following the Sn deposition, a capping layer comprised of TiN and TiO_2 layers was deposited in situ. Figure 8.3 shows the ToF-SIMS depth profile of the deposited Sn film and the two capping layers where the Sn and TiO_2 films were easily identified. The TiN ions could not be detected by the ToF-SIMS mass spectrometer and the TiO_2 signal was found to extend all the way to the Sn film. However, XPS scans of the N 1s peak confirmed the presence of the TiN bond, as will be shown later, so the TiN ion detection difficulty using ToF- SIMS is probably due to the high porosity of the TiN film deposited using TDMAT/NH_3 as reported in the literature[29]. Also, the titanium atoms in the TiN layer might have been oxidized during the aggressive ToF-SIMS sputtering which made it more difficult to detect the nitride ions. The TiN layer (Region II in Figure 8.3) was identified based on the chloride and CN ions. Of the three ALD chemistries used, TiN ALD is the only one which does not involve reactants with

chlorine atoms (recall TDMAT/NH_3). This may explain the drop in the chlorine ion intensity around ~75nm from the surface before its rise again at the Sn layer.

The Sn signal started to rise around where the TiN existed due to the expected porosity of the nitride layer, however it reached a constant intensity at ~130 nm depth. On the other hand the SnO_2 signal started to increase way after the metal signal and reached a constant value at a depth of ~175 nm. Such difference in the onset of the metal and metal oxide signals suggests the presence of an oxide layer underneath the metal film at the interface with the silicn substrate, which is also supported by the parallel trend of both the SnO_2 and the SiO_2 signals within the labelled SnO_2 layer (Region IV in Figure 8.3). By tracking the present oxygen signal within the labelled Sn metal layer (Region III in Figure 8.3), it can be found that the signal followed the same intensity drop trend of the TiO_2 signal up to the interficial SnO_2 layer which proposes that both TiO_2 and O_2 signals at the labelled Sn layer (Region III in Figure 8.3) are due to layers mixing because of the aggressive sputtering. The same analysis applies for the thickness of SnO_2 interficial layer, where it appears to be on the order of 10 nm, just because of the occuring ions mixing, during the sputtering, especially at the oxide layer interface with the metal. Although Sn was deposited on a H-terminated silicon surface, prepared by HF etching, some hydroxyl groups might have stayed on the surface and thin tin oxide (SnO_2) layer was formed through their interaction with the first few doses of $SnCl_4$ and DHP. In general, the ToF-SIMS data confirmed the ability of the DHP molecule to reduce $SnCl_4$ to the elemental Sn state (Sn^0).

The high intensities of the Cl and CN signals in the ToF-SIMS plot suggest the presence of these impurities in the Sn film but not their amount, since the SIMS tool has very high sputtering rate and detection sensitivity to these atoms. In its place, XPS was used to study the composition and purity of the capped Sn film. Argon sputtering was used to sputter through the capping layer until Sn and silicon peaks appeared in the scans as shown in Figure 8.3b. Figure 8.4 shows high reslution scans of various peaks for tin (Sn 3d), nitrogen (N 1s), carbon (C 1s) and chlorine (Cl 2p) after 125 min of argon ions sputtering. The Sn 3d spectrum in Figure 8.4a shows sharp Sn-Sn peaks at binding energies of 484.8 and 493.4 eV as well as broader peaks around ~486.5 and ~495.0 eV. Occurrence of broad peaks indicate the presence of multiple tin coordination states in that range and were attributed to SnO, SnO_2 and $SnCl_2$. No further analysis and deconvolution were done for these broad peaks and the concentration of the chlorine atoms in the film was determined using the relevant area under the Cl 2p peaks that are shown in Figure 8.4d. The N 1s spectrum in Figure 8.4b showed two clear peaks at binding energires of ~397.0 and 400.2 eV and were ascribed to TiN and CN respectively and the area under the latter peak was used to determine the concentration of the nitrogen contaminant in the Sn thin film layer. The presence of TiN and TiO_2 were expected since the XPS analysis area was found to be near the edge of the sputtering area, thus some edge effects were observed. Corresponding to the nitrogen-carbon coordination shown in the high resolution scan of the N 1s spectrum, a peak was present in the C 1s spectrum at a binding energy of 281.6 eV as shown in Figure 8.4c. The concentrations of the contaminants in the film have atomic percentages of 3% C, 4% N and 2% Cl. Area under the peaks as well as a relative sensitivity factor (RSF) for each element

were considered during the concentrations calculation by the CasaXPS software. Conversely, films deposited at lower temperature (130 ^{o}C) were found to have a much higher level of contaminants with atmomic percentages of 13 and 9% for nitrogen and chlorine respectively. Figure 8.4e shows the very large differene in the Cl 2p peak instensities for the films deposited at 130 and 190 ^{o}C. The high level of chlorine at the lower deposition temperature is probably due to the slower reaction kinetics with the DHP as well as the higher physisorbtion rate as suggested by the QCM data where continous mass uptake was shown to occur with multiple doses of $SnCl_4$ at 130 ^{o}C. On the other side, slow desorption rate can be the main cause for the high nitrogen contamination where DHP molecule or its byproducts fail to leave the surface during the given purge times for the low temperature depositions. Further analysis on the effect of temperature on the deposited films is discussed in the reduction reaction mechanism section.

Cross-sectional SEM imaging was used to measure the thickness of the Sn thin film layer for the capped sample deposited at 190 ^{o}C. The tin layer was easily identified in the multi-layer coating due to the high contrast between it and the less conductive layers of TiO_2, TiN and silicon, as shown in Figure 8.5. High thickness uniformity of the deposited film was noticed as shown over the ~12 μm width of the sample in Figure 8.5a. Also, the film thickness at three different spots on the sample showed variation of ~1.6% only. The high magnification SEM images shown in Figure 8.5b shows that the tin layer thicknes is ~40 ±2 nm which agrees very well with the determined value (~45 nm) by the less accurate profilometer measurment of the sputtered film using the ToF-SIMS instrument. Very high magnification SEM images could not be acquired to determine the thickness of the tin oxide

interfacial layer and thus the exact metal film thickness. Knowing the exact thickness of the metal, besides the known mass uptake per cycle from the QCM analysis, would have helped in determining the film density and thus its purity.

8.3.3 Reduction Reaction Mechanism

The exact mecahnism through which DHP reduces the metal precursor to its elemental state ($SnCl_4$ to Sn) is not clear yet but some guidlelines were suggested by Mashima et al.[30,31] and Klesko et al.[32] on their work using the DHP in the liquid and vapor phases, respectively. According to their findings, the reduction reaction should proceed through desilylation of the DHP molecule producing trimethylsilyl chloride (TMS-Cl), then the cyclic structure donates electrons to the Sn metal to change its oxidation before leaving the surface as a pyrazine product. Removal of tin-bound chlorine atoms by DHP is also consistent with the QCM data showed in this work, where a net mass loss occcured during the DHP doses. It follows that two possible surface reaction routes can be suggested and are shown in Figure 8.6, where either one or two chlorine atoms are removed from the surface for each DHP molecule. In the first route (1), metal amide covalent bonds are formed between the Sn molecule and the non-oxidized pyrazine molecule. The two bonds might occur on the same Sn molecule or by bridging two nearby molecules. After the metal surface is reduced, the oxidized pyrazine desorbs and leave the surface. Eventually, all the chlorine atoms on the surface will be removed by the incoming DHP, forming a Sn^0 surface. The expected reaction products for this route (1) are TMS-Cl and pyrazine. For the second reaction route (2), only one chlorine molecule is removed for each DHP molecule forming a single metal amide bond. This amide bond will tend to stay on the surface until the next

$SnCl_4$ dose, which will break such bond forming a DHP molecule derivative where a chlorine atom substitutes a trimethylsilyl molecule. Only TMS-Cl is expected to be generated during the DHP exposure while pyrazine based product will be produced during the $SnCl_4$ exposure. The second (2) reaction route is expected to lead to more steric hindrance challenges both during the DHP and $SnCl_4$ exposures which might lead to higher chlorine, carbon and nitrogen contaminants in the deposited film. The reduction reaction mechanism was tested using QMS and in situ FTIR measurements to investigate both reaction routes.

QMS analysis was done to determine the formed products during each reactant exposure. The data collected using analog scans for wide m/z range and through tracking specific m/z values of interest is shown in Figure 8.7. The peaks for both reactants were determined first to try to identify signature peaks for them that do not overlap with those of the expected products like TMS-Cl, pyrazine and their derivatives. To do so, the QMS was connected directly to the hold cell of each reactant so as to minimize the effect of any reactions that may occur on the reactor walls. Also, these analog scans were done after 50 sequential doses of each reactant through the hold cell, gas lines and QMS sampling chamber to make sure that no side reactions will occur during the desired sampling step where each reactant kept flowing continuously for 60 seconds. The spectrum for both reactants is shown in Figure 8.7 a and b. For the $SnCl_4$, m/z 225 was chosen to be its signature peak since it does not overlap with any of the DHP m/z values or those of the expected products. In case of DHP, m/z of 146 was chosen to be the signature peak since all of its major peaks (m/z 53, 65, 80, 73, 74, 76 92, 95) coincides with those of pyrazine (m/z 53, 80) and TMS-Cl (63, 65, 73, 93, 95). Other m/z values that were tracked in this work and were not detected during any of

the dose and purge steps are 188 (1-chloro, 4-trimethylsilyl dihydropyrazine) and 50 (chloromethane).

Due to the overlap between the m/z values of the DHP molecule and those of TMS-Cl and Pyrazine, the change in the partial pressures of these peaks were determined during 5 sequential doses of each of the reactants to test the formation of any of the predicted products. The results for deposition at 190 ^{o}C are summarized in Figure 8.7c. The partial pressure of the $SnCl_4$ peak was very low for the first dose and increased in the next two subsequent doses before reaching nearly constant values, consistent with high consumption of the reactant in the first three cycles to saturate all the available reaction sites in the reactor and the QMS sampling chamber. This result agrees well with the QCM analysis showed earlier for the growth saturation against the reactants exposure. For the DHP peak (m/z 146), the partial pressure was high at the first dose and reached a constant value by the third DHP dose which suggests that a fragment of one or more of the product species share the same m/z value. One possible species that could be identified to have m/z value of 146 was the two bonded trimethl silyl molecules, however its other characteristic peaks either were not present (m/z 131) or did not have the same trend of the change in partial pressure (m/z 74). In general, the peaks TMS-Cl (m/z 65, 73, 93, 95) showed a low partial pressure at the first dose compared to the next four doses which makes it difficult to determine their presence or absence. On the other side, none of these peaks occurred during the $SnCl_4$ dose which strongly suggest that the second reaction route (2) proposed in Figure 8.6 is not occurring or at least below the detection limit of the QMS. Finally, the shown data might suggest the presence of a volatile pyrazine product since the peak for m/z 80 was nearly constant over the

5 sequential doses which might indicate that its production compensated the decrease in the partial pressure due to the DHP consumption. However, the lower partial pressure for m/z 53 peak at the first DHP dose would suggest otherwise. In general, the QMS data confirmed the growth saturation of both reactants as shown earlier by the QCM analysis as well, also it suggested that no exchange reaction occurs on the surface during the $SnCl_4$ dose. Based on that, it can be proposed that the species present on the substrate surface after the DHP dose are either non-reactive to the incoming $SnCl_4$ or it is just a pure Sn surface as hypothesized in the first reaction route (1) shown in Figure 8.6.

In situ FTIR was used to investigate the presence of physisorbed pyrazine molecules on the surface after the DHP doses whether in the oxidized or non-oxidized state (before or after donating electrons to the Sn atoms). Based on the QCM and XPS data showed earlier, higher concentration of contaminants (carbon, nitrogen and chlorine) are present in the films deposited at low temperatures, presumably due to the physisorbed species. The FTIR spectra after different number of exposures on an anodic aluminum oxide (AAO) substrate at 130 and 190 ^{o}C are shown in Figure 8.8 a and b. All the shown spectra are refrenced to the bare AAO spectrum. AAO was used due to its high surface area which will allow higher absorbtion intensities of any present species on the substrate surface. The frequency range of interest (2500-4000 cm^{-1}) is where the absorption peaks for pyrazine are expected and away from the high absorbtion region of Al_2O_3 (~1300 cm^{-1}). The oscillation in the spectrum is due to the beam diffraction by the AAO pores as reported earlier.[33] One clear difference between the spectrum collected at 130 and 190 ^{o}C is the continous increase in absorption over the whole frequency range for the deposition at higher temperature, which indicates a continous

growth of the deposited film. Another possible reason for the high increase in the background absorbtion can be resulting from Drude's absorption due to the formation of metallic film.[34] This difference in infra red absorbance for coatings at low and high deposition temperatures agrees with the earlier QCM results which showed that Sn films nucleate more readily at higher temperatures. For coatings formed at 130 ^{o}C, high positive absorbtion peaks are noticed in the 3100-3400 cm^{-1} and 2800-3000 cm^{-1} frequency ranges, as shown in Figure 8.8a, which can be correlated to nitrogen bond and carbon bond vibrational modes, respectively. Multiple peaks exist within the 3100-3400 cm^{-1} which may indicated different nitrogen coordination due to the presence of neutral pyrazine molecule and its reduced state before losing electrons, also few molecules might be bonded to silyl groups. Concurrently, the C-H vibrations in the 2800-3000 cm^{-1} region have multiple modes where a peak is present at ~2910 cm^{-1} and a shoulder with a small peak at ~2855 cm^{-1}. None of these peaks are present for the coatings done at 190 ^{o}C, as shown in Figure 8.8b, which might suggest that a much faster pyrazine desorbtion is occuring at higher temperatures, in case the reduction mechanism actually follows reaction route (1) shown in Figure 8.6. The hypothesis of the faster desorption of the pyrazine molecules at high temperatures agrees well with the QCM and XPS analysis at the same temperature range that showed self-saturation growth and lower carbon and nitrogen contaminants for films deposited at high temperatures. Nonethless, the presented data is not conclusive about the reaction mechanisms occuring not only during the reduction step but also during the $SnCl_4$ exposure. Further FTIR analysis needs to be carried on a different high surface area substrate than AAO to minimize beam diffraction and increase its transmittance to get higher resolution spectrum to facilitate peaks

identification. Also, more spectra need to be collected at different purge time intervals to confirm if the peaks attributed to pyrazine will be changing in intensity due to its desorption as hypthosized.

8.4 Summary

A new ALD process using $SnCl_4$ and DHP for Sn metal thin film deposition is reported in this work. The process was found to adhere to the key ALD characteristic of self-saturation linear growth as determined by the in situ QCM measurments with an ALD temperature window between 170 to 210 ^oC. Also, deposited films were found to have a good thickness uniformity as depicted by the cross-sectional SEM images for the ~40 nm Sn film on a silicon substrate. ToF-SIMS and XPS analysis showed that the films deposited within the ALD temperature window were metallic with a thin oxide layer at the silicon substrate interface, which was attributed to the presence of a native oxide layer of the substrate material. Consistently, the film deposited at 190 ^oC was found to have low purity levels of carbon, nitrogen, and chlorine contaminants at concentrations of 3, 4 and 2 atomic% respectively. The contaminant concenrations were found to be much higher at lower deposition temperatures which was ascribed to slower reaction and desorption rates, as well as higher $SnCl_4$ physisorption tendency. In situ FTIR and QMS techniques were used to investigate the reduction reaction mechanism using DHP based on the available reports in the literature of plausible reaction routes. The FTIR spectra showed multiple absorption peaks at the 3100-3400 cm^{-1} and 2800-300 cm^{-1} frequency ranges for the film deposited at 130 ^oC which did not exist at the spectrum of 190 ^oC deposition consistent with slower reactants and by-product desorption rates at low temperatures. No volatile byproducts were detcted using

the QMS during the $SnCl_4$ exposure and there were non-conclusive evidences of the formation of TMS-Cl and pyrazine molecules during the DHP exposure. Further work needs to be done to attain a better understanding of the surface chemistry occuring during the $SnCl_4$/DHP ALD. The ability to deposit Sn metals using an ALD process opens new avenues for advancing lithium batteries electrodes and many other applications dependent on the Sn metal alloys.

8.5 Acknowledgments

The authors acknowledge the financial support from the Semiconductor Research Corporation (SRC task# 2401.001). Acknowledgement is also due to the Analytical Instrumentation Facility (AIF) at North Carolina State University, which is supported by the State of North Carolina and the National Science Foundation.

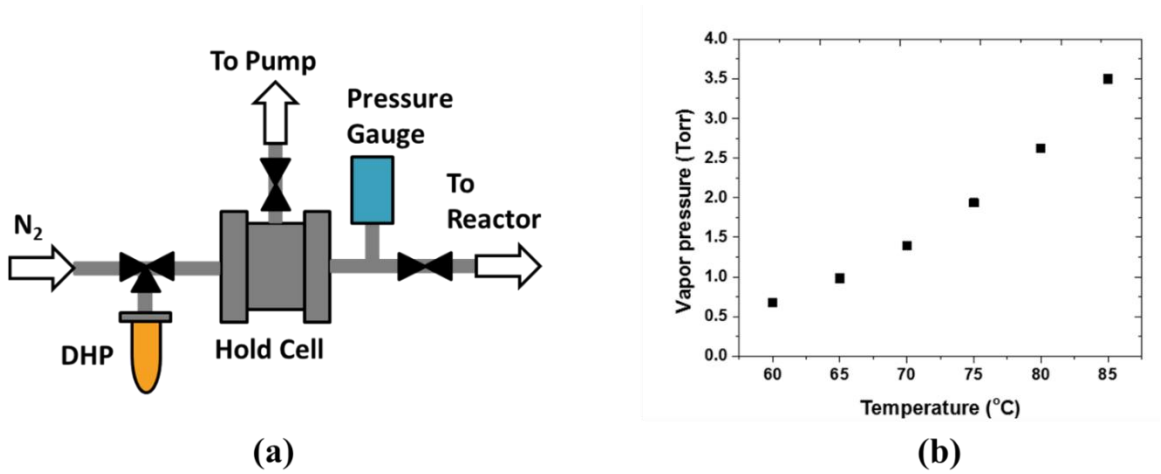


Figure 8.1. (a) A schematic of the precursor delivery setup that allowed measuring the co-reactant (DHP) vapor pressure at different temperatures via a known volume (hold cell). (b) Measured vapor pressure vs temperature. During deposition, the DHP vessel was kept at ~68 °C.

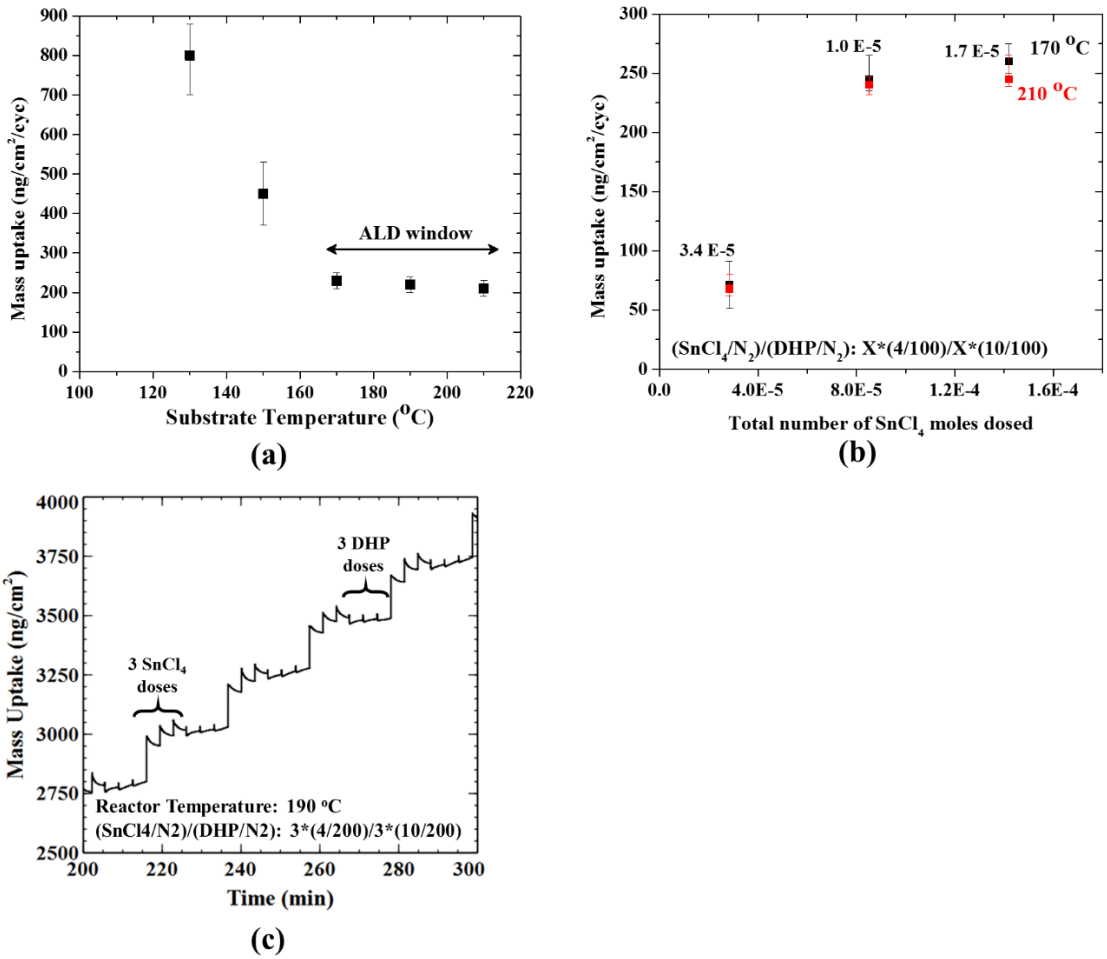


Figure 8.2. Thermal ALD process characteristics for tin deposition using $SnCl_4$ and DHP. (a) Mass uptake per cycle for 3x multi-doses (3x $SnCl_4$/ 3x DHP) at different reactor temperatures between 130 and 210 ^oC. (b) Mass uptake per cycle against the total number of dosed $SnCl_4$ moles at 170 ^oC and 210 ^oC. The number of dosed DHP moles for each $SnCl_4$ exposure is shown besides the data points on the plot. (c) Thin film growth against processing time using three sequential doses of $SnCl_4$ followed by three sequential doses of DHP at 190 ^oC. The results in the figures confirm the self-saturation nature of the $SnCl_4$/DHP ALD process within the shown temperature window.

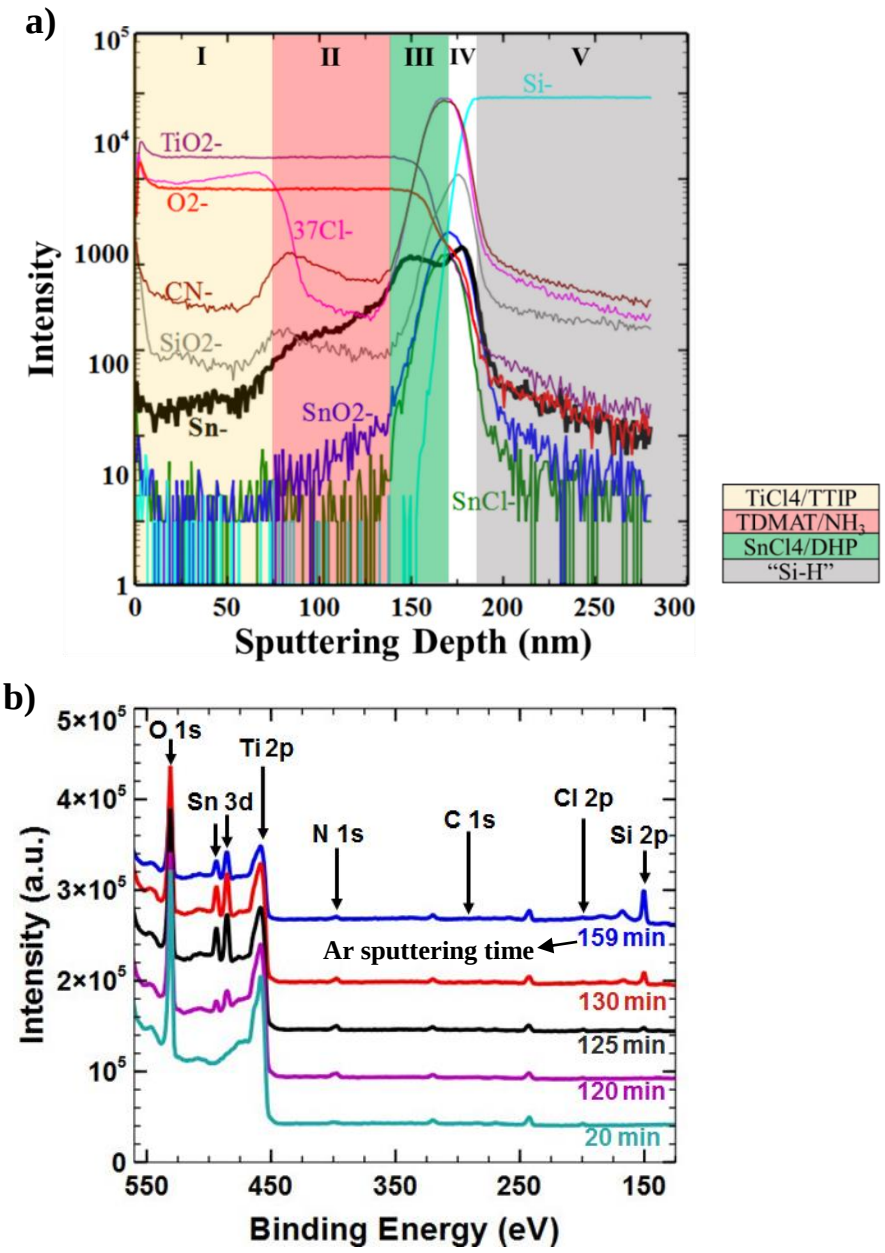


Figure 8.3. Analysis of the deposited tin metal thin film on silicon substrate using 1500 ALD cycles at a deposition temperature of 190 ^{o}C using a) ToF-SIMS and b) XPS depth profiles. The deposited metal was capped by titanium nitride (TiN) and titanium oxide (TiO_2) layers to prevent its oxidation on air exposure for the shown ex-situ analysis.

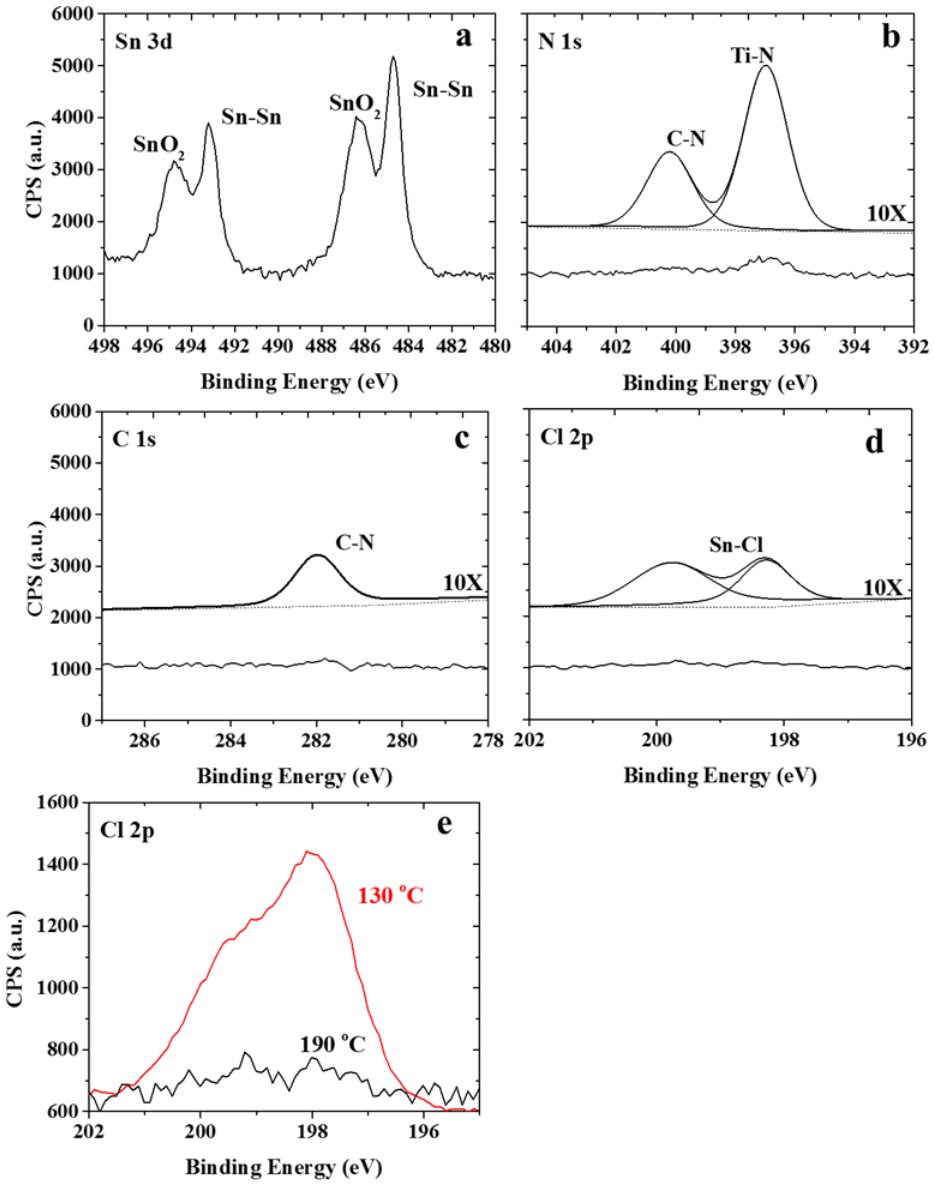


Figure 8.4. High resolution XPS spectra for (a) Sn 3d, (b) N 1s, (c) C 1s and (d) Cl 2p for the tin thin film deposited at 190 ^{o}C and capped with TiO_2 and TiN layers after 125 min of argon ions sputtering. (e) Comparison of the chlorine content in the tin films deposited at 130 and 190 ^{o}C using high resolution XPS for the Cl 2p of both films. Magnified spectra (10X) are also shown for the N 1S, C 1S and Cl 2P scans.

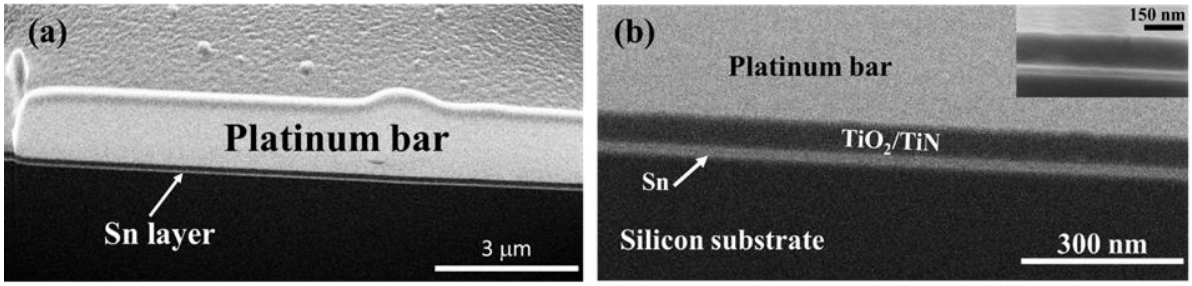


Figure 8.5. Cross-sectional SEM images at (a) low and (b) high magnifications for the capped tin thin film with TiO_2 and TiN. The results confirmed the deposition of a conductive layer of elemental Sn metal with a good thickness uniformity. The high magnification inset image in (b) was used to determine the Sn film thickness.

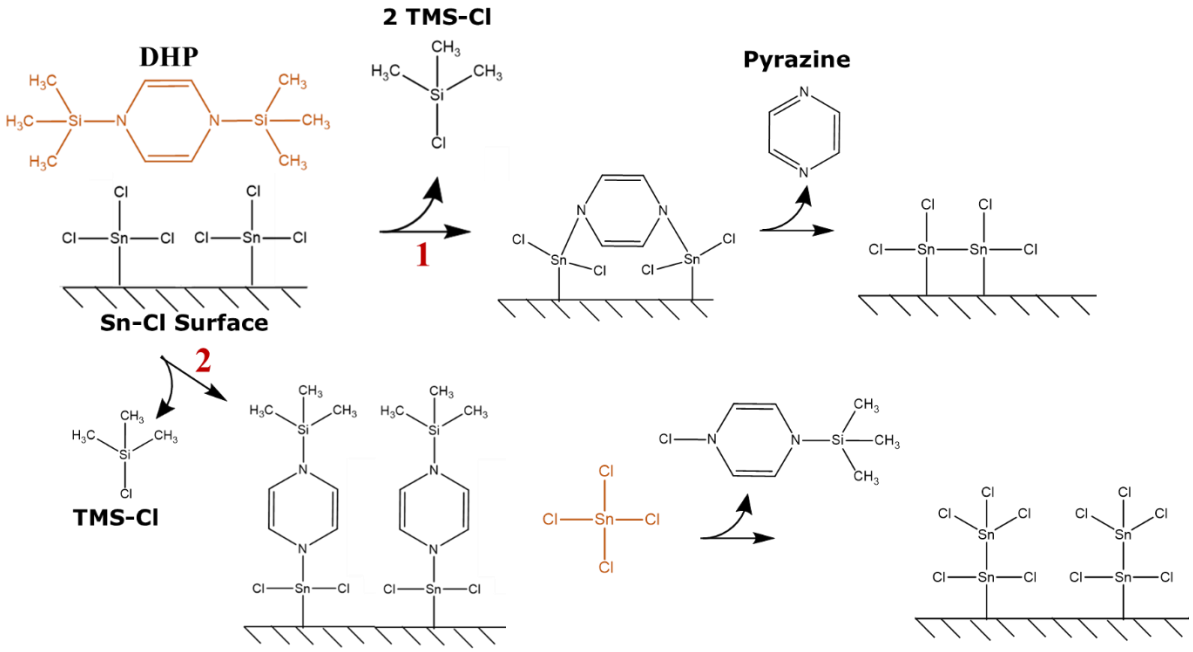


Figure 8.6. Working hypothesis of different reaction paths for the interaction of the DHP with a chlorine terminated surface. (1) Both tri-methyl silyl groups on the DHP strip off chlorine from the surface and leaves behind pyrazine molecule that desorbs later depending on the substrate temperature. (2) One chlorine atom reacts with each DHP molecule to form trimethylsilyl chloride (TMS-Cl) volatile product and leaves a methyl terminated surface which gets chlorinated again during the $SnCl_4$ dose.

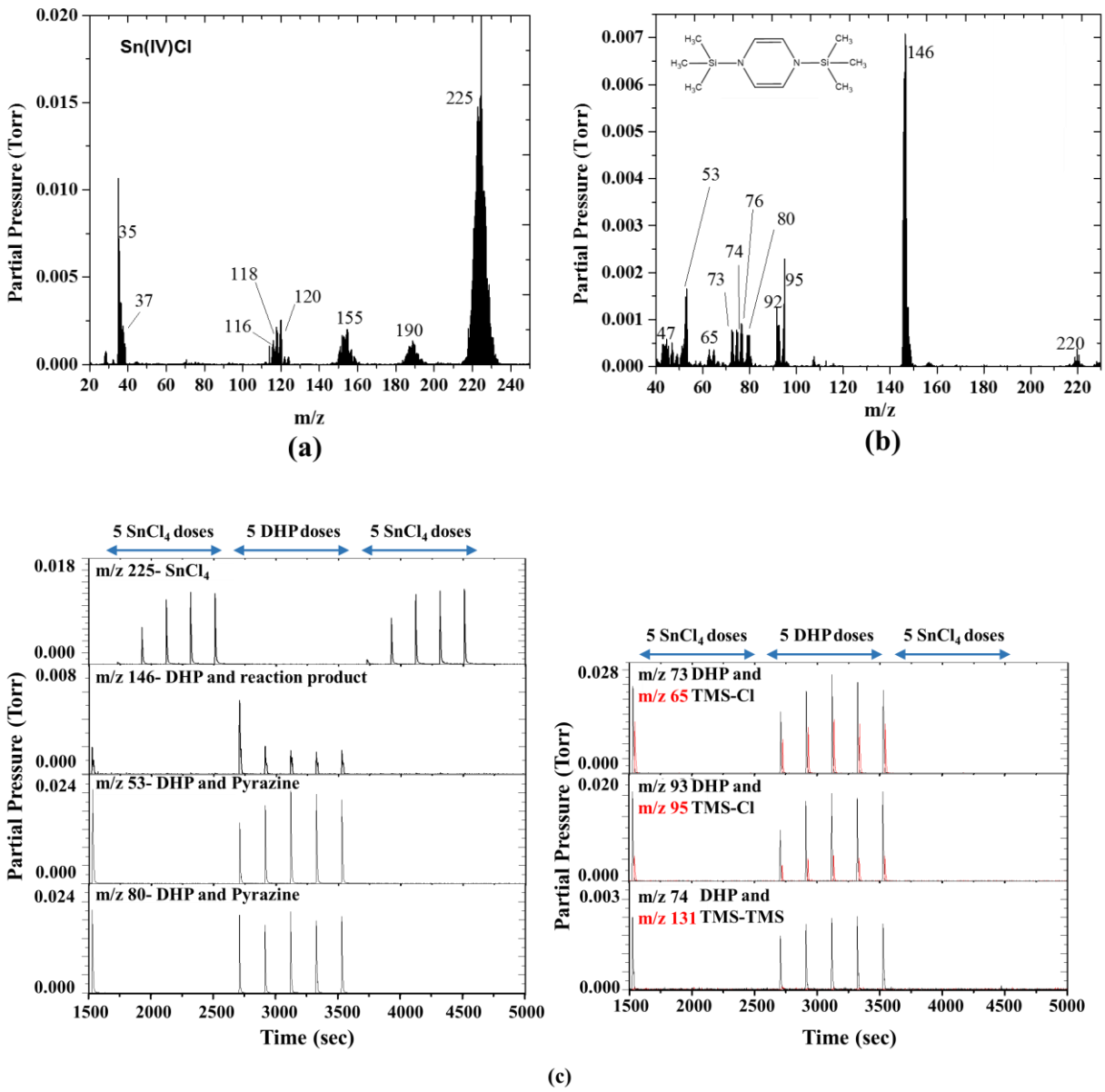


Figure 8.7. In situ QMS data for the $SnCl_4$/DHP ALD process. Analog scans for m/z range 20-240 during (a) $SnCl_4$ and (b) DHP doses through their respective hold cells; the major peaks are labelled. (c) Traces for selected m/z representing various reactant and product species during multiple sequential doses of the reactants.

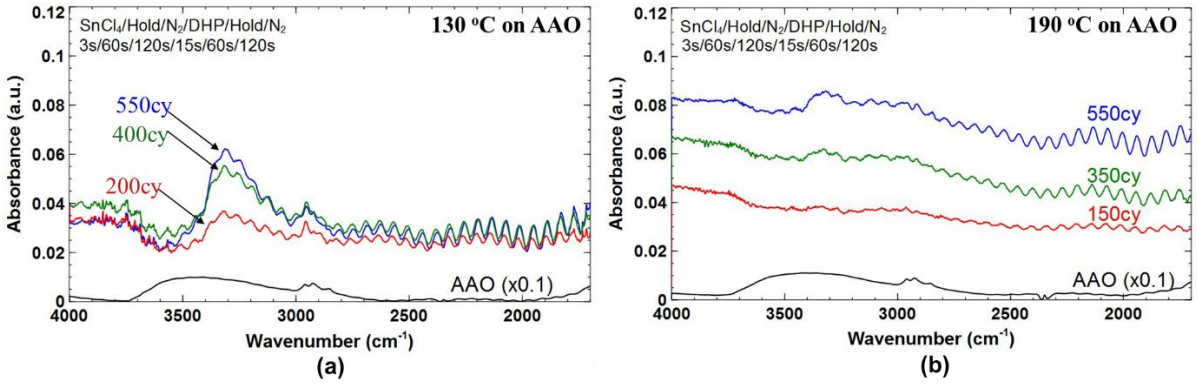


Figure 8.8. In situ FTIR spectra for tin coatings on anodic aluminum oxide (AAO) deposited at 130 ºC and 190 ºC. The spectra were taken after different number of ALD cycles and were referenced to the spectrum of the bare AAO substrate. The exposure and purge sequences for the depositions are also shown on the plots.

8.6 References

(1) Yoshio Nishi, Y.; Doering, R. Handbook of Semiconductor Manufacturing Technology, 2d Ed. December 2007.

(2) Leskela, M.; Ritala, M. Atomic Layer Deposition Chemistry: Recent Developments and Future Challenges. *Angew. Chem. Int. Ed.* **2003**, *42* (45), 5548–5554.

(3) *Atomic Layer Deposition for Semiconductors*; Hwang, C. S., Ed.; Springer US: Boston, MA, 2014.

(4) Knisley, T. J.; Kalutarage, L. C.; Winter, C. H. Precursors and Chemistry for the Atomic Layer Deposition of Metallic First Row Transition Metal Films. *Coord. Chem. Rev.* **2013**, *257* (23–24), 3222–3231.

(5) Lim, B. S.; Rahtu, A.; Gordon, R. G. Atomic Layer Deposition of Transition Metals. *Nat. Mater.* **2003**, *2* (11), 749–754.

(6) Labie, R.; Limaye, P.; Lee, K. W.; Berry, C. J.; Beyne, E.; De Wolf, I. Reliability Testing of Cu-Sn Intermetallic Micro-Bump Interconnections for 3D-Device Stacking. In *Electronic System-Integration Technology Conference (ESTC), 2010 3rd*; 2010; pp 1–5.

(7) Schurr, R.; Hölzing, A.; Jost, S.; Hock, R.; Voβ, T.; Schulze, J.; Kirbs, A.; Ennaoui, A.; Lux-Steiner, M.; Weber, A.; et al. The Crystallisation of Cu2ZnSnS4 Thin Film Solar Cell Absorbers from Co-Electroplated Cu–Zn–Sn Precursors. *Thin Solid Films* **2009**, *517* (7), 2465–2468.

(8) Hirose, Y.; Kahn, A.; Aristov, V.; Soukiassian, P.; Bulovic, V.; Forrest, S. R. Chemistry and Electronic Properties of Metal-Organic Semiconductor Interfaces: Al, Ti, In, Sn, Ag, and Au on PTCDA. *Phys. Rev. B* **1996**, *54* (19), 13748–13758.

(9) Chen, Y.; Kanan, M. W. Tin Oxide Dependence of the CO2 Reduction Efficiency on Tin Electrodes and Enhanced Activity for Tin/Tin Oxide Thin-Film Catalysts. *J. Am. Chem. Soc.* **2012**, *134* (4), 1986–1989.

(10) Hu, R.; Liu, H.; Zeng, M.; Liu, J.; Zhu, M. Progress on Sn-Based Thin-Film Anode Materials for Lithium-Ion Batteries. *Chin. Sci. Bull.* **2012**, *57* (32), 4119–4130.

(11) Tirado, J. L. Inorganic Materials for the Negative Electrode of Lithium-Ion Batteries: State-of-the-Art and Future Prospects. *Mater. Sci. Eng. R Rep.* **2003**, *40* (3), 103–136.

(12) Li, J.; Dozier, A. K.; Li, Y.; Yang, F.; Cheng, Y.-T. Crack Pattern Formation in Thin Film Lithium-Ion Battery Electrodes. *J. Electrochem. Soc.* **2011**, *158* (6), A689–A694.
(13) Alaf, M.; Gultekin, D.; Akbulut, H. Tin/Tinoxide (Sn/SnO2) Nanocomposites Thin Films as Negative-Electrode Materials for Li-Ion Batteries. *Acta Phys. Pol. A* **2013**, *123* (2), 323–325.
(14) Beaulieu, L. Y.; Hewitt, K. C.; Turner, R. L.; Bonakdarpour, A.; Abdo, A. A.; Christensen, L.; Eberman, K. W.; Krause, L. J.; Dahn, J. R. The Electrochemical Reaction of Li with Amorphous Si-Sn Alloys. *J. Electrochem. Soc.* **2003**, *150* (2), A149–A156.
(15) Beaulieu, L. Y.; Hatchard, T. D.; Bonakdarpour, A.; Fleischauer, M. D.; Dahn, J. R. Reaction of Li with Alloy Thin Films Studied by In Situ AFM. *J. Electrochem. Soc.* **2003**, *150* (11), A1457–A1464.
(16) Inaba, M.; Uno, T.; Tasaka, A. Irreversible Capacity of Electrodeposited Sn Thin Film Anode. *J. Power Sources* **2005**, *146* (1–2), 473–477.
(17) Zhang, W.-J. A Review of the Electrochemical Performance of Alloy Anodes for Lithium-Ion Batteries. *J. Power Sources* **2011**, *196* (1), 13–24.
(18) Pu, W.; He, X.; Ren, J.; Wan, C.; Jiang, C. Electrodeposition of Sn–Cu Alloy Anodes for Lithium Batteries. *Electrochimica Acta* **2005**, *50* (20), 4140–4145.
(19) Ui, K.; Kikuchi, S.; Kadoma, Y.; Kumagai, N.; Ito, S. Electrochemical Characteristics of Sn Film Prepared by Pulse Electrodeposition Method as Negative Electrode for Lithium Secondary Batteries. *J. Power Sources* **2009**, *189* (1), 224–229.
(20) Tamura, N.; Ohshita, R.; Fujimoto, M.; Fujitani, S.; Kamino, M.; Yonezu, I. Study on the Anode Behavior of Sn and Sn–Cu Alloy Thin-Film Electrodes. *J. Power Sources* **2002**, *107* (1), 48–55.
(21) Hu, R. Z.; Zeng, M. Q.; Zhu, M. Cyclic Durable High-Capacity Sn/Cu6Sn5 Composite Thin Film Anodes for Lithium Ion Batteries Prepared by Electron-Beam Evaporation Deposition. *Electrochimica Acta* **2009**, *54* (10), 2843–2850.
(22) Audisio, S. Chemical Vapor Deposition of Tin on Iron or Carburized Iron. *J. Electrochem. Soc.* **1980**, *127* (10), 2299–2304.
(23) Homer, H. J.; Orville, C. Gas Plating with Tin. US2916400 A, December 8, 1959.

(24) Arthur, T. S.; Bates, D. J.; Cirigliano, N.; Johnson, D. C.; Malati, P.; Mosby, J. M.; Perre, E.; Rawls, M. T.; Prieto, A. L.; Dunn, B. Three-Dimensional Electrodes and Battery Architectures. *MRS Bull.* **2011**, *36* (07), 523–531.
(25) Meng, X.; Yang, X.-Q.; Sun, X. Emerging Applications of Atomic Layer Deposition for Lithium-Ion Battery Studies. *Adv. Mater.* **2012**, *24* (27), 3589–3615.
(26) Wiley: Encyclopedia of Electrochemistry, Volume 5, Electrochemical Engineering - Allen J. Bard, Martin Stratmann, Digby Macdonald, et al.
(27) Nist X-Ray Photoelectron Spectroscopy Database, Version 4.1. National Institute of Standards and Technology 2012.
(28) Gong, B.; Peng, Q.; Parsons, G. N. Conformal Organic−Inorganic Hybrid Network Polymer Thin Films by Molecular Layer Deposition Using Trimethylaluminum and Glycidol. *J. Phys. Chem. B* **2011**, *115* (19), 5930–5938.
(29) Elam, J. W.; Schuisky, M.; Ferguson, J. D.; George, S. M. Surface Chemistry and Film Growth during TiN Atomic Layer Deposition Using TDMAT and NH3. *Thin Solid Films* **2003**, *436* (2), 145–156.
(30) Saito, T.; Nishiyama, H.; Tanahashi, H.; Kawakita, K.; Tsurugi, H.; Mashima, K. 1,4-Bis(trimethylsilyl)-1,4-Diaza-2,5-Cyclohexadienes as Strong Salt-Free Reductants for Generating Low-Valent Early Transition Metals with Electron-Donating Ligands. *J. Am. Chem. Soc.* **2014**, *136* (13), 5161–5170.
(31) Tsurugi, H.; Tanahashi, H.; Nishiyama, H.; Fegler, W.; Saito, T.; Sauer, A.; Okuda, J.; Mashima, K. Salt-Free Reducing Reagent of Bis(trimethylsilyl)cyclohexadiene Mediates Multielectron Reduction of Chloride Complexes of W(VI) and W(IV). *J. Am. Chem. Soc.* **2013**, *135* (16), 5986–5989.
(32) Klesko, J. P.; Thrush, C. M.; Winter, C. H. Thermal Atomic Layer Deposition of Titanium Films Using Titanium Tetrachloride and 2-Methyl-1,4-Bis(trimethylsilyl)-2,5-Cyclohexadiene or 1,4-Bis(trimethylsilyl)-1,4-Dihydropyrazine. *Chem. Mater.* **2015**, *27* (14), 4918–4921.

(33) Gong, B.; Parsons, G. N. Quantitative in Situ Infrared Analysis of Reactions between Trimethylaluminum and Polymers during Al2O3 Atomic Layer Deposition. *J. Mater. Chem.* **2012**, *22* (31), 15672–15682.
(34) Seghete, D.; Rayner, G. B.; Cavanagh, A. S.; Anderson, V. R.; George, S. M. Molybdenum Atomic Layer Deposition Using MoF6 and Si2H6 as the Reactants. *Chem. Mater.* **2011**, *23* (7), 1668–1678.

Appendix

Appendix A1

The results shown in this section are preliminary and further experiments and analysis need to be done before drawing conclusions.

Three Reactants ALD Process for ZnO Deposition using Diethyl Zinc, Water and Ozone

Zinc Oxide (ZnO) thin films deposited at low temperature ($\leq 150\ ^{o}C$) with controllable electrical properties is of a great interest for flexible electronics and other novel electronics applications. It was reported in the literature that ZnO films deposited using DEZ/O_3 ALD process leads to a higher resistivity films than those deposited using the typical DEZ/H_2O ALD process. Also, in a single report it was shown that a DEZ/H_2O/O_3 ALD process can lead to films of varying resistivity from 6E-3 to 20 Ωcm depending on the ozone dose time.[1]

So far, not many studies were done to understand the chemistry of DEZ/O_3 and its effect on the deposited films conductivity.

In the next pages, results using ex situ measurements (ellipsometery and XPS) and in situ analysis (QCM, FTIR and QMS) are shown for the two reactants (DEZ/H_2O or DEZ/O_3) and three reactants (DEZ/H_2O/O_3) ALD processes.

(1) Min, Y.-S.; An, C.-J.; Kim, S.-K.; Song, J.-W.; Hwang, C.-S. Growth and Characterization of Conducting ZnO Thin Films by Atomic Layer Deposition. *Bull. Korean Chem. Soc.* **2010**, *31* (9), 2503–2508.

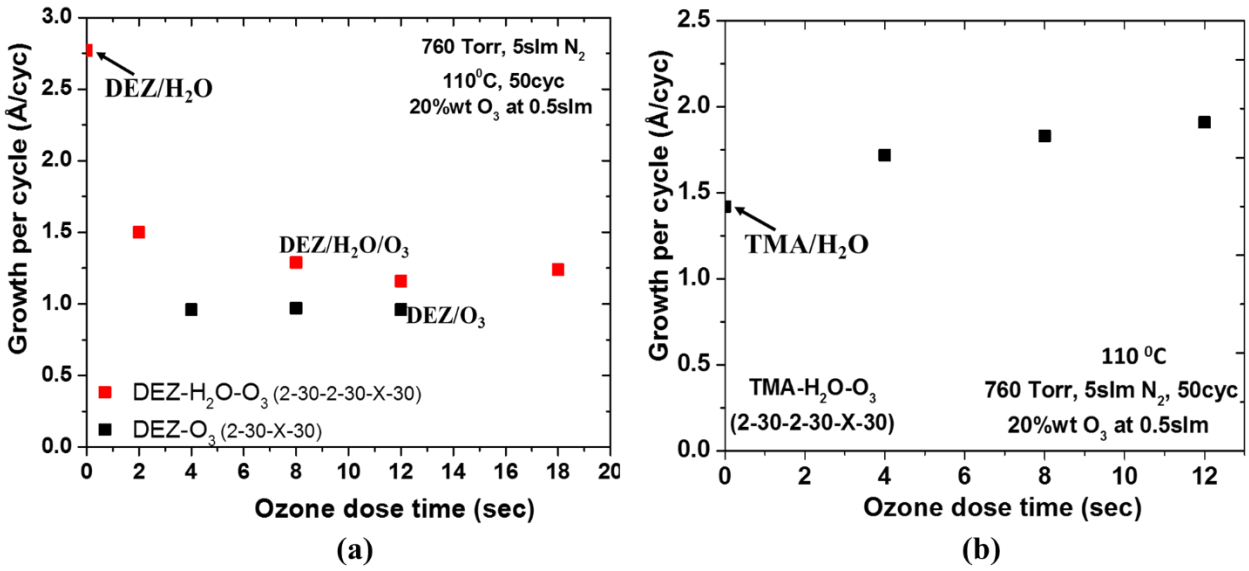


Figure A1.1. Thickness of deposited (a) ZnO and (b) Al_2O_3 films on native oxide silicon using a three reactants process (precursor/H_2O/O_3) against ozone dose time. Spectroscopic Ellipsometry was used to determine thickness. Adding ozone dose to the typical DEZ/H_2O and TMA/H_2O processes has led to a significant change in ZnO growth but a minor one for the Al_2O_3 deposition.

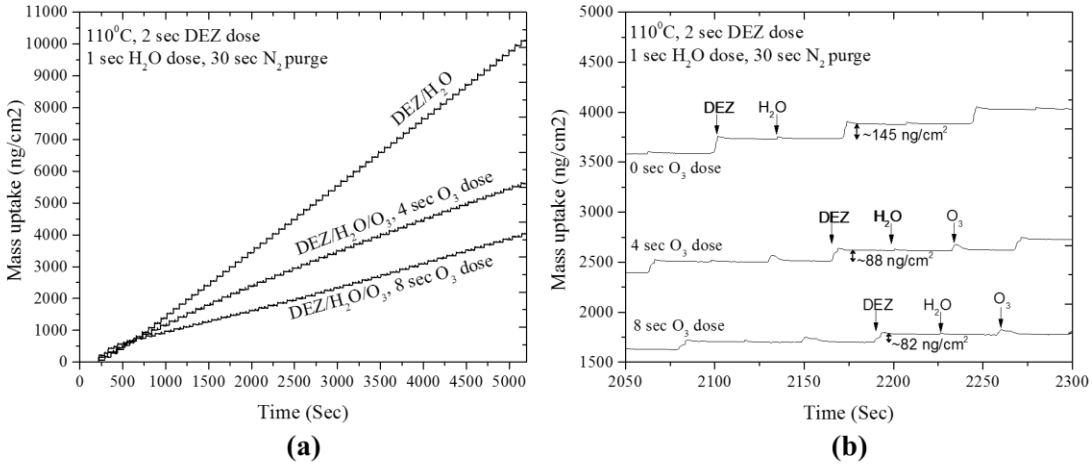


Figure A1.2. Mass uptake against ALD processing time for the two reactants (DEZ/H_2O) and 3 reactants ($DEZ/H_2O/O_3$) processes for ZnO deposition. As the dose time of ozone increases, the average mass uptake decreases. Figure (b) is a close up of (a) and shows that the decrease in mass uptake for longer ozone dose times is due to a lower uptake during the DEZ dose.

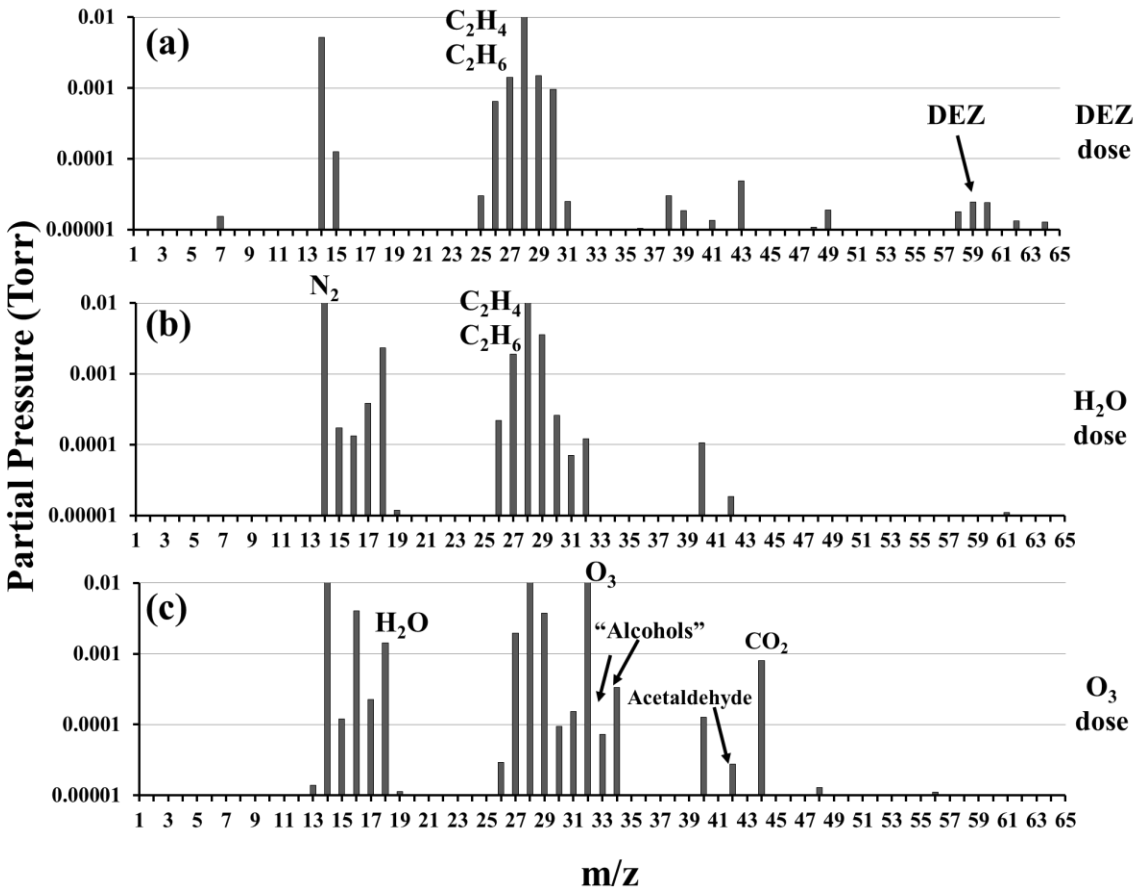


Figure A1.3. QMS analog scans during the doses of (a) DEZ, (b) H_2O and (c) O_3. Some peaks of interest are ascribed to relevant species. The production of CO_2, alcohols and acetaldehyde suggests that ozone leads to a combustion like reaction on the surface even after a long water dose.

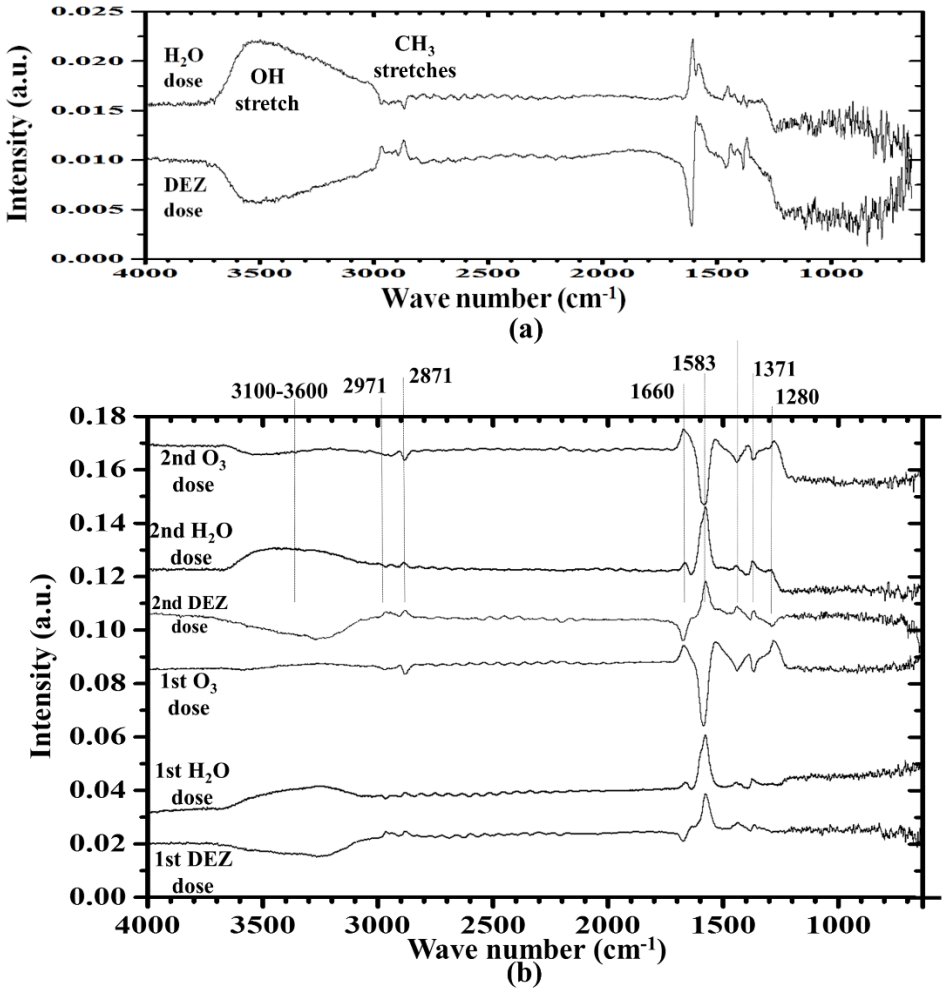


Figure A1.4. In-situ FTIR differential spectra using in situ scans for the two reactants (a) (DEZ/H_2O) and (b) three reactants ($DEZ/H_2O/O_3$) ALD of ZnO. Each spectra was referenced to the one collected from the previous dose and all the runs were done on AAO substrate at 110 ^oC. The spectra were collected after 5 ALD cycles of the same reactants sequence, either DEZ/H_2O or $DEZ/H_2O/O_3$.

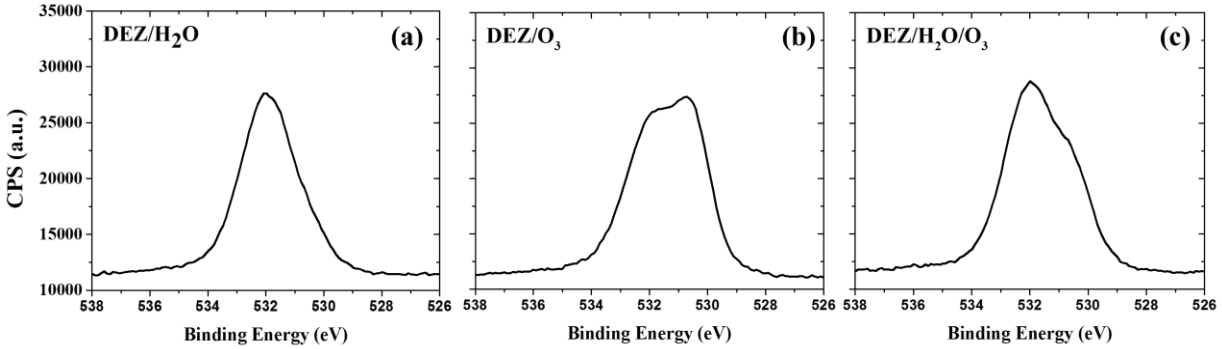


Figure A1.5. High resolution XPS scans of O 1s for ZnO ALD on native oxide silicon using (a) DEZ/H_2O, (b) DEZ/O_3, and (c) DEZ/H_2O/O_3 processes. A clear difference in the oxygen bonding states occurs for the different processes. In general the use of ozone in the ALD process lead to a significant increase in the bonding state occurring at ~530.5 eV binding energy.